CURING AND NANOSTRUCTURE DEVELOPMENT IN EPOXY/BLOCK COPOLYMER BLENDS

Kevin Bogaerts

Supervisors:
Prof. dr. B. Goderis, supervisor
Prof. dr. E. Nies, co-supervisor

Members of the Examination Committee:
Prof. dr. S. De Feyter, chair
Prof. dr. J. W. Seo
Dr. L. Gorbatikh
Prof. dr. M. Smet
Prof. dr. L. Van Meervelt
Dr. C. Gommes (Forschungszentrum Jülich GmbH)

Dissertation presented in partial fulfilment of the requirements for the degree of Doctor of Science (PhD): Chemistry

March 2022

© 2022 Bogaerts Kevin
Uitgegeven in eigen beheer, Bogaerts Kevin, Celestijnenlaan 200F – box 2404

Alle rechten voorbehouden. Niets uit deze uitgave mag worden vermenigvuldigd en/of openbaar gemaakt worden door middel van druk, fotokopie, microfilm, elektronisch of op welke andere wijze ook zonder voorafgaandelijke schriftelijke toestemming van de uitgever.

All rights reserved. No part of the publication may be reproduced in any form by print, photoprint, microfilm, electronic or any other means without written permission from the publisher.

Ter nagedachtenis aan mijn grootvader
die klaarblijkelijk altijd kon volgen als ik over mijn doctoraat sprak
Frans Gebruers (1937-2021)

ACKNOWLEDGEMENTS

Toen ik in augustus 2010 aan mijn doctoraat startte, had ik nooit gedacht dat ik deze acknowledgements pas in 2022 zou kunnen schrijven. Meer dan eens heb ik (en samen met mij ongetwijfeld vele anderen) gedacht dat het er misschien nooit meer van zou komen, maar hier zit ik dan toch, terug te denken aan het hele discours, waar uiteraard vele personen aan hebben bijgedragen. Vandaar dat ik deze kans aangrijp om iedereen te bedanken.

Allereerst zou deze thesis niet mogelijk geweest zijn zonder de stimulatie, expertise en begeleiding van Professor Bart Goderis, mijn promotor. De analyses en modellering waren moeilijke puzzels die door zijn tijd en toewijding mooi zijn opgelost en dus dit werk naar een hoger niveau hebben getild. Mijn oprechte dank, Bart, om ook na de periode dat ik full-time doctorandus was de moed erin te houden.

Zonder financiering is een project als dit ook niet mogelijk, daarom wil ik graag de onderzoeksraad van de KU Leuven bedanken. Mijn werk kaderde in onderzoeksproject GOA/10/004 'New-model based concepts for nanoengineered polymer composites'.

Mijn dank gaat ook naar Professor Erik Nies, voor de input wanneer het nodig was en mijn manuscript voor de preliminaire verdediging nog een keer kritisch na te lezen en enkele suggesties te doen.

Ik heb ook het plezier gehad om enkele studenten te mogen begeleiden, die hebben bijgedragen aan dit werk. In de eerste wil ik graag Anna Lavrenova bedanken, zij heeft heel wat werk verricht met betrekking tot de isotherme uithardingskinetiek. Ook Sander Neyens wil ik graag bedanken voor zijn werk met de koolstofnanobuisjes. Zijn werk is van groot belang geweest om verdere richting te bepalen in mijn thesis.

In an interdisciplinary project as this one, a lot of research is done in other departments, in collaboration with other people. So I would like to express my gratitude to the people of the composites material group of the department of materials engineering. Thank you, dr. Larissa Gorbatikh for sharing your knowledge about material properties. dr. Mohammadali Aravand for helping me around with material properties and dr. Niels Degreef for SEM and TGA measurements. And I would also like to thank dr. Rob Van Hooghten of Chemical Engineering for helping me out with rheology measurements and Anne Spoelstra of the TU/e for fantastic TEM measurements.

I would also like to thank the members of my jury for their constructive feedback. I hope you enjoyed reading this work.

Verder hebben mijn directe collega's van de groep polymeerchemie en -materialen ook bijgedragen door resultaten te bespreken en inzichten te verwerven, en gewoon door er een fijne tijd van te maken. Vooral de ESRF-"nachtjes door" zullen me altijd bijblijven, maar ook onze trips naar congressen en natuurlijke de gezellige office parties en andere randactiviteiten. Dikke merci Steven, Ellen, Maja, Lien, Dorien, Thomas en Olivier.

Ik kan hier zeker ook mijn vrienden niet vergeten. Vanbel, Maarten, Bram, ik heb heel mijn studententijd op jullie kunnen rekenen en dat was tijdens mijn doctoraat niet anders. Nochtans heeft de epoxy voor de SHG laser alleen een verkoold hoopje tot gevolg gehad, en ook dark field microscopie gaf helaas geen resultaat. Maar de middagen kaarten in den Alma, game-nights en allerlei andere activiteiten maakten van mijn studententijd een tijd die ik eigenlijk nooit wilde laten overgaan. Misschien heb ik dat laatste iets té letterlijk genomen;-) Ook nog een speciale vermelding voor 'Sempels' hier. Wouter merci om zo'n lange tijd geïnteresseerd te blijven in de vooruitgang, en te helpen met uw brede kennis, inzichten en contacten waar je kon.

Als laatste wil ik mijn familie bedanken om mijn werk van een afstand te volgen met veel interesse. In de eerste plaats aan mijn mama. Jij hebt mij gemaakt tot wat ik nu ben. Je hebt me altijd alle kansen en vrijheden gegeven waardoor ik mezelf kon ontwikkelen. Bedankt!

Degene aan wie ik het meeste te danken heb, is de vrouw die de hele tijd aan mijn zijde stond. Lieselotte, waar kan ik zelfs maar beginnen?
Sinds het begin van mijn doctoraat zijn er heel wat levensveranderende gebeurtenissen geweest -goede en slechte- en ik ben blij dat jij er altijd was om die samen te beleven. Dankjewel om mij te blijven steunen op de moeilijke momenten, ook al moest je mijn gedachten soms aflezen. Dankje om mij altijd te blijven motiveren en om mij de tijd te geven om nog aan mijn thesis te schrijven, zelfs als je je handen al volhad. Ik had dit nooit tot een goed einde kunnen brengen als jij niet alles gegeven had zoals je hebt gedaan en daarvoor kan ik je nooit genoeg bedanken.

Tieben, Wietse en Yinte: jullie waren misschien nog te klein om het te beseffen, maar ik heb heel wat tijd met jullie gemist tijdens het schrijven van mijn thesis. Ik beloof het goed te maken en zal er altijd voor jullie zijn!

SUMMARY

Throughout the last decades, material research has increasingly been exploring the potential of ordered nanostructures to enhance mechanical, electrical, optical or other properties. Nanostructuring most elegantly happens through processes of self-assembly, being the spontaneous association of molecules, through non covalent bonds.

When amphiphilic molecules, such as surfactants or block copolymers are introduced in a liquid matrix with which only one of the chemical moieties is compatible, nanostructuring is readily realized. When using rather high amphiphile concentrations, progressed molecular stacking may lead to structuring from nanometer to micrometer length scales.

From the perspective of structural materials, solid rather than liquid state structures are required. During material processing challenges arise to transfer the liquid state ordering to the solid state via vitrification or crystallization. Solidification via crystallization in particular may affect structure formation and in fact provides extra means to gain control over the materials' morphology and properties.

Besides purposely synthesized organic molecules, also nanoparticles can be considered to induce nanostructuring. In that case, properties may benefit from the establishment of ordered patterns in their topology, which vastly differ from disordered clusters or homogeneous dispersions within a given matrix. For instance theoretical work in the literature has demonstrated that certain patterns in the location of reinforcing nanoparticles may be very advantageous to the overall material toughness. This toughness increase may furthermore be related to the establishment of structural hierarchy, *i.e.* the presence of structural elements at different length scales. A second application of ordered nanoparticles can be found in nano-electronics, in which the conductivity of ordered nano-dispersions can be exploited for wearables or implantable technology applications. Generating ordered patterns in nanoparticle distributions is challenging and calls for innovative methodologies.

This work aimed at providing new pathways and recipes to generate ordered, nanostructured, solid materials. More specifically, in this dissertation nanostructure formation relied on the assembly of amphiphilic block copolymers when added to an epoxy matrix. Solidification was realized through vitrification of the curing epoxy matrix as well as block copolymer crystallization. The selected diblock copolymer was stearyl-*block*-poly(ethylene oxide$_{20}$), which is rather unique as both the aliphatic and the poly(ethylene oxide) block are crystallizable. The study included systems from very low to very high block copolymer concentrations.

At first the epoxy curing kinetics in the presence of the block copolymer was addressed. In a next stage the nanostructuring potential of the system was explored over the entire compositional range during isothermal epoxy curing and during cooling/heating cycles in the uncured and cured state. Using synchrotron small angle X-ray scattering and wide angle X-ray diffraction in conjunction with transmission electron microscopy, we were able to construct morphology maps involving micelles, vesicles and wormlike structures at low block copolymer fractions and stacked lamellar morphologies at high fractions. Intermediate block copolymer concentrations also exhibited hexagonally packed cylindrical micelles and showed complex transitions between different structures as function of the temperature. These transitions occasionally were triggered by the crystallization of the interconnected block copolymer moieties.

In the last part of this manuscript it was investigated to what extent the studied amphiphilic block copolymers may affect the dispersion and topology of carbon nanotube (CNT) reinforcements when added to a curing epoxy matrix. Unfortunately, it turned out that the block copolymer was not able to affect the CNT dispersion and patterning to any degree. Gaining control over the structural patterning of nanoparticles therefore remains a huge challenge.

SAMENVATTING

Tijdens de laatste decennia groeide het besef in materiaalonderzoek dat de mechanische, elektrische, optische of andere eigenschappen van materialen kunnen worden verbeterd door het oordeelkundig inbrengen van geordende nanostructuren. Nanostructurering gebeurt het meest elegant door processen van zelfassemblage, zijnde de spontane associatie van moleculen, via niet-covalente bindingen.

Wanneer amfifiele moleculen, zoals oppervlakte-actieve stoffen of blokcopolymeren, worden geïntroduceerd in een vloeibare matrix waarmee slechts één van de chemische delen compatibel is, wordt nanostructurering gemakkelijk gerealiseerd. Bij gebruik van vrij hoge concentraties kan de toenemende moleculaire stapeling leiden tot structuren van nanometer- tot micrometer- lengteschalen.

Echter, voor structurele materialen moeten de structuren in een vaste toestand verkeren in plaats van in een vloeibare. Het is dan ook een uitdaging om tijdens materiaalverwerking de structuur van de vloeibare toestand over te brengen naar de vaste toestand via verglazing of kristallisatie. Vooral stolling via kristallisatie kan de structuurvorming beïnvloeden. In feite biedt dit proces extra opties om controle te krijgen over de morfologie en eigenschappen van de materialen.

Naast doelbewust gesynthetiseerde organische moleculen, kunnen ook nanodeeltjes worden toegevoegd om nanostructurering te induceren. Wanneer dergelijke nanodeeltjes zich organiseren tot geordende patronen, kunnen eigenschappen worden gerealiseerd die enorm verschillen van ongeordende clusters of homogene dispersies. Theoretisch werk in de literatuur heeft bijvoorbeeld aangetoond dat bepaalde patronen in de locatie van versterkende nanodeeltjes zeer gunstig kunnen zijn voor de materiaaltaaiheid. Voor een toename van de taaiheid lijkt bovendien de verwezenlijking van een structurele hiërarchie, d.w.z. de aanwezigheid van structurele elementen op verschillende lengteschalen, van belang te zijn. Een tweede toepassing van geordende nanodeeltjes is te vinden in de nano-elektronica, waarbij de geleidbaarheid van geordende nano-dispersies kan worden benut in draagbare of implanteerbare technologische toepassingen. Het genereren van geordende patronen in nanodeeltjesdistributies is een uitdaging en vereist innovatieve methodologieën.

Dit werk was gericht op het vinden van nieuwe routes en recepten om geordende, nanogestructureerde, vaste materialen te genereren. Meer specifiek berustte de vorming van nanostructuren in dit proefschrift op de assemblage van amfifiele blokcopolymeren die aan een epoxymatrix zijn toegevoegd. Het stollen werd gerealiseerd door verglazing van de uithardende epoxymatrix en door

blokcopolymeerkristallisatie. Het gekozen diblokcopolymeer was stearylblok-poly(ethyleenoxide20), wat vrij uniek is omdat zowel het alifatische als het poly(ethyleenoxide)blok kristalliseerbaar zijn. De studie omvatte systemen van zeer lage tot zeer hoge blokcopolymeerconcentraties.

Eerst werd de epoxy-uithardingskinetiek in aanwezigheid van het blokcopolymeer behandeld. In een volgende fase werd het potentieel om nanostructuren te induceren, onderzocht over het volledige samenstellingsbereik tijdens isotherme epoxy uitharding en tijdens koel- en verwarmingscycli in de niet-uitgeharde en uitgeharde toestand. Met behulp van synchrotron kleine hoek röntgenverstrooiing en grote hoek röntgendiffractie in combinatie met transmissie-elektronenmicroscopie, waren we in staat om morfologiekaarten te construeren met micellen, vesikels en wormachtige structuren bij lage blokcopolymeerfracties en gestapelde lamellaire morfologieën bij hoge fracties. Intermediaire blokcopolymeerconcentraties vertoonden daarenboven hexagonaal gestapelde cilindrische micellen en complexe overgangen tussen verschillende structuren als functie van de temperatuur. Deze overgangen werden soms veroorzaakt door de kristallisatie van de onderling verbonden blokcopolymeerdelen.

In het laatste deel van dit manuscript werd onderzocht in hoeverre de bestudeerde amfifiele blokcopolymeren de dispersie en topologie van koolstof nanobuis- (CNT) versterkingen kunnen beïnvloeden wanneer ze worden toegevoegd aan een uithardende epoxymatrix. Helaas bleek dat het blokcopolymeer de CNT-dispersie en patroonvorming niet kon beïnvloeden. Controle krijgen over de structurele patronen van nanodeeltjes blijft daarom een enorme uitdaging.

LIST OF ABBREVIATIONS

CFRP	Carbon Fiber Reinforced Polymer
CNTs	Carbon nanotubes
DETA	Diethylenetriamine
DGEBA	Diglycidyl ether of bisphenol A
DOT	Disorder-order transition
DSC	Dynamic Scanning calorimetry
LC	Liquid Crystal
LCST	Lower critical solution temperature
MDA	Methylene dianiline
MWCNTs	Multi-walled carbon nanotubes
m-XDA	*meta*-Xylene diamine
OM	Optical microscopy
OOT	Order-order transition
PEO	Polyethylene oxide
POM	Polyoxymethylene
RIPS	Reaction induced Phase separation
SAXS	Small angle X-ray Scattering
TEM	Transmission electron microscopy
TGA	Thermogravimetrical analysis
TTT-diagram	Time-temperature-transformation diagram
UCST	Upper critical solution temperature
WAXD	Wide angle X-ray Diffraction

LIST OF SYMBOLS

a_0	cross sectional area of resinophilic head
d_i	mass density of a given compound
E_a	activation energy
F(q)	form factor
f_c	functionalities curing agent
f_e	functionalities epoxy
G*	complex shear modulus
G’	elastic modulus
G’’	viscous modulus
I(q)	intensity as function of the magnitude q of the scattering vector
l_c	length of resinophobic tail
L_p	long period
N	number of layers in a stack
p	packing parameter
q	scattering vector
Q_t	invariant at a given time
r	stoichiometric ratio
R	universal gas constant
S(q)	structure factor
T	temperature
T_{cure}	curing temperature
T_g	glass Transition Temperature
t_α	time at a given conversion
v	volume of resinophobic chains
W_x	weight fraction of compound x in a blend
α	epoxy conversion
α_{gel}	epoxy conversion at the gel point
β	fraction of crystallized phases
γ	sinusoidal strain
δ	phase
ΔG_m	Gibbs free energy of mixing
ΔH_0	total reaction enthalpy
ΔH_m	change of enthalpy upon mixing
ΔH_t	reaction enthalpy at time t
ΔS_m	change of entropy upon mixing
θ	half the scattering angle
λ	wavelength

η^*	complex viscosity
ρ	electron density
σ	shear stress
σ_{LP}	paracrystalline distortion parameter
ϕ_i	composition
ω	angular frequency

TABLE OF CONTENTS

PART I General Introduction, Literature Survey and Methodology 1
Chapter 1: General Introduction 3
1.1 Introduction 3
1.2 Research objectives and scientific approach 4
1.3 Overview of the thesis 5
Chapter 2: Literature survey 7
2.1. Curing, states of aggregation and mechanical properties of thermosetting epoxy resins 7
2.1.1 Curing of epoxy resins 7
2.1.2 States of aggregation of epoxy resins during curing 10
2.1.3 Mechanical Properties 13
2.2. Polymer miscibility and phase behavior 15
2.3. Block copolymer morphologies in solutions and polymer blends 18
2.3.1 Block copolymer morphologies in unreactive blends 18
2.3.2 Block copolymer morphologies in reactive blends 19
2.3.3 Blockcopolymer morphologies and crystallization 21
2.4 CNT dispersions 21
2.4.1 Toughening epoxy resin with CNTs 22
2.4.2 Fine-tuning the CNT topology 23
2.4.3 CNT based nano-electronics 24
Chapter 3: Materials and Methods 25
3.1 Materials and sample preparation 25
3.1.1 Materials 25
3.1.2. Sample preparation 26
3.2 Methods 27
Part II Curing kinetics, thermal behavior and morphology of epoxy/stearyl-block-poly(ethylene oxide) blends 31

Chapter 4: Isothermal curing kinetics and the morphology of epoxy resins with low amounts of block copolymer 33
4.1 Isothermal curing kinetics and morphology of *20%r* 33
4.1.1 Isothermal curing kinetics 33
4.1.2 morphology of 20%r 41
4.1.3 Influence of curing protocol on the morphology of 20%r 54
4.2 Curing kinetics and morphology of 30%r 55
4.2.1 DSC 55
4.2.2 WAXD 58
4.2.3 SAXS 62
4.3 Conclusions 68
Chapter 5: The morphology of pure block copolymer and the isothermal curing kinetics and morphology of epoxy resins with very high amounts of block copolymer 71
5.1. Thermal behavior and morphology of pure Brij® S-20 block copolymer 71
5.1.1. DSC 71
5.1.2 WAXD 71
5.1.3 SAXS 72
5.2 Thermal behavior of *90%r* 76
5.2.1. DSC 76
5.3 Morphology of uncured *90%r* 79
5.3.1 WAXD 79
5.3.2 SAXS 79
5.4 Morphology of cured *90%r* 84
5.4.1 WAXD 84
5.4.2 SAXS 85
5.4.3 TEM 89
5.5 Details on the SAXS pattern modelling 90
5.6 Conclusions 93
Chapter 6 The isothermal curing kinetics and the temperature dependent morphology of epoxy resins with intermediate amounts of block copolymer 95

6.1. The thermal behavior of *40%r* 95
6.1.1 Isothermal curing Kinetics.....95
6.1.2 Cooling and heating prior to curing 97
6.1.3 Cooling and heating after isothermal curing 98
6.2 The morphology of *40%r* during cooling and heating prior to isothermal curing 98
6.2.1 WAXD 98
6.2.2 SAXS 100
6.3 The morphology of *40%r* during cooling and heating after isothermal curing 111
6.3.1 WAXD 111
6.3.2 SAXS 111
6.3.3 TEM 118
6.4 The thermal behavior of *50%r* 118
6.6 The thermal behavior and TEM based morphology of 5*0%r* during cooling and heating after isothermal curing 124
6.7 The thermal behavior of *70%r* 125
6.7.1 Isothermal curing kinetics.....126
6.8 The X-ray based morphology and thermal behavior of *70%r* during cooling and heating prior to isothermal curing.....127
6.9 The thermal behavior and morphology of *70%r* during cooling and heating after isothermal curing 132
6.10 Summary and conclusions 137
Chapter 7: The curing, thermal behavior and morphology of epoxy Brij® S-20 blends as function of the blend composition 141
7.1 Resin curing and vitrification as function of Brij® S-20 concentration 141
7.1.1 Resin curing.....141
7.1.2 Resin vitrification 143
7.1.3 Brij® S-20 crystallization and resin vitrification in uncured blends.....145
7.1.4 Brij® S-20 crystallization and resin vitrification in cured blends.....150
7.2 Concentration-temperature morphology maps 151

Part III The dispersion of carbon nanotubes in epoxy/stearyl-block-poly(ethylene oxide) blends 157

Chapter 8: The carbon nanotube dispersion, epoxy resin curing and morphology of carbon nanotube containing epoxy/stearyl-block-poly(ethylene oxide) blends 159

8.1 Carbon nanotube Brij® S-20 master batches.....159

8.1.1 CNT- Brij® S-20 master batch preparation.....159

8.1.2 CNT dispersion quality in CNT- Brij® S-20 master batches 159

8.2 Epoxy resins loaded with CNTs through CNT- Brij® S-20 master batch mixing.....162

8.2.1 Preparation of CNT loaded Brij® S-20 epoxy resin systems.....162

8.2.2 CNT dispersion quality in CNT loaded Brij® S-20 epoxy resin systems 163

8.2 Epoxy resin curing and morphology of CNT loaded epoxy-Brij® S-20 blends 164

Chapter 9: Conclusions and recommendations for future work.....167

9.1 Conclusions 167

9.1.1 Conclusions Uncured Samples 168

9.1.2 Conclusions regarding the Curing Process and Morphology during Curing 169

9.1.3 Conclusions Cured Samples 170

9.1.4 Conclusions regarding CNT-loaded samples.....171

9.2 Future Outlook.....171

References 173

Health, Safety and Environment.....179

PART I

GENERAL INTRODUCTION, LITERATURE SURVEY AND METHODOLOGY

CHAPTER 1: GENERAL INTRODUCTION

1.1 INTRODUCTION

Throughout history, mankind has never ceased its quest for better materials. Better materials result in a technological advantage, often with a stunning impact. Think of the discovery of bronze, iron and steel which enabled totally new applications and industries. In the last century, focus has shifted to synthetic polymers since they are light, easy to process and raw materials are readily available.

Most recently, polymer material research has been exploring the potential of ordered nanostructures to enhance mechanical, electrical, optical or other properties. Nanostructuring elegantly happens through processes of self-assembly, being the spontaneous association of molecules, through non covalent bonds. When amphiphilic molecules, such as surfactants or block copolymers are introduced in a liquid matrix with which only one of the chemical moieties is compatible, nanostructuring is readily realized. When using rather high amphiphile concentrations, progressed molecular stacking may lead to structuring from nanometer to micrometer length scales.

Besides purposely synthesized organic molecules, also nanoparticles can be considered to induce nanostructuring within polymeric materials. In that case, properties may benefit from the establishment of ordered patterns in their topology, which vastly differ from disordered clusters or homogeneous dispersions within a given polymer matrix. For instance theoretical work in the literature has demonstrated that certain patterns in the location of reinforcing nanoparticles may be very advantageous to the overall material toughness. This toughness increase may furthermore be related to the establishment of structural hierarchy, *i.e.* the presence of structural elements at different length scales. A second application of ordered nanoparticles can be found in nano-electronics, in which the conductivity of ordered nano-dispersions can be exploited for wearables or implantable technology applications.

From the perspective of structural materials, solid rather than liquid state structures are required. During material processing challenges arise to transfer the self-assembled, liquid state nano-ordering to the solid state via vitrification or crystallization. Solidification via crystallization in particular may affect structure formation and in fact provides extra means to gain control over the materials' morphology and properties. Generating ordered patterns in nanoparticle distributions is even more challenging and calls for innovative methodologies.

1.2 RESEARCH OBJECTIVES AND SCIENTIFIC APPROACH

This work aimed at providing new pathways to generate ordered, nanostructured, solid polymeric materials. More specifically, in this dissertation the nanostructure formation due to the self-assembly of amphiphilic block copolymers when added to an epoxy matrix, was investigated. Solidification was realized through vitrification of the curing epoxy matrix as well as block copolymer crystallization. In the last part of this work it was investigated to what extent the studied amphiphilic block copolymer may affect the dispersion and topology of carbon nanotube (CNT) reinforcements when added to a curing epoxy matrix.

Diblock copolymers have been shown to improve the mechanical properties of epoxy particularly when they assemble into vesicles, spherical micelles or wormlike nanostructures.[1–3] Earlier work mostly focused on rather low copolymer concentrations. In this work, we also considered rather high blockcopolymer concentrations as progressed molecular stacking may lead to structuring from nanometer to micrometer length scales and trigger deformation mechanisms typical for hierarchically ordered materials. Focus in this work was, however, on exploring the potential of structure formation, not on mechanical testing.

The selected diblock copolymer was stearyl-*block*-poly(ethylene oxide$_{20}$), which is rather unique as both the aliphatic and the poly(ethylene oxide) block are crystallizable. Inspiration to use this copolymer to guide the dispersion and structuring of CNT's in epoxy was found in earlier work by Blanch et al.[4] who reported that this commercially available surfactant, known as Brij® S-20, can effectively disperse CNTs in aqueous solution.

It seemed therefore worthwhile to explore the potential of Brij® S-20 to bring structure in epoxy resins in the absence as well as in the presence of CNTs. To fully explore the nanostructuring potential of the selected blockcopolymer, the morphology over the entire range of block copolymer concentrations was studied during isothermal curing and during cooling/heating cycles in the uncured and cured state. In the last part of this manuscript CNTs were added to the mixture of epoxy and block copolymer. This part of the research focused on the potential role of the copolymer on the CNT dispersion quality and the overall material morphology.

Introducing nanoscale features within epoxy thermoset materials may affect the epoxy chemistry. Indeed, adding a second component to the epoxy resin may influence the rate and possibly the completeness of the curing reaction, which would affect the material mechanical properties. Therefore, it was judged necessary to also

address the epoxy curing kinetics in the presence of the diblock copolymer surfactant.

1.3 OVERVIEW OF THE THESIS

This thesis is divided in three parts. Part I provides a general introduction (chapter 1), a literature survey and theoretical background (chapter 2) and finally a material and methods section (chapter 3). In part II, the curing kinetics and morphology of diblock copolymer modified epoxy blends in absence of CNTs are discussed. The epoxy curing kinetics and morphology at low, high and intermediate block copolymer concentration are discussed in respectively the chapters 4, 5 and 6. Chapter 7 summarizes these results. Part III consists of chapter 8, dealing with the dispersion of CNTs in block copolymer modified epoxy as well as the morphology of epoxy blends containing CNTs. The thesis ends with general conclusions and an outlook in chapter 9.

Part I: General introduction, literature survey and methodology

Chapter 1 gives a general introduction, followed by the objectives and an overview of the thesis.

In Chapter 2 a literature survey is provided. Epoxy curing, aggregation states and properties are treated in a first section. General aspects related to polymer miscibility and phase behavior are discussed next. Attention is paid to block copolymer morphologies in unreactive and reactive polymer blends. A section is dedicated to crystallization aspects. The last part is devoted to dispersions of carbon nanotubes.

In Chapter 3 the materials including the epoxy resin, curing agent, block copolymer and carbon nanotubes are introduced as well as sample preparation. This chapter is concluded by an overview of the applied methods and devices.

Part II: Curing kinetics, thermal behavior and morphology of epoxy/stearyl-block-poly(ethylene oxide) blends

Chapter 4 is related to epoxy systems in which the block copolymer represents the minority fraction, i.e. samples with 20% and 30% block copolymer. First, the curing kinetics based on Differential Scanning Calorimetry (DSC) are discussed. This is followed by a morphological part, addressing the nanostructure at different temperatures before, during and after curing. It will be shown that the morphology is predominantly vesicular. Morphological information is retrieved from transmission electron microscopy (TEM), time-resolved small angle X-ray scattering (SAXS) and wide angle X-ray diffraction (WAXD). Modelling of the SAXS patterns revealed details of the vesicle walls during the course of curing.

Chapter 5 discusses the morphology of the pure block copolymer as well as of epoxy blended with 90% block copolymer. Based on SAXS experiments, the blend morphologies in these cases appeared to be exclusively layer like during cooling and heating, before as well as after curing.

In Chapter 6, blends of intermediate composition are discussed. The morphology of these samples after curing is layer like and hence resembles that of the low and high concentration samples. Non-cured samples of intermediate composition occasionally display non-layered structures besides layer like ones. All structures and their transitions are identified and characterized by DSC, WAXD and SAXS.

Chapter 7 is devoted to summarizing and discussing the concentration dependent thermal behavior and morphology of epoxy Brij® S-20 blends. The data presented in the chapters 4, 5 and 6 are grouped in single graphs for comparison.

Part III: The dispersion quality and morphology of epoxy/stearyl-block-poly(ethylene oxide) blends with carbon nanotubes

The emphasis in Chapter 8 is on the dispersion quality of carbon nanotubes when added to the investigated epoxy Brij® S-20 systems. This assessment predominantly relies on rheological and microscopic methods. It will be demonstrated that the dispersion is very poor and that an extensive aggregation of carbon nanotubes occurs.

Finally, in chapter 9, general conclusions and suggestions for future work are presented.

CHAPTER 2: LITERATURE SURVEY

2.1. CURING, STATES OF AGGREGATION AND MECHANICAL PROPERTIES OF THERMOSETTING EPOXY RESINS

2.1.1 CURING OF EPOXY RESINS

The curing reaction of an epoxy resin is a process in which at least two reactants, i.e. an epoxide and at least one curing agent (hardener), are transformed from a mixture of low molecular mass substances to a highly cross-linked polymeric structure.

Epoxies are molecules that contain one or more epoxide functional groups (Figure 2.1a). The epoxide group is planar with a three-membered ring composed of one oxygen and two carbon atoms. Its high reactivity results from the high ring strain. Most commercial epoxy resins are prepared from bisphenol A and epichlorohydrin, such as diglycidyl ether of bisphenol A (DGEBA) or an oligomer thereof as displayed in Figure 2.1b, which is one of the most commonly used epoxy resins.

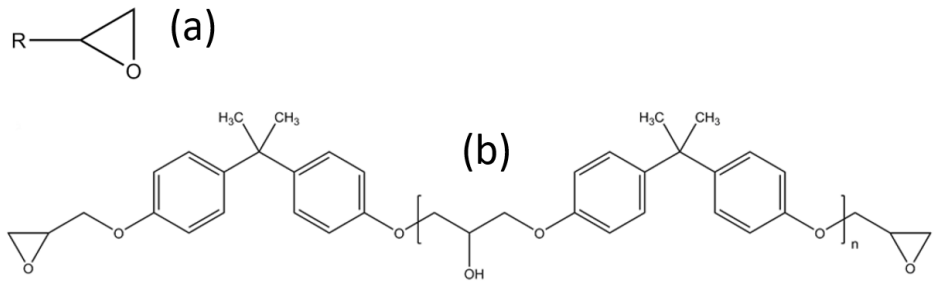


Figure 2.1: (a) Epoxide functional group and (b) Oligomer of Diglycidyl ether of bisphenol A (DGEBA)

Curing agents play an important role in the curing process of an epoxy resin as they influence the reaction rate, degree of cure, viscosity and final properties of cured products, such as hardness, flexibility, T_g, and so on. Especially the amount of functionalities on both the curing agent and the epoxy itself has a massive effect on states of aggregation and the properties. All nucleophiles can be good curing agents for epoxy resins. Amines are widely used as curing agent and different studies addressed their reactivity[5–8]. Compared to aliphatic amines, aromatic amines are less harmful to people but at the same time less reactive. Common examples of amines used as curing agents are diethylenetriamine (DETA, Figure 2.2a) and methylene dianiline (MDA, Figure 2.2b).

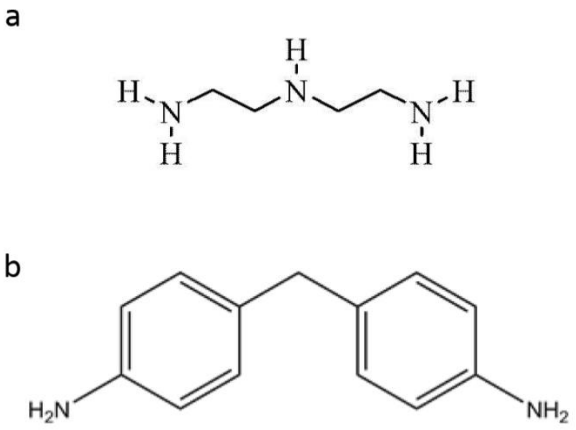


Figure 2.2: a) Diethylenetriamine (DETA), b) Methylene dianaline (MDA)

The curing reaction can be seen as the repeated process of the ring-opening reaction of epoxides, producing a higher molecular weight which finally results in a three-dimensional structure.[6] The classical epoxy curing mechanism based on amine hardeners involves three main reactions[9] and is illustrated in Figure 2.3. The two first reactions are called crosslinking reactions and involve a nucleophilic attack on one of the epoxy carbons by an amine. The last reaction, commonly called homo-polymerization, is a reaction between a hydroxyl and an epoxide group, leading to an ether. However, it is generally accepted that etherification occurs only at high temperatures, once all primary amines are exhausted or in the presence of large excess of epoxy groups.[10]

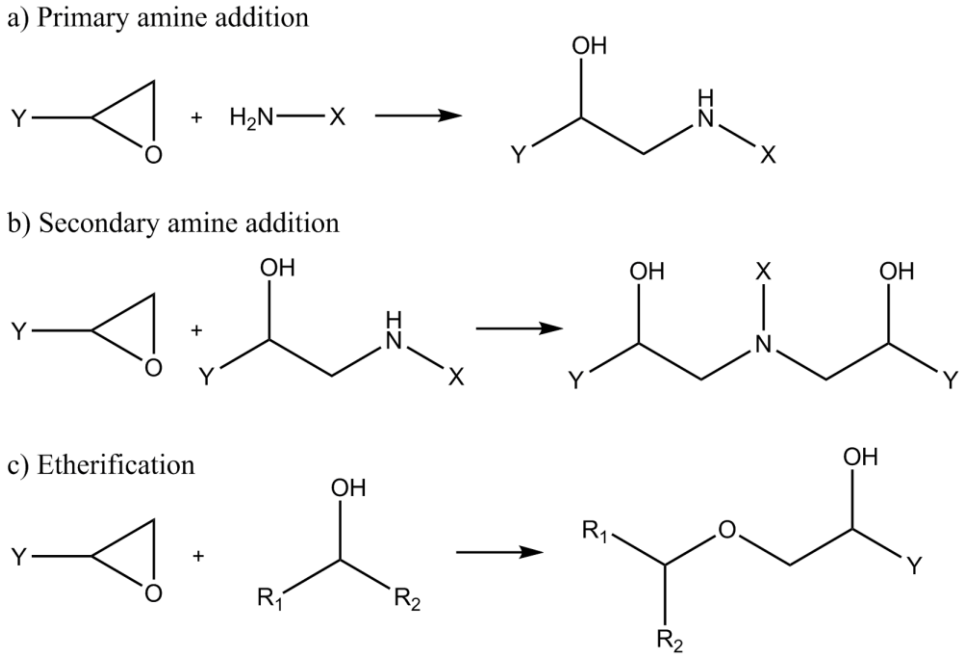


Figure 2.3: Curing process of an epoxy resin by amine hardeners[9] (a) Primary amine addition, (b) secondary amine addition, (c) etherification.

The process of epoxy curing is autocatalytic because the presence of hydroxyl groups facilitates the ring-opening reactions.[9,11]

It is known that the reactivity of primary amines is higher than that of secondary amines. An example is given in figure 2.4, by Paz-Abuin et al, with DGEBA as epoxy and *meta*-xylene diamine (m-XDA) as curing agent[12]. Initially, primary amines are being consumed by the curing reaction, transforming into secondary amines ([A1] in Figure 2.4 decreases, while [A2] increases). Secondary amines [A2] only begin to convert into tertiary amines [A3] once 40% of the primary amines [A1] have converted into secondary amines. Beyond that point the amount of secondary amines keeps increasing until 80% of the primary amines are consumed, implying that the reaction from primary to secondary amines remains faster than the subsequent reaction to tertiary amines until secondary amines are present in excess.

The ratio between the rate constant of the secondary amine addition and that of the primary amine depends on the electron donating properties of the amine and may vary with temperature.

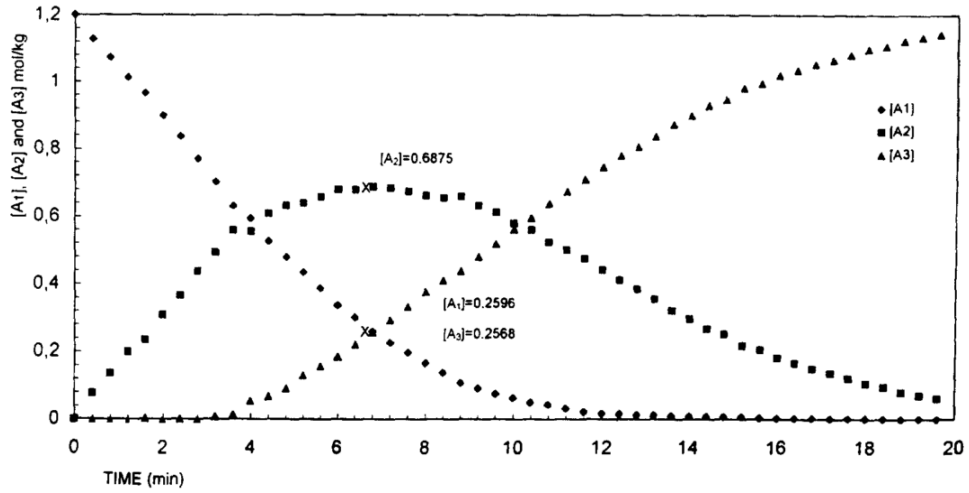


Figure 1.4: Variation of the concentrations of primary [A1], secondary [A2] and tertiary [A3] amines as a function of reaction time for meta-xylene diamine curing with DGEBA.[12]

As the reaction proceeds, the crosslinking density increases, leading to a reduction of the free volume and molecular mobility by which the curing regime changes from a kinetically controlled to a diffusion controlled process[13]. This transition occurs when the (increasing) material glass transition temperature (T_g) has reached the reaction temperature or when reagents become depleted. In the latter case, also diffusion becomes the rate determining step, even at temperatures above T_g. Also gelation can play a role here: when the reaction reaches very high conversion, some unreacted functionalities can be physically separated, unable to react further, even when being above the T_g. Vitrification and gelation are discussed in more detail in section 2.1.2.

Crosslinking during the curing reaction results in a significant entropy decrease. However, it is the exothermic reaction enthalpy which drives the process and which makes the Gibbs free energy change negative. Thus, curing is a thermodynamically spontaneous process and will proceed if the temperature is high enough to overcome the kinetic barrier of the activation energy.

2.1.2 STATES OF AGGREGATION OF EPOXY RESINS DURING CURING

The curing process begins with the formation of a chain which branches and subsequently crosslinks. As the curing reaction proceeds, the molecular weight increases fast and finally all chains become linked together into a tight network (Figure 2.5). During the formation of an epoxy network, two main transformations can take place: gelation and vitrification.

Gelation is a transition that can take place during polymerization. The exact point at which this transition occurs is called the gel point. At this point the polymer network spans the entire sample volume, which according to the Flory-Stockmayer equation (Eq. 2.1)[14] occurs when a polymer chain theoretically reaches an infinite molecular mass.

$$\alpha_{gel} = \left[\frac{1}{(f_e-1)(f_c-1)}\right]^{1/2} \qquad \text{(Eq. 2.1)}$$

In equation 2.1, α_{gel} is the conversion degree at gelation, f_e and f_c are the functionalities of the epoxy and curing agent respectively. This equation provides a means to estimate at which conversion degree gelation sets in for stoichiometric mixtures. It reveals that the higher the functionality of both reactants, the sooner gelation sets in. Gelation is of course of great interest for polymer processing. Beyond the gel point, a polymer no longer flows and is therefore no longer processable. On the other hand, it does not inhibit the curing reaction.

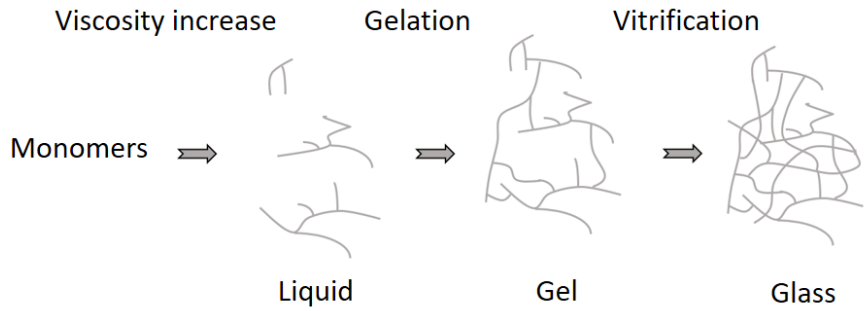


Figure 2.5: Schematic representation of the physical changes occurring during the curing of epoxy resin.

Another transition which a thermoset resin may undergo during curing is vitrification. Epoxies are amorphous materials, meaning that they are glassy and brittle below their glass transition temperature (T_g) and liquid or rubbery above their T_g. The glass transition temperature of epoxy resins increases upon curing. Vitrification thus occurs when T_g reaches the curing temperature. At this point, the material is transformed from a gel (or a liquid) into a glass. The onset of vitrification causes a shift from a kinetically controlled to a diffusion controlled reaction, resulting in a curing retardation (cfr. supra). Eventually curing ceases.

The different transformations that are observed during the curing of epoxy with a curing agent are generally cast into a time-temperature-transformation (TTT) diagram.[15–17] A typical example is shown in figure 2.6. In this diagram, temperatures are plotted as a function of the logarithm of isothermal curing time and

transformations (vitrification and gelation) are marked. Because the reaction rate varies exponentially with temperature, the time is represented in a logarithmic scale. The S-shaped gelation vitrification curve and the gelation line divide the TTT diagram into five distinct stages: liquid, gelled rubber, ungelled glass, gelled glass and char. The glass transition temperature of the initial formulation is denoted as T_{g0}.

Isothermal curing in this diagram is represented as a horizontal line at the given curing temperature. During curing, the growing network densifies until after a certain time it vitrifies. This happens at the time when the curing temperature coincides with the S-shaped T_g line in the TTT-diagram. At this stage, vitrification takes place and the reaction stops. The isothermal curing reaction can only start at $T_{cure} > T_{g0}$. At one particular temperature, $T_{g,gel}$, the liquid is directly transformed into a gelled glass. If the material is cured at a temperature between $T_{g,gel}$ and the glass transition temperature of fully cured epoxy resin ($T_{g\infty}$), gelation occurs prior to vitrification. If the polymerization reaction of a thermoset occurs at $T_{cure} > T_{g\infty}$, firstly a gelled rubber is formed and ultimately the undesirable char region can be reached.

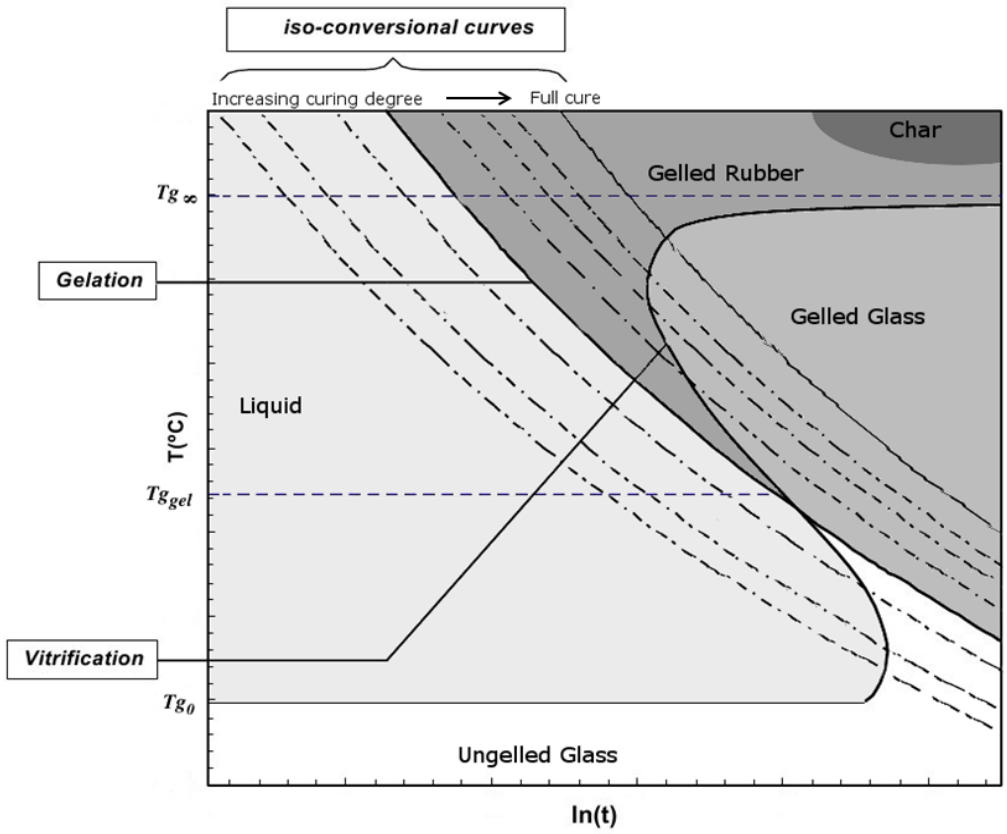


Figure 2.6: Time-temperature-transformation diagram, showing in which state an epoxy can be when imposing a certain temperature, T, during a certain time, t. (adapted from Perrin et al.[17])

The TTT diagram can be converted into a Conversion Temperature Transformation (CTT) diagram by changing the time scale into a conversion scale[18]. A typical example is shown in Figure 2.7. A CTT diagram is particularly important if one wants to follow non-isothermal polymerizations. In this diagram, three typical curves are shown: gelation, vitrification and degradation. The degradation curve represents the boundary with the high-temperature char region. It has been experimentally verified that the stability of thermosets to thermal degradation increases with increasing conversion.[19] The initial formulation (X = 0) may either be present as a liquid or as an ungelled glass, depending on the initial T_g. As the reaction proceeds and conversion increases, gelation occurs. Gelation involves the transition from an ungelled glass to a gelled glass or from a liquid to a rubber. In this diagram, the conversion at gelation is shown to be independent of temperature. The conversion at which vitrification occurs, on the other hand, increases with curing temperature due to the larger amount of free volume at high temperatures, requiring a higher degree of crosslinking, hence conversion.

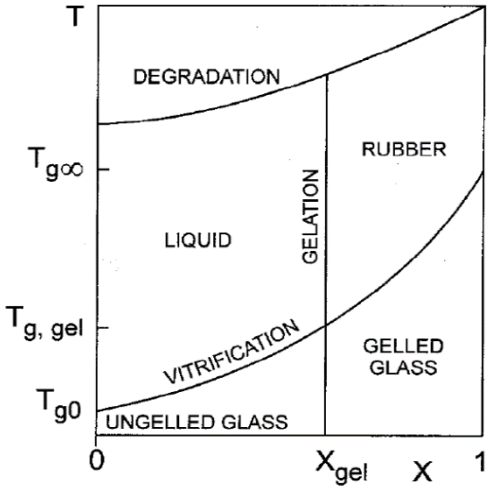


Figure 2.7: A CTT diagram defines the state of a material after being at a certain temperature at a certain conversion degree. The vertical axis displays the temperature (T) while the horizontal axis displays the conversion degree (X). (Adapted from Goossens et al [20])

2.1.3 MECHANICAL PROPERTIES

Thermosetting epoxy resins combine lightweight with high strength and stiffness and their thermoset character facilitates processing, making them seemingly ideal for e.g. the fabrication of fiber reinforced polymer composites. However, challenges remain. As epoxy resins are brittle, parts made from such resins or composites generally need to be over-dimensioned in order to pass fatigue tests undergoing repeated stress cycles.

Traditionally, thermosetting resins are toughened by blending with rubbers[21–23]. Unfortunately, while enhancing toughness, mixing rubber into an epoxy matrix also reduces the overall material stiffness and creep resistance. More recently, other routes of toughening have been explored.

A first alternative strategy involves blending a thermoplastic polymer to the epoxy resin rather than a rubber[24–29]. The rationale behind this approach is that when a thermoplastic polymer with a high glass transition temperature (T_g) is used, the toughness might be improved without seriously undermining the other properties. Quite often the components prior to resin curing are miscible while a reaction induced phase separation (RIPS) happens during the curing step. The RIPS-induced morphology can be quite complex and in general strongly depends on the blend composition, the epoxy curing temperature and reaction time.[30,31] Ali et al[32] explored the mechanical properties of epoxy resins, hierarchically structured by RIPS with polyoxymethylene (POM)[29]. A higher toughness was indeed found for the matrix in its pure form, but the properties of fiber reinforced composites based on this matrix were not resulting in the aspired effect. Controlling the morphology proved rather difficult, especially in the presence of carbon fibers. A poor reproducibility of the material morphology and hence properties is not desired. Furthermore, by blending with POM, the epoxy resin viscosity readily increased to unpractical levels.[32,33] The too high viscosity prevented a full penetration of the resin blend in between the composite fibers. The addition of low molecular weight diblock copolymers has also been shown to improve the mechanical properties of epoxy particularly when they assemble into vesicles, spherical micelles or wormlike nanostructures.[1–3] Because of their low molecular weight, such molecules evidently contribute less to the viscosity, which is an advantage for processing.

A second route is the addition of nano-reinforcements. Multiple publications have demonstrated that the homogeneous distribution of nano-particles[23] like silica[34], minerals[35] or carbon nanotubes[36–44] increase various material properties. However, it remains a challenge to disperse the nano-particles fully and quite often improvements on mechanical properties are limited to postponing fracture while the material essentially remains brittle. In section 2.4.1, a state of the art related to the toughening of epoxy resins with carbon nanotubes is provided.

Interestingly, a synergistic effect has been reported by Kinloch et. al.[45] when rubber and nanoparticles were added to the epoxy resin at the same time. The toughness increase was higher than expected from the sum of the individual increases. This observation might be related the hierarchical nature of the material morphology. It has been stated that when nano- and micrometer sized elements are ordered in a

suited way, the deformation mechanism may alter at the benefit of the overall material properties[46,47].

2.2. POLYMER MISCIBILITY AND PHASE BEHAVIOR

Mixtures of different components can exist either in a homogeneous or a phase separated (demixed) state. This can be thermodynamically expressed in terms of the Gibbs free energy of mixing (ΔG_m):

$$\Delta G_m = \Delta H_m - T\Delta S_m \quad \text{(Eq. 2.2)}$$

With ΔH_m and ΔS_m the change of enthalpy and the change of entropy upon mixing respectively, and T the absolute temperature. At a constant temperature and pressure, two conditions have to be fulfilled to ensure complete miscibility:

$$dG_m \leq 0 \quad \text{(Eq. 2.3)}$$

$$\left(\frac{\partial^2 \Delta G_m}{\partial \phi_i^2}\right)_{T,p} > 0 \quad \text{(Eq. 2.4)}$$

For binary mixtures, i = 2 in Eq. 2.4. If both conditions are fulfilled at all compositions, the system is completely miscible, depicted as curve A in Figure 2.8. If only the first condition is fulfilled, the system with e.g. a composition ϕ_1 (curve B) tends towards a lower ΔG_m by phase separating into phases with compositions ϕ_1' and ϕ_1'', despite ΔG_m already being negative for the mixed state. Curve C represents the free energy change for a partially miscible polymer system.

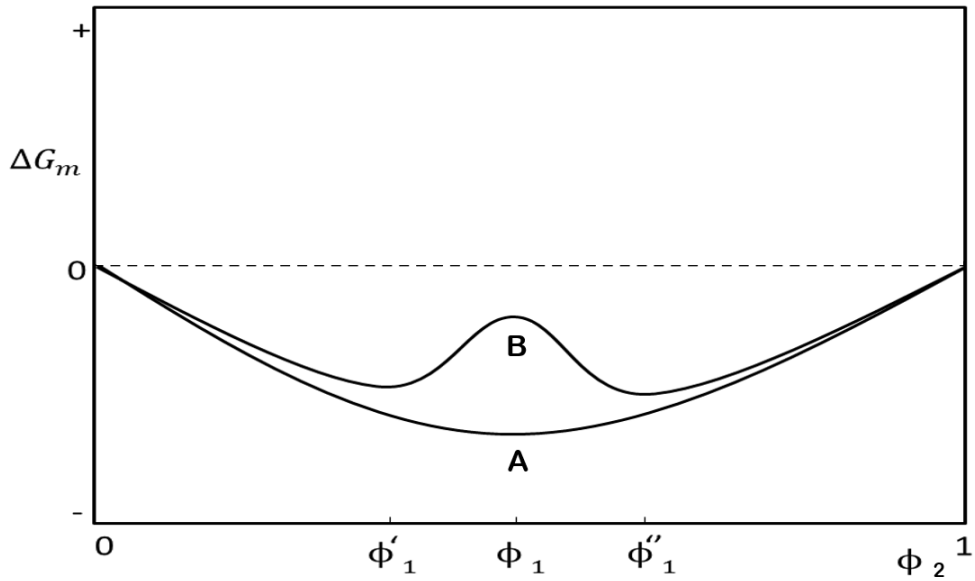


Figure 2.8: Curve A represents the free energy change (ΔG_m) for a completely miscible system, implying that that the conditions given by equations 2.3 and 2.4 are both fulfilled at all compositions. Curve B represents the situation for a partially miscible system as the first but not the second condition is fulfilled.

Phase separation in a polymer blend can occur both during heating and cooling, depending on temperature dependencies of ΔH_m and ΔS_m. Mixtures often turn opaque when phase separation happens.[48] The point at which the first sign of phase separation can be observed is called the cloud-point. If phase separation occurs during heating, the minimum of the cloud-point curve (shown in figure 2.9) is called the lower critical solution temperature (LCST). If phase separation occurs upon cooling, the maximum of the curve is the upper critical solution temperature (UCST). Below LCST and above UCST, the blend is completely miscible at all compositions. Crossing the cloud point curve induces phase separation.

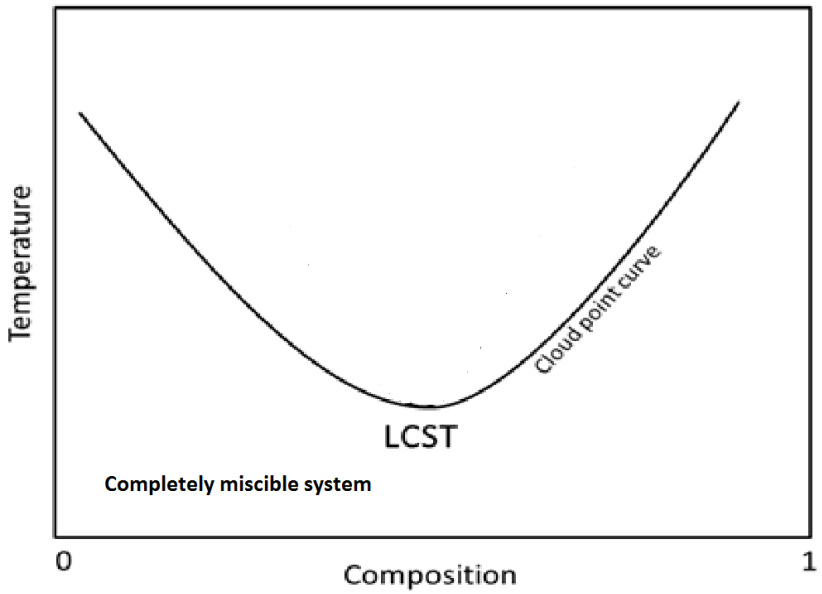


Figure 2.9: A schematic plot of the liquid-liquid phase behavior in a binary mixture of a monodisperse polymer and a solvent with an LCST.

The molar mass of a thermosetting resin increases during the polymerization. When this resin is part of a polymer blend, this leads to a decrease of the entropic contribution to the Gibbs free energy of mixing. Together with an unfavorable enthalpy of mixing liquid-liquid phase separation can occur. This process is called Reaction Induced Phase Separation (RIPS).

Phase separation can occur at different length scales. A mixture of two homopolymers can phase separate at macroscopic or microscopic level, depending on the mobility. If the mixture is very mobile, macroscopic phase separation is possible, otherwise diffusion is limited, leading to microscopic phase separation. The latter occurs e.g. in a thermoset-thermoplast mixture when phase separation is induced close to the gel point. A mixture with an amphiphilic block copolymer (a block copolymer with two blocks featuring different properties) on the other hand is stable against macroscopic separation, but one block – if immiscible with the epoxy phase – can have the tendency to phase separate. However, due to its physical attachment with the other, miscible block, this can only occur at a local scale (at nanometer level) and therefore does not exhibit a visible cloud point because they are homogeneous on the scale of visible light wavelengths. This is further elaborated in the next part.

2.3. BLOCK COPOLYMER MORPHOLOGIES IN SOLUTIONS AND POLYMER BLENDS

Block copolymers consist of at least two types of polymers linked together with a covalent bond. The most basic block copolymer type is a diblock copolymer in which one polymeric block is attached to another polymeric block (AB-block copolymer). Triblocks (ABA or ABC), tetrablocks (ABCD, ABAC,…) and multiblocks can also be made. Graft copolymers are a special type of block copolymer in which branches of a given polymer type are grafted upon a backbone of a different polymer type. Also star shaped block copolymers have been investigated and can attain a wide variety of structures, depending on the number of arms, the nature of the arms (homopolymer or block copolymer) and the overall macromolecular structure of the star (different types/lengths of arms). For the present work, diblock copolymers are most relevant.

Block copolymer morphologies depend on how the blocks respond differently to the chemical (pH, chemical composition, …) or physical (temperature, pressure, …) environment. Considering block copolymers in an epoxy matrix, miscibility is the most important factor as will be explained later. The blocks are either homogeneously mixed in the liquid state, which occurs when both blocks are compatible with the matrix, or they attempt to phase separate if at least one of the blocks dislikes the epoxy matrix. Blocks with a highly different affinity towards the matrix can be termed amphiphilic block copolymers. In this case, phase separation of one of the blocks is only possible on a local scale due to their physical attachment to the miscible block, resulting in a wealth of interesting morphologies unique to amphiphilic molecules. In this work only amphiphilic block copolymers will be used.

2.3.1 BLOCK COPOLYMER MORPHOLOGIES IN UNREACTIVE BLENDS

The key requirement to obtain nanostructures in a solvent (or a polymeric matrix) is to have one miscible block[49], preventing phase separation on a larger scale with the solvent, as well as an immiscible block, which tends to demix from the selective solvent on a nanoscale due to chain connectivity, thus forming composition depending nanostructures[50]. Lamellar, cubic, gyroïd, hexagonally-packed cylindrical, wormlike, spherical micellar and vesicular are part of the reported structures.[51,52] The morphology depends on several parameters, including the blockcopolymer concentration, the volume fraction each component takes, specific interactions between blocks or block-solvent interactions.

One can add a block copolymer consisting of A and B moieties with either an A-selective or B-selective solvent generating a binary system, or both A- and B-selective solvents, generating a ternary system.

An even greater morphology diversity can be achieved by increasing the functionality through chemically adding a third block to form ABC or ABA-type block copolymers [53–55]. A total of 9 phases has been reported by Alexandridis et al[56] in a ternary system of water, p-xylene and poly(ethylene oxide-*b*-propylene oxide-*b*-ethylene oxide) (EO_{19}-PO_{44}-EO_{19}).

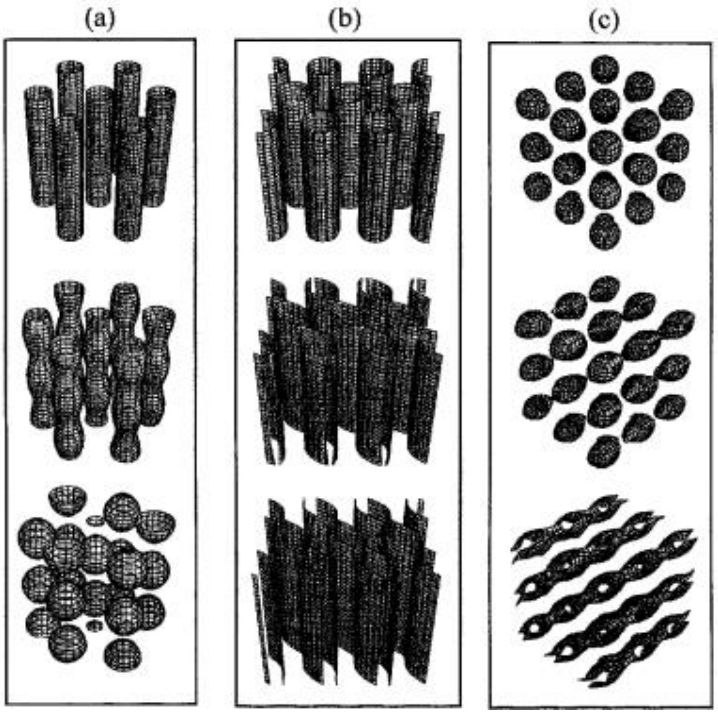
2.3.2 BLOCK COPOLYMER MORPHOLOGIES IN REACTIVE BLENDS

Blending of block copolymers to form different morphologies in a reactive system involves basically the same mechanism as in unreactive blends. The most obvious reactive blends involve epoxy resins, which cure into networks. In this case, epoxy can act as a selective solvent, analogously to unreactive blends. Specific to the case of reactive blends, however, is that the solvent quality and selectivity can change while the reaction progresses. So, a block can be miscible in the unreacted state, while upon curing it might become immiscible.

When an epoxy resin is curing, the miscibility of one or both blocks with the matrix may decrease, which can lead to structural transitions inside the material. This can be a disorder-order transition (DOT) or an order-order transition (OOT). The former may occur in an event in which both blocks are miscible (e.g. at high temperatures) after which curing decreases solubility of the least miscible entity and therefore creates nanoscale structure. According to Israelachvili[57], the packing parameter, *p*, dictates the most likely self-assembled morphology. This parameter is defined as:

$$p = \frac{v}{a_0 l_c} \qquad \text{(Eq. 2.5)}$$

With *v* the volume of the 'resinophobic' chains, a_0 the cross sectional area of the 'resinophilic' head and l_c the length of the resinophobic tail. In the case the system prior to curing was already in a self-assembled morphology, one can expect morphological changes due to the curing reaction. When an epoxy resin is curing, the miscibility of the resinophilic head with the matrix may decrease, by which the parameter a_0 decreases and consequently *p* increases. This implies that during the course of curing the self-assembled morphology may change, i.e. an OOT. Figure 2.10 shows some examples of OOTs in reactive block copolymer blends as reported by Laradji et al.[58] Generally, spherical micelles are favored when $p \leq ⅓$, cylindrical micelles when $⅓ \leq p \leq ½$ and vesicles are formed preferentially when $½ \leq p \leq 1$. This implies that during the course of curing the self-assembled morphology may change from micelles to vesicles.



Figuur 2.10: Examples of interfacial fluctuations at an OOT (a) hex-to-bcc, (b) hex-to-lam and (c) bcc-to-hex. Reproduced from Laradji et al. [58]

One can avoid macrophase separation by choosing one block which stays miscible up to the point when mobility has sufficiently decreased during the curing reaction. As such the morphology will be locked into place. Once this state is achieved, manipulations such as further curing or changing temperature (as long as degradation is avoided) will no longer affect the morphology.[59]

The immiscible block can either already be immiscible in the unreacted state, in which case we call the process of nanostructure formation: 'Fixation of self-assembled block copolymers by network formation'.[51,60,61] Or it can be miscible in the unreacted state, meaning that the block copolymer is completely dissolved at that moment and no structure whatsoever is present. Upon curing, it can demix on a local scale due to its covalent attachment to the miscible subchain. This process is proposed by Meng at al. as an alternative mechanism to generate nanostructures, i.e. a Reaction Induced Microphase Separation (RIMS).[62]

The above mechanisms for nanostructure formation are based on locking in a thermodynamically stable morphology. Nanostructuring can also be conserved by a very fast curing reaction, such as UV curing. This method may involve the fixation of a given a morphology beyond its stability limits and implies kinetically locking in a non-equilibrium structure.[63]

2.3.3 BLOCKCOPOLYMER MORPHOLOGIES AND CRYSTALLIZATION

The phase behavior of non-crystallizable block copolymers is already fairly well understood.[64] However, when one or both blocks are crystallizable, two possible modes can drive phase separation: liquid-liquid and liquid-solid microphase separation, resulting in a richer but more complex phase behavior and morphological diversity.

Crystallization in homopolymers is governed by a kinetic chain folding step. In semicrystalline block copolymers, equilibrium chain folding can occur due to confinement of the crystallizable block by microphase separation, with the equilibrium number (aspect ratio of surface energies in the basal and lateral surface directions) controlled by the non-crystallizable block. [65–69] Block copolymers in which both block are crystallizable, can display co-crystallization in contrast to a mixture of crystallizable homopolymers in which the different entities will segregate.[70] However, crystallization of one block can also influence the other as proven by Balsamo et al.[71] Crystallization of one block may suppress crystallization of the other. This is termed anti-nucleation. Morphological confinement of crystallizable blocks in between glassy domains or more generally the strong segregation between different domains may lead to homogeneous nucleation, which drastically reduces the crystallization kinetics.[65] This type of confined crystallization does not result in spherulites given the small length scale at which this occurs (typically 5-500nm). On the other hand, in homogeneous melts or weakly segregated blocks, crystallization of one block can overwhelm the other, producing spherulites nonetheless.[72,73]

2.4 CNT DISPERSIONS

Since their discovery in 1991 by Iijima et al., carbon nanotubes (CNTs) hold the promise of delivering exceptional electrical, mechanical[74] and thermal properties due to their conjugation of sp^2-hybridized carbon-carbon bonds as well as their distinctive aspect ratio which typically reaches 1 000 and results in a large surface area. However, to exploit these properties in polymeric matrices, proper dispersion and interfacial adhesion between CNTs and the matrix should be guaranteed[75] but this is hard to achieve due to the strong intertube π-π stacking which drives them to aggregate into bundles.

Dispersion quality is governed by two main parameters, the first being the dispersion itself and the other being the stability against re-agglomeration. Mechanical agitation and chemical functionalization are often employed to improve the dispersion quality.

Mechanical dispersion is achieved through stirring or shear mixing,[76] extrusion, calandering[40], ball milling or ultrasonication.[77] For low viscous components like

thermoset precursors, shear mixing or ultrasonication are the methods of choice, the latter leading to better dispersion results. However possible damage to the CNTs can be inflicted by sonication, deteriorating properties. While these techniques all have a tendency to improve the dispersion of carbon nanotubes, they will not prevent re-agglomeration. Literature[75–78] suggests that CNT functionalization should be adopted to keep the dispersion stable over time.

Dispersion improvement through functionalization can be divided into two subgroups: physical and chemical functionalization. The latter involves the covalent bonding of side groups to the carbon nanotubes by which the sp^2-hybridization is partially lost and transformed into sp^3 hybridization which leads to reduced intertube π-π interactions. Yang et al.[79] used amine functionalized CNTs to increase the dispersion quality in an epoxy matrix and to improve interfacial bonding with the matrix as the amines can react with epoxy. This reaction had only a minor influence on the epoxy-curing agent stoichiometry because of the low degree of functionalization and the lower reactivity compared to that of the amine curing agent. It does have a small impact on the curing kinetics, as the entire reaction is somewhat sterically hindered. The downside of functionalization is that it causes damage and fragmentation of the CNTs. The loss of sp^2-hybridization and hence pi-conjugation affects the electrical and thermal properties. Physical functionalization is a less invasive method to change the surface properties of carbon nanotubes and includes polymer wrapping or the use of surfactants[75,77]. The functionalization routes have the advantage that the mutual attraction between carbon nanotubes decreases and therefore, re-agglomeration is less likely to occur. Moreover, a combination of the aforementioned techniques can be applied[77,78], depending on the system and the desired properties. As mechanical dispersion is often more effective in dispersion and functionalization in preventing re-agglomeration, a combination of one or more of these is a good practical idea.

2.4.1 TOUGHENING EPOXY RESIN WITH CNTS

Carbon nanotubes have been considered extensively to increase the toughness and strength of brittle epoxy resins. Relying on a computational modelling of the deformation behavior of CNT nanocomposites under uniaxial tension, Liu et al.[80] identified three mechanisms that are at the origin of the CNT toughening power: 1) CNT debonding and pull-out, 2) suppression of stress concentration leading to delay in damage initiation and 3) damage diffusion/crack branching.

The first mechanism can be classified as a nanoscale toughening mechanism and is most effective when the CNTs are well dispersed and homogeneously distributed over the epoxy matrix. Furthermore, the interfacial adhesion between the CNTs and epoxy matrix should be strong. The other two mechanisms identified by Liu et al.[80]

are micrometer scale toughening mechanisms, which are most effective if the CNTs are gradually distributed and oriented in a particular way, depending on the material shape and deformation geometry. It goes beyond the scope of this chapter to outline the finer details of the most ideal CNT topologies. For sure, the gradual distribution should not be confused with CNT clustering because large clusters my act as unwanted stress concentrators, leading to a reduced toughness.

Liu et al stated that optimizing the CNT topology in view of triggering the micrometer scale mechanisms is more efficient to increase the material toughness compared to trying to call upon mechanism 1 via homogeneous CNT dispersions. These authors proved that a structurally optimized dispersion of CNTs in epoxy increased the strength and toughness by 90% and 277% respectively, compared to unfilled polymer, while the same polymer featuring homogeneously dispersed CNTs only improved by 6% and 14% respectively[80]. When the dispersion quality is poor, the mechanical properties are expected to not exceed those of the unfilled polymer.

To realize the desired but complex CNT patterns, besides control over the dispersion and adhesion, also strategies to induce the desired spatial distribution and CNT orientation should be established. Most elegantly, manufacturing processes that rely on self-assembly principles should be used with the assembly characteristics being sensitive to a relevant electromagnetic or stress field during morphology fixation. The field applied during synthesis should resemble the stress state the material would experience during its life time. In that way materials would be tailored towards the application.

2.4.2 FINE-TUNING THE CNT TOPOLOGY

Bose et al.[81] described polymer blend macrophase separation as a tool to control the CNT dispersion architecture at a larger length scale, with the CNTs driven to one phase. This preferred location leads to a lower percolation threshold, which can be of interest for electrical and mechanical properties. CNT orientation was not controlled.

Lakoubovskii reviewed methods to align CNTs[82]. CNT alignment may be induced during the synthesis, where the crowding of close placed CNTs on a catalyst surface confines the CNT growth direction[83]. Secondly, mechanical (stretching, fracture, compression, friction, ..), acoustic, magnetic or electric fields might be used to induce CNT orientation after synthesis and dispersion[84]. Liu et al. combined microwave assisted CNT orientation with epoxy resin curing to permanently settle the CNT orientation[85]. Both the synthesis and external field options seem, however, less suited to generate complex CNT orientation and concentration patterns.

Lakoubovskii[82] also mentions the use of liquid crystal (LC) matrices to induce CNT orientation. This approach exploits the self-assembly of LC, exhibiting long-range orientational order along a specific direction, known as the director. Jiang et al.[86] succeeded to trap multiwalled CNTs (MWCNTs) within the cylinders of lyotropic LCs. The solvent was an ionic liquid. The amphiphilic character of the LCs ensured a good CNT dispersion within the solvent and the hexagonal (CNT loaded) cylinder packing induced the common orientation. A similar approach was followed by Lagerwall et al, using single walled CNTs, sodium dodecyl sulfate (SDS) as surfactant and water as solvent[87]. Not all surfactant micelles were containing CNTs. The interaction between the surfactant-coated CNTs and the surrounding pure surfactant micelles was suggested to promote the tube alignment. This process requires a sufficiently high surfactant concentration. The application of a relatively weak (strength below 1T) magnetic field induced a large scale uniform orientation in these systems. Quite recently, Kasprzak et al.[88]exploited similar recipes but used shear forces to induce a common alignment and photopolymerizable surfactants to lock in the orientation pattern.

2.4.3 CNT BASED NANO-ELECTRONICS

A second application of ordered CNTs (besides mechanical reinforcement) can be found in nano-electronics, where the conductivity of ordered CNTs can be exploited for wearables or implantable technology applications. A CNT-filled liquid that can be jetted by an inkjet printer can be used to make biocompatible nano-electronics. The jetting technique is fast, reliable and has a high resolution. Moreover CNT alignment can be induced, thanks to the drying process of (*e.g.* waterbased) inks, albeit only in-plane alignment is possible.[84]

Miniaturization, versatility of printing, along with the flexibility/stretchability of CNTs, enables applications such as hearing aids or health trackers. Miniaturization also allows to build compact, high performance electronics, with improved speed and sensitivity, which are key requirements in devices such as sensors. For example, Lorwongtragool et al. report flexible chemical sensors, based on a CNT/polymer array and manufactured by an inkjet printing technology, which allows to build a wearable e-nose able to differentiate different between volatile compounds.[84]

CHAPTER 3: MATERIALS AND METHODS

3.1 MATERIALS AND SAMPLE PREPARATION

3.1.1 MATERIALS

The thermosetting system consists of an epoxy component and a curing agent (hardener). A Diglycidyl ether of bisphenol A (DGEBA) oligomer with epoxide equivalent weight of 184-190 g/mol (Epikote828LVEL) is the epoxy component (Figure 3.1a). In the thesis, this component will be denoted as DGEBA whereas in fact the oligomer is meant. 4,4'-methylenedianiline (MDA) serves as curing agent (Figure 3.1b). These components were mixed in equifunctional stoichiometric ratio, meaning that the epoxy to amine-hydrogen ratio in the mixture equals 1. When fully cured, this mixture has a glass transition temperature, $T_{g\infty}$, of 165-175 °C[89,90]. Using equation 2.1 with f_e = 2 and f_c = 4, one can calculate that gelation is theoretically reached at a conversion of 58%.

The structure forming amphiphilic diblock copolymer, stearyl-*block*-poly(ethylene oxide$_{20}$) (Fig. 3.1c) was supplied under the commercial name Brij® S-20 by Aldrich Chemical Co. The PEO block of the block copolymer is polydisperse, with the blocks length varying between 17 and 22 monomeric units according to GPC. The stearyl block is of course monodisperse.

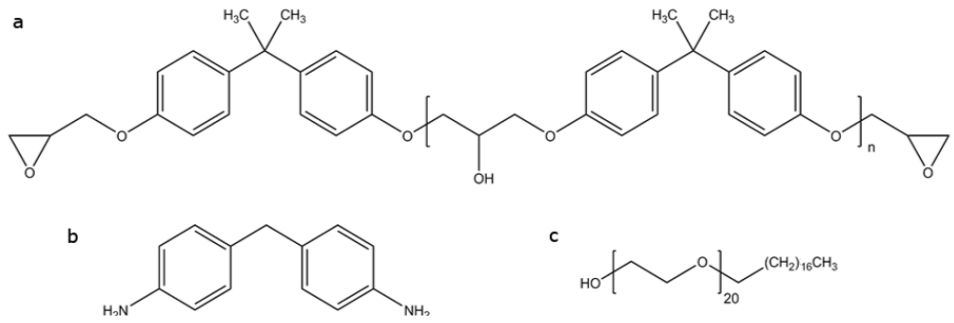


Figure 3.1: molecular structures of (a) Diglycidyl ether of bisphenol A (DGEBA), (b) 4,4'-methylenedianiline (MDA) and (c) stearyl-block-poly(ethylene oxide$_{20}$) with trade name Brij® S-20.

Two types of multi-walled carbon nanotubes (MWCNTs) supplied by Nanocyl were used: a pristine, non-modified one (NC7050) and an amine functionalized MWCNT (NC3152). According to the supplier, the average CNT dimensions of both grades are ca. 0.7 µm in length and 9.5 nm in diameter, resulting in an aspect ratio of ca. 75. Amine functionalization is 'below 0.5 wt %'.

3.1.2. SAMPLE PREPARATION

Although the epoxy resin is a two component system, it will be treated as a single, homogeneous epoxy resin in this thesis. Therefore, a binary blend of the epoxy and Brij® S-20 will be referred to as a two-component system. Such binary mixtures were made by mixing the appropriate amounts of epoxy (in absence of the curing agent) and Brij® S-20 in a beaker at room temperature. Next, they were brought to 70 °C and stirred for 10 min, followed by degassing at 70 °C in a vacuum oven for 60 min. Finally, the mixtures were brought to 100°C in an oil bath, and probe sonicated for 3 min. Sonication was performed to mimic the sample preparation method for the case when CNTs were added to the system. The two component systems serve as reference to the three-component systems with CNTs and therefore needed to be treated equally. Sonication increases the dispersion quality of the CNT loaded systems, but can also slightly increase the sample temperature. Subsequently, the curing agent was added in a stoichiometric ratio while sonication continued at 100°C. After 3 min, the crystalline curing agent was completely dissolved and the mixture was quench-cooled in salted ice water to prevent further curing and stored in a freezer up to further research. During handling or transport of these quench-cooled resins, curing was always minimized by keeping the samples as long as possible at or below freezer temperatures (-18°C).

For the CNT-loaded blends, a rather high amount of CNTs (unfunctionalized pristine CNTs or amine functionalized CNTs) was first mixed with Brij® S-20 at 70°C, which is slightly above its melting temperature. The mixture was stirred and probe-ultrasonicated for 5 min. Then, DGEBA was mixed with the right amount of the Brij® S-20/CNT mixture and additional pure Brij® S-20 such that the final formulation contains 0.01 w% CNTs. Mixing happened at 70 °C while stirring for 10 min. Degassing for 60 min at 70 °C in a vacuum oven followed. Finally, the mixtures were brought to 100 °C in an oil bath, probe sonicated for 3 min and mixed with the curing agent as for the blend without CNTs. Sonication was performed with a 200 W Hielscher Ultrasonic Processor UP200S, equipped with a 3 mm diameter S3 titanium Sonotrode. The amplitude was fixed at 50% (100 W output) and cycles were imposed of 0.5 s sonication alternated with 0.5 s resting time. The amplitude and cycle settings were a trade-off to increase dispersion while minimizing damage to the CNTs.[91] The precise settings were based on various values found in literature.

All CNT loaded blends contained 0.01 wt% CNT, irrespective of the Brij® S-20/epoxy resin ratio. Samples are abbreviated with a number followed by *%* and a letter '*a*', '*p*' or '*r*'. The number defines the Brij® S-20 wt%. The letter *'p'* stands for pristine CNTs, *'a'* for amine functionalized and *'r'* for the reference blend without CNTs. So, when referring to for example sample *'40%a'*, a sample with 40wt% of block copolymer

and 0.01wt% of amine functionalized CNTs is meant. The pure epoxy resin without CNTs is referred to as *'0%r'*.

3.2 METHODS

Temperature profile

Throughout this thesis, thermal or morphological analyses are often performed while imposing a given, standard temperature profile. Unless otherwise stated, the frozen samples were brought to 60 °C where measurements started. Next, the samples were cooled to -50 °C and subsequently reheated to the isothermal curing temperature of 130 °C, at which it was kept for at least 1 hour. Afterwards, a cooling ramp to -50 °C and a next heating ramp to 200 °C were imposed. All temperature cycles were performed at a heating/cooling rate of 10 °C/min. This standard profile is illustrated in Figure 3.2 (with the initial temperature being 25°C, rather than 60°C). The curing temperature of 130°C was selected based on DSC experiments as explained in chapter 4.

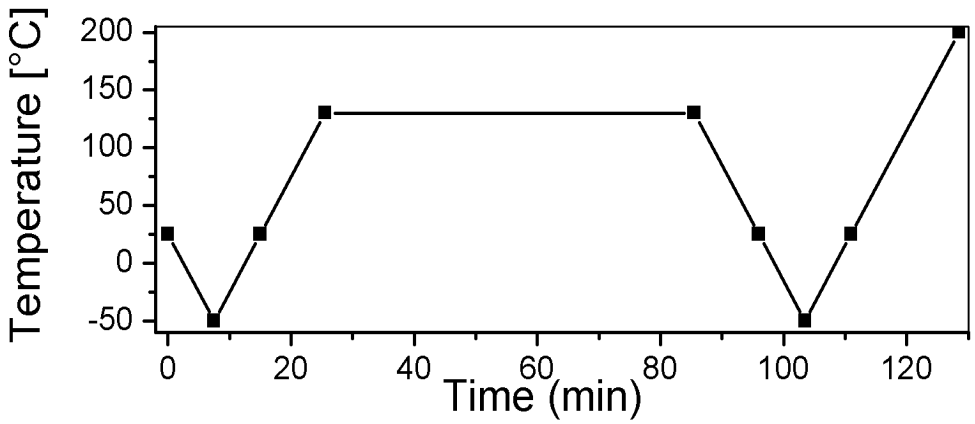


Figure 3.2: A graphical representation of the standard temperature profile showing a cooling/heating segment up to an isothermal segment at 130°C for curing and finally another cooling/heating segment on the cured material.

The first cooling and subsequent heating will be referred to as the first segment, the isothermal curing is the second segment and the second cooling with subsequent heating is the third segment.

DSC

Calorimetric measurements were carried out on a TA instruments Q2000 Differential Scanning Calorimeter (DSC), equipped with an RCS cooler. Nitrogen was used as purge gas. For enthalpy and temperature calibration indium standards were used. Samples between 12 and 25 mg were sealed in Tzero Aluminium Hermetic pans and

measured in a temperature profile as specified above. However, for addressing the isothermal curing kinetics the first ramp towards the curing temperature was performed at 100 °C/min instead of at 10 °C/min to avoid any curing during the heating ramp. Secondly, the curing temperature was varied in this study.

TGA

Thermogravimetrical Analysis was performed on a TA Instruments Q500 TGA. 5 to 15 mg of sample was loaded in an Aluminium DSC pan, which was in turn mounted in a Platinum TGA pan. Temperature controlled heating at 10 °C/min was imposed from 50 °C to 180 °C in nitrogen atmosphere or air.

Synchrotron SAXS & WAXD

Temperature-resolved synchrotron X-ray diffraction was performed at DUBBLE, the Dutch-Belgian Beamline (BM26) at the European Synchrotron Radiation Facility (ESRF; Grenoble, France) using a wavelength, λ, of 1.03 Å and a beam size measuring roughly 250 µm across. The samples were placed in Tzero Aluminium Hermetic DSC pans. The small-angle X-ray scattering (SAXS) parts of the diffraction were collected on a two-dimensional (2D) Pilatus 1M detector from Dectris, placed at 2 m from the sample after an evacuated tube. The wide-angle X-ray diffraction (WAXD) parts were collected on a Pilatus 300K-W detector, also from Dectris, put closely to the sample. The scattering angles were calibrated with Silver Behenate (SAXS) and High Density Polyethylene (WAXD). X-ray patterns were collected in consecutive frames of 6s during the entire temperature profile. After mounting the sample at room temperature, the temperature profile was imposed through a Linkam DSC 600 heating/freezing stage, equipped with a liquid nitrogen cooler.

The 2D data were averaged azimuthally using ConeX[92] and corrected for the scattering by an empty setup, taking into account sample and sample holder transmissions. Transmitted intensities were measured by a photodiode placed downstream from the sample on the beam stop. Background corrected SAXS and WAXD data were normalized by the integrated WAXD intensity. This procedure accounts for changes in the direct beam intensity and scales the measurements to a constant scattering mass. Scattering patterns are represented as a function of the scattering vector modulus $q = (4\pi\sin(\theta))/\lambda$, with λ being the wavelength and θ half the scattering angle.

TEM

Epoxy-copolymer blend samples were prepared for Transmission Electron Microscopy (TEM) by isothermal curing at 130 °C for 60 min and cooling down at 10 °C/min to room temperature. The samples were trimmed using a Diatome

trimming tool and subsequently ultrathin sections (70 nm) were obtained at -85°C using a Leica Ultracut S/FCS microtome, equipped with a Diatome 35° diamond knife. The sections were put on a 200 mesh copper grid with a carbon support layer. Staining was applied using the vapor of a rutheniumtetroxide (RuO_4)-solution prepared according to Montezinos et al. for 15-30 min.[93] TEM was performed using a Tecnai 20 microscope, operated at 200 kV.
In a second type of experiments, samples were cured at 45 °C for 2 days and postcured successively at 80 °C for 6 h and 150 °C for 90 min. After trimming, 90 nm sections were made using a Drukker International diamond knife at a sample temperature of -80 °C and with the knife at -60 °C. The sections were collected in a solution of water / dimethylsulfoxide (50/50) filled boat, attached to the diamond knife. They were deposited on 300 mesh copper grids and dried on a filter paper. Staining with vapors of a 0.5 wt% aqueous solution of RuO_4 was applied for 15-30 min, following the process described elsewhere.[94] TEM images were made with a Philips CM10, operating at 80 kV.
RuO_4 selectively stains the components in the order PEO > stearyl ether > cured epoxy, leading to an increased contrast between the potential phases. Note that RuO_4 is a powerful oxidizer, irritant to both the eyes and respiratory system. It has to be used with a maximum of safety conditions.

The first set of TEM experiments was performed by A. B. Spoelstra (Eindhoven University of Technology, The Netherlands) and the second one by N. Boyard (CNRS/Université de Nantes, France).

OM

Optical Microscopy (OM) was performed with an Olympus BHS microscope. Samples were placed between two glass plates. The standard temperature profile was imposed to the samples by a Linkam TMS 600 hotstage, with a Linkam TMS 91 driver. Pictures were taken with a JVC TK-C1381 color camera on time intervals programmed through scripts within the Leica Qwin Software, which was also capable of saving the pictures.

Rheology

Dispersion quality was analyzed by applying small sinusoidal shear strains to the sample in the linear viscoelastic regime. In this regime, a fingerprint of the microstructure of the sample is obtained by slightly perturbing the microstructure without destroying it. A sinusoidal strain γ with angular frequency ω results in a sinusoidal shear stress σ with the same frequency, but with a different phase δ. The constant of proportionality is the complex shear modulus $G^*=G'+iG''$: $\sigma^*=G^*\gamma^*$. The storage or elastic modulus G' represents the in-phase part of the stress and describes

the solid-like response of the material. The loss or viscous modulus G'' represents the out-phase part of the stress and characterizes the liquid-like behavior of the material.

Rheological measurements were performed on a strain-controlled rheometer (ARES-G2, TA Instruments) equipped with a cone and plate geometry (diameter 25 mm, angle 0.1 rad). Measurement were performed on pure Brij® S-20, loaded with CNTs. Mixing was performed either by normal mixing or sonication, the latter as described above in the sample preparation section. Since the Brij® S-20 melting point is around 45 °C, rheological measurements were performed at an elevated temperature of 50 °C. To avoid effects of loading and sample history, an equilibration period of 30 min was respected after sample loading. The rheological test was performed after this period.

PART II

CURING KINETICS, THERMAL BEHAVIOR AND MORPHOLOGY OF EPOXY/STEARYL-BLOCK-POLY(ETHYLENE OXIDE) BLENDS

In this part, the time and temperature dependent morphology of epoxy resins mixed with low (chapter 4), high (chapter 5) and intermediate (chapter 6) amounts of block copolymer is discussed. Chapter 7 is devoted to summarizing and discussing the concentration dependent thermal behavior and morphology of epoxy Brij® S-20 blends. In the latter chapter, the data presented in the chapters 4, 5 and 6 are grouped in single graphs for comparison.

The first part of chapter 4 deals with the temperature dependent isothermal epoxy curing kinetics. Based on this work, a curing protocol was selected that was used for all compositions of the epoxy/block copolymer blends. The second part of chapter 4 addresses morphological issues, just like the chapters 5 and 6 do for respectively blends with high and intermediate block copolymer amounts. Chapter 5 also includes work on pure Brij® S-20. The morphology of the samples discussed in chapter 6 after curing is layer like and hence resembles that of the low and high concentration samples. However, because also non-layered structures occur for the non-cured materials with intermediate block copolymer amounts, it was decided to discuss

these samples separately after having addressed the main structural features of the low and high concentration materials. Nanostructural transformations are probed via SAXS, whereas WAXD is used to identify crystallization related aspects. The morphology ultimately realized via high temperature curing is disclosed by means of TEM. DSC is used to characterize the curing reaction via its exothermic heat or the effect it has on the material T_g. Other thermal transitions are linked to the morphological changes revealed by SAXS and WAXD.

Collaborator contributions:

A. Lavrenova did valuable work on curing kinetics; A. B. Spoelstra and N. Boyard both performed TEM measurements; B. Goderis provided expertise in modelling and analysis of SAXS patterns, as well as general remarks and advice.

Part II is partly based on:

Bogaerts K., Lavrenova A., Sploelstra A. B., Boyard N., Nies E., Goderis B.; Curing Kinetics and morphology of a Nanovesicular epoxy/stearyl-block-poly(ethylene oxide) surfactant system; RSC Soft Matter, **11**, 6212-6222 (2015).

CHAPTER 4: ISOTHERMAL CURING KINETICS AND THE MORPHOLOGY OF EPOXY RESINS WITH LOW AMOUNTS OF BLOCK COPOLYMER

In this chapter, epoxy resins with low amounts of block copolymer are discussed. The first part treats materials with 20% Brij® S-20 (denoted as *20%r*). This part takes off with at a discussion on the isothermal curing kinetics of *20%r,* after which the morphological developments are disclosed by time/temperature resolved synchrotron SAXS/WAXD and TEM. In the second part, *30%r* is examined.

4.1 ISOTHERMAL CURING KINETICS AND MORPHOLOGY OF *20%R*

The isothermal curing of epoxy blended with 20% Brij® S-20 is discussed in great detail in this section. The results obtained for this particular Brij® S-20 amount serve as reference to also understand the curing behavior of other compositions, including those with CNTs. The curing of other compositions will be discussed more briefly in other chapters with emphasis on the isothermal reaction rate and final curing degree.

4.1.1 ISOTHERMAL CURING KINETICS

Figure 4.1 displays the heat flow of (initially uncured) pure resin (*0%r*) and *20%r*, as measured by DSC while heating from -90 °C to 300 °C at 10 °C/min. Curing *0%r* generates a broad exothermic peak, starting at around 80°C and peaking at 164 °C. The total reaction enthalpy (ΔH_0), calculated by integrating the area enclosed between the curves and straight baselines, amounts to 432.0 J/g for *0%r* and to 358.0 J/g for *20%r*. Since curing starts at 80 °C, it is clear that the preparation method, involving sonication at 100 °C, could already have induced limited curing. To estimate the conversions properly, the maximum total reaction enthalpy must be determined, further referred to as ΔH_{max}. *0%r* with stoichiometric amounts of DGEBA and MDA was prepared by stirring rather than sonicating at 100 °C for only 1 min in order to minimize curing during preparation. This system was subjected to a similar DSC heating run, yielding a ΔH_{max} of 447.8 J/g. These conditions cannot fully exclude resin curing but are mandatory to enable MDA melting (the melting point is 89°C) and resin mixing.

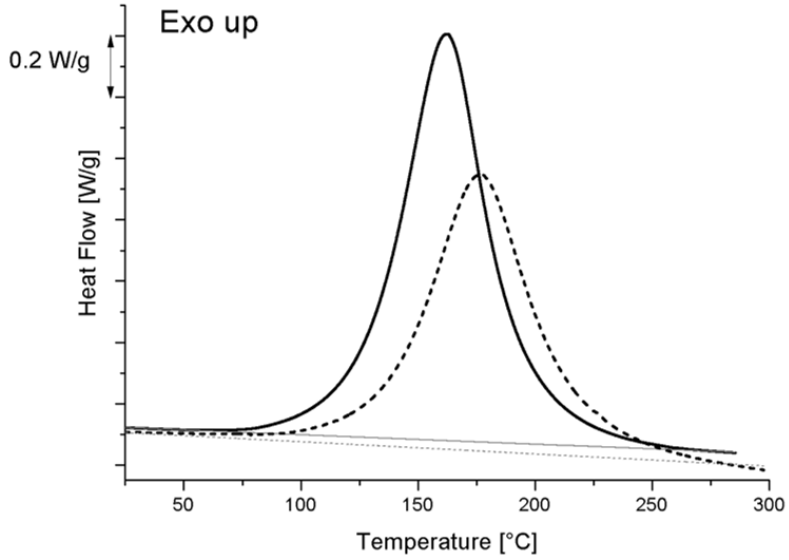


Figure 4.1: DSC heating runs at 10°C/min to determine the total curing reaction enthalpy, ΔH_0, of the pure reference resin, *0%r*, (solid black line) and *20%r* (dashed black line). The baselines used for integrating the reaction enthalpy are represented as gray solid and dashed lines respectively.

The curing enthalpy during sample preparation (ΔH_{prep}) can be calculated for both *20%r* and *0%r* through equation 4.1:

$$\Delta H_{prep} = \Delta H_{max} - \Delta H_0 \qquad \text{(Eq. 4.1)}$$

For *0%r* $\Delta H_{prep,0\%r}$ is calculated as follows:

$$\Delta H_{prep,0\%r} = \Delta H_{max} - \Delta H_0 \qquad \text{(Eq. 4.2)}$$

$$= 447.8J \cdot g^{-1} - 432.0J \cdot g^{-1} = 15.8J \cdot g^{-1}$$

For *0%r* it appears that (15.8/447.8)*100 = 3.5% cured during the standard sample preparation method, involving sonication. For *20%r*, the measured reaction enthalpy is 358.0 J/g. The curing enthalpy during sample preparation for this material ($\Delta H_{prep,20\%r}$), which contains 80% epoxy equals:

$$\Delta H_{prep,20\%r} = (\Delta H_{max} * 0.8) - \Delta H_0 \qquad \text{(Eq. 4.3)}$$

$$= 447.8J \cdot g^{-1} * 0.8 - 358.0J \cdot g^{-1} = 0.2J \cdot g^{-1}$$

One can readily compute that only 0.2/(447.8*0.8)*100 = 0.05% of the resin cured during blend preparation. The decreased conversion during mixing compared to *0%r* indicates that blending with Brij® S-20 reduces the reaction rate at 100 °C. Figure 4.1 reveals that the reaction kinetics in general is slowed down: the peak maximum is shifted to a higher temperature compared to *0%r*. Ultimately, during heating at

10 °C/min *20%r* reaches full curing once 280 °C has been exceeded. It should be mentioned though that pure Brij® S-20 starts decomposing at about 150 °C under influence of oxygen present in the air, following thermogravimetric evidence (Figure 4.2). This degradation of Brij®S-20 as well as the heat associated with it (expected to be 5.5 J/g in the blend) was neglected in the $\Delta H_{prep,20\%r}$ determination, but sets an upper limit to the useful isothermal curing temperature, which was limited to 130 °C in the present study.

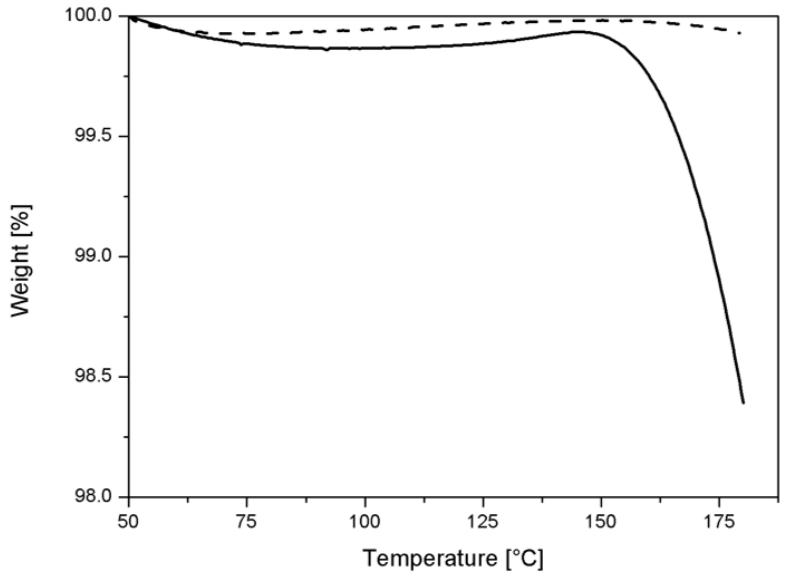


Figure 4.2 Thermogravimetric analysis of pure Brij® S-20 in air (solid line) and nitrogen atmosphere (dashed line) during heating from 50°C to 180°C at 10°C/min.

Figure 4.3 displays the heat flow generated during isothermal conditions after heating *0%r* (top) and *20%r* (bottom) to the desired temperature (T_{cure}) at 200 °C/min. This high heating rate was used to avoid curing during the heating run. As the heat flow is proportional to the reaction rate, the presence of an (isothermal) exothermic peak points at an acceleration of the initial reaction rate. This is known to be due to the formation of hydroxyl groups during the epoxy-amino reaction, which induce an autocatalytic effect.[11] After this maximum, the reaction rate decreases, which may be due to a decrease of available functional groups, exhaustion of more reactive primary amines, gelation or vitrification.[89] For both systems the maximum reaction rate is higher and the time to reach the maximum decreases at increasing isothermal temperatures. Reactions are thus accelerated by a thermal effect.

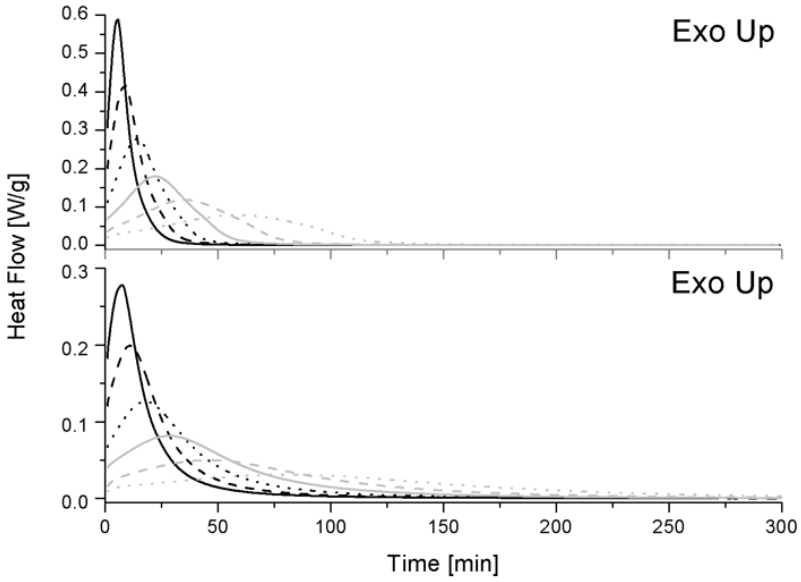


Figure 4.3: Heat flow during isothermal conditions for *0%r* (top) and *20%r* (bottom). Isothermal temperatures are indicated as follows: 130°C: black solid line, 120°C: black dashed line, 110°C: black dotted line, 100°C: gray solid line, 90°C: gray dashed line and 80°C: gray dotted line.

The epoxy resin conversion (α) at time t is calculated by dividing the reaction enthalpy at time t by the maximum total reaction enthalpy

$$\alpha = \Delta H_t / \Delta H_{max} \quad \text{(Eq. 4.4)}$$

Taking the reaction enthalpy during preparation (ΔH_{prep}) into account, equation 4.4 alters into

$$\alpha = (\Delta H_t + \Delta H_{prep,0\%\,r}) / (\Delta H_{max}) \quad \text{(Eq. 4.5)}$$

for *0%r*. For *20%r* equation 4.4 becomes:

$$\alpha = (\Delta H_t + \Delta H_{prep,20\%r}) / (\Delta H_{max} * 0.8) \quad \text{(Eq. 4.6)}$$

Obviously, the conversion-time plots in Figure 4.4 equally reveal the faster conversion rate with increasing isothermal temperature and the slower reaction kinetics for *20%r*. The ultimate conversion degree after 300 min for *0%r* increases from 82% to 98% in going from curing at 80°C to 120°C. At 130°C, however, the ultimate conversion (calculated using equation 4.5) declines to 94% although full curing is expected (data not shown). Given the high curing rate above 120°C (see Figure 4.1), it seems that 6 % conversion takes place during the heating ramp to 130°C. The conversion data in Figure 4.3 for *0%r* at 130°C are therefore shifted to reach an ultimate conversion of 1 at 300 min. This experimental problem does not

exist for the *20%r* systems. However, another complication exists for this material for curing at 90 °C and 80 °C since even after 400 min no stable DSC baseline was reached, indicating that the reaction was not fully over yet. The conversion data in Figure 4.4 for these temperatures are thus only indicative and based on using the heat flow value at 400 min as integration baseline. The experiments at these temperatures were excluded for further analysis. The DSC heating runs of *0%r* after cooling from T_{cure} displayed in Figure 4.5 reveal an enthalpy recovery peak about 25 °C above the respective T_{cure}, indicating that all samples vitrified and relaxed during curing and reached the (very) slow diffusion controlled stage of curing. All heating runs, except the one after curing at 130 °C, contain a significant exothermic peak right after devitrification due to residual curing. The residual heat is larger the lower T_{cure}. Conform the mentioned isothermal curing completeness, no residual exothermic heat was observed during heating the *20%r* resins, irrespective of the curing temperature (Figure 4.5). For the 80 and 90 °C experiment some residual heat was expected (cfr. supra), but it most likely escaped the observation due to being very small and smeared out over a broad temperature range. Most interestingly, a constant devitrification temperature was observed at about 60 °C, which is far below $T_{g\infty}$ of this pure resin. $T_{g\infty}$ refers at the ultimate glass transition temperature of the pure resin after complete curing, which has been reported to be 165 °C[89] or 175 °C[90] in two independent publications.

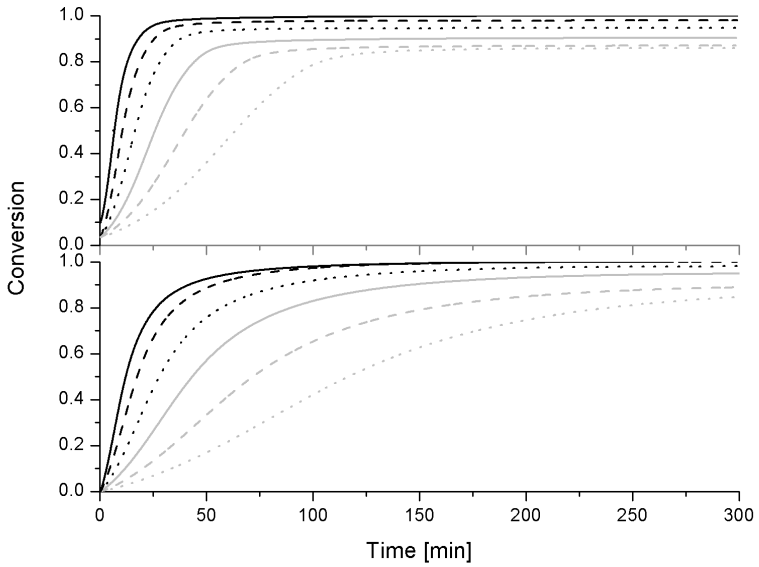


Figure 4.4: Conversion during isothermal curing for 0%r (top) and 20%r (bottom): 130°C: black solid line, 120°C: black dashed line, 110°C: black dotted line, 100°C: gray solid line, 90°C: gray dashed line and 80°C: gray dotted line.

Complete curing in combination with a T_g reduction, suggests that Brij® S-20 acts as a plasticizer for the epoxy resin. Whether or not Brij® S-20 interferes chemically can be deduced from an analysis of the curing reaction activation energy as outlined in the next paragraph.

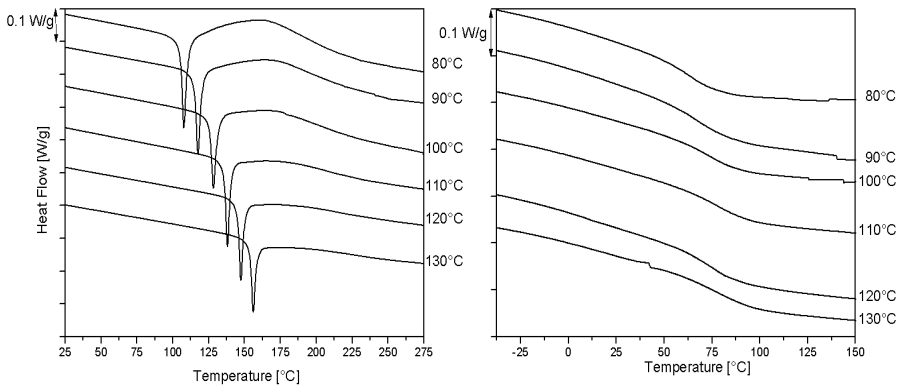


Figure 4.5: The DSC heating runs at 10°C/min for 0%r (left) and 20%r (right) after a prior curing step at different T_{cure} (ranging from 80°C to 130°C) and cooling down to -50°C at 10°C/min.

Following arguments by Lu and Kim,[89] the time to reach a given conversion, t_α, is related to the reaction activation energy, E_a and the absolute temperature , T, via:

$$\ln t_\alpha = \frac{E_a}{RT} + A \qquad \text{(Eq. 4.7)}$$

with *R* being the gas constant (8.31 $JK^{-1}mol^{-1}$) and *A* a constant, depending on the pre-exponential factor of the Arrhenius equation and a function describing how the conversion rate depends on the concentration of the reacting species. If the reaction mechanism is temperature independent, plotting $\ln t_\alpha$ as function of 1/T should yield straight lines with a slope equal to E_a/R. Changes in E_a as a function of the conversion may point to changes in the curing mechanism.

Figure 4.6 is such a graph with linear fits for *0%r*. Conversions above 70% (data not shown) produced non-linear graphs, likely because a diffusion controlled stage was entered at the lowest temperatures.[95] The experiment at 130°C was fully excluded because the exact conversion degree is hard to determine.

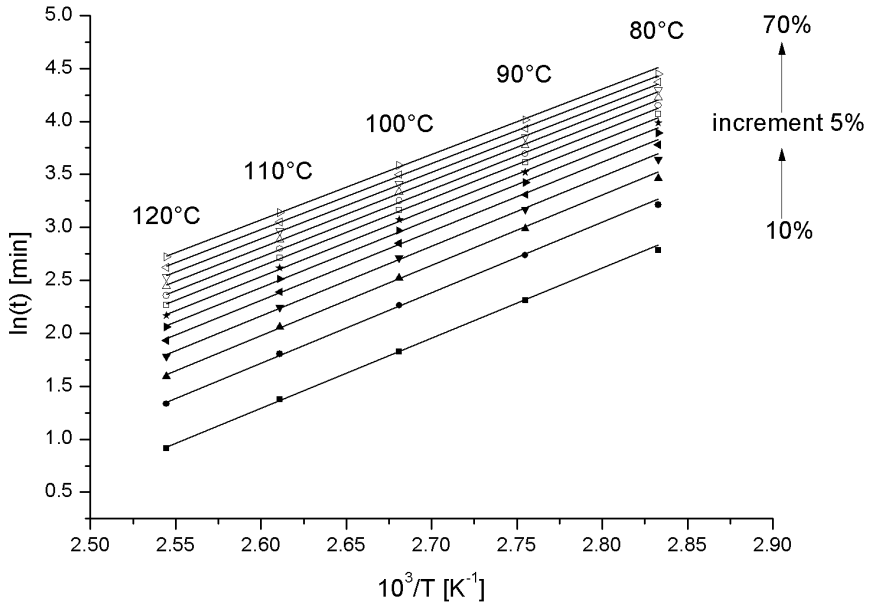


Figure 4.6: Correlation of the logarithm of time versus the inverse of the temperature for different conversions for 0%r.

In Figure 4.7, E_a extracted from the slopes of Figure 4.6 is displayed (open circles). These values are slightly higher compared to the ones reported earlier for the same resin[89]. The decrease in E_a with increasing conversion has been observed earlier and has been attributed to the formation of hydroxyl groups from the reaction between the amine and the epoxy.[96] The hydroxyl groups facilitate ring opening and thereby catalyze the curing reaction. This is accompanied by a reduction of the activation energy.[96] At higher conversions, one expects and often observes an increase in E_a

because of an increase of the viscosity of the reaction mixture.[96] But, as mentioned above, these data were excluded because of the non-linearity in the related graphs.

A change in the reaction mechanism by adding Brij® S-20, would show up in a change of E_a compared to in the pure epoxy resin. In Figure 4.8, the counterpart of Figure 4.6 is shown for *20%r* and the corresponding E_a values are included in Figure 4.7 (black squares).

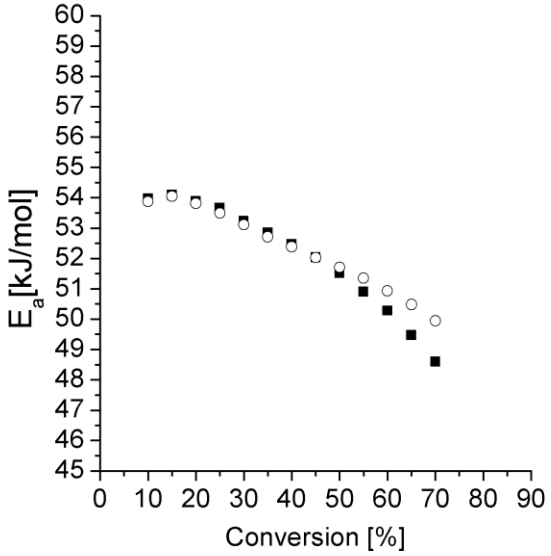


Figure 4.7: E_a for *0%r* (open circles) and *20%r* (closed squares) extracted from the slopes in the Figures 4.6 and 4.8 respectively.

Here the 130 °C data are included but the 80 °C and 90 °C data are left out for reasons mentioned above. The E_a values are not different from the *0%r* values, except at the highest temperatures where the *0%r* values are slightly higher. This result suggests that Brij® S-20 does not mechanistically interfere in the epoxy curing reaction. A plasticizing effect can be inferred from the lower E_a values for *20%r* at high conversions where *0%r* apparently starts experiencing mobility related problems. The slower curing rate for the *20%r* systems compared to for *0%r* can thus be fully attributed to a dilution effect.

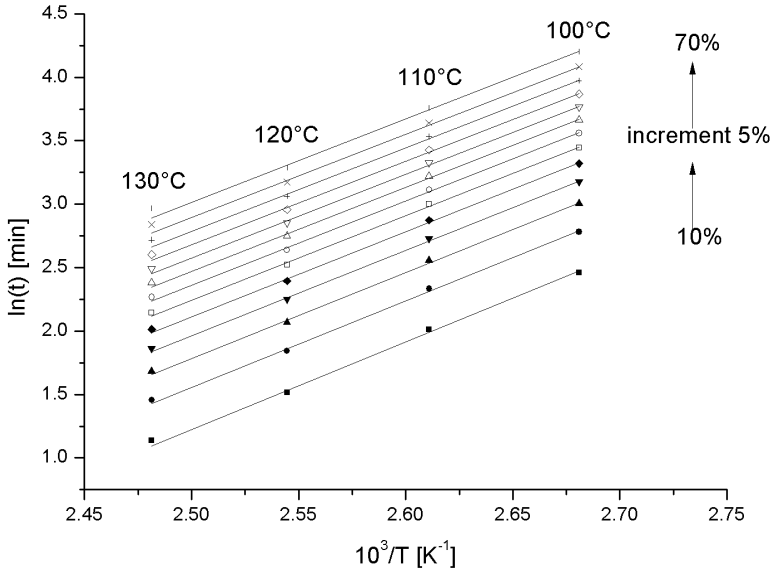


Figure 4.8: Correlation of the logarithm of time versus the inverse of the temperature for different conversions for *20%r*.

In what follows, isothermal curing protocols at 130°C will be used. At this temperature the thermal degradation of Brij® S-20 is avoided. On the other hand 130°C seemed necessary to induce full curing at reasonable rates.

4.1.2 MORPHOLOGY OF 20%R

This section focusses on the morphological changes that occur in *20%r* during the thermal protocol as depicted in Figure 3.2 and in which curing is induced at 130°C. The thermal transitions during the protocol as observed by DSC are outlined at first. The morphology reached after the isothermal curing and cooling step is then discussed based on TEM images. As the morphology seemed to be predominantly vesicular, the experimental time resolved SAXS data were interpreted in terms of such structures. The simultaneously collected WAXD data revealed the development of crystallinity.

4.1.2.1 DSC.

Figure 4.9 illustrates the DSC traces related to the thermal protocol used during the time resolved morphological characterization of *20%r*. In cooling 1 an exothermic signal (grey shaded area) is seen at temperatures just above the step like vitrification signal of the uncured resin at about -25 °C. During subsequent heating 1 an endothermic signal (grey area) is observed right after the devitrification. During further heating, heat is released starting from approximately 80 °C onwards due to the resin curing (amounting to 6.8% conversion). This reaction continues isothermally at 130 °C and seems to be virtually finished after 90 min. It can be shown (see section 4.1.1) that conversion of 90% is reached after 90 minutes at

130 °C. During subsequent cooling 2, the material vitrifies over a rather broad region from 90°C down to about 30°C and devitrifies again during heating 2 without having passed any exo- or endothermic events.

The thermal protocol up to the asterisk in the bottom panel of Figure 4.9, corresponds to the protocol imposed to the sample investigated by TEM.

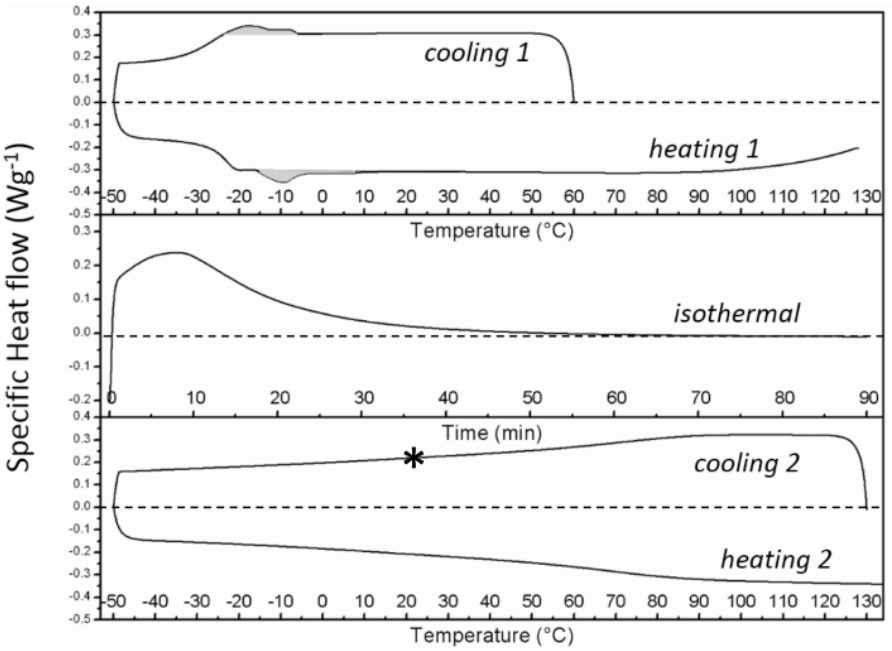


Figure 4.9: DSC thermograms for *20%r*, related to the thermal protocol used during time-resolved X-ray based morphological characterization and as depicted in Figure 3.2. Exothermic signals are plotted upwards. The program includes cooling 1 and heating 1 at 10 °C/min (top panel), isothermal curing at 130 °C for 90 min (middle panel), followed by cooling 2 and heating 2 at 10 °C/min (bottom panel). The grey areas in the top panel highlight the exo (cooling 1) and endothermic (heating 1) heats related to respectively the crystallization and melting of Brij® S-20. The asterisk indicates the temperature at which transmission electron microscopy pictures were collected. This point corresponds to point F in Figure 4.13 (see further below).

4.1.2.2 TEM

Figure 4.10A represents a typical TEM image, revealing closed loop features, dot-like droplets and linear streaks as well as rounded areas that are shaded grey. These features are due to the PEO topology since RuO_4 preferentially stains this component. The loops and areas are associated with vesicles of which the vesicular wall structure will be revealed via the SAXS experiments. The loops represent vesicular walls, running vertically through the entire section and seen edge on, whereas the areas are interpreted as vesicular caps enclosed within the section and seen flat on in

projection. The linear, non-closed streaks are associated with long, cylindrical micelles and the dot-like droplets to spherical ones.

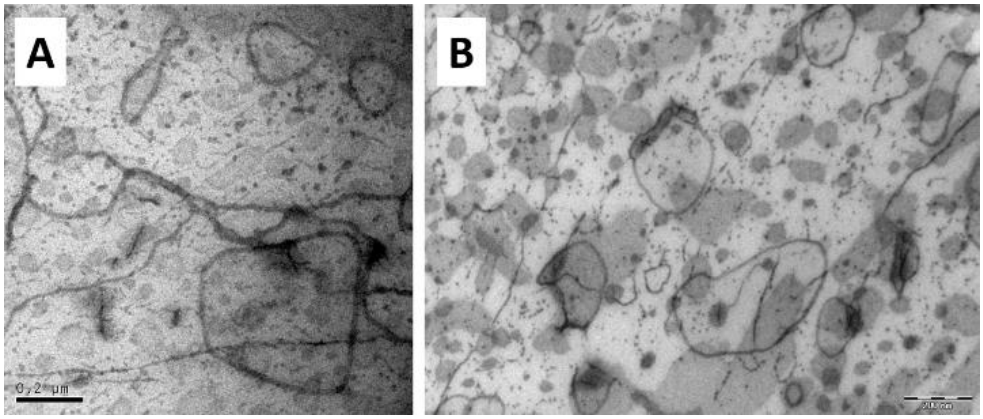


Figure 4.10: Transmission electron microscopy pictures of Brij® S-20 cured for 90 min at 130 °C and cooled down to room temperature (A) and after curing at 45 °C for a 48 hours, two postcuring steps and cooling down to room temperature (B). The loops are vesicles walls seen edge on, the dark grey areas are vesicular caps seen flat on. Linear streaks and dot-like droplets are interpreted as cylindrical and spherical micelles respectively.

4.1.2.3 WAXD

During the entire thermal protocol, synchrotron SAXS/WAXD patterns were collected as described in section 3.2 in order to assess the morphology development. The panel to the right in Figure 4.11 represents (part of) cooling 1 for *20%r* as measured by WAXD. The bold patterns are representative for two different situations and are repeated in the left side panel where a crystalline reflection in the -50°C pattern is highlighted in black.

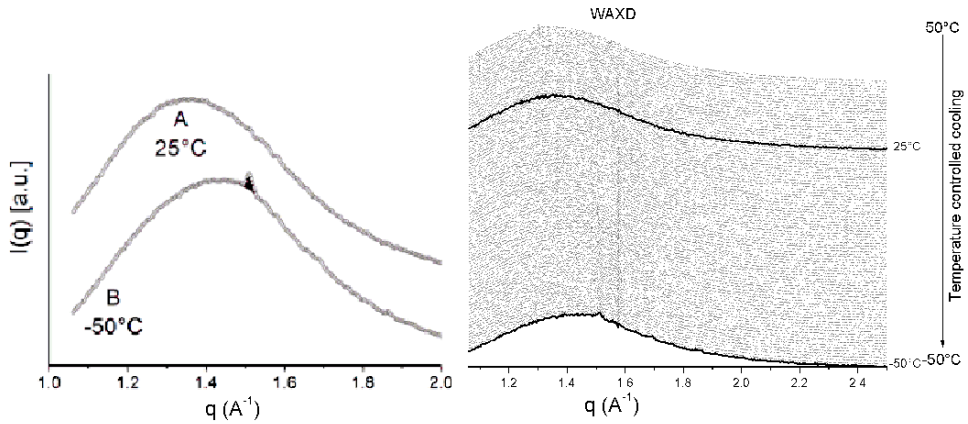


Figure 4.11: Left: WAXD pattern of amorphous Brij® S-20 in the epoxy resin at 25 °C (A) and of partially crystalline Brij® S-20 -50 °C (B), displaying one clear reflection at approximately q = 1.5 Å. The patterns A and B correspond to the temperatures labelled A and B in Figure 4.13. Right: WAXD patterns over the entire range from 50°C down to -50°C at a temperature resolution of one pattern per °C. Bold patterns correspond to the ones shown in the left side panel and also to the points A to B of Figure 4.13.

All WAXD patterns are very similar to pattern A in Figure 4.11, exhibiting a broad halo typical of amorphous material. Only at temperatures at and below the exothermic maximum during cooling 1 (gray area in Figure 4.9) and the subsequent endotherm during heating 1, the patterns include a small narrow reflection, which is shaded black in pattern B in Figure 4.11, left panel. Comparison with literature suggests that this reflection is due to either orthorhombically or hexagonally packed aliphatic stearyl chains.[97] For a hexagonal structure, one clear reflection at approximately q = 1.5 Å^{-1} is expected, whereas for orthorhombic material, besides the strongest (110) reflection at about q = 1.5 Å^{-1} also a weaker (200) reflection at approximately q = 1.7 Å^{-1} is expected. Because stearic acid is most prevalent in an orthorhombic phase[98], this is the most obvious crystal system here. The absence of the 200 reflection might be just a consequence of sensitivity with the amount of crystalline material being very small. The evolution of the area of this crystalline reflection is depicted as a function of time in the bottom panel of Figure 4.12. This area represents a WAXD crystallinity index and was normalized such that its maximum value equals 1. In further calculations, it will be assumed that all stearyl units are crystalline at the lowest temperature. The index thus represents the crystalline stearyl fraction.

The WAXD patterns during heating 1, the isothermal curing stage at 130°C as well as during cooling 2 and heating 2 are not shown as they only reveal an amorphous halo without any trace of crystalline reflections.

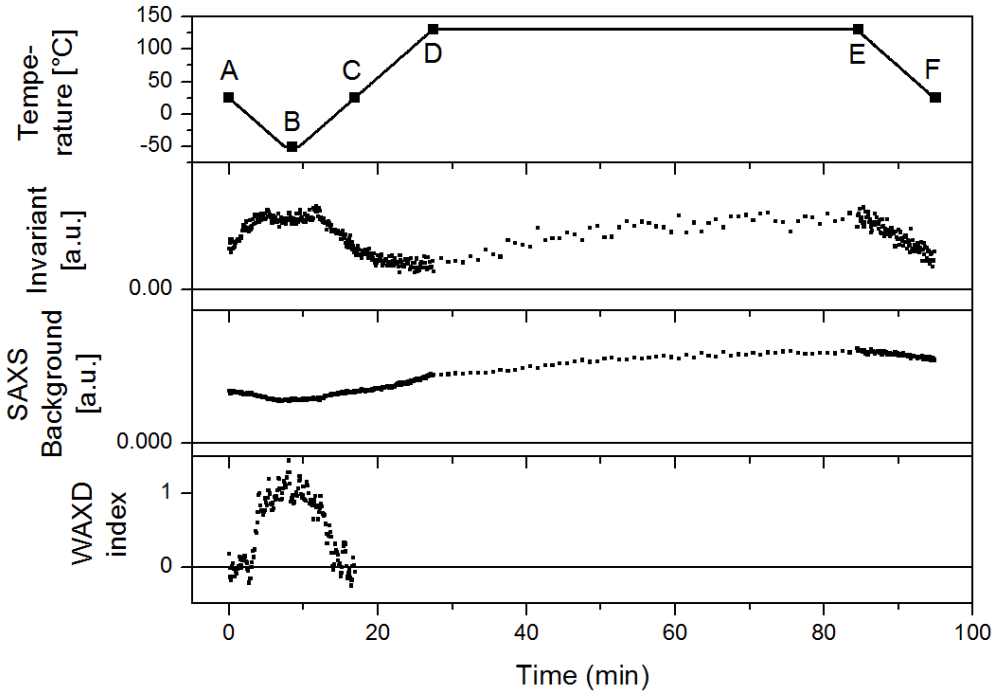
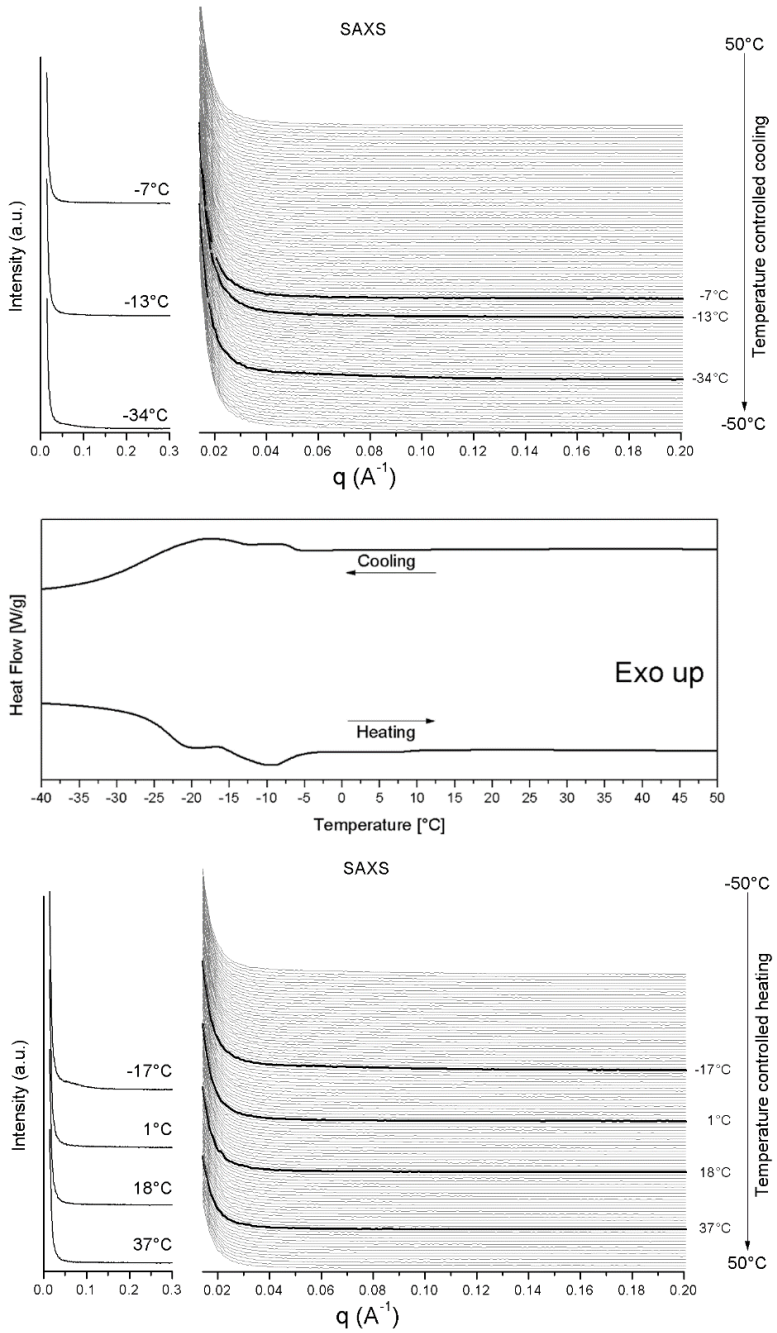


Figure 4.12: Top panel: The followed temperature profile with six key points highlighted. Second panel: The SAXS Invariant (Q_t) for all SAXS patterns. Third panel: SAXS background. Bottom panel: WAXD index, the surface of the WAXD reflection (seen as the black shaded area in figure 4.11) at all times and after normalization.

4.1.2.4 SAXS

Simultaneously with the WAXD data, also time-resolved synchrotron SAXS data were collected. The patterns during cooling 1 and heating 1 are depicted in respectively the top and bottom panels of Figure 4.13. No sharp reflections are observed, suggesting that the features as observed in Figure 4.10 scatter as individual objects rather than as (orderly) packed entities which would produce interference maxima in the patterns.



Figuur 4.13: Top panel: Time resolved SAXS patterns during cooling 1 with the highlighted profiles repeated in the left side panel. Middle panel: DSC profiles as in Figure 4.9 (top panel) during cooling 1 and heating 1. Bottom panel: Time resolved SAXS patterns during heating 1 with the highlighted profiles repeated in the left side panel.

The top panel in Figure 4.12 displays the followed temperature profile of which the part from 60 to 25°C during the first cooling run is omitted. The time in the abscissa

was set at zero when 25°C was reached during this cooling run. This profile also highlights six temperatures of which the corresponding SAXS patterns, *I(q)*, are shown in Figure 4.14 using a logarithmic scale. The total scattering power or the 'invariant' at a given time, Q_t, for all SAXS patterns was calculated as:

$$Q_t = \int_0^\infty [I(q) - B)] 4\pi q^2 dq \qquad \text{(Eq. 4.9)}$$

B is a constant background due to density fluctuations and equals the average scattered intensity in the range 0.33 $Å^{-1} < q < 0.35\ Å^{-1}$. The background values are represented by the horizontal full lines in Figure 4.14. The SAXS invariant and background are depicted using arbitrary units in Figure 4.12 since measurements were not conducted on an absolute scale.

Q_t was nevertheless interpreted in terms of (micro)phase density evolutions, relying on a scaling procedure and some assumptions. Given that the stearyl moieties dislike the epoxy resin, most realistically the vesicular walls and micelles should be composed of a central stearyl microphase (with electron density ρ_1), followed by a PEO layer on both sides (with electron density ρ_2). With the epoxy matrix, the minimum number of electron densities to account for in the interpretation of Q_t is three.

The mass density of the amorphous (liquid like) stearyl aliphatic chains, $d_{1,amo}$, resembles that of molten polyethylene, which can be approximated by:[99]

$$d_{1,amo} = 0.8674 - 6.313\ 10^{-4}\ T + 3.67\ 10^{-7} T^2 - 5.5\ 10^{-10}\ T^3\ [\frac{g}{cm^3}] \qquad \text{(Eq. 4.10)}$$

The density of orthorhombic crystalline material, d_{1cryst}, can be computed from:[100]

$$d_{1,cryst} = \frac{1}{0.994 + 2.614\ 10^{-4}\ T + 4.43\ 10^{-7}\ T^2}\ [\frac{g}{cm^3}] \qquad \text{(Eq. 4.11)}$$

In both equations 4.10 and 4.11, *T* is the temperature in °C. Multiplying these mass densities with 0.57 mole electrons/g yields the electron density [mole electrons/cm^3] as function of temperature as depicted in Figure 4.15 over the entire thermal protocol.

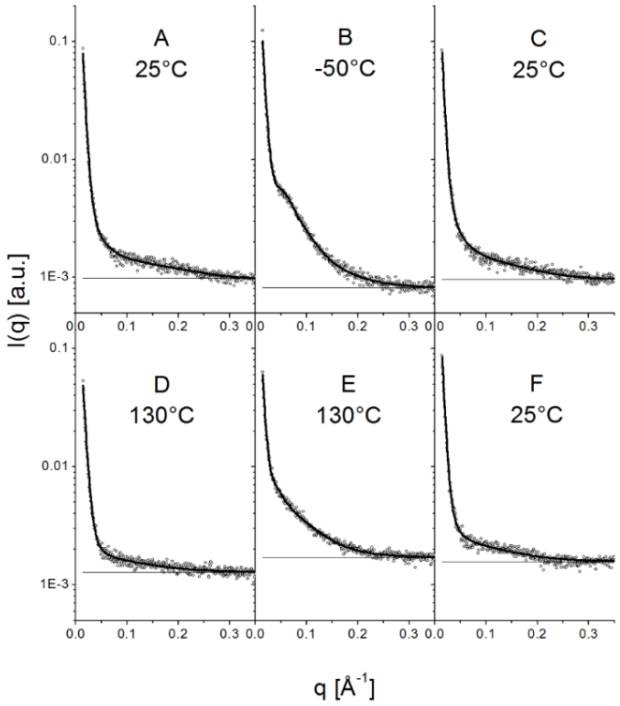


Figure 4.14: Selected SAXS patterns of the points highlighted in figure 4.12. Experimental patterns are depicted using open circles and the full lines are model curves based on equation 4.9. The horizontal full lines represent the background.

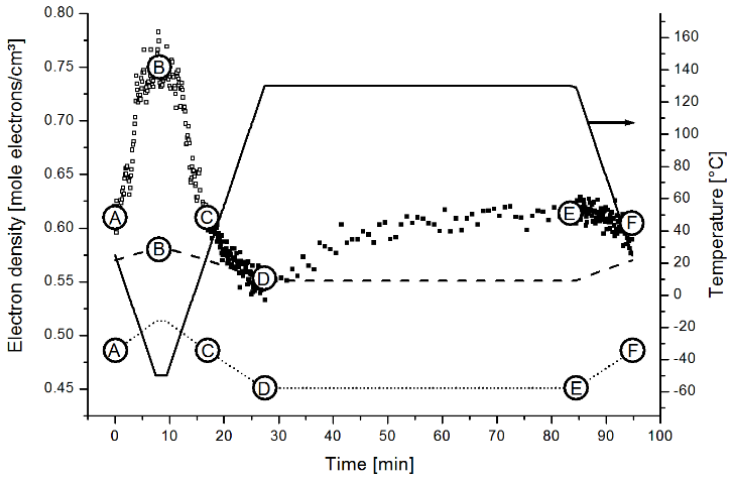


Figure 4.15: Electron densities of the different phases within 20%r. At times larger than point C, the system is in the amorphous state and the electron density of the (epoxy/PEO) matrix was calculated by equation 4.13 (full squares). At times shorter than point C, the system is (partly) crystalline, and therefore equation 4.14 was solved to find the matrix electron density (open squares). The dotted and dashed lines respectively represent the electron density of amorphous (based on equation 4.10 x 0.57 mole electrons/g) and crystalline (based on equation 4.11 x 0.57 mole electrons/g) stearyl aliphatic chains. The full line represents the temperature profile (right axis).

The density of amorphous PEO at 25 °C equals 1.092 g/cm³,[101] which after multiplying with 0.5448 mole electrons/g yields an electron density of 0.59 mole electrons/cm³. DGEBA has a mass density of 1.17 g/cm³ at room temperature and MDA a (liquid) density of 1.05 g/cm³ at 100 °C. Assuming additivity and neglecting the MDA liquid density difference between 100 °C and 25 °C, the density of a stoichiometric mixture is 1.14 g/cm³. Multiplying with 0.535 mole electrons/g yields the electron density of uncured resin at 25 °C, i.e. 0.61 mole electrons/cm³. This value is very similar to that of amorphous PEO but rather different from that of the (amorphous) aliphatic segments at point A or C (see Figure 4.15). With PEO and epoxy resin being well mixed, it can be assumed that Q_t is dominated by the contrast between the central stearyl layer and the rest (PEO plus epoxy), further referred to as the matrix with electron density, ρ_m.

Accordingly, one can write for the invariant at a given time, *t*, and irrespective of the actual morphology, the following expression:

$$Q_t = P\left(\rho_{m,t} - \rho_{1,t}\right)^2 \qquad \text{(Eq. 4.12)}$$

with *P* a proportionality factor. *P* should remain constant as long as the volume fraction of microphase separated stearyl units remains constant and Q_t should only differ from e.g. the invariant at point C, Q_C, because of a change in electron density difference between that of the stearyl phase, $\rho_{1,t}$, and the matrix $\rho_{m,t}$. Under these conditions and with knowledge of $\rho_{m,C}$, $\rho_{1,C}$ and $\rho_{1,t}$ one can calculate $\rho_{m,t}$ at any time:

$$\rho_{m,t} = \sqrt{\frac{Q_t}{Q_C}\left(\rho_{m,C} - \rho_{1,C}\right)^2} + \rho_{1,t} \qquad \text{(Eq. 4.13)}$$

Values for $\rho_{m,t}$ at times larger than point C, are presented in Figure 4.15 using full squares. For $\rho_{m,C}$ 0.61 mole electrons/cm³ was used. For $\rho_{1,C}$ and $\rho_{1,t}$ the density of liquid aliphatic chains (equation 4.10) was multiplied by 0.57 mole electrons/g. Point C thus represents the reference for these calculations.

At times shorter than point C, part of the stearyl phases is in the crystalline state. To find $\rho_{m,t}$ the following quadratic equation needs to be solved, assuming that the stearyl microphases scatter independently and are either fully crystalline or fully amorphous:

$$\frac{Q_t}{Q_C}\left(\rho_{m,C} - \rho_{1,C}\right)^2 = \beta\left(\rho_{m,t} - \rho_{1,cryst}\right)^2 + (1-\beta)\left(\rho_{m,t} - \rho_{1,amo}\right)^2 \qquad (4.14)$$

β is the fraction of crystallized stearyl phases. For β the WAXD crystallinity index in Figure 4.15 was used. The parameters $\rho_{1,amo}$ and $\rho_{1,cryst}$ were derived from the equations 4.10 and 4.11 and multiplication by 0.57 mole electrons/g. The result for

$\rho_{m,t}$ is added to Figure 4.15 using open squares. The evolution of $\rho_{m,t}$ is thus based on the assumption that changes in Q_t are solely due to contrast changes. This hypothesis only makes sense if the resulting $\rho_{m,t}$ evolution is meaningful. This seems to be the case, as is discussed next.

To a first approximation, $\rho_{m,t}$ in Figure 4.15 can be interpreted as being the evolution of the epoxy (electron) density. When cooled down from 25 °C (A) to -50 °C (B), the uncured epoxy density increases due to thermal contraction. The contraction decreases strongly from -22 °C onwards. This temperature coincides with the onset of vitrification seen in Figure 4.9. During subsequent heating, the material expands and does so more rapidly at temperatures above -23 °C, which is at the end of the devitrification range in Figure 4.9. The thermal expansion is not linear, in particular when surpassing 70 °C since the contraction due to the epoxy curing starts interfering. Once 130 °C is reached at D, curing progresses isothermally. The density increase at 130 °C is thus fully associated with the curing reaction. During cooling from E to F one expects a thermal contraction. Instead, the density remains rather constant, likely because of rapid vitrification during cooling. Interestingly, the vitrified, cured epoxy density at F is comparable with or even slightly lower than the uncured resin density at C (both 25 °C). This contra-intuitive effect has been reported earlier and can occur when rather fully cured systems vitrify isothermally or during cooling prior to reaching room temperature[102]. Note that the curing induced densification of epoxy resins appears to be rather heterogeneous. This can be deduced from the increase of the SAXS background during curing (Figure 4.12). In the simplest case, this background is only expected to increase with temperature due to increasing thermal density fluctuations. Curing seems to bring extra fluctuations, which are frozen in by gelation and vitrification because the expected background decrease during cooling from E to F is minimal. The heterogeneous nature of the epoxy resin can also be inferred from the broad glass transition range in the second cooling and heating runs of Figure 4.9. In the past, attempts have been made to link changes in the SAXS background to the epoxy curing chemistry or to the creation of microvoids[103]. The latter option is excluded since TEM did not provide any evidence for such voids (Figure 4.10A). In summary, the evolution of the epoxy electron density seems realistic, supporting the underlying assumption that the stearyl demixing remains at all temperatures and times.

4.1.2.5 SAXS MODELLING

The TEM picture in Figure 4.10A revealed that the morphology at point F in the thermal program (see Figure 4.12 top panel) is predominantly vesicular. Accepting that the demixing remains, does not imply that the vesicular morphology dominates at all times and temperatures. Attempts to describe the representative data in Figure 4.14 in terms of (layered) spherical or cylindrical micelles using earlier described

models[104] remained unsuccessful. In contrast, all data could adequately be described as being due to (predominantly) vesicles.

When sufficiently large, the vesicular curvature is limited and the SAXS patterns can be modelled as the scattering from flat vesicular walls. The black lines over the SAXS patterns in Figure 4.14 are interpretations in terms of such a layer like morphology. However, to accurately describe all features in the SAXS patterns, 4 electron density levels had to be used rather than 3 and transition zones between them needed to be incorporated. Following Goderis et al.,[105] such a 4 level system can be modelled as 3 superimposed block-like entities with electron density ρ_i and block length l_i on top of a constant 4th electron density level. All distances l_i are defined symmetrically around the center of the vesicle wall and the constraint holds that $l_i < l_{i+1}$. Equation 4.15 describes the corresponding SAXS pattern:

$$I(q) = \frac{C}{4\pi q^2} F(q)^2 + B \qquad \text{(Eq. 4.15)}$$

with

$$F(q) = \sum_{i=1}^{3} \frac{(\rho_i - \rho_{i+1})}{q} sin\left(\frac{q l_i}{2}\right) exp\left(-0.5\sigma_{i/i+1}^2 q^2\right) \qquad \text{(Eq. 4.16)}$$

$\sigma_{i/i+1}$ characterizes the widths of the transitions zones between the layers i and i+1. The parameters *B* and *C* respectively represent the background due to density fluctuations and a constant proportional to the volume occupied by the vesicles and the X-ray flux. The distance between the vesicle walls and/or the wall-to-wall stacking disorder is supposed to be large enough not to cause any inter-wall interference in the recorded *q*-range. In a first step, equation 4.15 was fitted to (the strongest) pattern B in Figure 4.14. This was done by minimizing the sum of squared differences between the experimental and theoretical (model) curve on a logarithmic scale, while varying the parameters in Equation 4.15. This action was done using the solver built into Microsoft Excel. ρ_1 and ρ_4 were set to the crystalline aliphatic density and epoxy matrix density highlighted at the points B in Figure 4.15. It furthermore turned out that $\sigma_{1\text{-}2}$ was close to zero. This parameter was therefore set to zero in a second fitting iteration, without affecting the quality of the fit. This reduced the number of fitting parameters to 9. Via this procedure, a value for C was obtained which was used as a fixed value in the fittings of the other SAXS patterns in Figure 4.14. For these patterns ρ_1 and ρ_4 were set equal to the relevant amorphous aliphatic (stearyl) and epoxy matrix densities highlighted in Figure 4.15 with the letter labels.

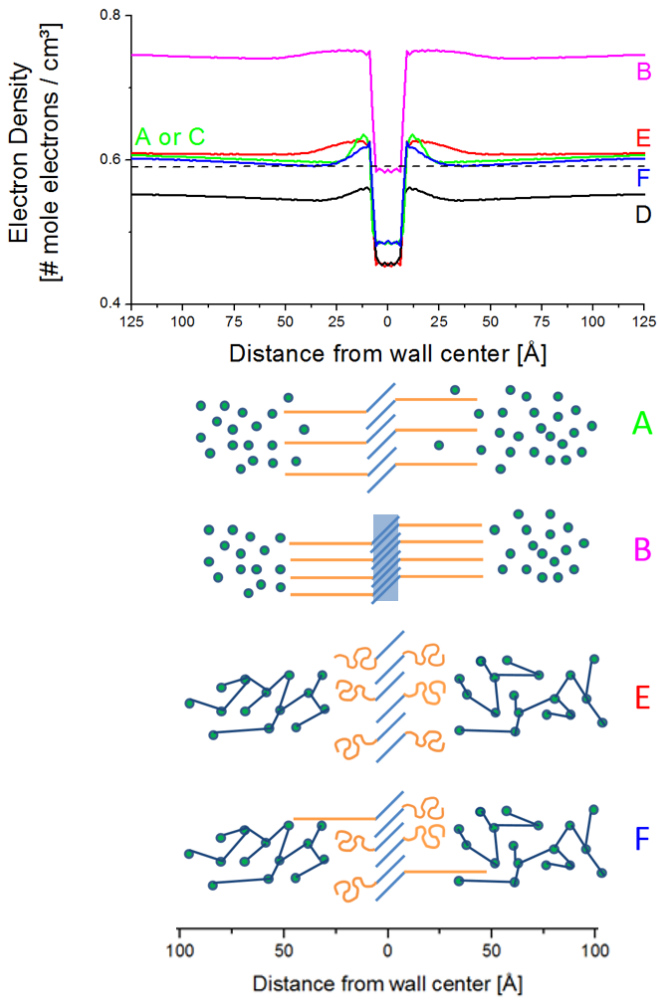


Figure 4.16: Electron density profiles across the vesicular wall (top) and sketches of corresponding structure (bottom). The blue lines in the sketches correspond to stearyl chains, the orange features to PEO. Epoxy is displayed as the green spheres, which are connected upon curing. The blue shaded area emphasizes the crystalline state of the aliphatic tails. The curve labels correspond to the letter labels in the Figures 4.12, 4.14 and 4.15.

Rather than reporting the resulting model parameters of equation 4.15, it is instructive to compute and discuss the electron density profiles across the vesicular wall. These were obtained via a Fourier cosine transformation of the model scattering amplitude according to:

$$\rho(x) = \frac{1}{2\pi}\int_0^\infty 2F(q)\cos(qx)\,dq + \rho_4 \qquad \text{(Eq. 4.17)}$$

The electron density profiles corresponding to the SAXS patterns of Figure 4.14 are displayed in Figure 4.16 together with sketches of the associated layer structure. Throughout this thesis, stearyl features (i.e. structures, SAXS/WAXD reflections, DSC transitions, …) are often displayed in blue and those related to PEO in orange. For all temperatures and times, the central, low electron density layer has a thickness of approximately 15 Å, which is shorter than an all-trans, fully stretched stearyl chain (22 Å), implying that the stearyl chains in the center of the bilayer are interdigitated and tilted (see the blue lines in the sketches of Figure 4.16). Since the thickness is fairly constant, the density of this layer can only vary by the lateral separation of the aliphatic chains. Changes are related to thermal expansion as well as to crystallization as in situation B.

Tilting and interdigitation of the aliphatic chains increases the chain cross-sectional area at the interface with the PEO zone (orange features in Figure 4.16). This allows for a further separation of the PEO chains compared to when the stearyl chains would be fully stretched and oriented perpendicular to the wall surface.

The (green) electron density profile for situation A as displayed in Figure 4.16, exhibits an excess electron density at the aliphatic layer borders, suggesting a congestion of PEO chains at the interface. This crowding – likely as a result of being connected to the aliphatic chains – relaxes at larger distances from the aliphatic layer down to a density slightly higher than that of amorphous PEO at 25 °C (0.59 mole electrons/cm³, represented by the dashed line in Figure 4.16). This may reflect the presence of (electron denser) epoxy resin in between the PEO chains. In fact, the driving force for the interdigitation and tilting of the aliphatic chains might be the swelling of PEO with epoxy resin. PEO is miscible with the uncured epoxy resin. The zones of lower density for situation A stretch out approximately 50 Å away from the central stearyl layer. This distance corresponds to a fully stretched PEO chain with 20 monomeric units (i.e. 49 Å). At this point the electron density levels off to that of the epoxy matrix, ρ_4. The uncured epoxy resin is represented with green spheres in Figure 4.16, thereby neglecting the two component nature of the resin.

At point B, all stearyl moieties are assumed to be closely packed in the crystalline state. The epoxy resin is in the uncured, vitrified state and has a higher density than in point A because of thermal contraction (see the magenta electron density profile in Figure 4.16). The PEO layers now seem to be (electron) denser than the epoxy matrix. It is suggested that – because of the closer aliphatic packing – the PEO congestion now exists over the entire PEO layer, leaving little space for epoxy resin in between them. Upon heating to point C, all crystals melt and a situation identical to as in A is obtained.

Upon further heating to point D at 130 °C, all densities further decrease because of thermal expansion. Otherwise, the (black) electron density profile for situation D in Figure 4.16 is very similar to that of A or C. However, the PEO regions do not stand out so clearly, suggesting less congestion at the interfaces with the stearyl layer and a higher degree of mixing with the epoxy resin compared to in A and C. Less congestion follows from the higher inter-chain distances in the central stearyl layer.

At E, the system is extensively cured and still at 130 °C. The density of the central stearyl layer is identical to D. In contrast, the cured epoxy density as well as the density of the PEO layers has increased compared to in D. The former is expected from the curing reaction. The PEO densification is accompanied by a contraction of the PEO layer, assuming that the regions of highest density represent the PEO layers. The thinner layers suggest that the PEO chains collapsed during the curing process, thereby segregating the epoxy. This process follows from the reduced mixing entropy during epoxy curing, as mentioned in section 2.3.2. The stearyl chain tilt and interdigitation in the present case might be controlled by the necessity of accommodating the collapsed PEO chains. However, the dynamic interaction of the soft PEO chains with the curing epoxy at 130 °C may induce its softening (plasticization) and decrease of the glass transition temperature even up to distances relatively far away from the actual interface. With 20% Brij® S-20 and vesicles that are approximately 100 Å thick, it can be calculated that (for the hypothetic case of periodically stacked layers) the interaction penetration only needs to be 200 Å to affect the entire material volume. A progressively decaying interaction of the PEO chains with epoxy matrix may contribute to the heterogeneous nature of the epoxy matrix, inferred from the large SAXS background and the broad vitrification range.

After cooling down the cured material to 25 °C at point F, an electron density profile is obtained very similar to in A or C. The PEO density beyond the congestion points now reaches that of amorphous PEO, suggesting that it is a rather pure PEO phase. To avoid PEO overcrowding at the interface with the central stearyl layer, part of the PEO chains must have succeeded in stretching out to within the cured epoxy resin prior to its vitrification. The absence of exothermic heat in the DSC cooling run 2 in Figure 4.9 demonstrates that the central stearyl layer is no longer able to crystallize after epoxy curing. The closer aliphatic chain packing required for crystallization seems to be prevented by the matrix vitrification prior to reaching the supercooling needed for crystallization.

4.1.3 INFLUENCE OF CURING PROTOCOL ON THE MORPHOLOGY OF 20%R

To check the robustness of the obtained morphology, a second curing protocol was followed involving curing at 45 °C for 2 days and postcuring successively at 80 °C for 6 h and 150 °C for 90 min. The temperature of 45°C falls below the ultimate *20%r* T_g

after full curing. Using equation 4.7 and the data obtained in Figure 4.8, one can estimate that the gelation point (70% conversion was taken) will be reached in less than 6 hours. This ensures that the morphology is fixed. Most likely curing was rather complete after 2 days, making the two post-curing steps at 80 °C and 150 °C pointless. Be that as it may, the morphology after this curing protocol as illustrated in Figure 4.10B was identical to after curing at 130 °C, proving the morphological robustness of this formulation.

4.2 CURING KINETICS AND MORPHOLOGY OF 30%R

In this section, the curing kinetics and morphology of *30%r* are discussed and compared to the results obtained on *20%r*.

4.2.1 DSC

Figure 4.17 displays the thermograms of *30%r* obtained while imposing the standard temperature profile as depicted in Figure 3.2. The top graph contains cooling 1 and heating 1 of the first segment, the middle graph represents the exothermic heat recorded in the isothermal segment at 130°C and the bottom panel shows the cooling and heating runs recorded during the third segment. In the next paragraph the isothermal curing kinetics will be discussed.

4.2.1.1 ISOTHERMAL CURING KINETICS

In the kinetic study of section 4.1.1. high heating rates of 200°C/min were used to reach the isothermal curing temperature without curing during the heating run. It was also proven that adding 20% Brij® S-20 considerably slowed down the reaction speed due to a dilution of the reacting species. Diluting these species further by adding more Brij® S-20 is expected to induce a further rate reduction. The top graph of Figure 4.17 shows, however, that curing cannot be suppressed fully during heating at 10°C/min as some exothermic heat is observed at the end of heating 1, just like for *20%r* in Figure 4.9.

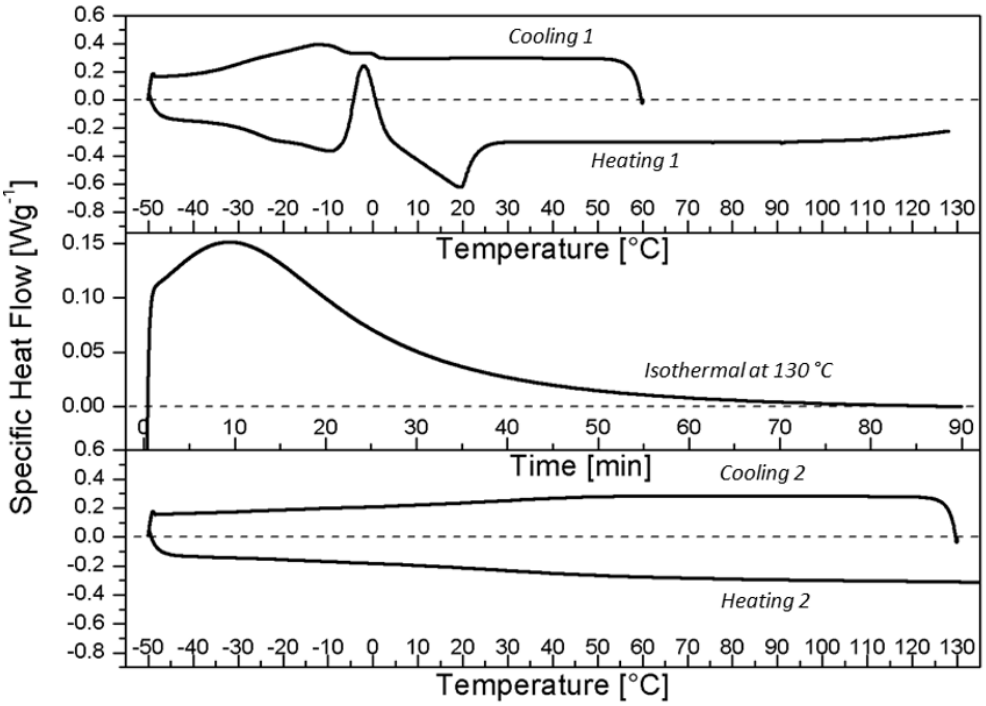


Figure 4.17: DSC thermograms for *30%r*, related to the thermal protocol used during time-resolved X-ray based morphological characterization and as depicted in Figure 3.2. Exothermic signals are plotted upwards. The program includes cooling 1 and heating 1 at 10 °C/min (top panel), isothermal curing at 130 °C for 90 min (middle panel), followed by cooling 2 and heating 2 at 10 °C/min (bottom panel).

The epoxy resin conversion (α) at time t during the isothermal segment after heating at 10°C/min was calculated by dividing the reaction enthalpy at time t by the maximum total reaction enthalpy. To do so Equation 4.18 was used, which is the equivalent of equation 4.6 in which ΔH_h, the heat evolved during the heating run at 10°C/min to 130°C, was added to ΔH_{prep} and in which the factor for ΔH_{max} is 0.7 instead of 0.8:

$$\alpha = (\Delta H_t + \Delta H_{prep} + \Delta H_h)/(\Delta H_{max} * 0.7) \qquad \text{(Eq. 4.18)}$$

In fact, ΔH_{prep} for *30%r* and all samples containing higher amounts of Brij® S-20 was found to be zero. Integration of the isothermal specific heat flow (Figure 4.17, middle panel) resulted in the epoxy conversion as function of time (Figure 4.18). It does not start at a zero conversion value due to the 6.5% conversion realized during heating towards 130°C. The conversion is only slightly slower compared to for *20%r* (dashed line in Figure 4.18 – calculated with Equation 4.18, with a factor 0.8 instead of 0.7 and with proper values for ΔH_h and ΔH_{prep}). After 90 min the conversion reached 82% for *30%r* instead of 90% for *20%r*, indicating that complete epoxy curing is prevented by further dilution with Brij® S-20. Note that the material T_g after curing is centered

around 25°C as can be read from the broad step like transition in the cooling 2 and heating 2 DSC profiles displayed in Figure 4.17 (bottom panel). It seems that plasticization due to the presence of Brij® S-20 is more severe compared to for *20%r*, for which the T_g was centered around 60°C. It might be that the reagents are spatially separated from each other due to preferred interactions with the PEO segments or by the specific Brij® S-20 nanomorphology, which - assuming it to be predominantly vesicular - contains impenetrable aliphatic walls.

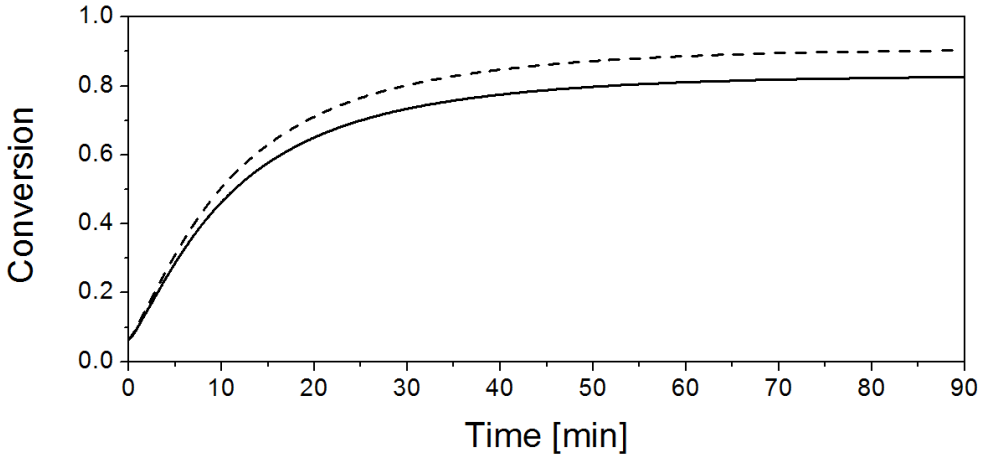


Figure 4.18: Epoxy conversion during isothermal curing at 130°C after heating at 10°C/min for *30%r* (full line) and *20%r* (dashed line).

4.2.1.2 COOLING AND HEATING SEGMENTS

The top panel of Figure 4.17 shows the DSC cooling 1 and (subsequent) heating 1 runs executed on *30%r* prior to isothermal curing. Cooling 1 is very similar to cooling 1 of *20%r*, the only differences being a slight upwards shift of the onset temperature of the stearyl crystallization (2 °C) and an increase of the heat involved, as expected for a higher block copolymer content. More clearly than for *20%r*, the exothermic signal during cooling 1 in fact is bimodal, with onsets at 2°C and -5°C for the first and second event. The WAXD data in section 4.2.2 will demonstrate that those signals are related to the formation of different stearyl crystal types. The T_g in this cooling run is shifted approximately 3°C lower compared to for *20%r*. The first heating run of *30%r* exhibits major differences compared to heating 1 of *20%r*. A strong exothermic signal is observed, which - given its magnitude - cannot be due to crystallization of the aliphatic segments of Brij® S-20. It will be shown in section 4.2.2 that this signal is due to the crystallization of the PEO segments. The endothermic signal, peaking at about 20°C is due to melting of these PEO crystals. Melting of the crystalline aliphatic chains (formed during the preceding cooling run) coincides with the PEO (cold) crystallization, as will be clear from the WAXD data.

The second cooling and heating runs, following isothermal curing, only revealed vitrification and devitrification at temperatures close to the melting points seen during the first heating run. Obviously, with the matrix being vitrified and with the PEO chains being part of this vitreous matter, crystallization cannot be expected. It should be remarked though that although the DSC data during cooling 2 and heating 2 were reproducible, this was not the case for the X-ray experiments. In the X-ray experiments, faint signs of crystallization were occasionally observed during cooling 2. This observation appeared to depend on the exact spot of the sample the X-ray beam passed through. It therefore seems that the temperature profile and hence the curing degree in the X-ray measurements was not entirely homogeneous, with some parts having reached a sufficiently high conversion to induce vitrification and hence prevent crystallization, whereas at other places the conversion was insufficient to do so. Such effects were not observed for *20%r* for which the conversion was sufficiently high throughout to prevent crystallization during cooling 2. As will be discussed in chapters to come, in samples with Brij® S-20 contents above 30%, crystallization and melting was always observed during cooling 2 and heating 2 because the material T_g in all these cases remained low due to the low conversion degrees reached after 90 min at 130 °C. Because of the variability in the X-ray experiments during cooling 2 and heating 2, only the X-ray results during cooling 1 and heating 1 will be discussed below for *30%r*. Furthermore, given the similarity in post curing DSC behavior with *20%r* it is safe to assume that the morphological developments during and after curing for *30%r* are very similar to those of *20%r*.

4.2.2 WAXD

Temperature-resolved WAXD data of *30%r* during cooling 1 and heating 1 are summarized in Figure 4.19 in respectively the top and bottom panels. The displayed upper temperature was limited to 50°C as above that temperature the samples were fully amorphous. The middle panel shows the relevant part of the corresponding DSC data.

The DSC data suggested that crystallization during first cooling for *30%r* is similar to the crystallization observed in *20%r*. Indeed, just like for *20%r* a clear WAXD reflection is observed at q = 1.52 $Å^{-1}$, at 1°C and below due to the stearyl crystallization. However, close inspection suggests that concomitantly a very weak second reflection appears and shifts to about q = 1.7 $Å^{-1}$ at the lowest temperatures, pointing at an orthorhombic aliphatic subcell with the 110 and 200 reflection at respectively 1.5 $Å^{-1}$ and 1.7 $Å^{-1}$. Blue lines are drawn along these reflections in Figure 4.19. Recall that throughout this thesis various PEO and stearyl features are highlighted in respectively blue and orange. Very clearly, the peaks drift away to higher q-values with decreasing temperature as a result of thermal contraction. This contraction is most pronounced for the 200 reflection and is arrested when the

system T_g is crossed, presumably because of being connected to the glassy matrix via the PEO segments. Besides the two reflections due to orthorhombic material, an extremely weak reflection appears at q = 1.48 $Å^{-1}$ upon cooling to within the temperature range of the low temperature DSC exothermic signal. This reflection could only be identified in *30%r*, based on the DSC data and knowing that a similar reflection appears in samples with a higher Brij® S-20 content. In Chapter 6 it will be revealed that this reflection is associated with the crystallization of aliphatic segments within cylindrical micelles into a poorly ordered, fairly open lattice. The sharper, orthorhombic reflections are due to aliphatic crystallization within vesicle walls. Also in samples with a higher Brij® S-20 (see chapter 6), the aliphatic segments within the vesicles crystallize at a higher temperature than the ones in cylindrical micelles. Note that the two aliphatic crystallization events also apply to *20%r*, given the bimodal DSC cooling 1 exotherm (see Figure 4.9). The presence of crystallizing cylindrical micelles could nevertheless be neglected in the SAXS data analysis because the fraction of these features was very low.

The area contained by all aliphatic reflections for *30%r* relative to the total area of the WAXD pattern is slightly larger compared to the area of the (single) reflection for *20%r*, revealing a higher crystalline content for *30%r*, which is in agreement with the slightly larger exothermic heat observed in the DSC cooling 1 curve. The crystalline content remains constant when T_g is crossed during cooling.

Once the T_g is surpassed during subsequent heating at about -8 °C, reflections (highlighted in orange in the Figure 4.19 bottom panel) start appearing at q = 1.36 $Å^{-1}$ and q = 1.63 $Å^{-1}$. Both strong reflections are in fact combinations of several overlapping reflections due to monoclinic PEO crystals with the (120) reflection contributing most strongly to the one at q = 1.36 $Å^{-1}$ and the (112), (-212) and (032) reflections governing the peak at q = 1.63 $Å^{-1}$.[106] Concomitantly to the growth of the PEO reflections, the stearyl reflections shrink and finally disappear completely. Interestingly, all the stearyl crystals in *30%r* actually disappear *below* the stearyl crystallization onset temperatures seen during preceding cooling. Such a phenomenon would not occur if it were not coupled to another phase transition. This suggest that the PEO crystallization assist the stearyl melting, which in turn implies that stearyl and PEO crystallinity most likely cannot coexist in one and the same Brij® S-20 nanostructure. According to this view, the temperature region in which *both* stearyl and PEO crystallinity are observed (from -8 till -3 °C), relates to the coexistence of vesicles which still have stearyl crystallinity and others which already converted to have PEO crystallinity. It will be shown more clearly in chapter 6 that the PEO crystallization is able to actively disrupt the stearyl crystallinity.

With this information from WAXD, it was possible to assign the DSC signals to stearyl or PEO transitions. The segments in the middle panel of Figure 4.19 belonging to stearyl are highlighted in blue, the PEO governed transitions are colored in orange.

One may wonder why PEO does not crystallize in *20%r* whereas it does so in *30%r*. Most likely, at low Brij® S-20 concentrations, i.e. below 30%, the PEO segments are fully saturated with resin monomers, preventing their crystallization. Given the nanophase separation, these saturated PEO regions coexist with pure epoxy resin volumes. At higher Brij® S-20 concentrations, no pure resin volumes exist and the mixed resin phase is supersaturated in PEO, enabling PEO crystallization. But, nucleation seems problematic, by which PEO crystallization is not taking place during the cooling run, leaving the stearyl moieties to crystallize. Stearyl crystallization leads to a squeezing out of the epoxy from the PEO layers (see discussion on *20%r*) by which PEO crystal nucleation should be facilitated, provided vitrification does not impose kinetic constraints, which actually is the case during cooling 1. Therefore, only during subsequent heating above T_g, the gained mobility permits PEO (cold) crystallization.

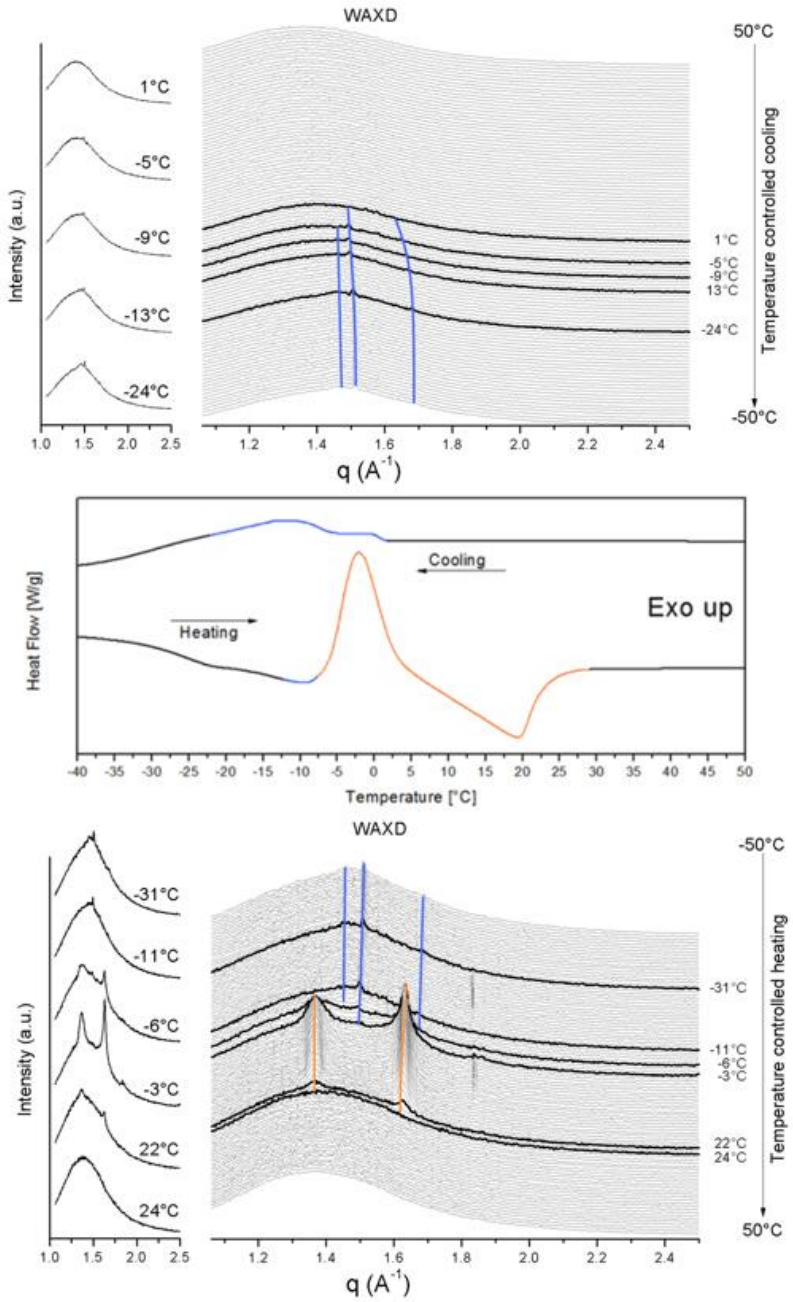


Figure 4.19 Top panel: Time resolved WAXD patterns collected during cooling 1 of *30%r*. The patterns highlighted in bold are displayed separately in the left side window. Middle panel: DSC thermograms during cooling 1 and heating 2 of *30%r*. Bottom panel: Time resolved WAXD patterns during heating 1 for *30%r* with highlighted patterns displayed separately in the left side window. Blue and orange features belong to transitions (in DSC) or reflections (in the WAXD patterns) of respectively the stearyl or PEO moieties.

4.2.3 SAXS

Figure 4.20 displays the SAXS data (measured simultaneously with WAXD) of cooling 1 (top panel) and heating 1 (bottom panel). The corresponding DSC data are once again displayed in the middle panel.

The high temperature SAXS patterns of *30%r* are rather featureless and very similar to those of *20%r*, suggesting the presence of similar vesicular nanostructures. In contrast, clear differences in the SAXS patterns are seen with respect to *20%r* for *30%r* being in a (partially) crystalline state. Whereas the SAXS patterns of *20%r* remained without correlation maxima, the patterns of *30%r* do exhibit clear maxima.

Using the WAXD information one can associate the scattering maximum at approximately $q = 0.07$ Å^{-1} with structures in which stearyl is crystalline whereas the structures with a maximum at approximately $q = 0.05$ Å^{-1} should contain crystalline PEO. Therefore, the peaks in the SAXS patterns of Figure 4.20 are highlighted in blue and orange for the structures that are generated by the crystallization of respectively the stearyl and PEO moieties.

While discussing the WAXD data, it was suggested that two different aliphatic crystalline structures exist. There are, however, no indications for two different structures in the SAXS patterns. It therefore seems that the crystalline cylindrical micelles contribute very little to the SAXS patterns, just like for *20%r*. Their presence is therefore neglected in the analysis. Furthermore, as the TEM images (after curing) of *20%r* and the ones of the samples with higher Brij® S-20 concentrations (see Chapter 6), display mostly vesicular structures, the basic morphology of *30%r* should also be vesicular, say layer-like.

Because of the maxima in the SAXS patterns, some of these vesicles (in the semicrystalline state) might be of a multi-walled type or some vesicles might be packed so closely that interference is observed in the SAXS patterns. It furthermore seems that the crystallization process is responsible for this stacking (order), since maxima are no longer observed in the SAXS patterns once the material is fully in the liquid like state at high temperatures.

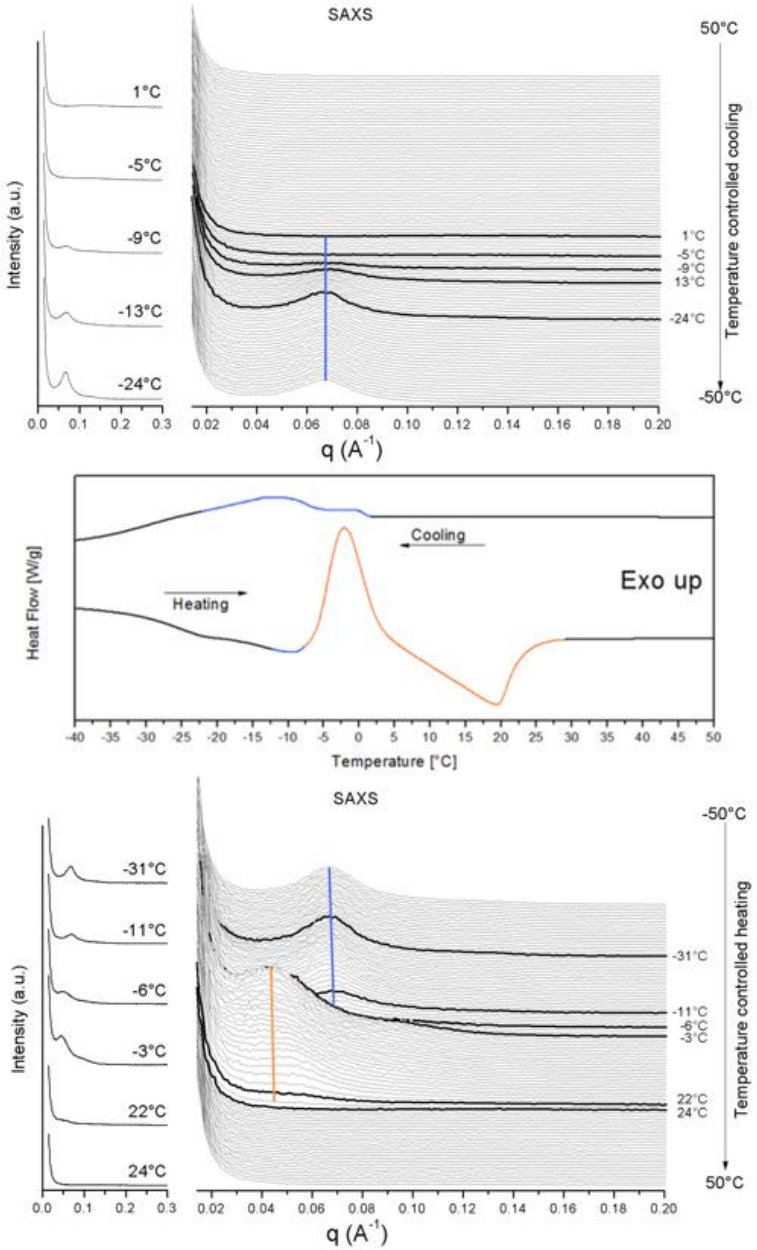


Figure 4.20: Top panel: Time resolved SAXS patterns collected during cooling 1 of *30%r*. The patterns in bold are displayed separately in the left side window. Middle panel: DSC thermograms during cooling 1 and heating 2 of *30%r*. Bottom panel: Time resolved SAXS patterns of heating 1 for *30%r* with highlighted, characteristic patterns displayed separately in the left side window. Blue and orange features belong to transitions (in DSC) or peaks (in the SAXS patterns) of respectively the stearyl or PEO moieties.

Therefore the SAXS patterns for *30%r* in the semicrystalline state were modelled in terms of a morphology composed of a fraction of single bilayer vesicles and a fraction of stacks made from such bilayers. The equation used to approach the experimental SAXS patterns reads:

$$I(q) = \frac{C}{4\pi q^2} F(q)^2 [(1-\beta) + \beta S(q)] + B \qquad \text{(Eq. 4.19)}$$

with *C* and *B* being defined as in equation 4.15. *F(q)* compares well to *F(q)* given by equation 4.16, but in the present case, the number of electron density levels was limited to 3, implying that *'i'* only runs up to 2:

$$F(q) = \sum_{i=1}^{2} \frac{(\rho_i - \rho_{i+1})}{q} sin\left(\frac{q l_i}{2}\right) exp\left(-0.5\sigma_{i/i+1}^2 q^2\right) \qquad \text{(Eq. 4.20)}$$

In this equation, ρ_1, ρ_2 and ρ_3 represent the aliphatic, PEO and epoxy densities. The parameter l_1 corresponds to the thickness of the aliphatic layer and l_2 to the sum of the aliphatic layer thickness and two neighboring PEO layers. The width of the transition zone between the aliphatic and PEO layers, $\sigma_{1/2}$, was found to be zero throughout. The parameter $\sigma_{2/3}$ represent the width of the sigmoidal transition layer between the PEO and epoxy zones. The parameter β represents the share to the scattering due to stacks and can take values between zero and one. Obviously, (1-β) is the share taken by individual bilayers. These shares actually represent the shares in the integrated intensity, the so-called 'invariant'. *S(q)* represents the structure factor, accounting for interlayer interference, as originally proposed by Guinier in 1963:[103,104]

$$S(q) = N + 2\sum_{k=1}^{N-1}(N-k)cos(kqL_P)exp(-0.5k^2q^2{\sigma_{LP}}^2) \qquad \text{(Eq. 4.21)}$$

This structure factor assumes paracrystalline stacks of *N* bilayers (with *N* being an integer number), separated by an average repeat distance L_P with a mean square fluctuation of this repeat distance given by σ_{LP}.

Fitting the patterns on a logarithmic scale by minimizing the sum of squared residuals was done by using the Microsoft Excel solver. ρ_1 and ρ_3 were set to the aliphatic density and (non-cured) epoxy matrix density as defined earlier for *20%r* and $\sigma_{1/2}$ was actually fixed at zero. All other parameters were left to vary during the fitting procedure. Values for ρ_1 are temperature dependent and were based on the Equations 4.10 and 4.11 for the cases the aliphatic layers were – according to the WAXD data - either amorphous or crystalline. These mass densities were multiplied with 0.57 mole electrons/g to yield electron densities [mole electrons/cm³]. For the electron density of non-cured epoxy, ρ_3, the values as represented in Figure 4.15 (open squares) were taken.

To allow for a discussion of the results, electron density profiles were computed for the single bilayers according to equation 4.17 with ρ_4 replaced by ρ_3 and *F(q)* given by equation 4.20. The electron density profile of the stacks was computed from:

$$\rho(x) = \langle\rho\rangle + \frac{1}{2\pi}\int_0^\infty 2F(q)\frac{sin(0.5NqL_P)}{sin(0.5qL_P)}\cos(qx)\,dq \qquad \text{(Eq. 4.22)}$$

with <ρ> the average electron density within the stacks. In representations of the stack electron density profiles, *N* (the number of layers in the stack) was always taken rather large irrespective of the actual *N* value returned by the fitting procedure. These profiles are furthermore free of paracrystalline disorder, which is artificial but functional for representation purposes. To produce the profiles of single bilayers, *N* in Eq. 4.22 was set to 1.

The discussion of non-cured *30%r* focusses on the structure at two representative temperatures, i.e. -31°C and -3°C collected during heating 1. At these temperatures the SAXS patterns reach a maximum intensity. At -31°C, the stearyl moieties are crystalline and those of PEO amorphous. At -3°C the opposite applies. Realistic values for amorphous and crystalline PEO (ρ_2) were obtained via the SAXS fitting procedure at -31°C and -3°C respectively. Moreover, the fits returned very similar *C*-values for both fits, underlining the consistency of the approach.

The experimental data (in black) together with the fit according to equation 4.19 (in red) are shown for *30%r* at -31°C and -3°C in Figure 4.21 A and C respectively. The black horizontal lines in these graphs correspond to the background, *B*. The blue and green dashed curves are the shares due to the scattering of respectively the isolated bilayers and stacks. Both curves are plotted on top of the background. The stack share for *30%r* at -31°C, β, amounts to 87% and at -3°C β is 40%. At -31°C, *N* equals 8, L_p equals 86 Å and σ_{LP} equals 18 Å. At -3°C *N* equals 2, L_p equals 121 Å and σ_{LP} equals 17 Å. Clearly the high temperature morphology with crystalline PEO is less perfectly stacked compared to the low temperature structure with stearyl crystallinity. This effect is most visible through the lower stack fraction and *N* value.

The electron density profiles are depicted in Figure 4.21 B and D for the cases at -31°C and -3°C and using green and blue curves for respectively the stacks and isolated bilayers. The electron density of the central feature corresponds to that of the aliphatic Brij® S-20 tails, which are crystalline at -31°C and liquid at -3°C. In Figure 4.22 an interpretation is provided on these electron density profiles.

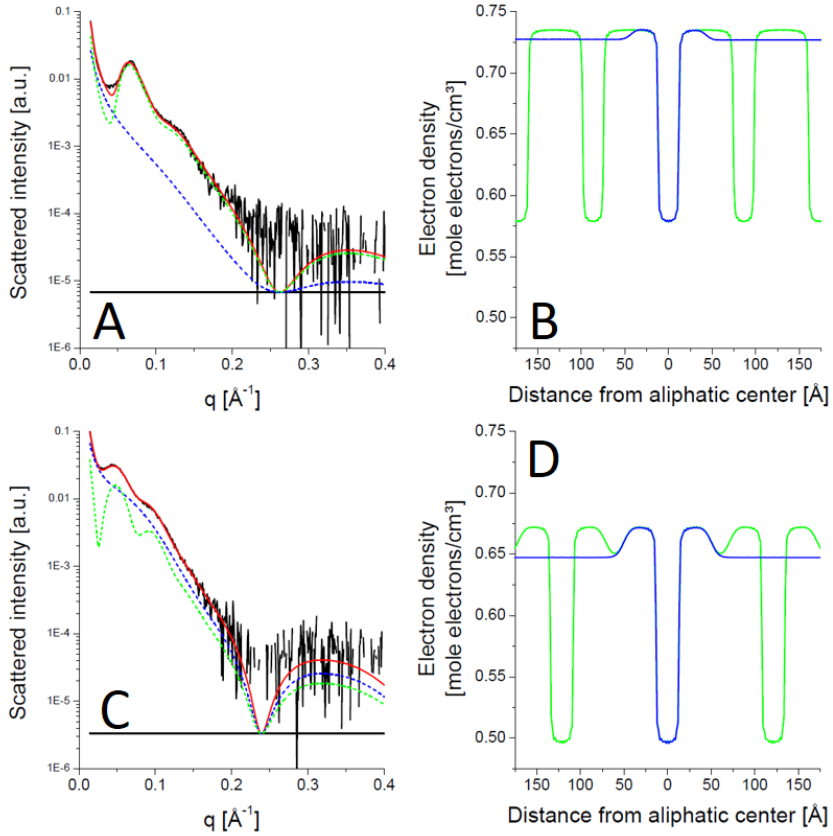


Figure 4.21: For *30%r* during heating 1 at -31°C in (A) and -3°C in (C), the experimental SAXS patterns (black) together with the fit according to equation 4.19 (red), the constant background (black horizontal line), the share due to isolated, single bilayers (blue dashed curve on top of the background) and share due to stacks of bilayers (green dashed curve on top of the background). In the right side panels the corresponding electron density profiles are depicted for *30%r* at -31°C in (B) and -3°C in (D). The profiles for the single bilayers are drawn in blue, those of the bilayer stacks in green.

At -31 °C the thickness of the central layer measures 24 Å, which is very close to the length of fully stretched stearyl chains (22 Å). As interdigitation is a favorite configuration in the fully liquid like state for *20%r* and as this is not expected to be different for *30%r*, it is conceivable that the aliphatic crystallization for *30%r* also starts from and locks in an interdigitated configuration. The structural representations for stacked and isolated bilayer vesicular walls in Figure 4.22 for *30%r* at -31 °C (where the aliphatic tails are in the crystalline state) therefore involves interdigitation. However, unlike for *20%r* at -50°C (situation B in Figure 4.16) no chain tilting is needed to arrive at the aliphatic layer thickness experimentally found. Given the periodicity of 86 Å, the PEO chains cannot be stretched in the stack direction unless the chains of neighboring layers overlap in the middle of the PEO layer. This

overlapping should produce a higher density in the center of the PEO layer, which is not observed (see Figure 4.21, B, green curve). To allow for a homogeneous electron density in the PEO layer, the PEO chains should be partially coiled or folded as illustrated at the top in Figure 4.22. In this PEO configuration only little space is available for epoxy resin. For *20%r* at -50°C it was argued that the stearyl crystallization squeezed out the epoxy from the PEO zones. For larger Brij® S-20 concentrations, such as in *30%r*, this effect also seems to induce a layer by layer stacking and the segregation of epoxy in separate volumes. On the other hand, the isolated bilayers should be in rather close contact with the epoxy resin, as illustrated in Figure 4.22 in the cartoon below that of the stack. This fraction at -31 °C only amounts to 13%.

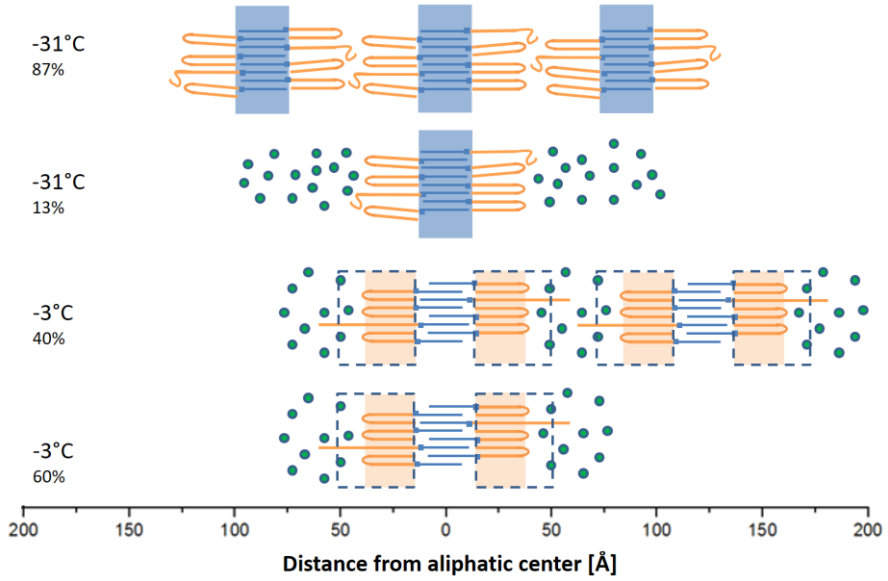


Figure 4.22: Representation of the possible structures of *30%r* at -31°C and -3 °C during heating 1. For each temperature isolated bilayers are depicted below the stacked versions. The % occurrence of each structure is indicated below the temperature. The blue and orange lines correspond to stearyl and PEO chains respectively. The blue blocklets highlight the link between those moieties. Shaded areas indicate a crystalline state. Epoxy monomers are displayed as the green spheres.

The stack periodicity is larger (121 Å) at -3 °C and stacks are rather short, counting only 2 layers according to the model fit. This reflects a high degree of disorder, likely because of an ingress of epoxy resin in between the bilayers, concomitantly to the PEO crystallization. The electron density profiles in Figure 4.21 D, suggest that the PEO chains are not fully stretched in the crystalline state because otherwise the high density zone should have a length comparable to that of stretched PEO chains (i.e. 49 Å). The blue dashed line boxes in Figure 4.22 indicate the size of the fitting based high density regions up to half way the sigmoidal transition zone. The cores of

the high density zones, neighboring the central aliphatic layer only measure about half the stretched PEO length, suggesting that the PEO chains in the crystals are folded. Apparently, the PEO ordering drags the stearyl chains out of register by which they de facto 'melt'. The slightly staggered configuration of the aliphatic chains naturally accounts for that central layer being slightly larger (26 Å) than the length of fully stretched stearyl chains (22 Å). Adding twice the length of a fully stretched PEO chain to this stearyl layer thickness leads to 124 Å, which is very comparable to the experimentally found stack periodicity value (121 Å), suggesting a causal relationship. Some of the PEO chain might indeed be fully stretched and thereby leaving the PEO crystals as illustrated in Figure 4.22 to form a mixed PEO-epoxy phase.

The enthalpy of PEO crystallization is larger than the stearyl melting enthalpy, essentially because the PEO chains are longer and thus represent a larger mass. Therefore, the combined change is exothermic and leads to more stable structures with a lower enthalpy. Yet more stable structures might exist in which the PEO chains are fully stretched. However, to allow for such structures the chains in the liquid stearyl layer can no longer be interdigitated, because that would prevent the close packing of stretched PEO chains. No efforts were made to try and induce such structures by e.g. high temperature annealing. It will be demonstrated in Chapter 6 that such more stable structures are formed naturally in systems with a higher Brij® S-20 content.

4.3 CONCLUSIONS

In the first part of this chapter an epoxy system, DGEBA/MDA, was blended with 20% Brij® S-20, leading to sample *20%r*. The isothermal curing kinetics of this material were studied and compared to the behavior of neat epoxy resin. Furthermore, the morphology of *20%r* during and after curing was studied in detail using time resolved X-ray scattering methods and TEM.

20%r cures slower compared to pure epoxy resin because Brij® S-20 dilutes the epoxy reagents. However, irrespective of the studied curing temperature, which was varied between 80 °C and 130 °C, conversion progressed up to unity after curing for a sufficiently long time. Brij® S-20 does not interfere mechanistically in the resin curing reaction since the activation energies of the Brij® S-20 modified systems are identical to pure epoxy resin, at least in the early conversion stages.

At high conversions the pure resin starts experiencing mobility related problems, which lead to higher activation energies. This effect is absent in the Brij® S-20 modified system. Brij® S-20 acts as a plasticizer, bringing the cured resin glass

transition temperature down from 170 °C for the pure resin to a broad T_g centered around 60 °C (30-90°C), irrespective of the imposed isothermal curing temperature.

At any time prior to and during epoxy resin curing, Brij® S-20 self-assembles into predominantly vesicles, together with a smaller fraction of cylindrical and spherical micelles. Relying on a modelling of the small angle X-ray scattering (SAXS) patterns, the vesicle walls are bilayers with stearyl moieties in the center and PEO facing the epoxy resin on both sides. The stearyl chains in the central 15 Å thick layer are tilted and interdigitated throughout the entire thermal protocol studied.

At room temperature, uncured epoxy is present in between the PEO chains which are presumably stretched out, emanating from the central stearyl layer. During cooling in the non-cured state, the stearyl layers crystallize. The associated densification forces the PEO chains into a closer packing by which the uncured epoxy resin is squeezed out prior to when the resin vitrifies. Upon heating and devitrification, the stearyl layer melts again and the PEO layers again absorb epoxy resin. Heating was conducted up to 130°C where curing was followed for 90 min. Epoxy resin curing reduces the PEO compatibility with the resin. As a result, the PEO chains coil up and segregate from the developing epoxy network. After 90 min at 130°C a conversion of 90% was reached. Because of this high degree of curing, the central aliphatic layers are no longer able to crystallize upon cooling, likely as a result of being connected with a vitrified PEO-epoxy matrix at temperatures where stearyl crystallization is expected to occur.

When curing is finished, vesicular morphologies are found with TEM. The formation of vesicular nanostructures seems to be rather robust during the entire curing cycle and even withstands changes to the curing protocol.

In the second part of this chapter, blends of the epoxy resin with 30% Brij® S-20 were discussed, i.e. *30%r*. Curing at 130°C was slower compared to in *20%r* due to a further dilution of the epoxy resin. After 90 min at 130°C a conversion of only 82% was reached.

Just like for *20%r*, crystallization of the aliphatic central layers was observed for uncured *30%r* prior to vitrification. Concomitantly, some of the Brij® S-20 bilayers aggregated into stacks. The suggestion was made that besides vesicles also cylindrical micelles are present and able to crystallize. Traces of this process were found in DSC and WAXD but not convincingly in SAXS, suggesting that the concentration of such cylindrical micelles is rather low. Upon reheating, the PEO chains crystallized and actively assisted stearyl melting. At the same time, stacking was largely disrupted, likely as a result of epoxy resin infusion. The crystallized PEO chains assumed a folded configuration. Upon further heating, the PEO chains melted

prior to reaching 130 °C where curing was executed. Upon cooling, just like for *20%r*, no crystallization was found in cured *30%r*. Most likely, a morphology composed of well distributed vesicles is formed. Since both *20%r* and *40%r* (see chapter 6) reveal dispersed vesicles in TEM images after curing, *30%r* likely has a similar morphology.

CHAPTER 5: THE MORPHOLOGY OF PURE BLOCK COPOLYMER AND THE ISOTHERMAL CURING KINETICS AND MORPHOLOGY OF EPOXY RESINS WITH VERY HIGH AMOUNTS OF BLOCK COPOLYMER

In the present chapter the temperature dependent morphology of the pure block copolymer is discussed as well as the morphology and curing of Brij® S-20 blended with 10% epoxy resin. This material contains 90% Brij® S-20 and will be referred to as *90%r*. For the pure block copolymer the discussion is limited to the morphology during heating as no time resolved X-ray data are available for the pure Brij® S-20 cooling run. Obviously, for pure Brij® S-20 no curing needs to be discussed.

5.1. THERMAL BEHAVIOR AND MORPHOLOGY OF PURE BRIJ® S-20 BLOCK COPOLYMER

5.1.1. DSC

The DSC profiles for pure Brij® S-20 block copolymer during cooling and subsequent heating at 10°C/min are displayed in the top panel of Figure 5.1. Crystallization starts at about 32 °C and peaks at 26 °C. The main peak exhibits a small, rather sharp shoulder and a second, broad low temperature exothermic peak running roughly between 25 and 12°C. The origin of the underlying phenomena remains to be disclosed in future X-ray work. During heating a single melting endotherm is observed with a clear rise at approximately 34 °C and a peak at 40 °C. The melting process is over at 43 °C. The orange color of the endothermic peak indicates that it is entirely related to the melting of PEO moieties as will be revealed unambiguously by WAXD.

5.1.2 WAXD

A cooling and subsequent heating run is performed just as in DSC at 10°C/min while collecting simultaneously synchrotron SAXS and WAXD patterns with increments of 1°C. However, only the heating run data were retrieved successfully. These heating run WAXD patterns are displayed in the Figure 5.1 lower panel. At low temperatures these patterns reveal reflections due to monoclinic PEO crystals[115]. For this reason these reflections are highlighted using orange vertical lines. In contrast to for *30%r*, the reflection at q = 1.36 $Å^{-1}$ is split into two well resolved reflections at 1.33 $Å^{-1}$ and 1.36 $Å^{-1}$, associated with respectively the (111) and (120) reflection. The fact that these peaks are well resolved, suggest the presence of well-ordered PEO crystals, composed of reasonably large grains. High order and large crystal grains leads to narrow WAXD reflections. The reflection at q = 1.63 $Å^{-1}$ remains an unresolved clustering of the (112), (-212) and (032) reflections. All mentioned peaks disappear

over the temperature interval where DSC displays an endothermic signal, implying PEO crystal melting. Note that some small reflections remain in the high temperature WAXD patterns above the PEO melting range. These are artifacts due to the sample holder. They are present throughout and are of no interest.

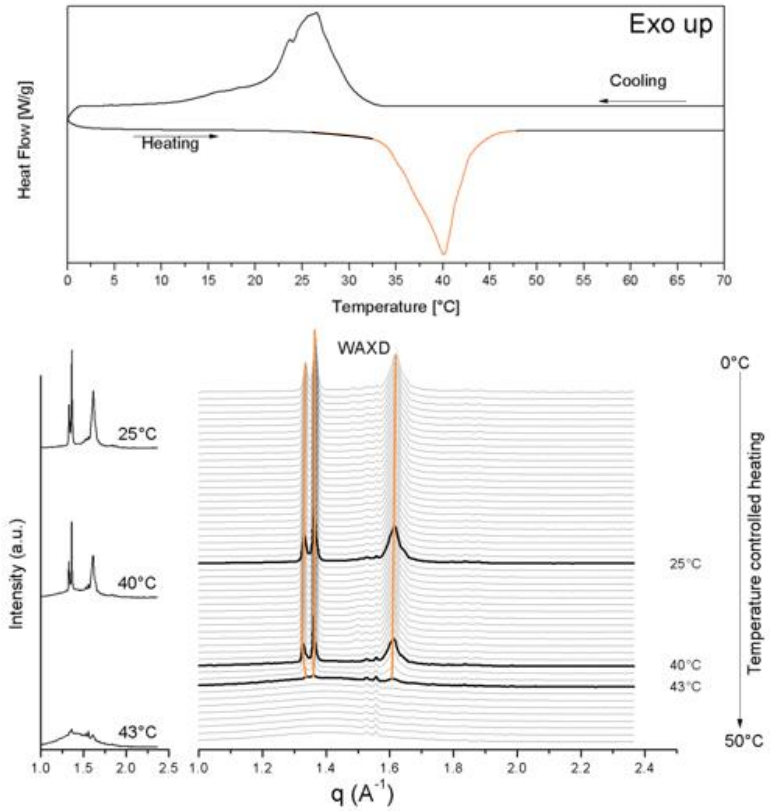


Figure 5.1 Top panel: DSC thermogram showing crystallization while cooling and melting during subsequent heating at 10°C/min for pure pure Brij® S-20. Bottom panel: Time resolved WAXD patterns during the heating run following cooling at 10°C/min with a series of highlighted patterns displayed on the left. Orange features belong to transitions (in DSC) or reflections (in the WAXD patterns) of the PEO moieties.

5.1.3 SAXS

The SAXS pattern at the end of the cooling (which is the first pattern of the heating run) contains two very clear reflections at q = 0.043 Å^{-1} and q = 0.086 Å^{-1}, with the latter apparently being the second order reflection of the former. The shape of this scattering pattern does not change with temperature as illustrated in Figure 5.2. The reflections only disappear in the melting range revealed by DSC and WAXD. The SAXS pattern at 25°C was analyzed in detail. Representing this pattern on a logarithmic scale (Figure 5.3, A-panel) reveals up to 8 orders of the primary reflection at 0.043 Å^{-1}, implying a high degree of structural regularity and the presence of layer

stacks with a periodicity, $L_{p,2}$ (see section 5.5 for the parameter definition), of 144 Å, which is twice the length of fully stretched Brij® S-20 molecules.

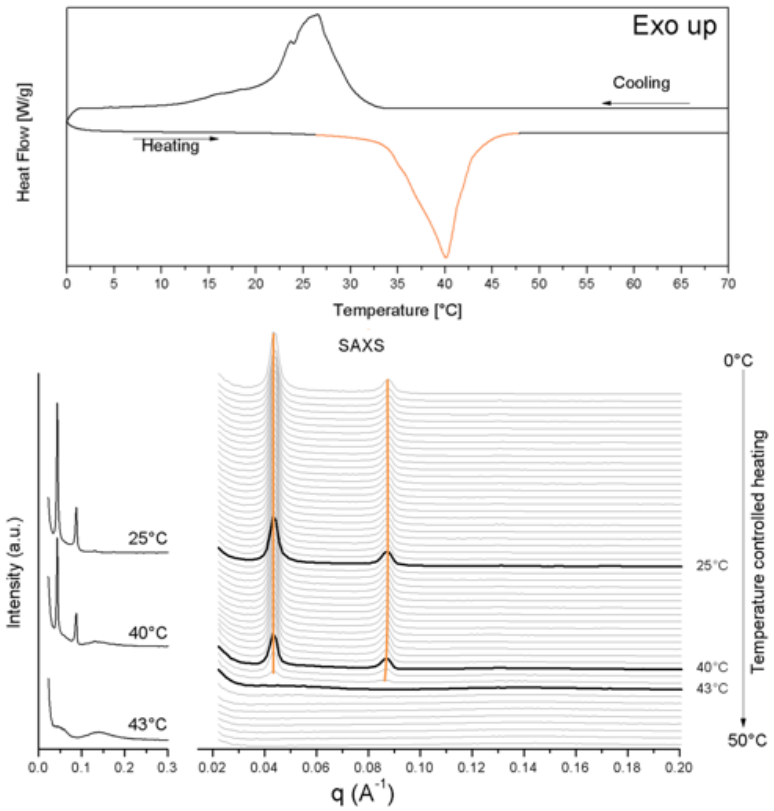


Figure 5.2 Top panel: DSC thermogram showing crystallization during cooling and melting during subsequent heating at 10°C/min for pure Brij® S-20. Bottom panel: Time resolved SAXS patterns collected during the heating run following cooling at 10°C/min with a series of highlighted patterns displayed on the left. Orange features belong to transitions (in DSC) or peaks (in the SAXS patterns) of the PEO moieties.

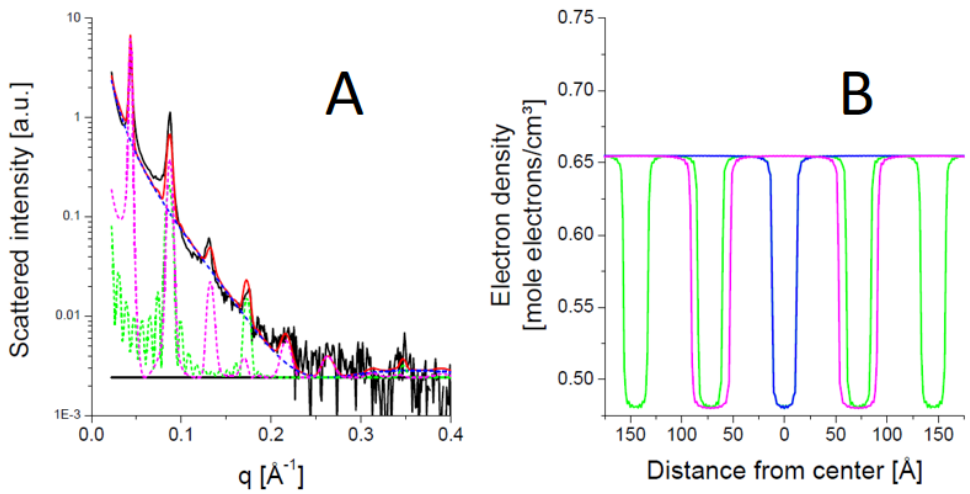


Figure 5.3 In the left side panel (A): For pure Brij® S-20 the experimental SAXS pattern (black) at 25°C during heating, together with the fit according to equation 5.1 (red), the constant background (black horizontal line), the share due to randomly packed stacks modelled as isolated layers (blue dashed curve on top of the background), the share due to head to head stacks (green dashed curve on top of the background) and share due to head to tail stacks (magenta dashed curve on top of the background). In the right side panel (B): the corresponding electron density profiles for each share, using the same colors as the curves in the left side panel. Note that the central part of the green electron density profile overlaps with and hence is covered by the blue profile.

Therefore a most logical structure would be the one as shown in Figure 5.4 at the bottom. This regular structure is composed out of stretched molecules with the stearyl and PEO moieties mutually facing each other. In this arrangement with the molecules in a head-to-head arrangement, the PEO layers should be crystalline, as highlighted with the orange shading in Figure 5.4. The theoretical SAXS pattern associated with such a structure can, however, not cover the experimentally observed 25°C SAXS pattern well.

An elaborate modelling of the 25°C SAXS pattern revealed that this type of structure is present only for 24% and that 12% is taken by structures with only half the periodicity (middle structures in Figure 5.4) and 64% by structures that are irregularly packed (structure at the top in Figure 5.4). The mathematical equations that produce the different shares in the SAXS patterns and details of the SAXS curve fitting procedure will be discussed at the end of this chapter in section 5.5 after also having discussed the *90%r* sample. This allows presenting the relevant equations and parameter definitions in more general terms, applicable to both pure Brij® S-20 and *90%r*.

The remaining part of section 5.1.3 focusses on how the morphological sketches in Figure 5.4 relate to the SAXS based electron density profiles in Figure 5.3 (B-panel).

The magenta electron density profile in Figure 5.3 B relates to the structure that is present for 24% (bottom sketch in Figure 5.4). Here, the central, high density feature in the stacks is a 105 Å thick (according to the SAXS analysis) crystalline PEO bilayer in which two PEO chains are fully stretched. The stearyl chains in the low density, aliphatic bilayers neighboring the central PEO bilayer are also stretched but yet they are liquid according to the WAXD data. The fact that the crystalline PEO bilayer needed to be put centrally in the SAXS data modelling, indicates that the highest disorder (in terms of a thickness distribution) is to be found in the stearyl layers. This makes sense given their liquid state. Furthermore, the SAXS profile analysis returned 29 for the number of bilayers, N_2, which is quite high and which explains the narrow SAXS peaks observed.

In the stacks with a periodicity equal to only one molecular length (central two structures in Figure 5.4 and corresponding green electron density profile in Figure 5.3 B) the central feature is the liquid stearyl layer. One can imagine two types of structures with half the periodicity and the molecules being fully stretched: a head-to-tail packing (bottom sketch of two middle structures) and a layer like stacking in which all molecules are interdigitating (top sketch of the middle structures). SAXS cannot discriminate between these options. Furthermore, although being composed of respectively parallel or anti-parallel PEO chain, the PEO crystals in these structure are also not different, given the symmetry of the PEO chains. In any case, the structures responsible for this share in the SAXS patterns are less disorder compared to head-to-head stacked case (i.e. the structures present for 24%). Indeed, although the number of layers in the stacks with reduced periodicity is only 9, the paracrystalline distortion parameters, $\sigma_{LP,1}$, is very low, i.e. only 0.08 compared to 3.7 ($\sigma_{LP,2}$) for the head-to-head stacks. The high disorder in the head-to-head stacks may originate from the non-covalently linked interruptions at the PEO-PEO and stearyl-stearyl interfaces. Such interruptions do not exist in the stack with interdigitation, suggesting that these structures prevail above the head-to-tail stacks. In the latter case also non-covalently linked interruptions exist, which might induce disorder, which is not observed.

A rather large fraction (64%) of isolated layers with a thickness equal to the length of a single stretched stearyl moiety was also found (blue electron density profile in Figure 5.3). These layers are surrounded by crystalline PEO. Such isolated layers are in fact not realistic for pure Brij® S-20. It is therefore assumed that these isolated layers are due to fragments within stacks that are combinations of head-to-head and head-to-tail builds, as illustrated in the top sketch of Figure 5.4. Here, the structures

at the left and right side of the central aliphatic layer are different. This difference creates an aperiodic fragment (the structural fragment emphasized by the dashed line box in Figure 5.4) and leads to apparently isolated layers.

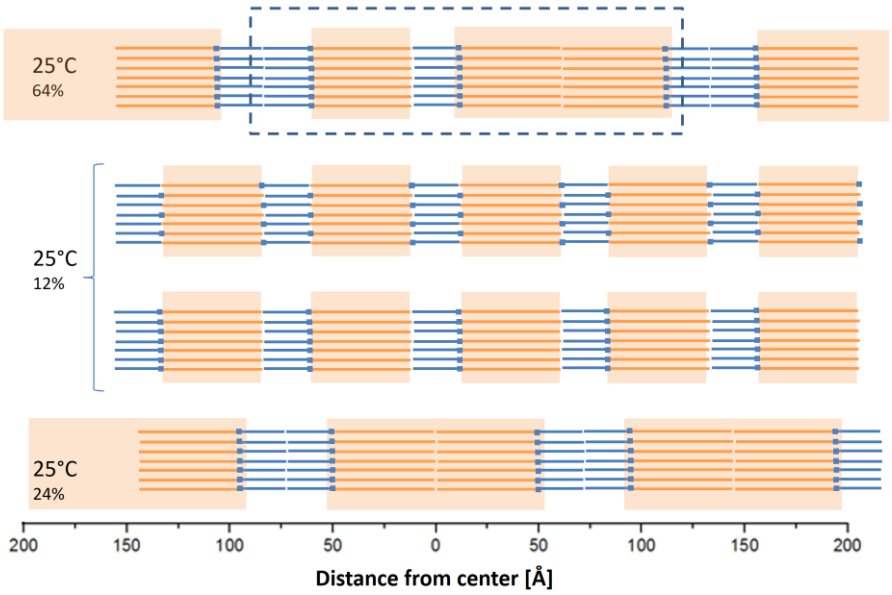


Figure 5.4: Representation of possible pure Brij® S-20 structures at 25°C as seen during heating at 10°C/min after cooling at 10°C min. The blue and orange lines correspond to stearyl and PEO chains respectively. The blue blocklets highlight the links between those moieties. Shaded areas indicate a crystalline state. A modelling of the SAXS pattern reveals that the structure at the bottom (head-to-head packing) is present for 25%. SAXS cannot discriminate between the two structures in the middle, which together account for 12%. One of the middle structures is a head to tail packing, the other involves interdigitation. The remaining 64% share is due to irregularly stacked layers with a mixed head to head and head to tail stacking.

Finally, it should be mentioned that electron densities were constrained in the SAXS pattern fitting procedures to 0.655 mole electrons/cm³ for crystalline PEO and 0.48 mole electrons/cm³ for liquid stearyl aliphatic chains. The latter value results from equation 4.10 and multiplication with 0.57 mole electrons/g. The former is based on the PEO crystalline density at 25°C reported by Li et al.[110], i.e. 1.203 g/cm³, and a multiplication by 0.5448 mole electrons/g. These constraints explain the electron density values in Figure 5.3.

5.2 THERMAL BEHAVIOR OF *90%R*

5.2.1. DSC

Figure 5.5 displays the thermograms of *90%r*, following the standard temperature profile as illustrated in Figure 3.2. The top graph displays the first cooling and heating segments, the middle panel represents the isothermal segment at 130°C and the

bottom one shows the final cooling and heating segments. First, the isothermal curing kinetics will be discussed, based on the data in the middle panel.

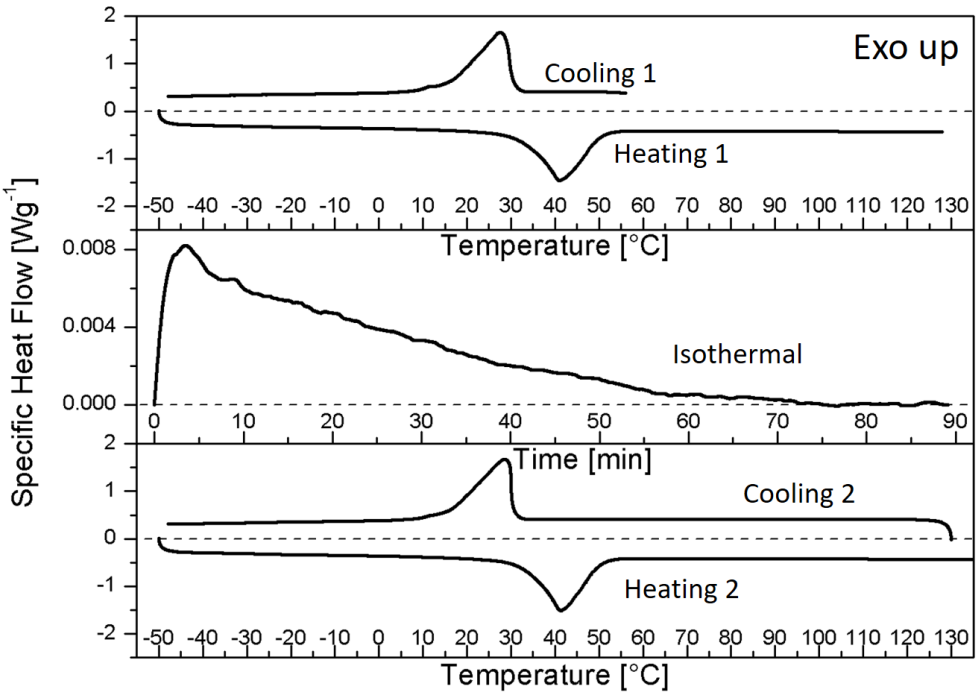


Figure 5.5 DSC thermograms for *90%r*, related to the thermal protocol used during time-resolved X-ray based morphological characterization and as depicted in Figure 3.2. Exothermic signals are plotted upwards. The program includes cooling 1 and heating 1 at 10 °C/min (top panel), isothermal curing at 130 °C for 90 min (middle panel), followed by cooling 2 and heating 2 at 10 °C/min (bottom panel).

5.2.1.1 ISOTHERMAL CURING KINETICS

In *90%r*, the material consists of only 10% resin, which is expected to hinder its fast and complete curing because of dilution. Potentially, the physical barriers and associated molecular separation due to the blockcopolymer morphology can further retard or prevent curing (shielding effect). The epoxy conversion with time during curing at 130°C for 90 min was calculated using equation 4.18 with ΔH_{prep} and ΔH_h both set to zero and the factor for ΔH_{max} set to 0.1 (instead of 0.7), reflecting the epoxy resin fraction in the system. The conversion reached after 90 min was only 36% for *90%r*, compared to 90% for *20%r*. This low degree of curing is not sufficient to establish an epoxy network. To form a gel, the conversion should typically exceed 58% (see section 3.1.1). Hence, likely only oligomeric epoxy species are formed. Besides a lower ultimate conversion, also the curing rate was much lower compared to for *20%r* and *30%r* as can be judged from the shallow slope of the conversion curve in Figure 5.6. Because of the lower rate, no curing occurred during the sample

preparation and heating ramp to 130°C. Therefore both ΔH_{prep} and ΔH_h are equal to zero.

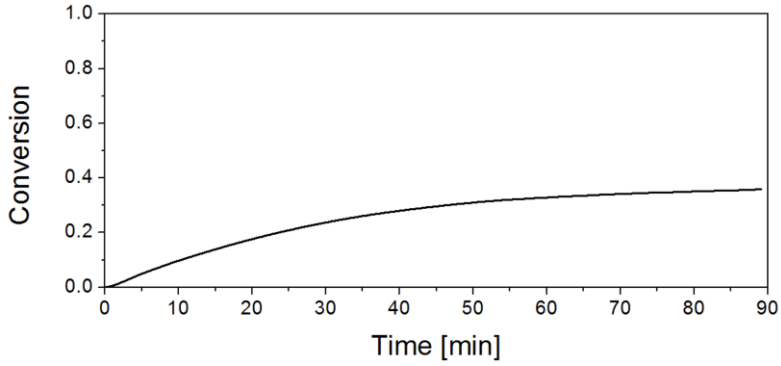


Figure 5.6 Epoxy conversion during isothermal curing at 130°C after heating at 10°C/min for *90%r*.

5.2.1.2 COOLING AND HEATING SEGMENTS

The DSC first cooling run on uncured *90%r* (Figure 5.5, top panel, cooling 1) shows one major exothermic transition. Crystallization during the first cooling run occurs at approximately the same temperature as observed in the pure block copolymer. However, the shoulder at the lower temperature side of the crystallization peak is absent, suggesting a slightly different and likely more complex crystallization process in pure Brij® S-20, the nature of which remains to be explored. The simultaneously recorded WAXD data for *90%r* reveal that the *90%r* cooling 1 exothermic peak is indeed simple and entirely related to the crystallization of PEO.

The area below the cooling 1 crystallization peak is reduced compared to for pure Brij® S-20 (Figure 5.1, top panel), implying a reduced crystallinity. The reduction is in line with expectations as the amount of crystallizable blockcopolymer is reduced with 10% in *90%r*. The endothermic signal during heating reflects the PEO crystal melting and concludes at 50 °C, which is higher than for pure Brij® S-20. The reason for this increased melting temperature is unclear. In the presence of a foreign, miscible (with PEO) component one expects a melting point depression, rather than an increase. At higher epoxy concentrations (> 10%) a decreased melting point with respect to pure Brij® S-20 is indeed observed (see chapters 4, 6 and 7).

The crystallization and melting behavior of the cured material (Figure 5.5, bottom panel) is nearly identical to that prior to curing. It seems that the oligomeric species obtained at a conversion of only 36% do not impose strong restrictions to the crystallization process and structure formation.

5.3 MORPHOLOGY OF UNCURED *90%R*

5.3.1 WAXD

Crystallization and melting in *90%r* is fully associated with the PEO moieties. In Figure 5.7 (top and bottom panel) PEO typical crystal reflections appear and disappear during cooling 1 and heating 1 in the temperature intervals of the DSC exothermic and endothermic signals. The reflections are sharp and the ones at 1.33 $Å^{-1}$ and 1.36 $Å^{-1}$ are well resolved just like for pure Brij® S-20. The split of the latter two, however, decreases towards lower temperatures. This most likely results from a difference in thermal contraction of the interplanar spacings as this process is thermally reversible.

5.3.2 SAXS

The SAXS patterns of uncured *90%r* during cooling 1 and heating 1, depicted in Figure 5.8, appear featureless except where the WAXD data indicate that the PEO moieties are in the crystalline state. In these temperatures ranges, several reflections are visible, with the main low angle reflection corresponding to a periodicity of 158 Å, which is 14 Å more than pure Brij® S-20. Qualitatively, this can be understood as a (roughly) 10% increase due to the presence of 10% epoxy resin between the Brij® S-20 layers. However, just like for pure Brij® S-20, the SAXS patterns cannot simply be explained by the presence of one single stack type.

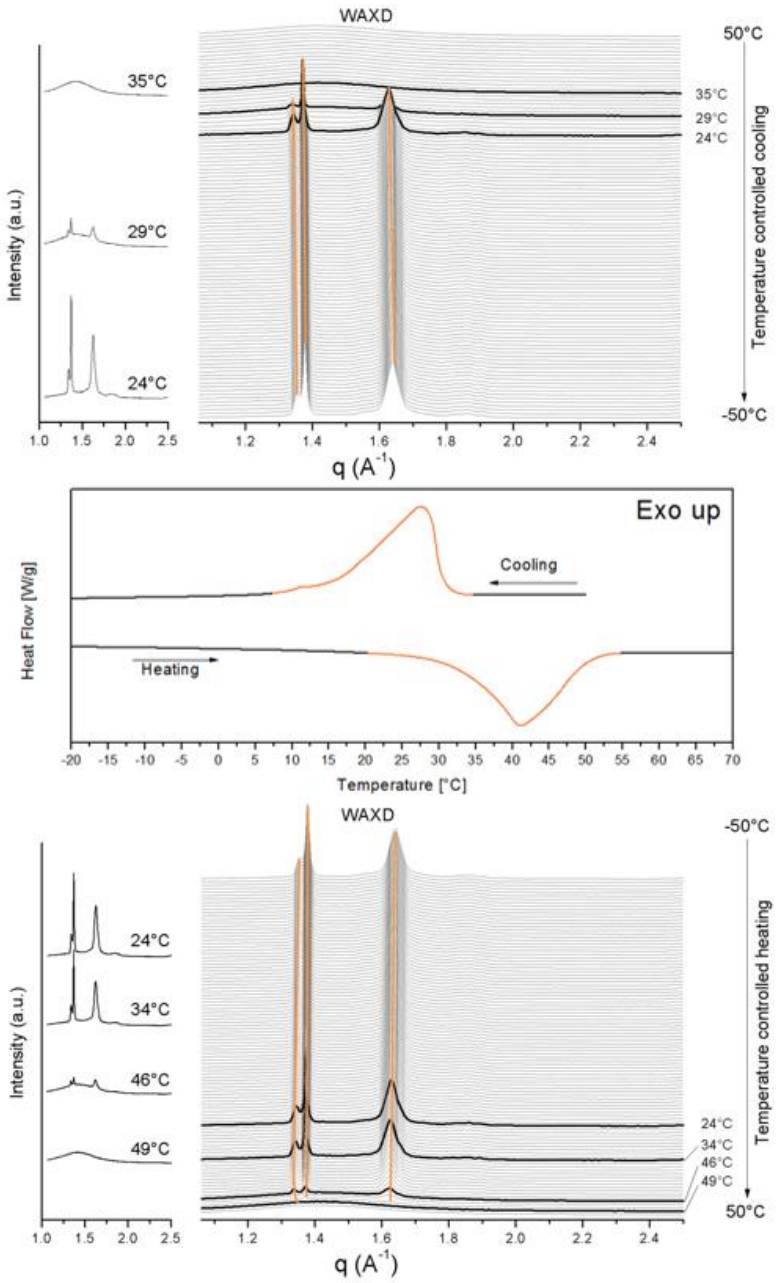


Figure 5.7. Top panel: Time resolved WAXD patterns collected during cooling 1 of *90%r*. The patterns highlighted in bold are displayed separately in the left side window. Middle panel: DSC thermograms during cooling 1 and heating 1 of *90%r*. Bottom panel: Time resolved WAXD patterns during heating 1 for *90%r* with highlighted patterns displayed separately in the left side window. Orange features belong to transitions (in DSC) or reflections (in the WAXD patterns) of the PEO moieties.

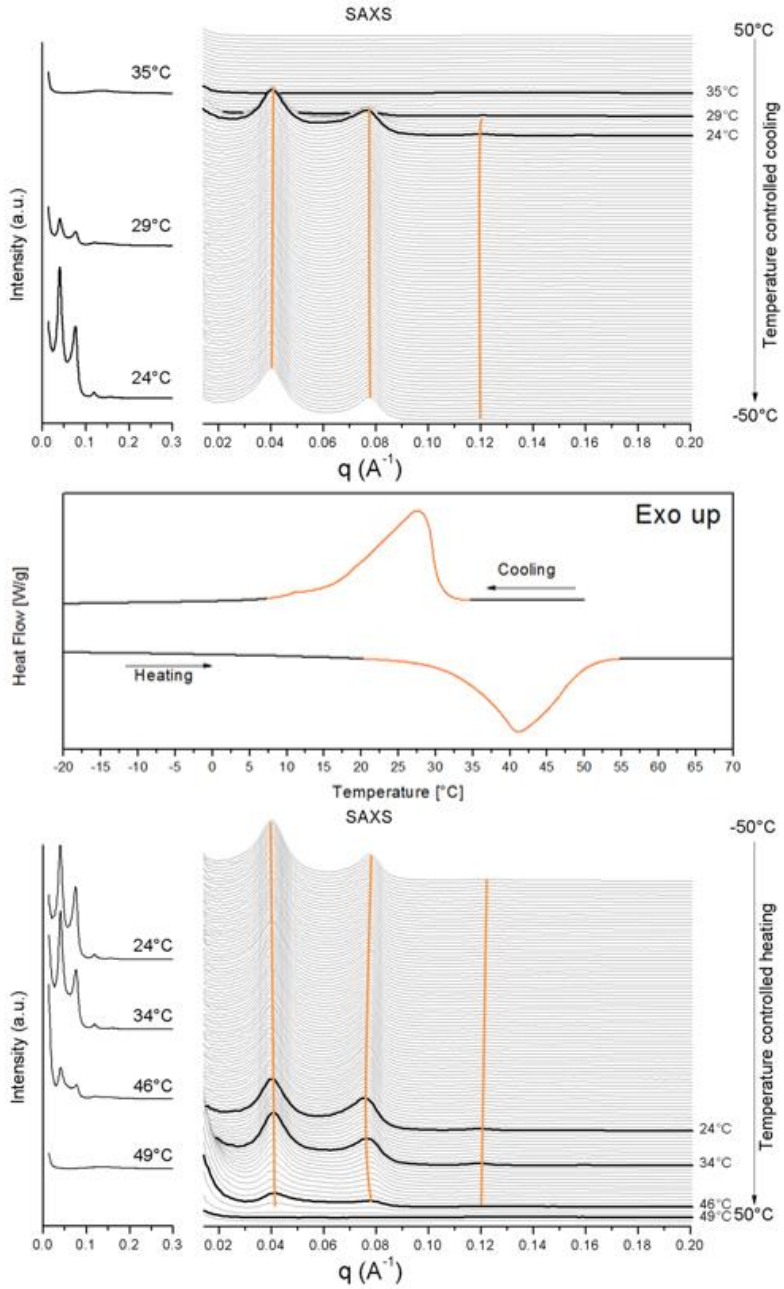


Figure 5.8. Top panel: Time resolved SAXS patterns collected during cooling 1 of *90%r*. The patterns highlighted in bold are displayed separately in the left side window. Middle panel: DSC thermograms during cooling 1 and heating 1 of *90%r*. Bottom panel: Time resolved SAXS patterns during heating 1 for *90%r* with highlighted patterns displayed separately in the left side window. Orange features belong to transitions (in DSC) or peaks (in the SAXS patterns) of the PEO moieties.

The SAXS pattern at 25°C during the first heating run was analyzed in detail. This pattern is depicted in Figure 5.9. Using a logarithmic representation, multiple peaks are visible. The maximum of the second peak occurs at a lower q value (q = 0.075 Å^{-1}) than expected if it were the second order peak of the first one, occurring at q = 0.401 Å^{-1}. This results from the fact that multiple stack types contribute to this SAXS pattern. Just like for pure Brij® S-20, stacks are present for 27% with a large periodicity (in the present case 158 Å) next to stacks (40%) with approximately half that periodicity (83 Å) and isolated layers (present for 33%). The profiles and SAXS shares of the large periodicity stacks are depicted using green lines in Figure 5.9. The stacks with half the periodicity are shown in magenta and the isolated layers in blue. The mathematical relations that produce these shares in the SAXS pattern are discussed in section 5.5.

The electron density profile of the large periodicity structure resembles that of the head-to-head stacking of pure Brij® S-20. The periodicity (158 Å) is, however, larger than the sum of two fully stretched molecules (144 Å) due to the presence of epoxy resin. Furthermore, the number of motives (N_1, see section 5.5) is only 3, compared to 29 for pure Brij® S-20. A potential structure is represented in the middle cartoon of Figure 5.10. Given the compatibility of the epoxy resin with PEO, the epoxy resin should be in the vicinity or be mixed with non-crystalline PEO. The staggered type of molecular arrangement allows reaching a higher periodicity than given by the molecular length. Secondly, it explains the thickness of the central, low density aliphatic layer (28 Å) which is smaller than the sum of two stretched out stearyl groups (44 Å) but larger compared to a single stretched out stearyl group (22 Å). The borders of the central aliphatic layer are mixed with PEO and have a rather high density, approaching that of crystalline PEO. This higher density is assumed to follow from being connected to the densely packed crystalline PEO layers. There are no separate epoxy regions visible in the electron density profile (the green curve in Figure 5.9B). Therefore, the epoxy holding regions in between the PEO crystals, the PEO crystals and mixed PEO/aliphatic regions are suggested to all together make up the large high density zones which are highlighted using dashed boxes in the middle cartoon of Figure 5.10. Just like for pure Brij® S-20, the maximum and minimum electron density during SAXS pattern fitting were fixed to respectively the values of crystalline PEO (0.655 mole electrons/cm³) and liquid stearyl aliphatic chains (0.48 mole electrons/cm³).

The repeated feature in these large periodicity stacks at the same time occurs for 33% as isolated layers, the structure of which is depicted at the bottom in Figure 5.10. The corresponding electron density profile and contribution to the SAXS pattern is represented in blue in Figure 5.9. The central part of these isolated layers consists of liquid like stearyl chain aliphatic chains, and is flanked by crystalline PEO

at both sides. Given the staggered configuration of the chains, some PEO chains at the outsides of these PEO layers mix up with epoxy resin (see Figure 5.10 at the bottom). The electron density of the epoxy matrix in which the isolated layers reside equals 0.615 mole electrons/cm³. This value came as a result from the fitting procedure and equals the value of the electron density of uncured resin at 25 °C as estimated in chapter 4, i.e. 0.61 mole electrons/cm³. Note that the epoxy electron density closely resembles the average electron density of the combined stearyl – crystalline PEO layers, by which the corresponding share in the SAXS pattern (blue curve in Figure 5.9) falls to very low values at low *q*-values. This feature is typical for so-called hyper uniform structures, lacking large scale electron density fluctuations[107].

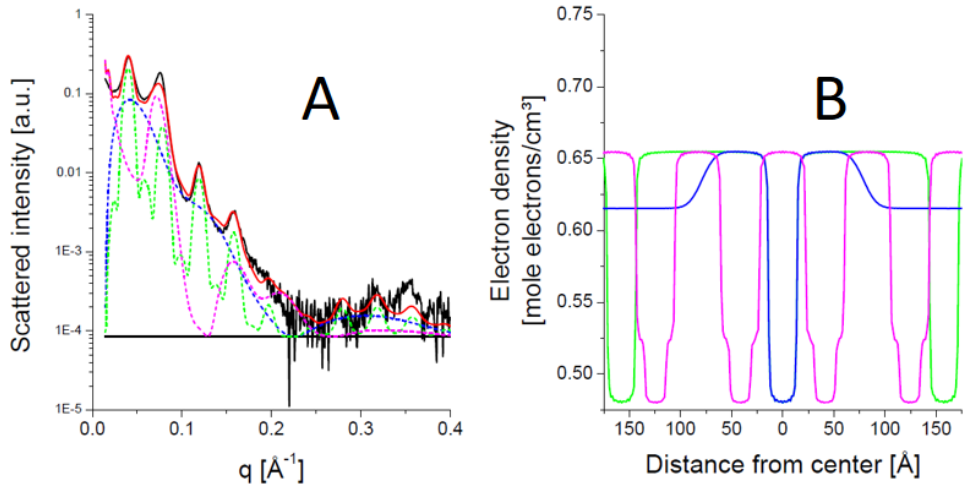


Figure 5.9 In the left side panel (A): For *90%r* the experimental SAXS pattern (black) at 25°C during first heating, together with the fit according to equation 5.1 (red), the constant background (black horizontal line), the share due to isolated layers (blue dashed curve on top of the background), the share due to layer stacks with a large periodicity (green dashed curve on top of the background) and share due layer stacks with a short periodicity (magenta dashed curve on top of the background). In the right side panel (B): the corresponding electron density profiles for each share, using the same colors as the curves in the left side panel. Note that the central part of the green electron density profile overlaps with and hence is covered by the blue profile.

The third and last structure present in *90%r* for 40%, consists of stacks with a periodicity of 83 Å, which is a bit larger than half the periodicity of the 158 Å stacks and which explains why the second peak in the SAXS pattern does not occur at the position expected for the second order of the first peak. In the modelling of this structure, the PEO crystals were put centrally in the stack, implying that the stacking disorder in these kind of stacks is predominantly related to disorder (thickness distribution) in the aliphatic layers. The electron density profile of this stack type

(magenta curve in Figure 5.9 B) reveals a transition layer of intermediate electron density in between the (high electron density) PEO crystalline and (low electron density) aliphatic liquid like layers. This can be explained as follows. Given the simple DSC melting and crystallization behavior it seems that the PEO crystals should be similar in all stack types. The PEO crystals in the 83 Å period stacks, shown at the top of Figure 5.10, are therefore drawn equal to those in the other *90%r* structures. The associated chain staggering together with the aliphatic layers that are 21 Å thick (i.e. very close to the stearyl molecular length) leads to transition layers with some open space in between the non-crystalline PEO chain fragments. These open spaces might be partially occupied by epoxy monomer as illustrated in Figure 5.10 (top).

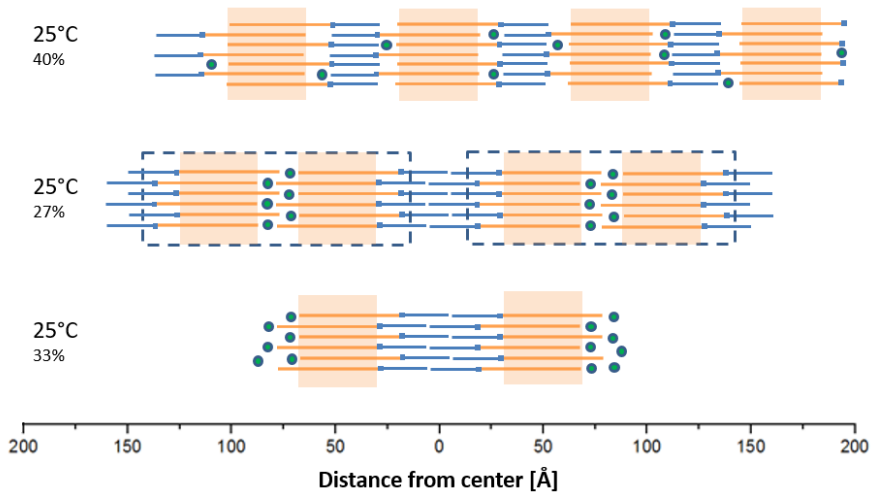


Figure 5.10: Representation of the possible structures within *90%r* at 25°C during the first heating at 10°C/min after cooling at 10°C min. The blue and orange lines correspond to stearyl and PEO chains respectively. The blue blocklets highlight the links between those moieties. Shaded areas indicate a crystalline state for PEO. Modelling of the SAXS pattern reveals that the structure at the bottom is present for 33%, the structure in the middle for 27% and the structure at the top for 40%.

5.4 MORPHOLOGY OF CURED *90%R*

5.4.1 WAXD

The WAXD profiles of the second cooling and heating segments are displayed in Figure 5.11. In line with the DSC traces, being almost identical to those measured during cooling 1 and heating 1, also the WAXD data are very similar to cooling 1 and heating 1 recorded prior to isothermal curing (Figure 5.7). The exothermic and endothermic transitions during cooling 2 and heating 2 are entirely due to the crystallization and melting of the PEO segments. After curing, the PEO reflections are slightly broader, suggesting smaller and/or more disordered crystallites. It seems that the (incompletely) cured epoxy resin more strongly hinders the PEO

crystallization compared to when the resin is not cured at all. The difference, however, remains very small.

5.4.2 SAXS

Figure 5.12 displays the time-resolved SAXS patterns of cured *90%r* during cooling 2 and heating 2. They are very similar to the SAXS patterns of the uncured material during cooling 1 and heating 1. Rather arbitrarily the SAXS pattern at -50°C was selected for further analysis. The result is illustrated in Figure 5.13. This pattern can also be understood as a superposition of three contributions. Given the high similarity with the uncured situation, the sketches in Figure 5.10 can also serve to explain the morphology after curing.

The large periodicity stacks contribute for 29% and the number of motives within these stacks was found to be 3 just like for in the uncured counterpart at 25°C. The periodicity of this stacks equals 154 Å, which is lower than the 158 Å for the uncured sample. This reduction might be due to the thermal contraction associated with lowering the temperature down to -50°C or to the partial segregation of epoxy from within the stacks. The share of isolated layers for the cured sample amounts to 44%, which is larger compared to the 35% prior to curing at 25°C. This leaves 27% for the stacks with reduced periodicity. For this type of stacks, the periodicity was found to be very close to that of the uncured sample at 25°C, i.e. 82 Å. However, in contrast to for the uncured sample, no transition layer of intermediate density was found in between the non-crystalline stearyl and the crystalline PEO layers. These transition layers are added to the low density zone, suggesting that also in these stacks less epoxy is present which might locally lift up the electron density.

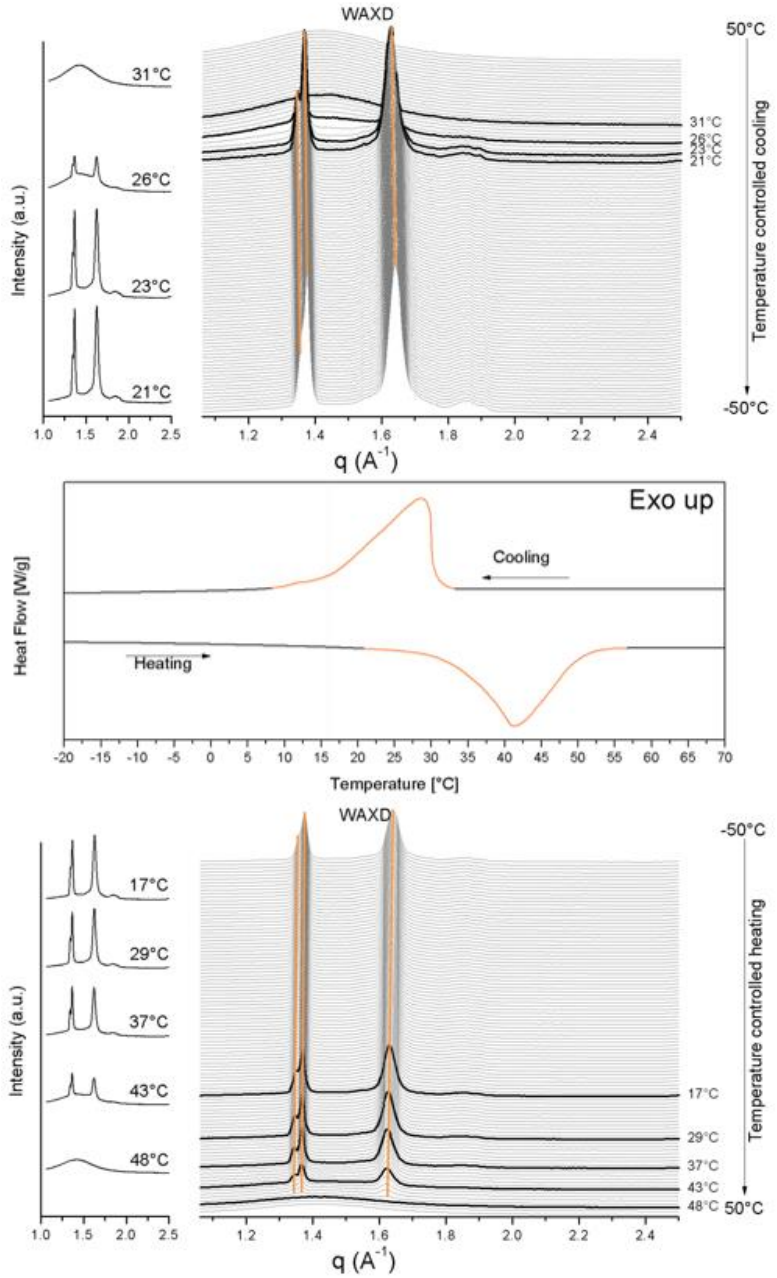


Figure 5.11. Top panel: Time resolved WAXD patterns collected during cooling 2 of *90%r*. The patterns highlighted in bold are displayed separately in the left side window. Middle panel: DSC thermograms during cooling 2 and heating 2 of *90%r*. Bottom panel: Time resolved WAXD patterns during heating 2 for *90%r* with highlighted patterns displayed separately in the left side window. Orange features belong to transitions (in DSC) or reflections (in the WAXD patterns) of the PEO moieties. Vertical dashed lines assist in linking the reflections to their *q*-values. Full lines in the WAXD patterns indicate that these reflections are actually present at these temperatures.

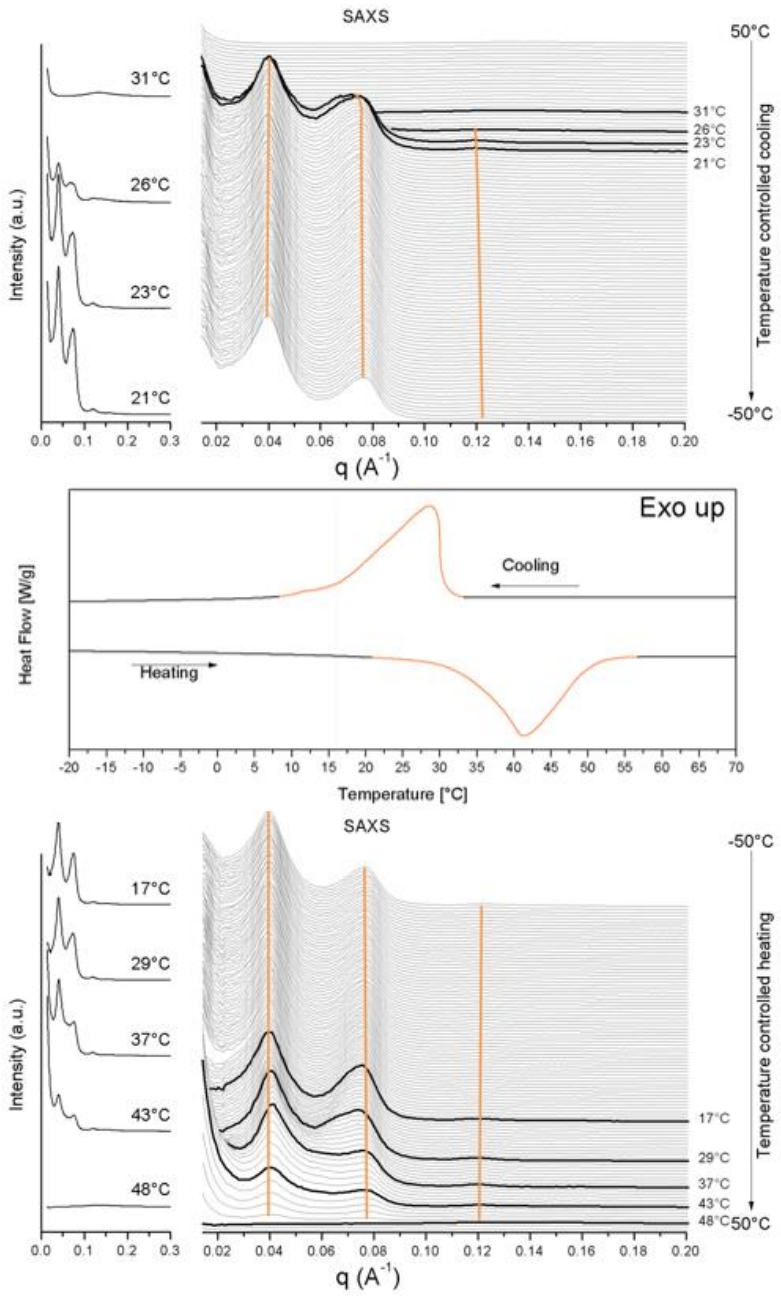


Figure 5.12. Top panel: Time resolved SAXS patterns collected during cooling 2 of *90%r*. The patterns highlighted in bold are displayed separately in the left side window. Middle panel: DSC thermograms during cooling 2 and heating 2 of *90%r*. Bottom panel: Time resolved SAXS patterns during heating 2 for *90%r* with highlighted patterns displayed separately in the left side window. Orange features belong to transitions (in DSC) or reflections (in the SAXS patterns) of the PEO moieties. Vertical dashed lines assist in linking the reflections to their *q*-values. Full lines in the SAXS patterns indicate that these reflections are actually present at these temperatures.

These differences with respect to uncured *90%r* suggest that the compatibility of PEO with epoxy has reduced as a result of (partial) curing. The reduced compatibility is also visible in the considerably sharpened electron density transition between crystalline PEO and the epoxy matrix in the profile of the isolated layers (blue curve in Figure 5.9-B; to be compared with the blue curve in Figure 5.9 for the uncured counterpart).

In the SAXS pattern fitting of cured *90%r* at -50°C, the C-factor (see section 5.5 for details) was kept identical to the value obtained by fitting the uncured sample at 25°C. The electron density of the liquid like aliphatic layers was confined to 0.51 mole electrons/cm³, which is the value resulting from Eq. 4.10 and multiplication by 0.57 mole electrons/g. These constrained lead to values at -50°C for crystalline PEO of 0.67 mole electrons/cm³ and for epoxy of 0.65 mole electrons/cm³.

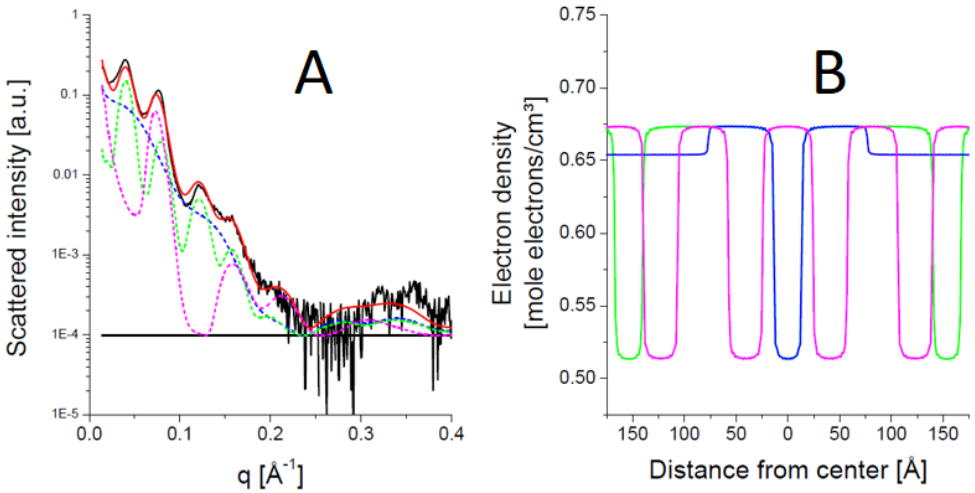


Figure 5.13 In the left side panel (A): For cured *90%r* the experimental SAXS pattern (black) at 25°C during first heating, together with the fit according to equation 5.1 (red), the constant background (black horizontal line), the share due to isolated layers (blue dashed curve on top of the background), the share due to layer stacks with a large periodicity (green dashed curve on top of the background) and share due layer stacks with a short periodicity (magenta dashed curve on top of the background). In the right side panel (B): the corresponding electron density profiles for each share, using the same colors as the curves in the left side panel. Note that the central part of the green electron density profile overlaps with and hence is covered by the blue profile.

The crystalline PEO density value is fairly realistic. Note, however, that this value is lower than the density obtained earlier for amorphous PEO in the case of *30%r* at -31°C (Figure 4.22). The density in the latter case might be abnormally high as a result of the closely packed, crystalline aliphatic chains the PEO chains are connected to. The epoxy density obtained for cured *90%r* at -50°C is lower than the value for

non-cured epoxy obtained earlier for uncured *20%r* (see Figure 4.15). This might be due to a vitrification at higher temperatures for (partially) cured epoxy compared to for non-cured epoxy[102].

5.4.3 TEM

The TEM image of *90%r* (Figure 5.14) was made after isothermal curing and cooling (cooling 2) down to room temperature. The image clearly reveals black parallel lines, which indicates where PEO is located due to the preferential staining with RuO_4. Stearyl and epoxy are stained less and are expected to reside in between the PEO layers.

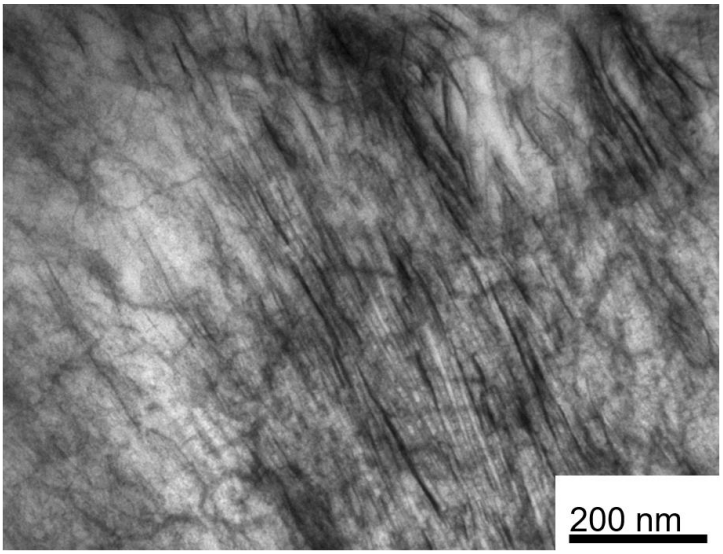


Figure 5.14 TEM image of cured 90%r

Very clearly, cured *90%r* contains stacks of layers. The regions without clear stack like features might be epoxy resin rich and occupied by more isolated block copolymer layers. Alternatively, featureless regions might be associated with layer stacks being seen flat on. According to SAXS, the (two types of) layer stacks occupy 61% of the sample volume. However, given the low epoxy content, the isolated layers cannot be heavily isolated from the stack areas and likely their presence in the SAXS patterns (just like for pure Brij® S-20) merely reflects a high degree of stacking disorder. Note that the number of layers within the long periodicity stacks is only 3. The difference between such short stacks and apparently isolated layers is not very big.

5.5 DETAILS ON THE SAXS PATTERN MODELLING

The theoretical curves used to describe the experimentally observed SAXS patterns of pure Brij® S-20 and *90%r* are defined as:

$$I(q) = \frac{C}{4\pi q^2}\begin{Bmatrix}\Phi(1-\beta)F_1(q)^2 + \Phi\beta F_1(q)^2 S_1(q) + \\ (1-\Phi)F_2(q)^2 S_2(q)\end{Bmatrix} + B \qquad \text{(Eq. 5.1)}$$

with Φ the volume fraction of separate layers and layer stacks with aliphatic sublayers in the center and $(1-\Phi)$ the fraction of layer stacks in which a PEO sublayer is positioned centrally. The product $\Phi\beta$ is the fraction of stacks in which the aliphatic layers are put centrally and the product $\Phi(1-\beta)$ is the fraction of non-stacked, isolated layers of that type. Both Φ and β are real numbers and can take values between 0 and 1.

$F_1(q)$ and $F_2(q)$ take the form of equation 4.20 with the three layer motive composed of a central sublayer with electron density ρ_1 and thickness l_1 and two identical sublayers with a density ρ_2 surrounding the central layer. The sum of the thickness of the central sublayer and the two neighboring sublayers is given by l_2. The matrix in which these three-layer structures reside has an electron density ρ_3. The structures of type 1 and 2, given by $F_1(q)$ and $F_2(q)$ respectively, each have their own set of parameters: $l_{1,1}, l_{2,1}, \rho_{1,1}, \rho_{2,1}, \rho_{3,1}, \sigma_{1/2,1}, \sigma_{2/3,1}$ and $l_{1,2}, l_{2,2}, \rho_{1,2}, \rho_{2,2}, \rho_{3,2}, \sigma_{1/2,2}, \sigma_{2/3,2}$ respectively. The indices after the comma refer at the structure type (1 or 2). The σ parameters relate to the thickness of transition zones between the layers. $S_1(q)$ and $S_2(q)$ both take the form of equation 4.21 with the parameters $N_1, L_{P,1}$ and $\sigma_{LP,1}$ for $S_1(q)$ and $N_2, L_{P,2}$ and $\sigma_{LP,2}$ for $S_2(q)$. The parameter N is an integer number and represent the number of repeats in the stacks, L_P stands for the repeat distance in the stacks and σ_{LP} is the mean square fluctuation of this repeat distance, i.e. a parameter describing paracrystalline distortions.

Fitting the patterns to equation 5.1 on a logarithmic scale was done by minimizing the sum of squared residuals using the Microsoft Excel solver. If all parameters were left free, this minimization would involve the variation of 24 parameters (with the density values and the C-parameter in fact not being independent). However, when approaching the experimental SAXS patterns some parameters were constrained.

For pure Brij® S-20, the following constraints were applied:

$$l_{2,1} = L_{p,1} \qquad \text{(Eq. 5.2)}$$

$$\rho_{3,1} = \rho_{2,1} \qquad \text{(Eq. 5.3)}$$

$$l_{2,2} = L_{p,2} \qquad \text{(Eq. 5.4)}$$

$$\rho_{3,2} = \rho_{2,2} \quad \text{(Eq. 5.5)}$$

$$\rho_{1,2} = \rho_{2,1} = 0.655 \quad \text{(Eq. 5.6)}$$

$$\rho_{1,1} = \rho_{2,2} = 0.48 \quad \text{(Eq. 5.7)}$$

$$\sigma_{1/2,1} = \sigma_{2/3,1} = \sigma_{1/2,2} = \sigma_{2/3,2} = 0 \quad \text{(Eq. 5.8)}$$

The constraints (Eq. 5.2), (Eq. 5.3), (Eq. 5.4) and (Eq. 5.5) ensured that there was no epoxy phase in this case. In doing so, the model, which in fact is designed for 3 phase structures, can be applied to pure two-phase Brij® S-20, which only has a crystalline PEO and liquid-like aliphatic phase. The constraint (Eq. 5.6) and (Eq.5.7) assign the crystalline PEO density to the central layer in structures of type 2 and the aliphatic liquid density to the central layer in structures of type 1. (Eq. 5.8) in fact came as a result of a first fitting iteration in which these transition layer parameters remained virtually zero. In a second run these parameters were effectively set to zero. This set of constraints reduced the number of free fitting parameters from 24 to 11 for pure Brij® S-20.

For uncured *90%r*, the following constraints were applied:

$$\rho_{1,2} = \rho_{2,1} = 0.655 \quad \text{(Eq. 5.9)}$$

$$\rho_{1,1} = \rho_{3,2} = 0.48 \quad \text{(Eq. 5.10)}$$

$$\sigma_{1/2,1} = \sigma_{1/2,2} = \sigma_{2/3,2} = 0 \quad \text{(Eq. 5.11)}$$

In addition, the following restrictions were used:

$$l_{1,1} \leq l_{2,1} \leq L_{p,1} \quad \text{(Eq. 5.12)}$$

$$l_{1,2} \leq l_{2,2} \leq L_{p,2} \quad \text{(Eq. 5.13)}$$

The constraints (Eq. 5.9) and (Eq.5.10) allocate the crystalline PEO density to the central layer in structures of type 2 and the aliphatic liquid-like density to the central layer in structures of type 1.

In structures of type 2, the central PEO layer is surrounded by epoxy containing layers with a density $\rho_{2,2}$ obtained through parameter variation. These epoxy layers are situated *in between* the (central) crystalline PEO layer with electron density $\rho_{1,2}$ and the aliphatic layers with density $\rho_{3,2}$. In Figure 5.9B, the electron density profile of such structures is represented by the magenta curve.

In structures of type 1, the epoxy containing phase forms *the matrix* with density $\rho_{3,1}$ in which isolated type 1 structures reside. These structures are composed of a central liquid aliphatic layer, flanked by crystalline PEO layers on both sides. The density of

crystalline PEO layers gradually evolves to that of the epoxy matrix, given by the transition layer parameter $\sigma_{2/3,1} = 10$. All other transition layer parameters remained zero during the fit, as expressed in constrained (Eq. 5.11), which was introduced after a first fitting cycle indicating that such a constrained was appropriate. The type 1 structures also form stacks with an average periodicity, $L_{P,1}$. However, restriction (Eq. 5.12) resulted in $l_{2,1} = L_{p,1}$upon fitting. As a result, clear epoxy regions are missing in the corresponding stack electron density profiles (the green electron density profile in Figure 5.9B).

The constraints for the SAXS pattern of uncured *90%r* at 25°C reduces the number of variables from 24 to 17.

For cured *90%r* at -50°C, the following constraints were applied:

$$C = C_{uncured} \quad \text{(Eq. 5.14)}$$

$$\rho_{1,2} = \rho_{2,1} \quad \text{(Eq. 5.15)}$$

$$\rho_{1,1} = \rho_{2,2} = 0.51 \quad \text{(Eq. 5.16)}$$

$$\rho_{3,2} = \rho_{2,2} \quad \text{(Eq. 5.17)}$$

$$l_{2,2} = L_{p,2} \quad \text{(Eq. 5.18)}$$

$$\sigma_{1/2,1} = \sigma_{2/3,1} = \sigma_{1/2,2} = \sigma_{2/3,2} = 0 \quad \text{(Eq. 5.19)}$$

In addition, (Eq. 5.12) and (Eq. 5.13) were used as restrictions. This brings the number of variable parameters in the SAXS pattern fitting of cured *90%r* to 14. Applying constraint (Eq. 5.14) brought the option of finding via the curve fitting procedure a value for the PEO crystalline density at -50 °C, which is $\rho_{1,2}$ in type 1 structures and $\rho_{2,1}$ in type 2 structures (see Eq. 5.15). (Eq. 5.16) assigns the aliphatic layer densities in type 1 and type 2 structures. Then constraints (Eq.5.17) and (Eq. 5.18) ensures that in type 2 stacks there are no epoxy layers involved. This constraint followed after a first minimization without these constraints and the observation that when the presence of an epoxy containing layer was allowed *in between* the PEO and aliphatic layers (similar as in type 2 stacks for uncured *90%r*) an unrealistically thin aliphatic layer was obtained. Constraint (Eq. 5.19) followed after a first fitting iteration in which these transition layer parameters virtually remained zero.

The different electron density profiles as depicted in the Figures 5.3, 5.9 and 5.13 were computed using equation 4.22 with either $F_1(q)$ or $F_2(q)$ and N set to a rather large value as was done in chapter 4 for *30%r*. To produce the profiles of single bilayers, *N* in Eq. 4.22 was set to 1.

5.6 CONCLUSIONS

In this chapter, the thermal behavior and temperature resolved morphology of pure Brij® S-20 was investigated and this revealed that this material solidifies by the crystallization of the PEO moieties. This crystallization induces stacking into layers in which stretched out molecules are arranged in a head-to-head or a head-to-tail fashion. Mixed stacking modes likely also exist and lead to the apparent presence of isolated layers in the SAXS patterns. SAXS cannot exclude the presence of stacks in which the Brij® S-20 molecules are stacked while being interdigitated.

The thermal behavior during cooling and heating of *90%r*, i.e. the block copolymer to which 10% epoxy resin was added, prior to and after isothermal curing at 130°C cannot be discriminated from each other. This for sure results from the fact that the epoxy resin in *90%r* only cured for 36% after a 90 min treatment at 130°C, which is too little to lead to a gelled network.

Apart from the ability to cure, the thermal behavior and morphology development during cooling and heating is very similar to that of pure Brij® S-20. Just like for Brij® S-20, head-to-head and head-to-tail layer stacks are formed, which prior to curing are lightly swollen with epoxy resin. Curing leads to a reduced compatibility between PEO and (partially cured) epoxy and exclusion from within the layer stacks.

The PEO moieties crystallize at low temperatures whereas the stearyl chains remain liquid, irrespective of the temperature. The presence of epoxy resin induces stacking disorder, in particular after curing.

CHAPTER 6 THE ISOTHERMAL CURING KINETICS AND THE TEMPERATURE DEPENDENT MORPHOLOGY OF EPOXY RESINS WITH INTERMEDIATE AMOUNTS OF BLOCK COPOLYMER

In the present chapter, temperature dependent thermal behavior and morphology of epoxy resins with 40, 50 or 70% Brij® S-20 will be discussed. The samples are referred to as *40%r*, *50%r* and *70%r*. Besides morphological features that have been encountered at very low (Chapter 4) and very high (Chapter 5) Brij® S-20 concentrations also new ones appear. For *40%r*, the DSC based thermal behavior during cooling and heating prior to and after isothermal curing at 130°C for 90 min is introduced after having outlined the isothermal curing kinetics. A discussion on the morphology under DSC-like thermal conditions follows, relying on time-resolved synchrotron WAXD and SAXS as well as on room temperature TEM images. Discussion on the morphology of *50%r* and *70%r* is shorter due to a lag of data in some instances or because of strong analogies with samples that have been discussed earlier.

6.1. THE THERMAL BEHAVIOR OF *40%R*

Figure 6.1 displays the DSC curves of *40%r*, following the standard temperature profile as illustrated in Figure 3.2. The top graph displays the first cooling and heating segments at 10°C/min, the middle panel represents the isothermal segment at 130°C and the bottom one shows the final cooling and heating segments, also at 10°C/min. The isothermal curing kinetics will be discussed based on the data in the middle panel.

6.1.1 ISOTHERMAL CURING KINETICS

The epoxy conversion degree with time during isothermal curing at 130 °C after heating at 10°C/min was calculated using equation 4.18 with ΔH_{prep} set to zero and the factor for ΔH_{max} set to 0.6 (instead of 0.7), reflecting the epoxy resin fraction in the system. The result is depicted in Figure 6.2. In fact ΔH_{prep} was zero for all samples in this work with more than 20% Brij® S-20. The conversion during the heating run (based on ΔH_h in equation 4.18) amounts to 3.4% for *40%r*, which is less compared to for *30%r* (6.5%). Furthermore, the curing degree after 90 min at 130 °C is only 68%, which is less than the 82 and 90% for respectively *30%r* and *20%r*. Since conversion is significantly above the theoretical gelation point of 58% conversion (see section 3.1.1), the curing reaction does not stop after network formation and there is still sufficient amount of mobility in the matrix to continue the reaction.

These effects might be associated with the increased epoxy resin dilution in *40%r*, which is expected to reduce the curing rate.

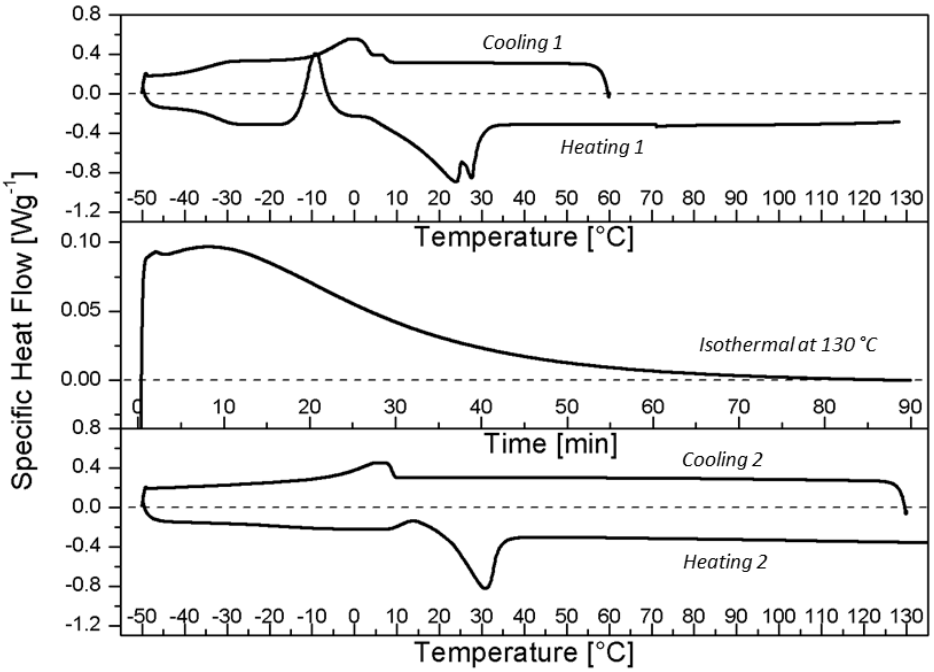


Figure 6.1 DSC traces for *40%r*, related to the thermal protocol used during time-resolved X-ray based morphological characterization and as depicted in Figure 3.2. Exothermic signals are plotted upwards. The program includes cooling 1 and heating 1 at 10 °C/min (top panel), isothermal curing at 130 °C for 90 min (middle panel), followed by cooling 2 and heating 2 at 10 °C/min (bottom panel).

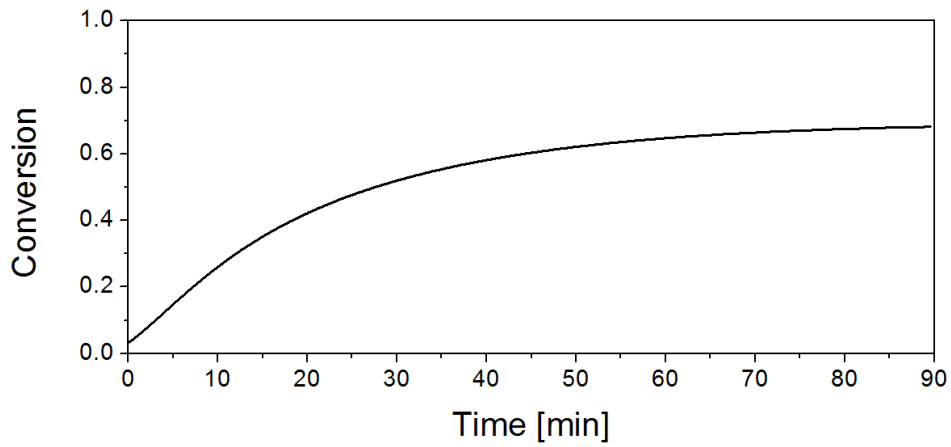


Figure 6.2 : Epoxy conversion during isothermal curing at 130°C after heating at 10°C/min for *40%r*.

However, increasing the curing time at 130°C would most likely not induce a much higher ultimate conversion degree as the curing rate strongly decreases with time at

130°C and as the conversion evolves to a plateau level already after 90 min. Likely, the reactants are separated as a result of the Brij® S-20 nanofeatures that act as physical barriers or the epoxy reagents are separated by a preferential dissolution of one of the resin components within the PEO moieties of Brij® S-20. The curing degree for *40%r* exceeds that of *90%r*, which only reaches 36% (see Chapter 5). In the latter case, dilution effects and physical entrapment are expected to be even more pronounced.

6.1.2 COOLING AND HEATING PRIOR TO CURING

The top panel of Figure 6.1 shows the DSC traces of cooling 1 and (subsequent) heating 1. During cooling 1, a first, small exothermic signal is observed with an onset at about 8°C. Another larger exothermic process starts at 3 °C and the overall exothermic signal peaks at 0 °C. The DSC signal falls back to the baseline at approximately -20°C, which at -32°C reveals a step like discontinuity due to vitrification. Below the T_g, structural transitions are no longer expected within the vitrified phase. As mentioned in Chapter 4, also the exothermic signals for *20%r* and *30%r* during the first cooling have a bimodal character. The magnitude of the low temperature event seems to gain importance in going form *20%r*, over *30r%* to *40%r*. For the *20%r* and *30%r*, the exothermic signals were associated with the crystallization of the aliphatic moieties. The WAXD and SAXS data for *40%r* will confirm that this is also the case for *40%r*. In addition, it will be revealed that the two signals are due to the development of two different nanostructures with aliphatic crystallinity of a different nature.

The higher Brij® S-20 concentration in *40%r* leads to a larger exothermic peak area (17 J/g) compared to for *20%r* and *30%r* as well as a shift of the transitions to higher temperatures. In chapter 7, the structural transitions and associated temperatures prior to and after epoxy resin curing will be discussed systematically as a function of the Brij® S-20 concentration.

After having passed the T_g during heating 1, a strong exothermic signal with an onset at about -15°C appears for *40%r*, which in the case of *30%r* was associated with a conversion from nanostructures with aliphatic crystallinity to structures with PEO crystallinity. The X-ray data will show that this explanation also applies to *40%r*. The onset of this transition occurs at a lower temperature compared to for *30%r* and is – just like the exothermic signals during cooling 1 - bimodal in character, with a first peak maximum at -8°C and a second one of much lower intensity at approximately 3°C. These signals are related to the distinct conversions of the two structures that were formed during cooling 1, as X-ray data will prove. Upon further heating, the small high temperature exothermic peak links up with the onset of the endothermic signal due to PEO crystal melting. PEO melting is finished at approximately 30°C,

whereas 23°C was the endset for *30%r*. Interestingly, the melting endotherm for *40%r* is also bimodal with peaks at 24 and 28°C. X-ray data will unambiguously show that this is related to a recrystallization process in which part of the initially formed PEO crystalline structures transform into more stable ones that melt in the high temperature peak.

6.1.3 COOLING AND HEATING AFTER ISOTHERMAL CURING

The bottom panel of Figure 6.1 displays the cooling and heating segments after curing the material at 130 °C for 90 min. The onset of crystallization occurs at about the same temperature as for the uncured material (10 °C), however only one exotherm is present, suggesting the formation of a single crystal type. Indeed, the X-ray data will only identify aliphatic segments crystallizing orthorhombically in vesicles. This suggests a reduced presence of crystallizable cylindrical micelles after curing. A faint, broad T_g is observed at -17.5 °C during further cooling. Clearly, Brij® S-20 acts as a plasticizer since the pure resin T_g after curing up to 68% is expected to fall around 76°C[90]. The small T_g step compared to for *20%r* and *30%r* relates to the decreased resin fraction in *40%r*.

Once the T_g in the heating 2 run has passed, a broad endothermic signal appears, reflecting the progressive melting of the species crystallized during cooling 2. This process coincides with and at 10°C is clearly overtaken by an exothermic process. Just like in heating 1 for the uncured situation, X-ray data will reveal that this is due to a reorganization from stearyl into PEO crystalline structures. At slightly higher temperatures, the exothermic signal links up with the endotherm due to PEO crystal melting. After peaking at 31 °C, the endotherm sets off at approximately 35 °C where the sample is no longer semicrystalline.

6.2 THE MORPHOLOGY OF *40%R* DURING COOLING AND HEATING PRIOR TO ISOTHERMAL CURING

6.2.1 WAXD

Above the DSC crystallization onset, the WAXD data during cooling (top panel in Figure 6.3) only exhibit an amorphous halo. At decreasing temperatures, small reflections appear that were also reported for *30%r* in Chapter 4. At first, reflections appear which shift with the temperature and finally arrive at q = 1.52 Å^{-1} and q = 1.7 Å^{-1}. The latter reflection is only well-resolved at relatively low temperatures. Blue lines are drawn along these (110) and (200) reflections of orthorhombically ordered aliphatic crystalline Brij® S-20. These reflections are labelled 1 in Figure 6.3 and shift along the q-axis as a result of (reversible) thermal contraction like in the *30%r* case. Once cooled to approximately -2°C, another single reflection appears at q = 1.46 Å^{-1} and remains in position down to the lowest temperatures. It is labelled 2 in Figure

6.3. Clearly, the two exothermic processes seen in DSC should be inked to the creation of type 1 and type 2 crystals although the onsets of formation in DSC occur at slightly higher temperatures as a result of a higher DSC sensitivity.

The nature of the type 2 structure remains unclear. For sure orthorhombic and hexagonal aliphatic unit cells are excluded as in those cases a strong reflection should occur at q = 1.52 $Å^{-1}$. The strongest low angle reflections for monoclinic and triclinic unit cells occur at respectively q = 1.42 $Å^{-1}$ and 1.37 $Å^{-1}$ which is too low to be associated with the reflection at q = 1.46 $Å^{-1}$. In the past, Rastogi et al[108] coined the idea of an open orthorhombic unit cell to account for a similar reflection in high pressure crystallized ethylene copolymers. The density of this phase is lower than that of the regular orthorhombic unit cell. Moreover, this type 2 reflection is rather broad, suggesting high disorder or small grain sizes. This disorder also explains why no higher order reflections are observed. Good reasons to crystallize into such a poorly ordered fashion will be provided in section 6.2.2 when discussing the SAXS data.

Upon heating, the type 2 reflection disappears concomitantly to when PEO monoclinic crystalline reflections appear[115], highlighted in orange in the lower panel of Figure 6.3 and labelled 3. The reflection at q = 1.36 $Å^{-1}$ is a combination of the (111) and (120) reflections. The one at q = 1.63 $Å^{-1}$ is a clustering of the (112), (-212) and (032) reflections. This conversion from aliphatic to PEO crystals occurs within the large exothermic signal seen in DSC. As this process is driven by PEO, it is colored orange in the Figure 6.3 middle panel. The type 1 orthorhombic reflections only disappear at about 0°C and are gone by 4°C. This process coincides with the small exothermic DSC signal seen in this temperature range. Processes in which crystalline reflections disappear are usually endothermic melting processes at temperatures higher than the crystallization temperatures. Here, the type 1 and type 2 reflections disappear at *lower* temperatures and the processes are *exothermic*. Clearly, aliphatic crystal melting is induced by the creation of PEO crystals, which leads to a thermodynamically more stable situation. The overall conversion process is exothermic. To the best of our knowledge, the phenomenon in which the crystallization of one component disrupts the crystallinity of an earlier crystallized one has not been reported before. However, it is known for certain block copolymers that the liquid-liquid microphase separated morphology can be disrupted by the crystallization of one of the blocks[109]. Whether or not this disruption occurs, depends on the liquid-liquid segregation strength of the different blocks. At a strong segregation, crystallization remains confined within the liquid-liquid nanophase separated morphology whereas at a weaker segregation, crystallization of one of the blocks may lead to a (partial) disruption of the earlier morphology[110].

When the sample finally approaches the melting offset (around 30 °C), the PEO (111) reflection at q = 1.33 Å^{-1} splits off from the (120) reflection at q = 1.36 Å^{-1}. This points at a conversion to rather perfect PEO crystals (labelled 4 in Figure 6.3) as already observed in pure Brij® S-20 and *90%r* (see Chapter 5). Such a conversion was not seen for *30%r* (Chapter 4). The associated nanomorphological changes as revealed by SAXS will be key to understanding the origin and nature of this high temperature transition from poorly ordered (type 3) to more perfectly ordered (type 4) crystalline PEO structures. This conversion process, which should be exothermic, starts at approximately 21°C (according to the WAXD data) but its heat is annihilated by the main endothermic DSC signal due to the melting of (the majority of) the less perfect PEO crystals. The small but sharp high temperature endothermic DSC peak is due to the melting of the more perfect PEO crystalline type 4 structures.

6.2.2 SAXS

Simultaneously with the appearance of the type 1 orthorhombic reflections, a SAXS-reflection at 0.074 Å^{-1}appears during cooling 1 (Figure 6.4, top panel, reflection labelled 1). When type 2 crystals appear in WAXD and DSC exhibits its second exothermic signal, a second set of SAXS reflection appears (labelled 2), with the strongest one at q = 0.080 Å^{-1} and weaker ones at q = 0.142 Å^{-1} and q = 0.162 Å^{-1}. The latter is not highlighted in Figure 6.4 because of being too weak. Very quickly these type 2 reflections become pretty strong, suggesting that type 2 structures are ultimately more predominantly present than type 1 structures. This observation aligns with the larger exothermic signal seen in DSC. The q-positions of the type 2 reflections occur (relative to the position of the strongest reflection) at 1, $\sqrt{3}$ and $\sqrt{4}$. This is characteristic for a 2D hexagonally packed cylindrical structure and a P6/mm space group. The Miller indices of the mentioned three reflections are (100), (110) and (200) respectively. Upon heating, the signals due to type 3 structures grow at expense of the type 1 and type 2 signals (Figure 6.4 bottom panel). These events concur with the exothermic DSC signals in heating 1. When type 4 structures appear in WAXD (Figure 6.3, bottom panel), two new peaks appear in SAXS, which in Figure 6.4 are labelled accordingly.

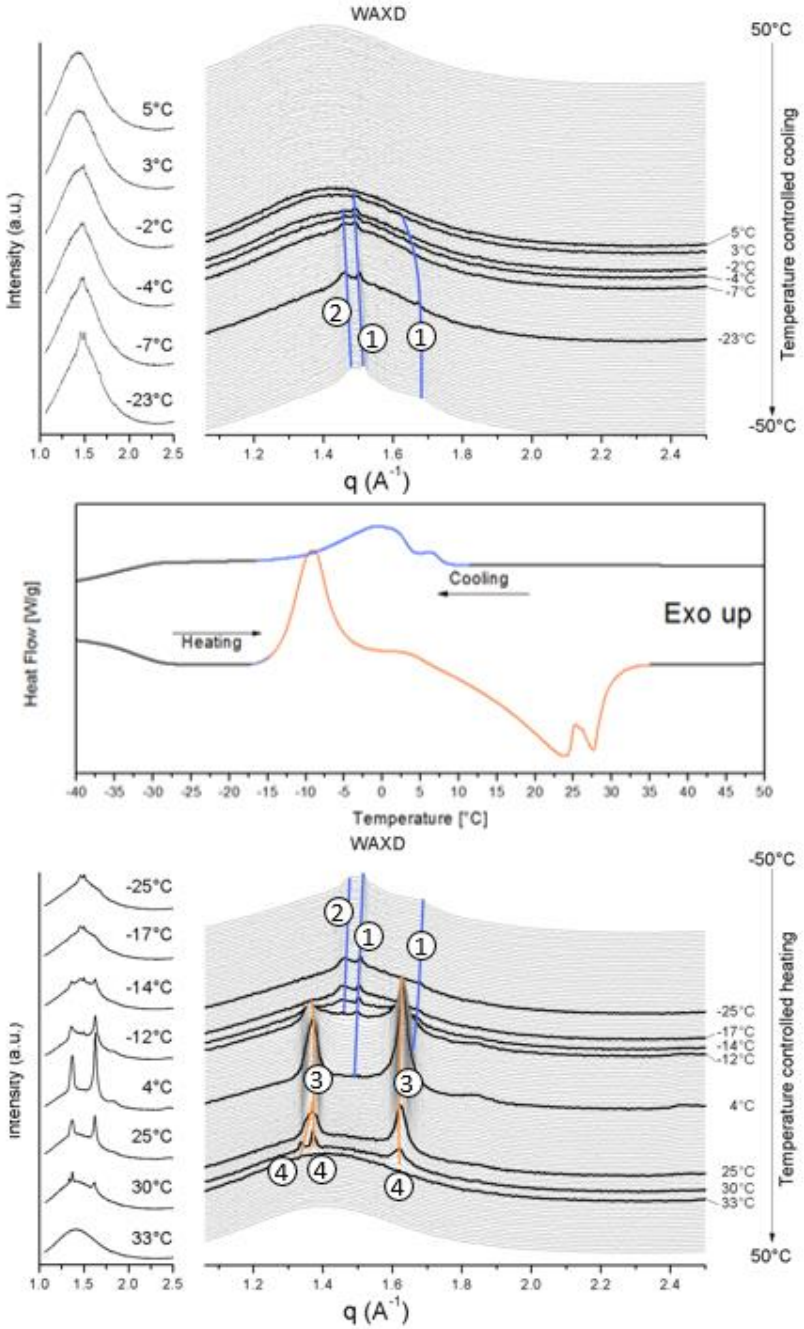


Figure 6.3. For *40%r*. Top panel: Time resolved WAXD patterns collected during cooling 1. Middle panel: DSC curves during cooling 1 and heating 1. Bottom panel: Time resolved WAXD patterns during heating 1. Blue and orange features belong to transitions (in DSC) or reflections (in the WAXD patterns) of respectively the aliphatic and PEO moieties. The number labelling groups reflections that belong to the same structure. The patterns highlighted in bold are displayed separately in the left side windows.

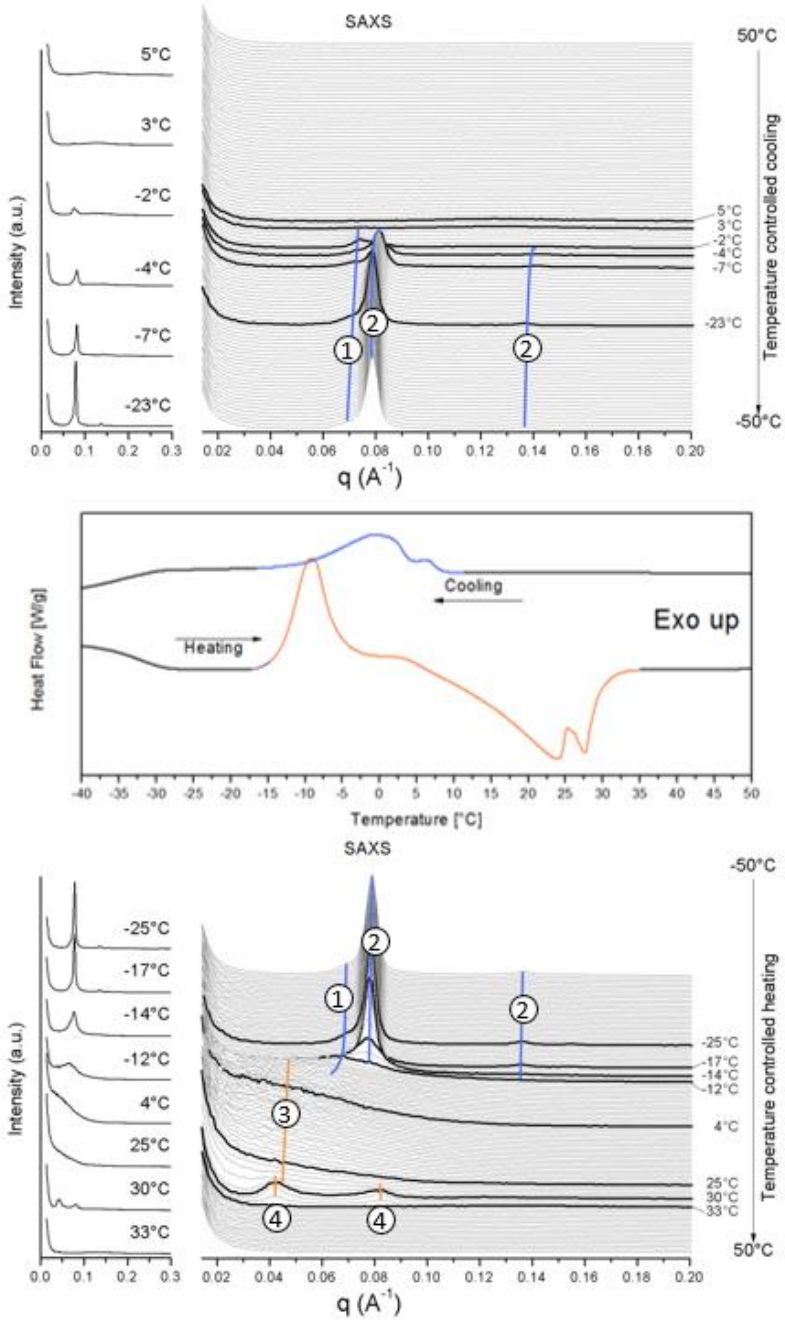


Figure 6.4. For *40%r*. Top panel: Time resolved SAXS patterns collected during cooling 1. Middle panel: DSC curves during cooling 1 and heating 1. Bottom panel: Time resolved SAXS patterns during heating 1. Blue and orange features belong to transitions (in DSC) or signals (in the SAXS patterns) of structures that are either aliphatic or PEO crystalline. The number labelling groups SAXS signals that belong to the same structure as the labels indicate in Figure 6.3. The patterns highlighted in bold are displayed separately in the left side windows.

To identify the type 1, 2, 3 and 4 nanostructures, selected SAXS patterns were analyzed in detail. At most temperatures, different structures are present at the same time. This complicates the analysis as the SAXS patterns have to be treated in terms of suitable superpositions. Such efforts were made throughout, except for the pattern at -25 °C, which was selected to represent the case in which hexagonally packed cylindrical micelles are predominantly present.

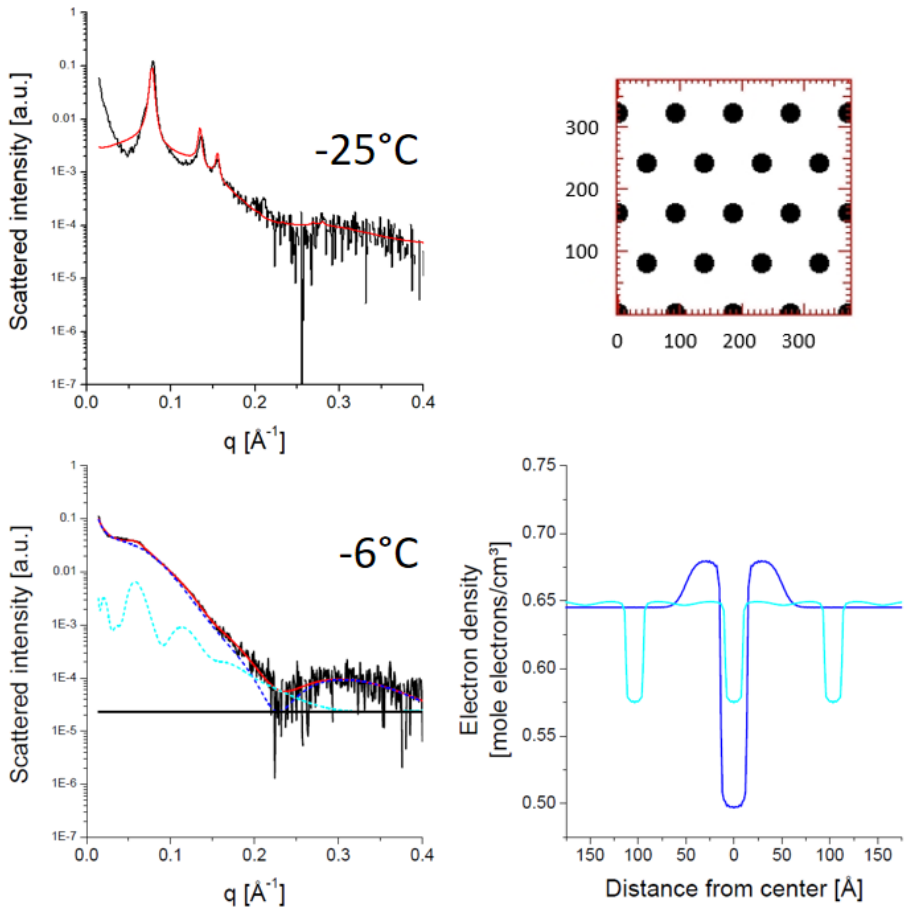


Figure 6.5 In the top row, the experimental SAXS pattern (black) at -25°C during heating 1 for 40%r together with a theoretical fit (red) obtained by using the program Scatter and assuming a structure of hexagonally packed cylinders with aliphatic crystallinity (type 2 structures). A top view of this structure is represented in the upper right panel with the black circles representing the cylinder cross sections. The left bottom panel displays the experimental SAXS pattern of *40%r* during heating 1 at -6°C (black) together with a fit according to equation 6.1 (red). The fitting is a superposition of a constant background (black horizontal line), a share due to type 3 isolated layers in which the PEO moieties are crystalline (dark blue dashed curve on top of the background) and a share due to stacked type 1 bilayers in which the central aliphatic layer is crystalline (cyan dashed curve). The electron density profiles for each share are depicted in the bottom right side panel, using corresponding colors.

The black curve in the upper left panel of Figure 6.5 displays this SAXS pattern at -25 °C during heating 1 on a logarithmic scale. This pattern was approached, assuming that only hexagonally packed cylinders (type 2 structures) contribute. To this end, the program Scatter developed by S. Förster, was used[111]. This program is able to produce theoretical SAXS patterns of assemblies of randomly oriented domains of hexagonally packed cylinders. A P6/mm space group is assumed and Lorentzian peak shapes are used for the reflections of which the positions are depending on the cylinder to cylinder distance, *a*. The intensities depend on the radius of the homogeneous cylinders, R_c, which has a characteristic polydispersity. Finally, in fitting the theoretical to the experimental pattern, a scaling factor is used together with a constant background. The result of the fitting procedure is represented by the red curve in the upper left panel of Figure 6.5. This curve covers the experimental main reflections rather well but fails to reproduce the pattern in the low *q*-range as a result of neglecting the small fraction of type 1 structures. The parameters describing the P6/mm structure are nevertheless believed to be reliable as they are predominantly based on the SAXS intensities at higher *q*-values. The obtained cylinder diameter measures 19.1 Å, the standard deviation of its size distribution equals 1.7 Å, and the cylinder to cylinder distance equals 93.3 Å. A top view of this structure is represented in the upper right panel of Figure 6.5. In Figure 6.6 a physical interpretation is provided in which the cylinders are composed of crystalline Brij® S-20 aliphatic moieties and the matrix of epoxy resin swollen PEO segments. A fully stretched stearyl chain measures 22 Å, which is quite close to the cylinder diameter. Very clearly, the cylindrical shape of the packed micelles is not compatible with the orthorhombic geometry of crystallized aliphatic chains. The WAXD data do reveal aliphatic crystallinity, but of a very disordered, open (not dense) nature. Likely, the cylinders convert into a crystalline state in small patches with the chains configured to still allow connectivity with the PEO segments. These constraints apparently do not allow for a regular, dense crystalline packing.

The SAXS pattern at -6°C during heating 1, depicted in Figure 6.5 at the bottom left, is representative for a situation in which type 3 and a small fraction of type 1 structures are present (see the Figure 6.3 and 6.4). This SAXS pattern was approach with equation 6.1, which is an expanded version of equation 5.1.

$$I(q) = \frac{C}{4\pi q^2}\left\{\begin{matrix}\Phi(1-\beta_1)F_1(q)^2 + \Phi\beta_1 F_1(q)^2 S_1(q) + \\ (1-\Phi)(1-\beta_2)F_2(q)^2 + (1-\Phi)\beta_2 F_2(q)^2 S_2(q)\end{matrix}\right\} + B \quad \text{(Eq. 6.1)}$$

This equation is used throughout this chapter to model all remaining SAXS patterns in terms of a superposition of scattering contributions from two different layer kinds of which the structures enter via $F_1(q)$ and $F_2(q)$. The definitions of $F_1(q)$ and $F_2(q)$ and the associated structural parameters have been outlined in section 5.5.

Equation 6.1, in contrast to equation 5.1, allows both layer kinds to be present as either isolated layers or layer stacks. The Layer stacking is characterized by the functions $S_1(q)$ and $S_2(q)$ given by equation 4.21, which has also been outlined in section 5.5. Φ represents the volume fraction of layers of the first kind and $(1-\Phi)$ the fraction of layers of the second kind. The product $\Phi\beta_1$ is the fraction of stacks of layers of the first kind and the product $\Phi(1-\beta_1)$ is the fraction of non-stacked, isolated layers of that kind. $(1-\Phi)\beta_2$ and $(1-\Phi)(1-\beta_2)$ are the equivalent fractions for layers of the second kind. In contrast to in Chapter 5, layers of the first and second kind are not necessarily different because of having a central aliphatic or PEO layer. In the present chapter layer kinds may differ in e.g. thickness or crystallinity rather than local chemistry. Fitting the SAXS patterns on a logarithmic scale to equation 6.1 was done by minimizing the sum of squared residuals using the Microsoft Excel solver. Rather than discussing the resulting structures in terms of the actual fitting parameters, electron density profiles were computed using equation 4.22 with either $F_1(q)$ or $F_2(q)$ and N set to a rather large value for the stacks. To produce the profiles of single layers, *N* in Eq. 4.22 was set to 1.

To limit the number of free parameters in the analysis of the *40%r* SAXS pattern at -6°C and to adequately reach realistic solutions, the *C*-factor in equation 6.1 was constrained to be identical to that of in the analysis of the *40%r* 30°C SAXS pattern (see further below). Furthermore, the central layers were assumed to be aliphatic but liquid and crystalline for respectively the bilayers of the first (type 3 structures) and second kind (type 1 structures). Electron densities for those layers were taken from the equations 4.10 and 4.11 at the appropriate temperature and multiplication with 0.57 mole electrons/g. Furthermore, it was assumed that the PEO layers in bilayers of the first kind were crystalline (type 3 structures) and the ones in the second kind liquid (type 1 structures). In the fitting procedure, the liquid PEO density was constrained to be lower or identical to that of crystalline PEO. The epoxy electron density outside the layers was left as a free parameter but defined to be identical for both layer kinds. After a first fitting iteration it was decided to keep the interfaces between the aliphatic and PEO layers sharp, i.e. $\sigma_{1/2,1} = \sigma_{1/2,2} = 0$. Allowing stack formation in both layer kinds induced a zero stack fraction in either the type 1 or type 3 structures in two equivalent solutions, which can be reached depending on the starting values of the fitting parameters. As the small maximum on top of the broad SAXS signal in the 6°C pattern at q = 0.07 Å^{-1} is due to type 1 structures, only the solution in which the type 1 structures are stacking, was kept. To actually induce this solution, stacking for type 3 structures was eventually prohibited during fitting. As a result the fitting procedure involved the variation of 14 parameters. Parameter optimization produced a solution in which no isolated type 1 structures are present besides the stacked ones.

The share in the SAXS pattern at -6°C of stacked type 1 structures and the corresponding electron density profile are represented in cyan in Figure 6.5. The second contribution, depicted in dark blue is due to isolated type 3 bilayers. Physical interpretations of the electron density profiles are shown in Figure 6.6 together with the shares each of the structures take.

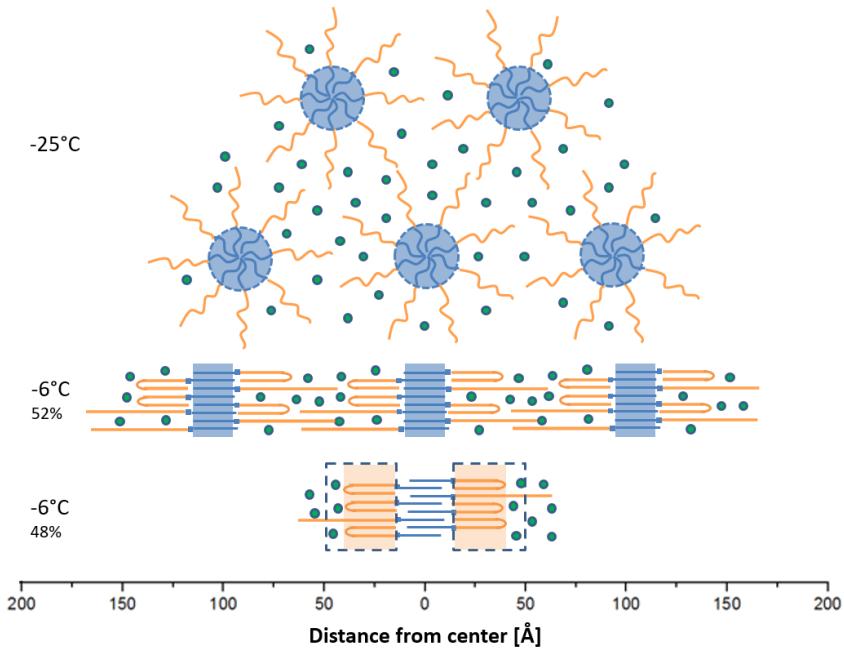


Figure 6.6: Representation of the possible structures within *40%r* at -25°C and -6°C during the first heating at 10°C/min after cooling at 10°C min. The blue and orange lines correspond to stearyl and PEO chains respectively. The blue blocklets highlight the links between those moieties. Shaded areas indicate a crystalline state in blue or orange for the corresponding moieties. The greenish dots represent resin monomers. The structures as well as their indicated relative percentages are based on a modeling of the SAXS patterns.

Clearly, the type 3 structures, which according to the analysis are present for 48% in *40%r*, are very similar to the PEO crystalline structures observed earlier for 60% at -3°C in *30%r* (Figure 4.22). The dimensions of the layer structure suggest that the aliphatic moieties are interdigitated, stretched out and connected to crystals composed of folded PEO chains. The dashed boxes around the PEO crystallites in Figure 6.6 indicate the high density zones, which at the borderline between PEO and epoxy runs up to half way the sigmoidal transition in the dark blue electron density profile of Figure 6.5.

Likewise, the electron density profile of type 1 structures (cyan profile in Figure 6.5) does not differ very much from the aliphatic crystalline bilayer stacks seen for *30%r* at -31°C (Figure 4.21), except that the densities at -6°C are somewhat lower because

of the higher temperature. In addition, the periodicity is larger for *40%r*, suggesting that the PEO layers are more strongly swollen with epoxy at -6°C (for *40%r*) compared to at -31°C (for *30%r*). Note that the periodicity of the type 1 structures approaches the sum of the length of a single stretched stearyl unit and 1.5 times the length of a stretched PEO chain. A situation in which the PEO chains are partially folded and partially stretched is compatible with this dimension, as illustrated in the middle cartoon of Figure 6.6.

Unexpectedly the type 1 structures represent the majority fraction at -6°C (52%) although the SAXS signal for type 1 structures is very weak (the cyan curve in the bottom left panel of Figure 6.5). This effect results from the relatively small difference between the electron density of the crystalline aliphatic layer and the other microphases (PEO and epoxy). However, 52% remains very high compared to the very small amount of crystalline aliphatic matter seen in the -6°C WAXD pattern. Most likely part of the aliphatic microphases in the type 1 structures are liquid rather than crystalline. In fact, when imposing a liquid aliphatic density in the SAXS data analysis, one obtains type 1 like structures with very similar dimensions but rather than 52%, a share of 20% is obtained relative to the type 3 structures. The finding that the increased electron density contrast (as a result of imposing liquid aliphatic microphases) balances against a reduced share at an equal fitting quality, implies that there is no unique solution to the SAXS pattern at -6°C. All in all, a situation in which the type 1 structures are only partially crystalline seems most realistic and attuned with the semicrystalline nature of the type 2 structures discussed above.

At 25°C during heating 1, type 1 structures are no longer present according to Figure 6.4 and the SAXS pattern is supposed to be predominantly due to the scattering of type 3 structures. The top left panel of Figure 6.7 shows this SAXS pattern together with an interpretation in terms of equation 6.1. This treatment revealed the existence of two different kinds of isolated layer structures of which physical representations and share percentages are provided in Figure 6.8. The dark blue share in the 25°C SAXS pattern and the corresponding electron density profile in Figure 6.7 are due to type 3 structures, which are present for 23% as depicted in Figure 6.8. The share that takes up 77% (magenta curves) resembles the liquid like vesicular wall scattering as discussed for *20%r* in section 4.1.2.5 of Chapter 4. In these structures the high electron densities close to the 15 Å thick central aliphatic layers were attributed to PEO congestion, rather than to crystalline PEO. This allotment of the SAXS pattern seems very realistic since 25°C is found towards the end of the major endotherm in the DSC heating 1 curve (Figure 6.5), where a large fraction of Brij® S-20 should be in the molten state. The constraints applied to the SAXS data analysis are shortly outlined in the next paragraph.

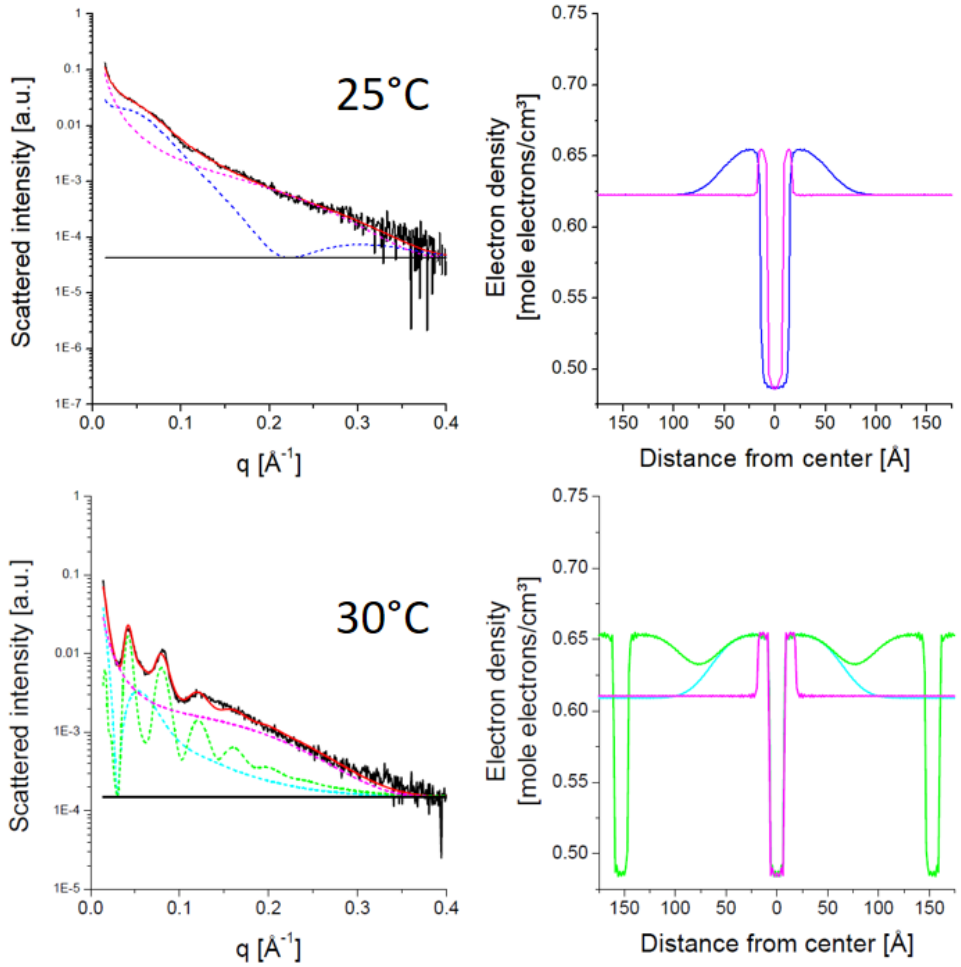


Figure 6.7 In the left side panels: For *40%r* the experimental SAXS pattern (black) at the indicated temperatures during heating 1, together with the fit according to equation 6.1 (red), the constant background (black horizontal line), the share due to isolated type 3 structures (blue dashed curve on top of the background), the share due to isolated type 4 layers (cyan dashed curve on top of the background) and type 4 layer stacks (green dashed curve on top of the background) and the share due to liquid vesicle walls (magenta dashed curve on top of the background). In the right side panels: electron density profiles for each share using corresponding colors. Note that the central part of the green and cyan electron density profiles are hidden by overlap with the magenta profile.

A first fitting iteration on the 25°C *40%r* SAXS curve with equation 6.1 proved that no stacks were present. Therefore, in a next iteration β_1 and β_2 were both set to zero and the stack related parameters $N_1, L_{P,1}, \sigma_{LP,1}, N_2, L_{P,2}$ and $\sigma_{LP,2}$ no longer contributed in the procedure. Furthermore, both structures were assumed to be composed out of a central aliphatic liquid layer with an electron density at 25°C given by equation 4.10 and multiplication with 0.57 mole electrons/g. The electron density

of the neighboring PEO layers in both the first and the second kind structures was constrained to 0.655 mole electrons/cm^3, i.e. the density of crystalline PEO as deduced in Chapter 5. Constraining the PEO density in the liquid vesicular structures to the crystalline value merely prevented the congestive PEO density from peaking excessively high. The epoxy matrix density was fixed at 0.62 mole electrons/cm^3, i.e. the value found in Figure 4.15 for *20%r* at 25°C. Furthermore, the interfaces between the aliphatic and PEO layers sharp were kept sharp, i.e. $\sigma_{1/2,1} = \sigma_{1/2,2} = 0$. The *C*-factor in equation 6.1 was constrained to the value found in the analysis of the *40%r* SAXS pattern at 30°C. The ultimate analysis in terms of equation 6.1 required the optimization of 8 parameters: $B, \Phi, l_{1,1}, l_{2,1}, \sigma_{2/3,1}, l_{1,2}, l_{2,2}$ and $\sigma_{2/3,2}$.

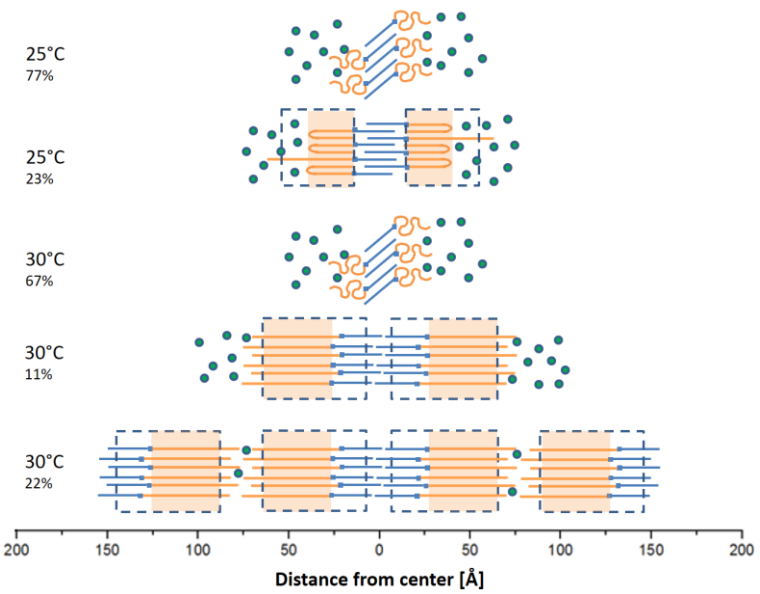


Figure 6.8: Representation of the possible structures within *40%r* at 25°C and 30°C during the first heating at 10°C/min after cooling at 10°C min. The blue and orange lines correspond to stearyl and PEO chains respectively. The blue blocklets highlight the links between those moieties. Shaded areas indicate a crystalline state in blue or orange for the corresponding moieties. The greenish dots represent resin monomers. The structures as well as their indicated relative percentages are based on a modeling of the SAXS patterns.

At the highest temperatures within the DSC heating 1 endotherm, type 3 structures reorganize into type 4 structures, characterized by clear reflections in the SAXS patterns and well resolved PEO (111) and (120) reflections in the WAXD patterns. The latter points at progressed PEO crystalline perfection. The layer morphology that allows for such a more perfect PEO crystallinity was deduced from the *40%r* SAXS pattern at 30°C taking during heating 1 (Figure 6.7).

Treatment in terms of equation 6.1 revealed a 67% presence of liquid like vesicles with a 25°C like structure as depicted once more in Figure 6.8. The remaining 33% is due to type 4 structures, of which one third (11%) occurs as isolated bilayers. The liquid vesicular share in the SAXS pattern and the corresponding electron density profile is depicted in magenta in Figure 6.7 bottom panels. The shares and profiles of the type 4 stacks and isolated layers are shown in respectively green and cyan. All parameters varied in the analysis of the 25°C SAXS pattern were also varied in the 30°C case. In addition, the parameter *C* was left as a free parameter. This resulting *C* parameter was kept in the analysis of all other *40%r* SAXS patterns to ensure consistency. Furthermore, the type 4 stack parameters $N_1, L_{P,1}$ and $\sigma_{LP,1}$ and stack share (β_1) were varied as well. The central liquid aliphatic electron densities in both structures were defined by equation 4.10 and multiplication with 0.57 mole electrons/g, the (crystalline or congested) PEO density was constrained to be equal to 0.655 electrons/cm^3 and the epoxy density to 0.61 electrons/cm^3 (based on the 30°C epoxy resin value for *20%r* in Figure 4.15). The transitions between the aliphatic and PEO microphases were kept sharp, i.e. $\sigma_{1/2,1} = \sigma_{1/2,2} = 0$.

The number of layers, N_1 in the type 4 stacks was 6 and $\sigma_{LP,1}$ was found to be 11.5 Å. These values embody a reasonably high stacking order and account for the rather sharp SAXS reflections. The type 4 structures (present for 11% and 22% at 130°C as illustrated in Figure 6.8) are furthermore characterized by stretched out PEO chains. Apparently, this stretching out allows for a better PEO crystal order compared to in type 3 structures with folded PEO chains, which in contrast to type 4 structure do not exhibit well resolved PEO (111) and (120) reflections in WAXD. These more stable type 4 structures melt at the highest temperatures after having been created during heating 1 run.

The dashed boxes in the 30°C structures in Figure 6.8 highlight the high density regions in the green and cyan electron density profiles in Figure 6.7 up to half way the sigmoidal transition zones. These high density regions basically have a PEO crystalline density but are larger than the areas covered by the orange shaded PEO crystals. Similar sketches were made for some of the *90%r* structures in Figure 5.10. These sketches imply that the PEO ordering and electron density is transferred to the liquid aliphatic zones. This is realistic because of the chain connectivity. Secondly, one oxygen atom in the PEO structure is equivalent to a methylene unit (CH_2) in the aliphatic structure, having both 8 electrons and assuming an sp^3 hybridization. The (lower) liquid density is obtained only in the very central zones of the aliphatic regions where the chain ends reside.

At temperatures above the heating 1 DSC endotherm endset, all structures are in the molten state. These *40%r* patterns were not analyzed in detail, but the liquid shares

in the SAXS patterns at 25 and 30°C predominantly point to *20%r* like vesicular structures, although a small fraction of cylindrical micelles cannot be excluded.

6.3 THE MORPHOLOGY OF *40%R* DURING COOLING AND HEATING AFTER ISOTHERMAL CURING

6.3.1 WAXD

The WAXD data in Figure 6.9 demonstrate that only orthorhombic aliphatic crystals are formed over the entire exothermic DSC signal. For *40%r* prior to curing, this polymorphic form was associated with aliphatic crystallization within vesicular nanostructures, referred to as type 1 structures. The WAXD signal, labelled with number 1 in Figure 6.9, is, however, much stronger after the isothermal curing segment. Matrix curing thus seems to promote the formation of vesicular morphologies. Indeed, as no open orthorhombic aliphatic type 2 crystals are formed, one may suspect that (hexagonally packed) cylindrical micelles are not abundantly present. This will be confirmed through the SAXS data in Figure 6.10. Crystallization into type 1 structures might be further promoted by a more pronounced segregation of Brij® S-20 from the epoxy matrix upon curing. More pronounced segregation upon epoxy curing was suggested earlier for *20%r* in section 4.1.2.5. Note, however, that matrix curing ultimately prevented the crystallization in *20%r* and *30%r* because vitrification occurred above the expected Brij® S-20 crystallization temperature. In *40%r* the matrix T_g after curing is only -17.5 °C, which allows for Brij® S-20 crystallization at higher temperatures.

The WAXD data during subsequent heating, depicted in the Figure 6.9 bottom panel, reveal that the aliphatic crystallinity is replaced by PEO crystallinity where DSC displays its exothermic signal. The absence of well resolved (111) and (120) PEO reflections at the onset of this changeover suggests the formation of type 3 structures. At higher temperatures, the type 3 structures seem to convert into more perfect type 4 structures with well resolved (111) and (120) PEO reflections. In contrast to heating 1 for non-cured *40%r*, the DSC high temperature endothermic signal in heating 2 does not exhibit a split, suggesting that after curing less type 4 structures are formed. It seems that matrix curing inhibits the associated PEO chain stretching process to some extent. At and above 35 °C, only an amorphous halo is left in the WAXD patterns.

6.3.2 SAXS

When the aliphatic orthorhombic (type 1) reflections appear in WAXD during cooling 2 for cured *40%r*, the type 1 typical reflection observed for non-cured *40%r* (Figure 6.4) appears in SAXS, as illustrated in Figure 6.10. In contrast to uncured *40%r* (Figure 6.4), no type 2 SAXS reflections appear when cooling cured *40%r*, proving that

hexagonally ordered cylindrical micelles are not formed. This corresponds well with the unimodal exothermic signal in DSC and the absence of open orthorhombic reflections in WAXD (Figure 6.9). The type 1 SAXS reflection remains down to the lowest temperatures and remains in place during subsequent heating up to when it is replaced by signal that is typical of the type 3 structures identified in uncured *40%r* and which involve crystallinity from chain folded PEO. Although the WAXD data suggest the formation of more perfect and more stable PEO chain extended type 4 structures upon further heating, no clear signatures thereof are seen in SAXS. It thus seems that type 4 structures in cured *40%r* are only present as isolated bilayers. No stacks are formed, which in non-cured *40%r* during heating 1 produced clear reflections in the high temperature SAXS patterns (Figure 6.4).

The SAXS pattern at -15°C during heating 2 was analyzed in terms of equation 6.1 and is representative for temperatures where vesicular type 1 structures with orthorhombic aliphatic crystallinity are present. The outcome of the analysis is illustrated in Figure 6.11 and sketches of the different structures with their shares are given in Figure 6.12. During fitting, the *C* factor as obtained for *40%r* at 30°C during heating 1 was used for consistency (the same *40%r* sample was used throughout all heating and cooling runs). Other than that, only the central aliphatic density was constrained to be the crystalline value at -15°C given by equation 4.10 and multiplication with 0.57 mole electrons/g and just like for the previous *40%r* cases, the interfaces between the central aliphatic microphases and the liquid PEO layers were kept sharp, i.e. $\sigma_{1/2,1} = \sigma_{1/2,2} = 0$. The theoretical curve produced by equation 6.1 only covered the experimental one if two kinds of layers were assumed. Therefore, fitting involved the variation of 18 parameters. Ultimately, one of the layer kinds appeared to be present as layer stacks only.

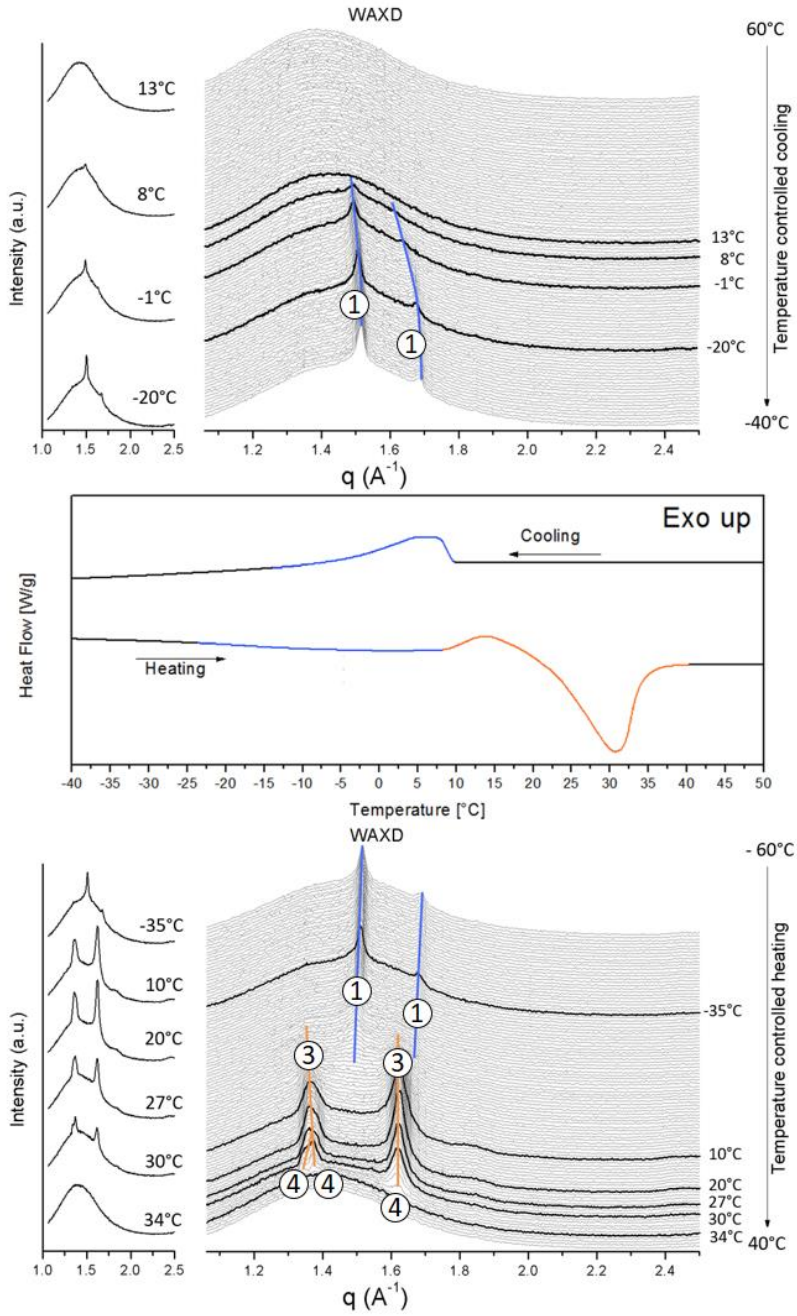


Figure 6.9. Top panel: Time resolved WAXD patterns collected during cooling 2 of *40%r* after the isothermal curing step. Middle panel: DSC curves during cooling 2 and heating 2 of *40%r*. Bottom panel: Time resolved WAXD patterns during heating 2 for *40%r*. Blue and orange features belong to transitions (in DSC) or reflections (in the WAXD patterns) of respectively the aliphatic and PEO moieties. The number labelling groups reflections that belong to the same structure. The patterns highlighted in bold are displayed separately in the left side windows.

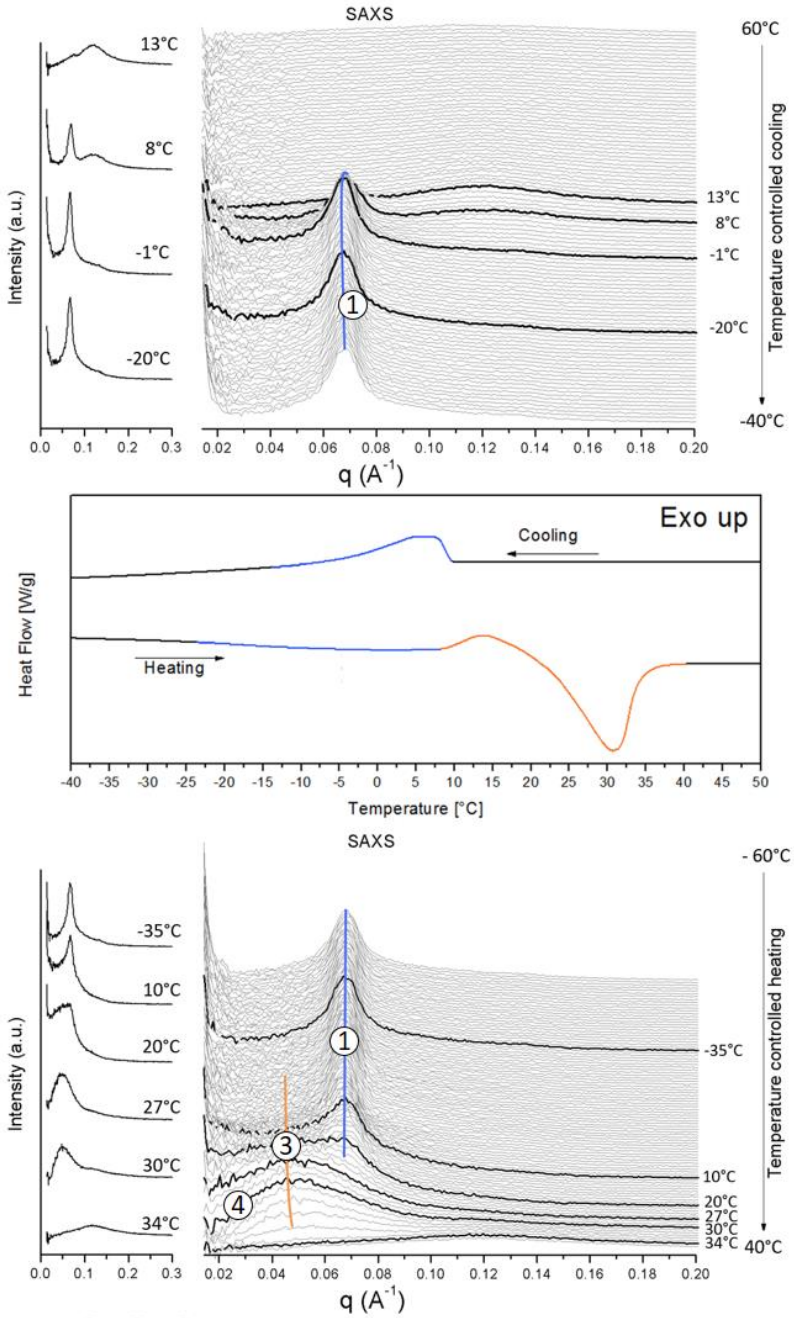


Figure 6.10. Top panel: Time resolved SAXS patterns collected during cooling 2 of *40%r* after the isothermal curing step. Middle panel: DSC curves during cooling 2 and heating 2 of *40%r*. Bottom panel: Time resolved SAXS patterns during heating 2 for *40%r*. Blue and orange features belong to transitions (in DSC) or signals (in the SAXS patterns) of respectively the aliphatic and PEO moieties. The number labelling groups reflections that belong to the same structure. The patterns highlighted in bold are displayed separately in the left side windows.

The two layer types essentially differ in the thickness of the central aliphatic layer, which amount to 16 and 32 Å respectively. According to the analysis, structures with the thickest aliphatic layers are present for 9% in fairly ordered bilayer stacks. The share in the SAXS pattern and the corresponding electron density profile are depicted using magenta curves in Figure 6.11. These structures are responsible for the peak observed in the -15°C SAXS pattern. The relevant stack parameters $N_1, L_{P,1}$ and $\sigma_{LP,1}$ are 7, 92 Å and 5 Å. The structures with thinner aliphatic layers are present for 23% as isolated bilayers and for 68% as layer stacks. The shares in the SAXS pattern and the electron density profile are represented in Figure 6.11 using respectively blue and green colors. Stacks of that type are characterized by $N_2, L_{P,2}$ and $\sigma_{LP,2}$ with values of 4, 81 Å and 24 Å. Clearly, these stacks are more disordered as reflected by the low N_2 and high $\sigma_{LP,2}$ values. Values for the PEO and epoxy electron density were retrieved from the fitting procedure and seem realistic. The epoxy density found in the present case at -15°C is 0.715 electrons/cm³, which is close to the 0.73 electrons/cm³ found at that temperature for non-cured epoxy in *20%r* (Figure 4.15).

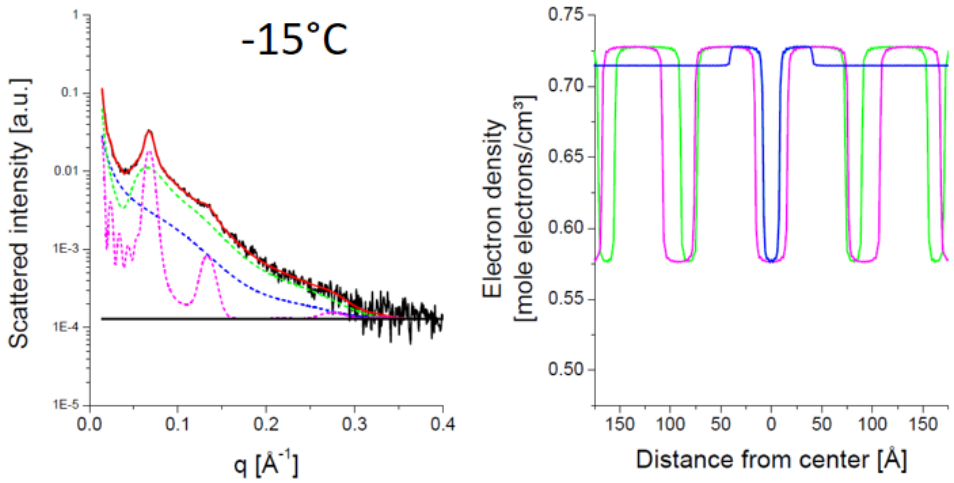


Figure 6.11 In the left side panel for *40%r* the experimental SAXS pattern (black) at -15°C during heating 2, together with the fit according to equation 6.1 (red), the constant background (black horizontal line), the share due to stacks of the first layer kind (magenta dashed curve on top of the background), isolated layers of the second kind (blue dashed curve on top of the background) and the share due to stacks of the first layer kind (green dashed curve on top of the background). In the right side panel: the corresponding electron density profiles for each share, using the same colors as the curves in the left side panel. Note that the central part of the green electron density profile overlaps with and hence is covered by the blue profile.

Potential physical representations of the two layer kinds (both supposed to represent forms of type 1 structures) are shown in Figure 6.12. The disorder in the layers with thin crystalline aliphatic centers potentially relates to a pronounced sorption of epoxy resin within the PEO layers and the inability of the resin to segregate form the vesicle walls upon crystallization due to resin network formation in the direct vicinity. Besides inducing disorder, the epoxy resin swelling drives the PEO chains apart. This effect might translate to the connected aliphatic moieties and prevent close packing and crystallization, unless the latter assume a tilted packing with respect to the layer surface. This tilting allows for a close crystalline packing while spatially separating the PEO chains at the crystal borders to accommodate epoxy resin. It leads to crystalline aliphatic layers that are thinner (16 Å) than the length of fully stretched stearyl chains (22 Å). Tilting is not unusual in lipid crystallization.

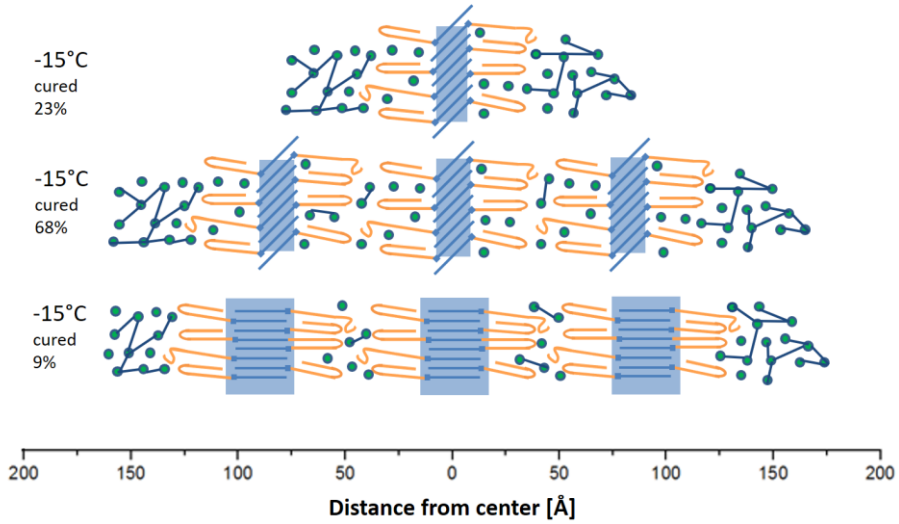


Figure 6.12: Representation of the possible structures within *40%r* at -15°C during the second heating run at 10°C/min after isothermal curing and cooling 2 at 10°C min. The blue and orange lines correspond to stearyl and PEO chains respectively. The blue blocklets highlight the links between those moieties. Shaded areas indicate a crystalline state in blue or orange for the corresponding moieties. The greenish dots represent resin monomers. The structures as well as their indicated relative percentages are based on a modeling of the SAXS pattern.

The ordered stacks with thicker central aliphatic layers might originate form epoxy lean, Brij® S-20 rich volumes. Here, crystallization is expected to happen rather unhindered with stretched out, not tilted aliphatic chains. The periodicity of 92 Å suggest moderate resin presence within the PEO regions. A similar morphology was observed for *30%r* at -31°C prior to resin curing (Figure 4.22). The smaller periodicity observed in the that case (86 Å) may represent a limiting situation in which resin is

completely excluded. That stage is reached after curing likely because of a reduced resin mobility.

The fact that two different type 1 layer structures are observed, is indicative for the presence of Brij® S-20 rich and lean zones, which may exist purely on statistical grounds or alternatively because of liquid-liquid phase separation. However, liquid-liquid phase separation is rather unlikely as no evidence could be found for regions with highly different Brij® S-20 concentrations in the TEM images (see section 6.3.3).

Note that the (low density) aliphatic zones in the ordered type 1 stacks are in fact larger (32 Å) than the length of fully stretched stearyl chains (22 Å). This can be seen in the magenta electron density profile in Figure 6.11. 32 Å is just twice the thickness of the aliphatic zones in the other layer kinds with tilted aliphatic chains (16 Å). Therefore, an alternative representation of the structures with thick aliphatic layers may involve the formation of double layers in which tilted chains are not interdigitating but laying side by side. However, this morphology can be excluded as it is impossible to accommodate the (doubled) amount of PEO chains that emanate from such a double aliphatic layer within the 60 Å thick PEO microphase. The inflated aliphatic layer thus rather implies a transfer of the aliphatic packing to within the PEO zones. Recall that one oxygen atom in the PEO structure is equivalent to a methylene unit (CH_2) in the aliphatic structure.

Another remarkable finding is that the type 1 SAXS reflection in Figure 6.10 during heating 2 is visible as a shoulder on the type 3 peak up to approximately 27°C whereas the type 1 typical orthorhombic reflections are gone already at 0°C. This implies that type 1 like structures in which the aliphatic chains are liquid also contribute to the type 1 typical SAXS signal up to when they are converted into type 3 structures by PEO crystallization or up to when the long range order is destroyed at high temperatures. Most likely, the type 1 structures are only semicrystalline in the aliphatic microphases, in line with what was observed for *40%r* prior to resin curing. Treatments of the 15°C SAXS pattern in terms of equation 6.1 with the density of the aliphatic regions in one of the types fixed at the liquid value were of equal quality but yielded different relative shares.

Analyzing higher temperature SAXS patterns to gain information on the type 3 structures was attempted but remained unsuccessful because besides type 3 structures, also type 4 structures (as demonstrated through the WAXD patterns) and liquid like type 1 structures may contribute. Equation 6.1 is not compatible with such a multitude of potential contributors. More expanded forms of equation 6.1 would yield un unrealistically high number of parameters for optimization.

6.3.3 TEM

Figure 6.13 displays the TEM image of *40%r* after isothermal curing and cooling (cooling 2) down to room temperature. The dark parts are due to PEO as a result of the preferential staining with RuO_4. The PEO topology mainly consists of closed loops, representing vesicular walls running vertically through the section and seen edge on. The gray shaded areas represent top views of the vesicular walls. The different shades of grey most likely are related to vesicles with different wall thickness. Thicker walls, composed of stacked Brij® S-20 bilayers are expected to produce darker grey tones. These structures are more numerously present compared to in *20%r* (Figure 4.10) because of the higher Brij® S-20 concentration in *40%r*.

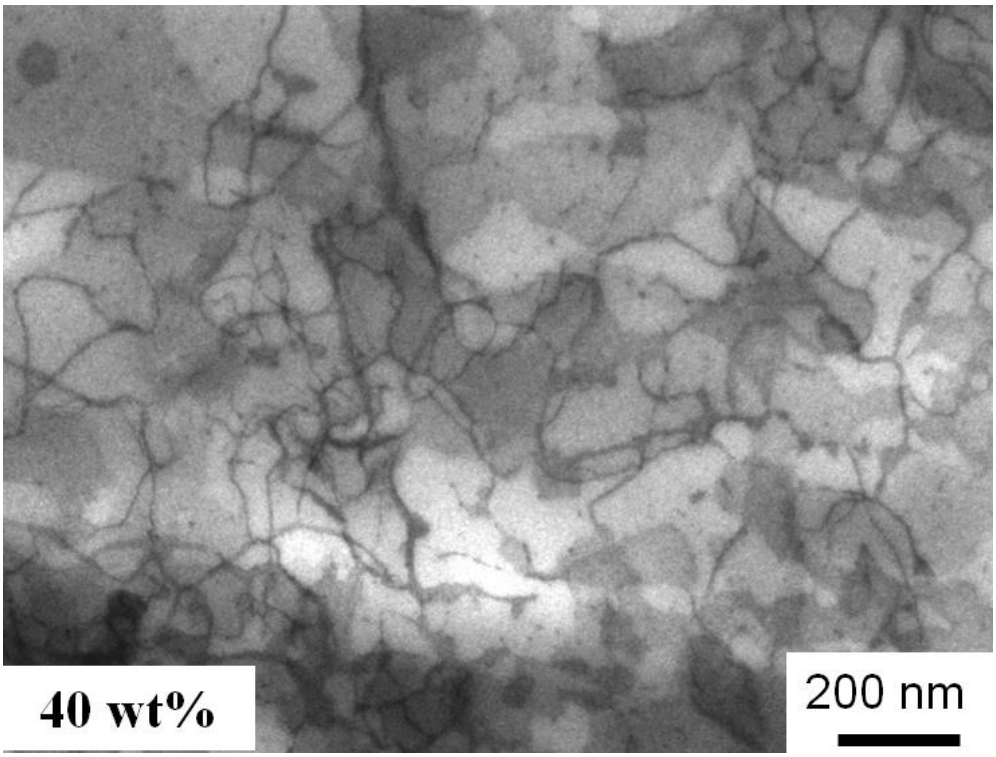


Figure 6.13: TEM picture of *40%r* after curing for 60 min at 130°C and cooling down to room temperature at 10°C/min where staining and sectioning took place.

6.4 THE THERMAL BEHAVIOR OF *50%R*

Figure 6.14 displays the thermograms of *50%r*, following the usual temperature profile shown in Figure 3.2. To avoid the repetition of arguments, the DSC cooling and heating runs for the uncured sample will be discussed together with the

concomitant X-ray based morphological changes in section 6.5. A discussion on the thermal behavior and TEM based morphology of cured *50%r* follows in section 6.6. The isothermal curing behavior is outlined in section 6.4.1 below, based on an analysis of the exothermic signal recorded over 90 min at 130°C and shown in the Figure 6.14 middle panel.

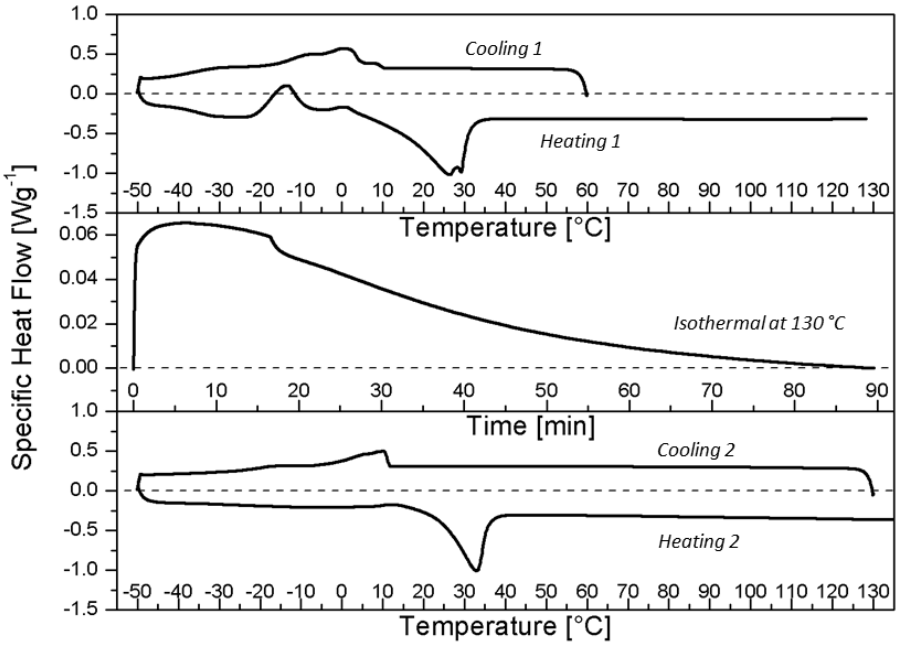


Figure 6.14 DSC traces for *50%r*, related to the thermal protocol used during time-resolved X-ray based morphological characterization and as depicted in Figure 3.2. Exothermic signals are plotted upwards. The program includes cooling 1 and heating 1 at 10 °C/min (top panel), isothermal curing at 130 °C for 90 min (middle panel), followed by cooling 2 and heating 2 at 10 °C/min (bottom panel).

6.4.1 Isothermal curing kinetics

The epoxy conversion as function of time at 130 °C after heating *50%r* at 10°C/min was calculated using equation 4.18 with ΔH_{prep} set to zero and the factor for ΔH_{max} set to 0.5 (instead of 0.7), reflecting the epoxy resin fraction in the system. In contrast to for systems with lower Brij® S-20 concentrations the conversion during the heating run (based on ΔH_h in equation 4.18) was zero, which can be understood from the flat high temperature baseline of the heating 1 DSC curve in Figure 6.14. The conversion reached after 90 min at 130°C is 69%, which is comparable to the 68% for *40%r*. Figure 6.15 suggests that the curing rate of *40%r* is slightly higher than for *50%r*, judging from the fact that higher conversions are reached more rapidly by *40%r* than by *50%r*. For comparison, the *40%r* conversion curve is added to Figure 6.15 using a dashed line.

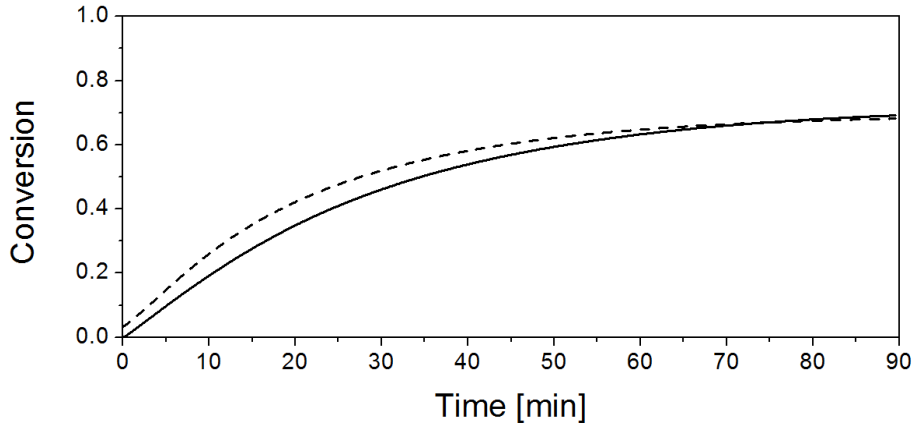


Figure 6.15 Epoxy conversion during isothermal curing at 130°C after heating at 10°C/min for *50%r* (full line) and *40%r* (dashed line).

6.5 The X-ray based morphology and thermal behavior of 5*0%r* during cooling and heating prior to isothermal curing

In the *50%r* DSC cooling 1 run, three exothermic signals are present with onsets at approximately 11°C, 5°C and -2.5°C. Vitrification can be seen in Figure 6.14 where the cooling 1 curve displays an inflection point at approximately -37°C. The two high temperature transitions were also observed in *40%r* although at slightly lower temperatures and are due to the creation of type 1 (11°C) and type 2 (5°C) structures. The type 1 layer structures are revealed in the Figure 6.16 WAXD data through the aliphatic orthorhombic reflections, labelled 1. The subsequent creation of hexagonally ordered cylindrical micelles is witnessed through the type 2 typical reflection, previously associated with open orthorhombic aliphatic unit cells. Concomitantly, the type 1 and type 2 characteristic SAXS maxima appear in Figure 6.17, which allows for an unambiguous identification. The cartoon at the top of Figure 6.6 represents type 2 structures and the central layer like structure is of type 1. Recall that the type 1 and type 2 structures were suspected to be semicrystalline in *40%r*. This likely also holds for *50%r*. A detailed analysis of the *50%r* SAXS patterns was, however, not made.

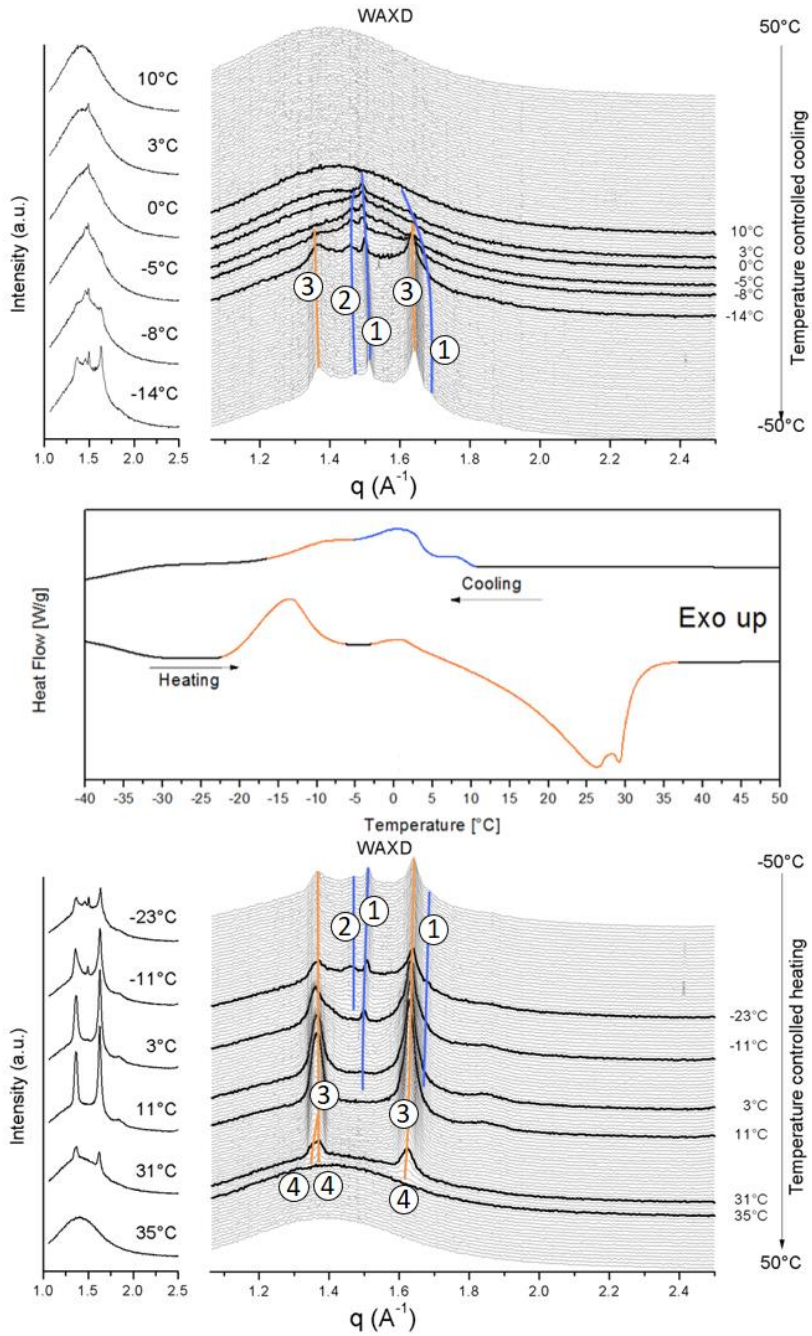


Figure 6.16 . For *50%r*. Top panel: Time resolved WAXD patterns collected during cooling 1. Middle panel: DSC curves during cooling 1 and heating 1. Bottom panel: Time resolved WAXD patterns during heating 1. Blue and orange features belong to transitions (in DSC) or reflections (in the WAXD patterns) of respectively the aliphatic and PEO moieties. The number labelling groups reflections that belong to the same structure type. The patterns highlighted in bold are displayed separately in the left side windows.

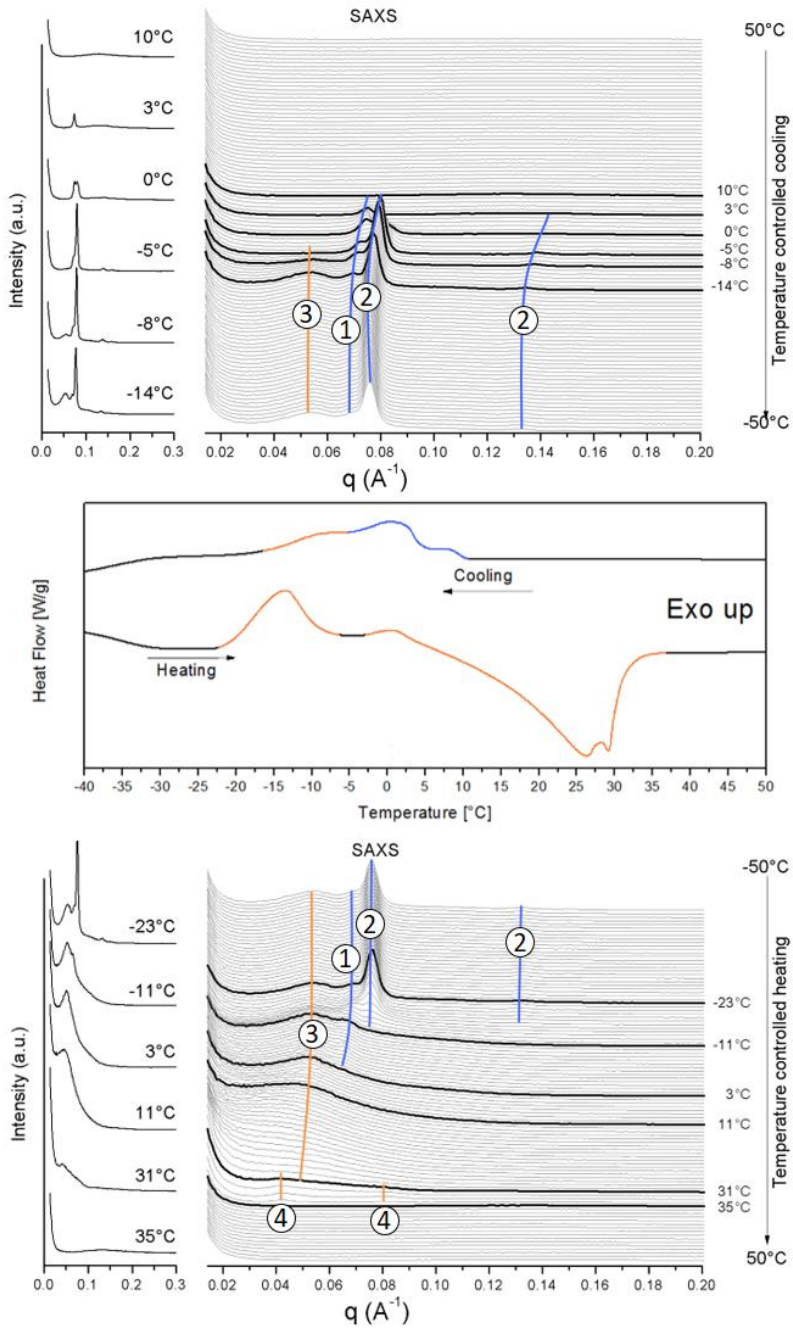


Figure 6.17 For 5*0%r*. Top panel: Time resolved SAXS patterns collected during cooling 1. Middle panel: DSC curves during cooling 1 and heating 1. Bottom panel: Time resolved SAXS patterns during heating 1. Blue and orange features belong to transitions (in DSC) or signals (in the SAXS patterns) of structures that are either aliphatic or PEO crystalline. The number labelling groups SAXS signals that belong to the same structure types as the labels indicate in Figure 6.16. The patterns highlighted in bold are displayed separately in the left side windows.

The exothermic signal with an onset at -2.5°C has no counterpart in *40%r* and is due to the creation of type 3 structures. Type 3 structures are PEO crystalline with folded PEO chains and interdigitated liquid stearyl moieties central in the bilayer as illustrated in the bottom cartoon of Figure 6.6. In *40%r* type 3 structures only appeared at the expense of the type 2 and type 1 structures during heating 1. For *50%* this happens already during cooling 1 and predominantly consumes the type 2 structures as the type 2 WAXD (Figure 6.16) and SAXS (Figure 6.17) signals reduce when the type 3 signals appear. This conversion is arrested when the system approaches its T_g. At -50°C, the vitrified sample contains type 1, type 2 and type 3 structures.

During heating 1, the conversion process resumes after devitrification. A major exothermic signal develops in DSC with an onset at about -22°C. In this exothermic peak, the type 2 structures disappear completely while the WAXD and SAXS signals of type 3 structures grow. At -10°C no traces of type 2 structures are left. This can most clearly be observed in Figure 6.17 where the SAXS reflections of the hexagonally packed cylinders (labelled 2 in Figure 6.17) vanish. The WAXD and SAXS signals of type 1 structures remain up to when a second, smaller exothermic signal is reached in the DSC heating 1 run with an onset at approximately -5°C. At the offset of this signal at 3°C, all type 1 structures have disappeared while the type 3 signals have further gained intensity. Note that these conversions from type 1 and type 2 structures to type 3 structures, just like for *40%r*, happen at lower temperatures than the temperatures at which the type 1 and type 2 structures were created during the preceding cooling 1. The fact that this conversion in *50%r* already partially happens during cooling 1 at low temperatures highlights once more that PEO crystallization actively disrupts the aliphatic crystallinity while forming thermodynamically more stable structures.

Shortly after the two exothermic signals in the DSC heating 1 run, a broad endothermic signal appears. During this event, the type 3 signals weaken, reflecting PEO melting. At the highest temperatures of this major endothermic signal, a small extra peak appears, which just like for *40%r* is due to the melting of type 4 structures, which have formed during the course of type 3 melting. Recall that the type 4 structures are more stable than the type 3 structures because of being built from stretched out PEO chains and having more ordered PEO crystals with sharp and well resolved PEO (111) and (120) reflections at respectively q = 1.33 $Å^{-1}$ and q = 1.36 $Å^{-1}$. These reflection are labelled 4 in Figure 6.16. The SAXS counterparts in Figure 6.17 are labelled likewise. As the type 4 SAXS signals are very similar to those of *40%r*, one can safely state that for *50%r* these structures are also composed of large crystals from stretched out PEO chains. The sample is completely molten at 35 °C.

6.6 THE THERMAL BEHAVIOR AND TEM BASED MORPHOLOGY OF *50%R* DURING COOLING AND HEATING AFTER ISOTHERMAL CURING

The bottom panel of Figure 6.14 displays the DSC cooling 2 and heating 2 segments after curing *50%r* at 130 °C for 90 min. Unfortunately, no WAXD and SAXS data are available for cured *50%r*, implying that a morphological interpretation needs to be made based on what is known for *40%r*. This makes sense because the DSC curves of cured *50%r* are very similar to those of *40%r* in Figure 6.1.

The onset of crystallization during cooling 2 occurs at about 12°C, like for uncured *50%r*. Just like for *40%r*, only one exotherm is observed, which falls back to the base line at approximately -7°C. Relying on information from *40%r*, most likely only type 1 vesicles with orthorhombic aliphatic crystallinity are formed. Finally, a step like T_g transition is observed at -22 °C. This T_g occurs at a slightly lower temperature than for *40%r* (-17.5°C) although the epoxy conversion is similar (68-69%). This points to a more pronounced PEO plasticization for *50%r* because of the higher Brij® S-20 concentration.

At temperatures above the T_g in the heating 2 run, an endothermic signal appears with clearly some exothermic superposition in the temperature range between 0 and 20°C. In analogy with *40%r*, this can be explained by the progressive melting of the type 1 structures, an exothermic reorganization into type 3 (and perhaps also type 4) structures and finally the melting of the type 3 and type 4 structures at the high temperature side of the endotherm.

Figure 6.18 displays the TEM image of 5*0%r* after isothermal curing and cooling (cooling 2) to room temperature. The dark parts are due to PEO and just like for *40%r* reveal closed loops, representing vesicular walls, together with gray shaded areas representing top views of the vesicular walls. The similarity with the *40r* structure in Figure 6.13 is high, except that in Figure 6.18 some of the edge on vesicle walls appear thicker, which might be indicative for a higher population of multi-walled (stacked) vesicles compared to in *40%r*. Shaded areas due to top viewed thicker, multilayer walls appear darker.

Note that for *40%r* and *50%r* the TEM sample preparation happened while the samples were above their T_g. Moreover, according to the DSC cooling 2 profiles in the Figures 6.1 and 6.14, the samples should still be in their non-crystalline state when room temperature is reached. It can however not be excluded that prior to TEM sample preparation some isothermal crystallization happened. Accordingly, there is no one to one match with the thermal history imposed in the DSC and X-ray experiments.

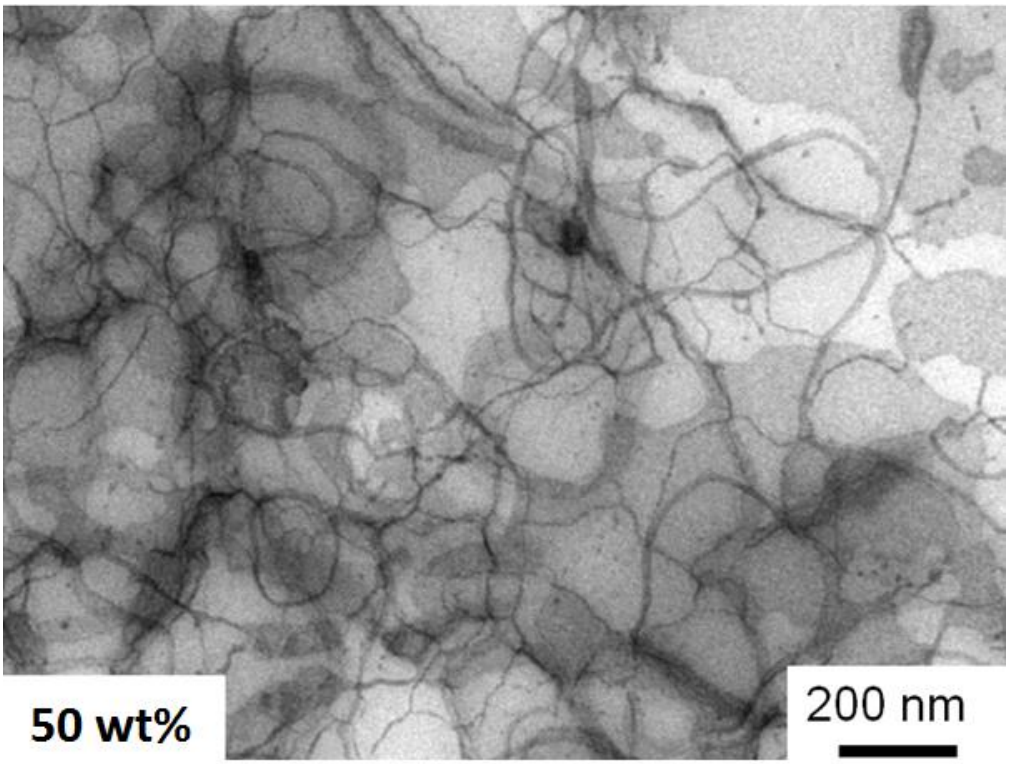


Figure 6.18: TEM picture of *50%r* after curing for 60 min at 130°C and cooling down to room temperature at 10°C/min where staining and sectioning took place.

6.7 THE THERMAL BEHAVIOR OF *70%R*

Figure 6.19 displays the thermograms of *70%r* while being subject to the thermal profile in Figure 3.2. Clearly, the cooling and heating runs prior to and after curing shown in respectively the top and bottom panels are not very different. This similarity was also observed for *90%r* and relates to the low epoxy content and conversion degree in *70%r*, as outlined below in section 6.7.1. A discussion on the thermal behavior and morphology of *70%r* during cooling and heating follows in the sections 6.8 and 6.9, paying special attention to differences with respect to *40%r* and *50%r*.

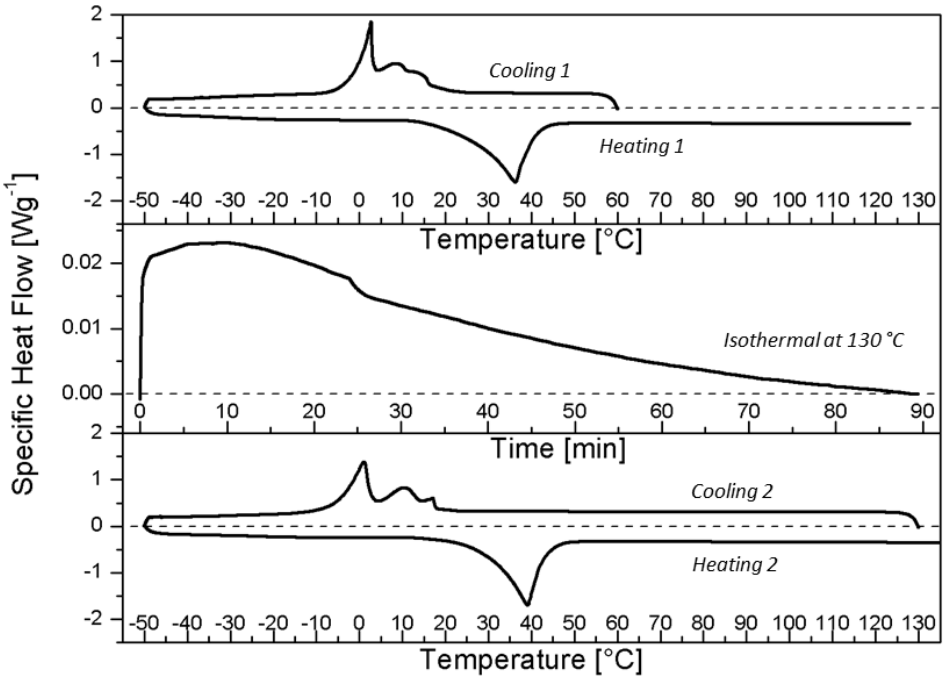


Figure 6.19 DSC traces for *70%r*, related to the thermal protocol used during time-resolved X-ray based morphological characterization and as depicted in Figure 3.2. Exothermic signals are plotted upwards. The program includes cooling 1 and heating 1 at 10 °C/min (top panel), isothermal curing at 130 °C for 90 min (middle panel), followed by cooling 2 and heating 2 at 10 °C/min (bottom panel).

6.7.1 ISOTHERMAL CURING KINETICS

The epoxy conversion as function of time at 130 °C for *70%r* is illustrated in Figure 6.20 and was calculated using equation 4.18 with ΔH_{prep} set to zero. For comparison, the *50%r* conversion curve is added to this Figure using a dashed line. No curing happened during the preceding heating run in *70%r*, implying that ΔH_h in equation 4.18 was also zero. The factor for ΔH_{max} was set to 0.3 (instead of 0.7), reflecting the epoxy resin fraction in the system. The conversion degree reached after 90 min at 130°C is 58%, implying gelation and arrest of the curing reaction concur (see section 3.1.1). The degree of polymerization should, however, be higher than for *90%r* for which a 36% conversion was calculated. Clearly, the curing rate of *70%r* is lower than of *50%r* as evidenced by the shallower slope of the conversion curve for *70%r*.

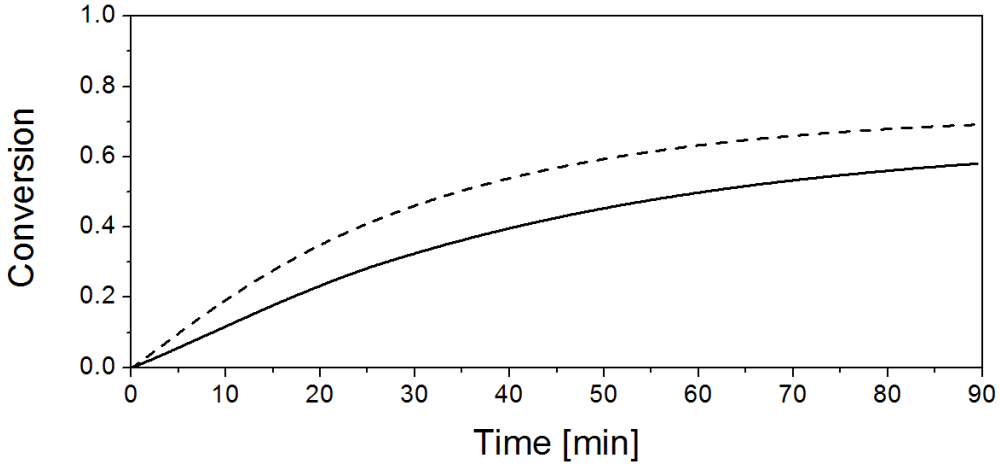


Figure 6.20 Epoxy conversion during isothermal curing at 130°C after heating at 10°C/min for *70%r* (full line) and *50%r* (dashed line).

6.8 THE X-RAY BASED MORPHOLOGY AND THERMAL BEHAVIOR OF *70%R* DURING COOLING AND HEATING PRIOR TO ISOTHERMAL CURING

70%r during cooling 1 exhibits 3 clear exothermic peaks with onsets at respectively 17°C, 12°C and 4°C, which is similar to *50%r* but at higher temperatures. However, this series of peaks is preceded by another, smaller event with an onset at 25°C, which in the Figure 6.21 DSC cooling 1 curve has been highlighted in orange, implying that it is governed by the PEO moieties. Indeed, the first reflections that become visible in the WAXD patterns during cooling 1 are due to well-ordered PEO crystallites with well resolved PEO (111) and (120) reflections at q = 1.33 $Å^{-1}$ and q = 1.36 $Å^{-1}$. These reflections are a signature for type 4 structures with crystalline stretched out PEO chains and are labelled 4 in Figure 6.21. The (weak) accompanying SAXS signals in Figure 6.22 are labelled likewise. The type 4 SAXS and WAXD signals remain present down to the lowest temperatures in the cooling 1 segment.

Type 4 structures are the most stable ones observed so far in Brij® S-20 epoxy blends, but were only formed during the heating 1 run by recrystallization from type 1 or type 3 structures in samples with Brij® S-20 contents below 70%. The preceding formation of other structural types seemed to be a prerequisite for type 4 nucleation, likely by facilitating the segregation of epoxy resin form the PEO microphases. In *70%r*, the epoxy concentration appears to be sufficiently low to allow for direct type 4 nucleation. However, concomitantly to type 4 structure formation, the epoxy concentration in the surrounding material increases by which the further spontaneous creation of type 4 structures is inhibited. Consequently, crystallization in *70%r* proceeds like in *50%r* by the kinetically favored formation of

type 1 and type 2 structures. This type of crystal nucleation is less resin inhibited because of the intrinsic incompatibility of the aliphatic segments with the resin and the already establish separation in the liquid state. The exothermic signals with onsets at 17 and 12°C are highlighted in blue in the Figures 6.21 and 6.22 and are respectively due to the formation of type 1 and type 2 structures. The associated WAXD reflections in the top panel of Figure 6.21 are rather weak compared to the clearly visible peaks in SAXS (Figure 6.22 top panel), suggesting that these layered (type 1) and stacked cylindrical (type 2) structures are only semicrystalline in the aliphatic segments.

In contrast to the type 4 signals, the WAXD and SAXS signals of the type 1 and type 2 structures do not remain down the lowest temperatures during cooling 1 but are replaced by type 3 signals in the temperature range of the exothermic peak with an onset at 4°C. This exothermic signal in the Figures 6.21 and 6.22 middle panels is highlighted in orange because type 3 structure formation involves folded chain PEO crystallization. The chain packing in type 3 structures is more disordered and leads lumped PEO (111) and (120) reflections. However, a faint split in those reflections remains because the well-resolved type 4 reflections are superimposed onto the lumped type 3 reflections at any time. The type 3 structure formation completely consumes the type 2 structures as all related WAXD (open orthorhombic) and SAXS (P6/mm) reflections have vanished prior to reaching -10°C. A very small amount of type 1 structures is left, which can be observed most clearly in the WAXD patterns. The area of the low temperature exothermic signal is very strong compared to in *50%r*. The incomplete conversion from type 2 and type 1 to type 3 structures during cooling 1 accounts for the small signal in *50%r*. For that sample the conversion continues during heating 2. Note that in Figure 6.21 only the strongest (110) orthorhombic reflection of type 1 structures could be highlighted in blue during cooling 1. The presumably present (200) reflection could not confidently be traced because of being too weak. A DSC baseline shift due to vitrification at the lowest temperatures cannot clearly be resolved for *70%r*, likely because of the low amount of resin.

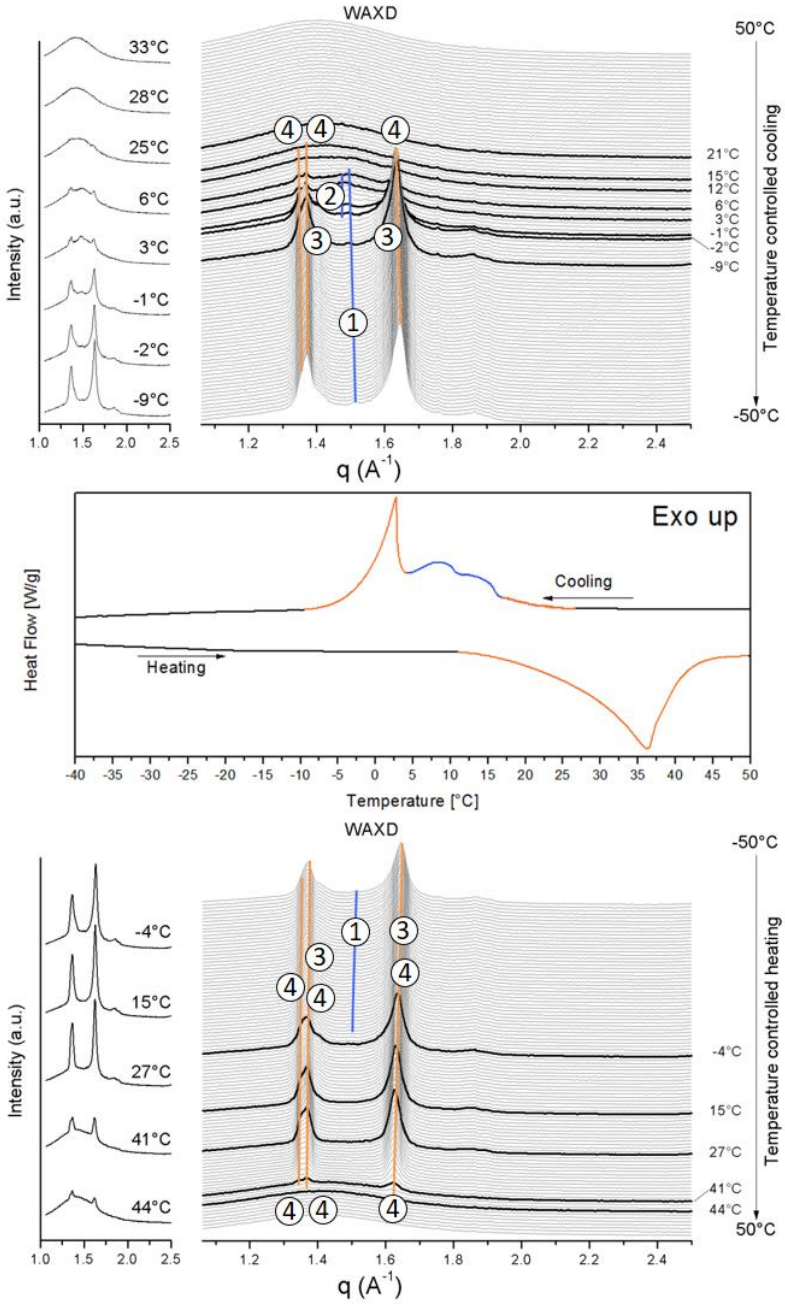


Figure 6.21 . For *70%r*. Top panel: Time resolved WAXD patterns collected during cooling 1. Middle panel: DSC curves during cooling 1 and heating 1. Bottom panel: Time resolved WAXD patterns during heating 1. Blue and orange features belong to transitions (in DSC) or reflections (in the WAXD patterns) of respectively the aliphatic and PEO moieties. The number labelling groups reflections that belong to the same structure type. The patterns highlighted in bold are displayed separately in the left side windows.

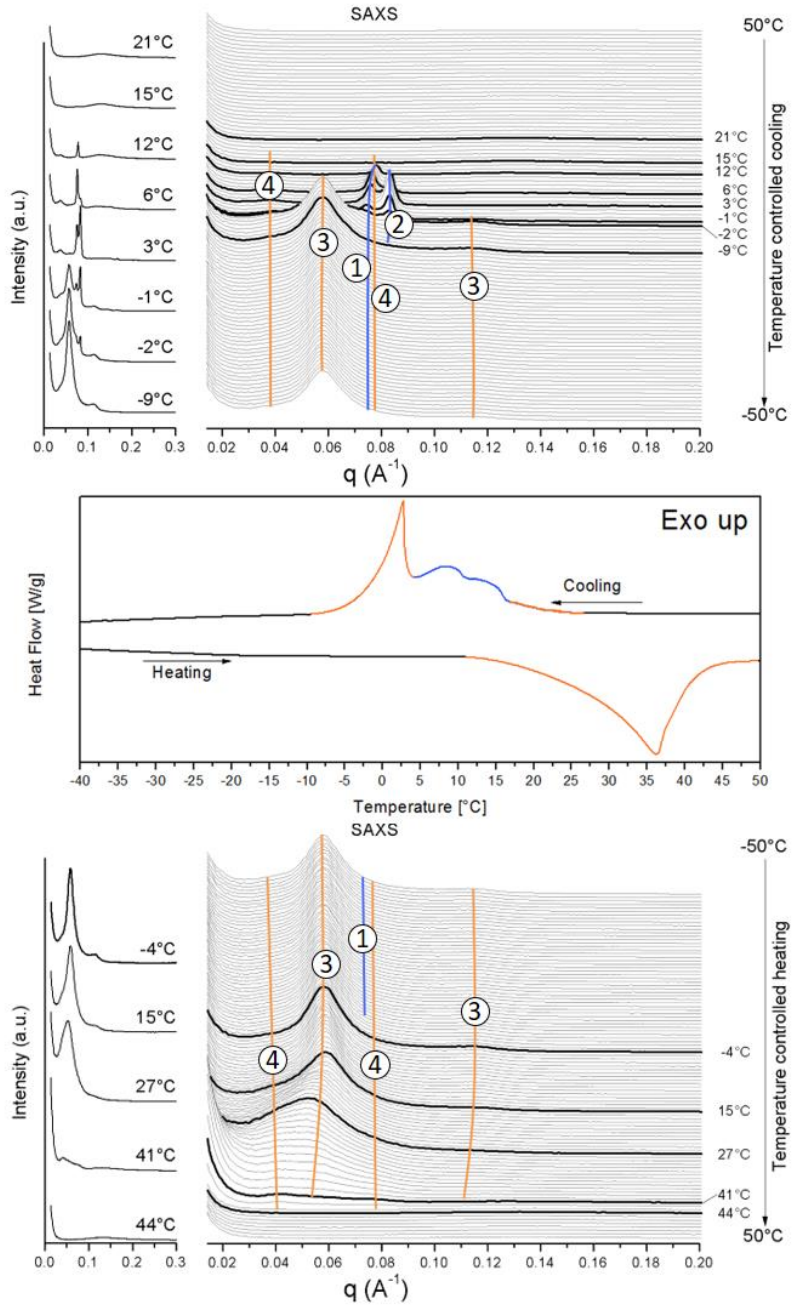


Figure 6.22 For *70%r*. Top panel: Time resolved SAXS patterns collected during cooling 1. Middle panel: DSC curves during cooling 1 and heating 1. Bottom panel: Time resolved SAXS patterns during heating 1. Blue and orange features belong to transitions (in DSC) or signals (in the SAXS patterns) of structures that are either aliphatic or PEO crystalline. The number labelling groups SAXS signals that belong to the same structure types as the labels indicate in Figure 6.16. The patterns highlighted in bold are displayed separately in the left side windows.

The SAXS pattern at -9°C, depicted in Figure 6.23 is representative for temperatures at which predominantly type 3 structures are present during cooling 1. This –9°C pattern was successfully interpreted in terms of equation 6.1, neglecting the small fraction of type 4 and type 1 structures. The SAXS pattern fitting involved the optimization of 10 parameters: $C, B, l_{1,1}, l_{2,1}, L_{P,1}, N_1, \sigma_{LP,1}, \beta_1, \sigma_{2/3,1}$ and the electron density of crystalline PEO, $\rho_{2,1}$. The interface between liquid aliphatic and crystalline PEO, was found to be sharp, i.e. $\sigma_{1/2,1} = 0$. The electron density of the central aliphatic liquid layer, $\rho_{1,1}$, was constrained at the value given by equation 4.10 and multiplication with 0.57 mole electrons/g. The epoxy density, $\rho_{3,1}$, was fixed at 0.67 mole electrons/cm^3, i.e. the value found for *20%r* at -9°C and shown in Figure 4.15. The electron density profiles associated with the stack and isolated shares are shown in the Figure 6.23 right side panel. Physical interpretations are provided in Figure 6.24. This picture also shows that 45% occurs as stacks and 55% as isolated type 3 bilayers. The cartoons are very similar to those of *30%r* in Figure 4.22 at -3°C during heating 1, except that the periodicity of the *70%r* stacks is half a PEO chain length shorter, likely because of the lower epoxy content in *70%r*. The number of layers in the stacks at -9°C, N_1, is 5, $L_{P,1}$ is 106 Å and $\sigma_{LP,1}$ is 11 Å. These data will be compared further below with the type 3 stack parameters of cured *70%r*.

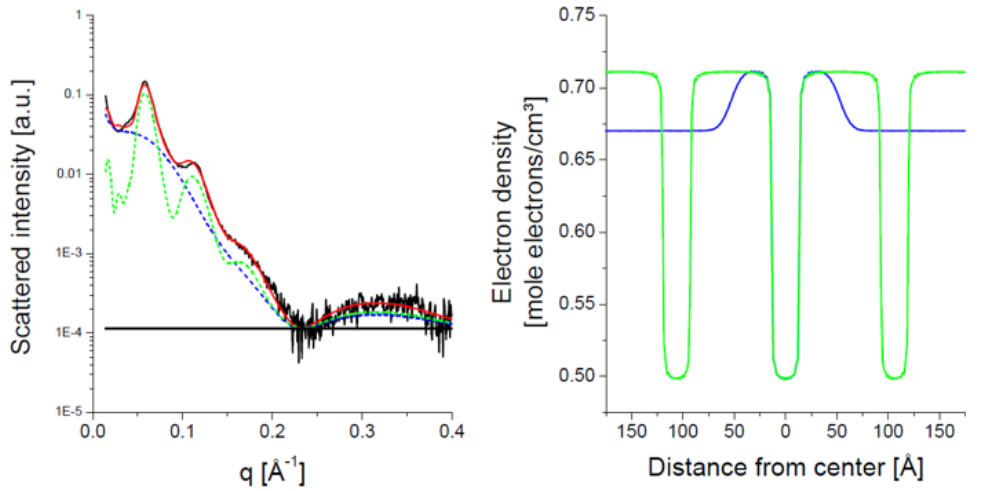


Figure 6.23 In the left side panel for *70%r* the experimental SAXS pattern (black) at -9°C during cooling 1, together with the fit according to equation 6.1 (red), the constant background (black horizontal line) and the shares due to stacked (green) and isolated type 3 layers (blue). In the right side panel: the corresponding electron density profiles for each share, using the same colors as the curves in the left side panel. Note that the central part of the blue electron density profile overlaps with and hence is covered by the green profile.

70%r during heating 1 produces a single, broad melting endotherm, which from low to high temperatures involves the melting of the remaining type 1 structures, type 3 structures and finally type 4 structures. The WAXD data in the Figure 6.21 bottom panel demonstrate that all type 1 structures have vanished when reaching 2°C. Based on the WAXD information a blue line was also drawn in the corresponding SAXS data of Figure 6.22, although the actual type 1 SAXS signals are barely visible. It cannot be excluded that the molten type 1 structures convert partly into type 3 structure, but this cannot be ascertained from the X-ray data. Upon further heating from about 25°C onwards the type 3 WAXD and SAXS signals weaken, reflecting type 3 PEO crystal melting. At the highest temperatures only the type 4 typical signals remain and ultimately by reaching 43°C also disappear because of complete melting. It seems that the type 4 signals do not gain intensity while the type 3 signals are disappearing. This differs from *40%r* and *50%r* in which the type 4 structures were only formed during heating 1 when the type 3 structures melted and reorganized. For *70%r* most, if not all of the type 4 structures were formed early on during cooling 1.

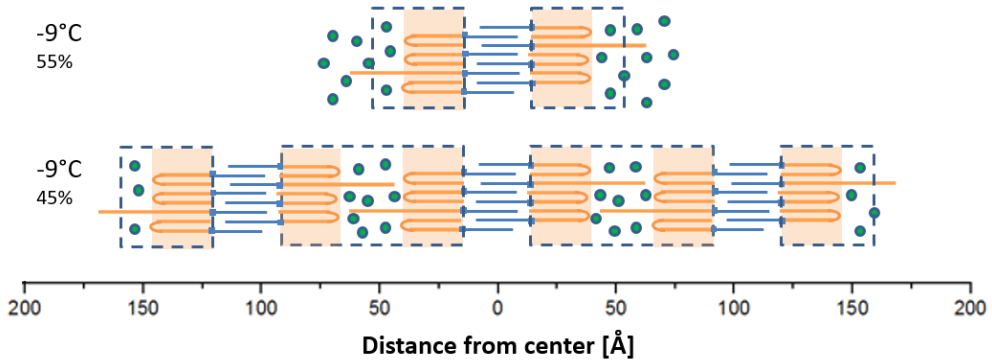


Figure 6.24: Representation of the possible structures within *70%r* at -9°C during the first cooling run at 10°C/min. The blue and orange lines correspond to stearyl and PEO chains respectively. The blue blocklets highlight the links between those moieties. Orange shaded areas indicate a PEO crystalline state. The greenish dots represent resin monomers. The structures as well as their indicated relative percentages are based on a modeling of the SAXS pattern.

6.9 THE THERMAL BEHAVIOR AND MORPHOLOGY OF *70%R* DURING COOLING AND HEATING AFTER ISOTHERMAL CURING

Given the low curing degree in *70%r*, the thermal behavior and morphology during cooling and heating after isothermal curing closely resembles the cooling and heating data prior to curing. The cooling 2 DSC run also displays tree major exothermic peaks, preceded by a weak exothermic signal at the highest temperatures. The assignment of the underlying transitions mirrors that of *70%r*

prior to curing although the X-ray data in the Figures 6.25 and 6.26 for cured *70%r* do not allow distinguishing the initial type 4 structure formation, suggesting that the amount of type 4 structures formed after curing is rather lower. Accordingly, no type 4 signals could be labelled in the Figures 6.25 and 6.26. Their creation can only be inferred from the DSC data. Another difference is that only type 3 structures are present at the lowest temperatures, implying that the conversion of type 2 and type 1 structures into type 3 structures is complete, whereas a small fraction of type 1 structures was left when cooled prior to curing.

Upon subsequent heating, a single broad endothermic signal is observed in DSC, due to type 3 structure melting. However, the WAXD data in Figure 6.26 reveal the presence of type 4 structures at the highest temperatures prior to the melting endotherm offset. Apparently an additional amount of type 4 structures is created during the heating run. No type 4 typical counterpart can be observed in the SAXS data, suggesting that the type 4 structures occur as isolated bilayers rather than as stacks. A type 4 label was added to the SAXS data, knowing about their presence via the WAXD data.

Finally, it is worth mentioning that curing has some effect on the actual type 3 morphology. In Figure 6.27 The SAXS pattern collected at 1°C during heating 2 is displayed together with an interpretation in terms of equation 6.1. The SAXS pattern fitting involved the optimization of 10 parameters: $B, l_{1,1}, l_{2,1}, L_{P,1}, N_1, \sigma_{LP,1}, \beta_1, \sigma_{2/3,1}$, the electron density of crystalline PEO, $\rho_{2,1}$, and of cured epoxy resin, $\rho_{3,1}$. The C parameter was taken from the fitting of *70%r* prior to curing at -9°C. The interface between liquid aliphatic and crystalline PEO, was sharp, i.e. $\sigma_{1/2,1} = 0$. The electron density of the central aliphatic liquid layer, $\rho_{1,1}$, was constrained at the value given by equation 4.10 and multiplication with 0.57 mole electrons/g. The electron density profiles associated with the stack and isolated shares are shown in the Figure 6.27 right side panel. Physical interpretations are provided in Figure 6.28, which also shows that 56% occurs as stacks and 44% as isolated type 3 bilayers. The number of bilayers in the stacks of cured *70%r* at 1°C, N_1, is 2 (compared to 5 prior to curing) and $\sigma_{LP,1}$ is 16 Å (compared to 11 Å prior to curing). Curing seems to induce a more even distribution of the bilayers over space with some of them being sufficiently close for scattering interference. This global disorder is reflected in the slightly higher $\sigma_{LP,1}$ value. The bilayer to bilayer distance, $L_{P,1}$ is 104 Å, which is very close to the 106 Å prior to curing.

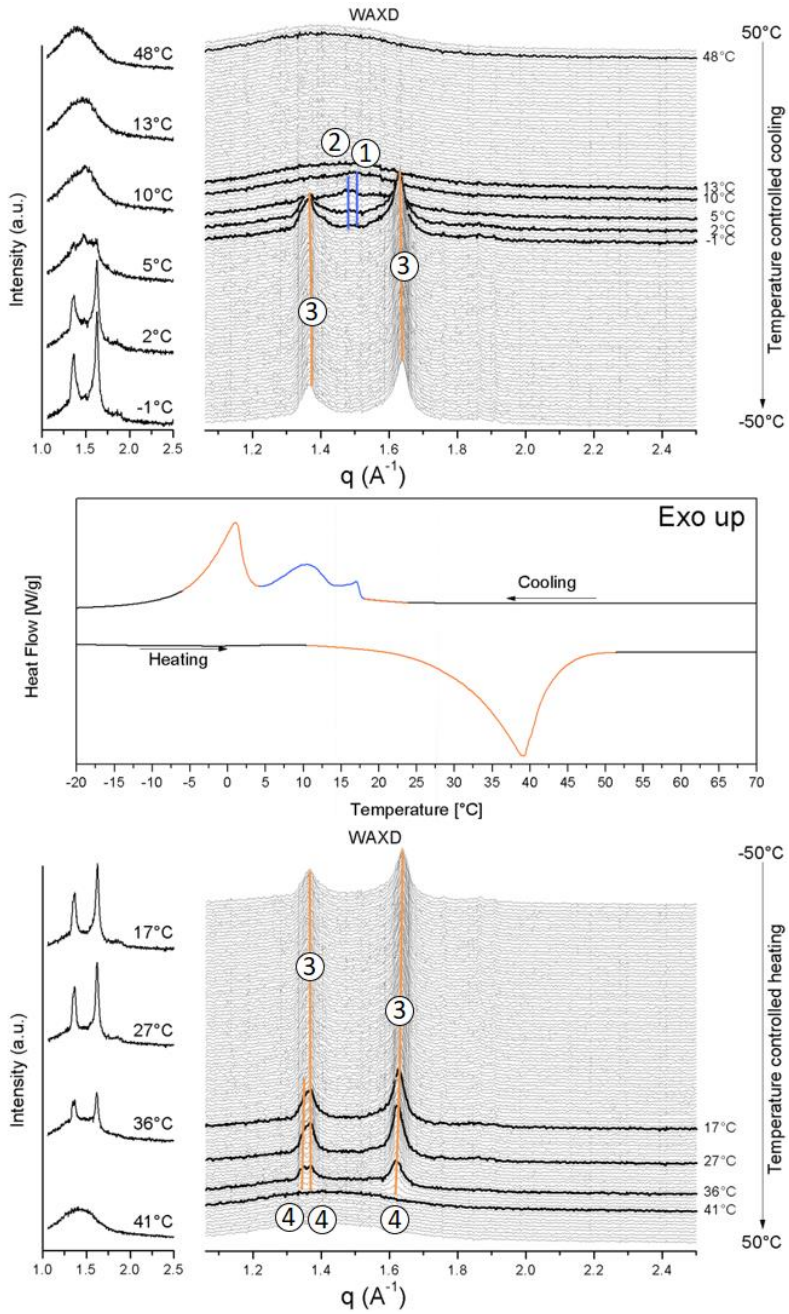


Figure 6.25. For *70%r*. Top panel: Time resolved WAXD patterns collected during cooling 2 after isothermal curing at 130°C. Middle panel: DSC curves during cooling 2 and heating 2. Bottom panel: Time resolved WAXD patterns during heating 2. Blue and orange features belong to transitions (in DSC) or reflections (in the WAXD patterns) of respectively the aliphatic and PEO moieties. The number labelling groups reflections that belong to the same structure type. The patterns highlighted in bold are displayed separately in the left side windows.

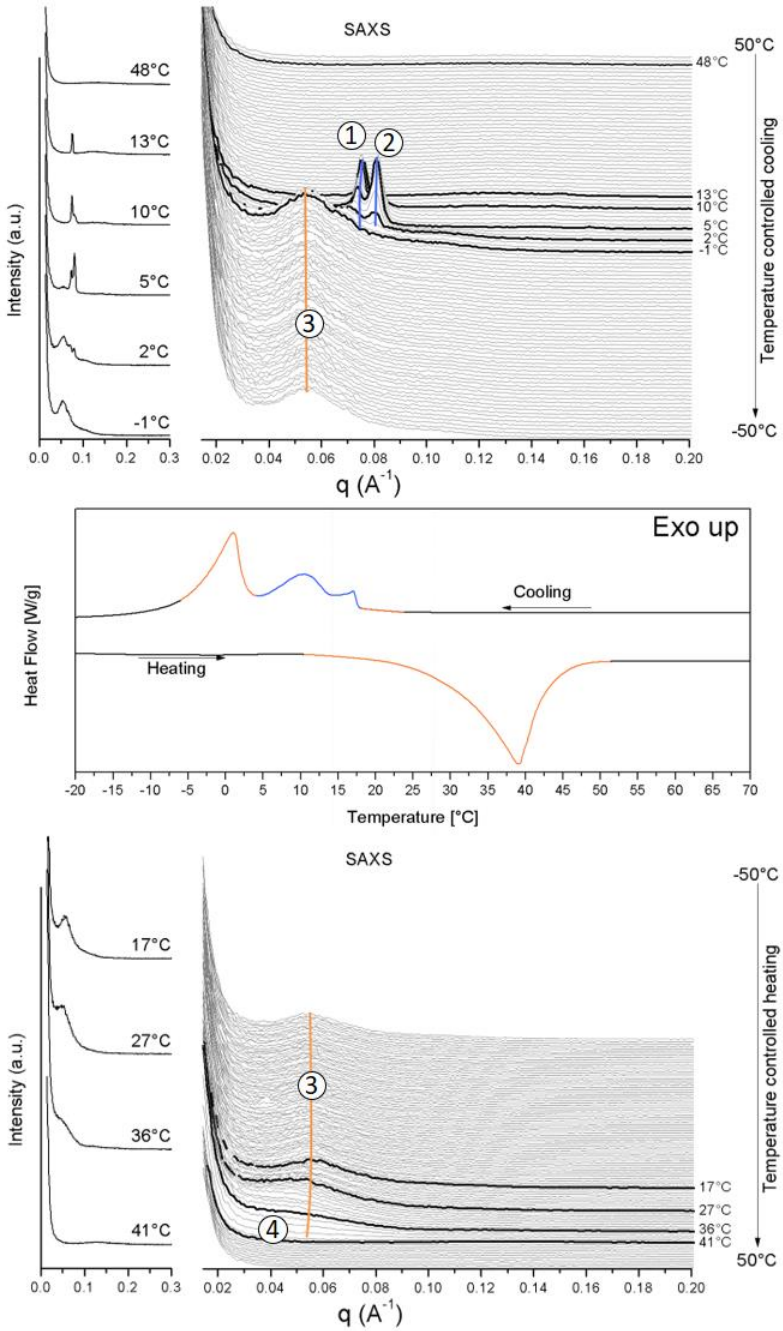


Figure 6.26 For *70%r*. Top panel: Time resolved SAXS patterns collected during cooling 2 after isothermal curing. Middle panel: DSC curves during cooling 2 and heating 2. Bottom panel: Time resolved SAXS patterns during heating 2. Blue and orange features belong to transitions (in DSC) or signals (in the SAXS patterns) of structures that are either aliphatic or PEO crystalline. The number labelling groups SAXS signals that belong to the same structure types as the labels indicate in Figure 6.16. The patterns highlighted in bold are displayed separately in the left side windows.

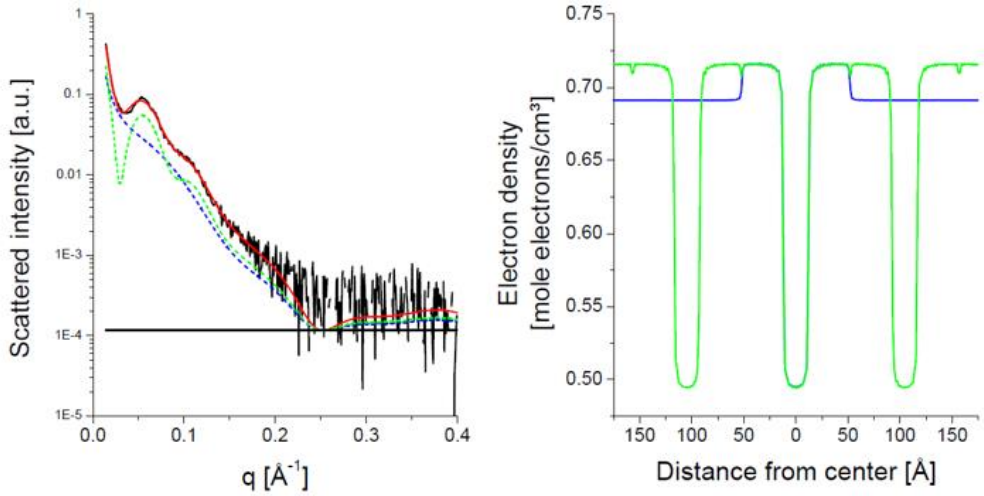


Figure 6.27 In the left side panel for *70%r* the experimental SAXS pattern (black) at 1°C during heating 2, together with the fit according to equation 6.1 (red), the constant background (black horizontal line) and the shares due to stacked (green) and isolated type 3 layers (blue). In the right side panel: the corresponding electron density profiles for each share, using the same colors as the curves in the left side panel. Note that the central part of the blue electron density profile overlaps with and hence is covered by the green profile.

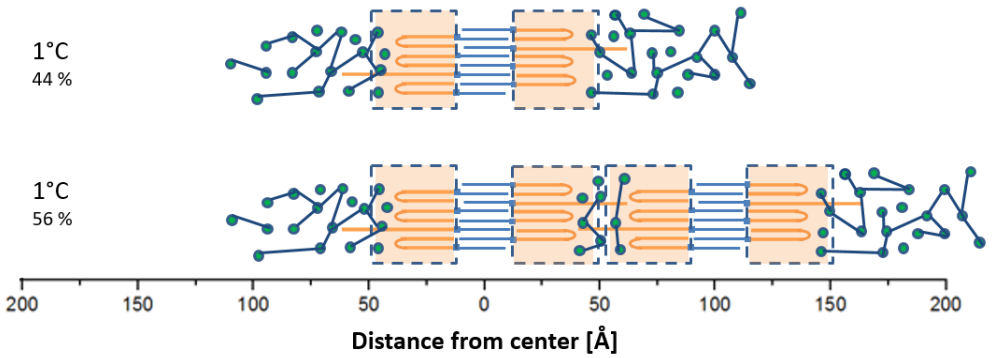


Figure 6.28: Representation of the possible structures within *70%r* at 1°C during the (second) heating run after isothermal curing and subsequent cooling at 10°C/min. The blue and orange lines correspond to stearyl and PEO chains respectively. The blue blocklets highlight the links between those moieties. Orange shaded areas indicate a PEO crystalline state. The greenish dots represent resin monomers. The structures as well as their indicated relative percentages are based on a modeling of the SAXS pattern.

The *70%r* TEM image in Figure 6.29 was taken after isothermal curing and cooling to room temperature. The PEO related dark parts reveal an increasing amount of unsystematically stacked layers, which can be interpreted as an intermediate morphology between on the one side *40%r* and *50%r* in which individual vesicles can

clearly be observed and on the other side *90%r* which solely contains stacked Brij® S-20 layers.

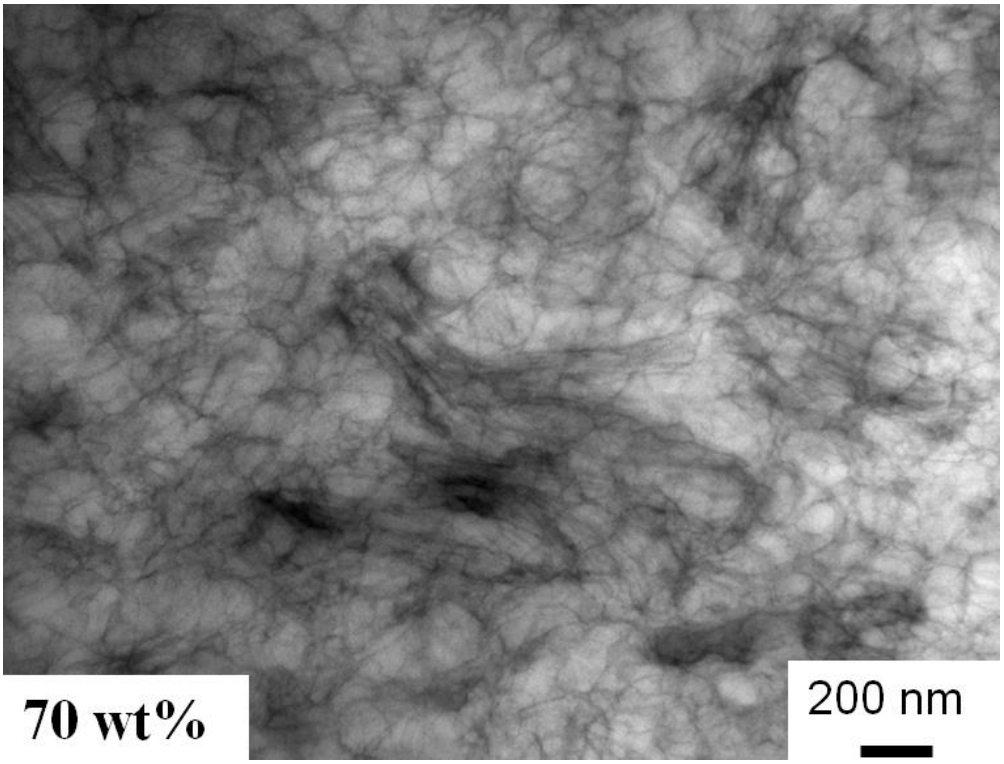


Figure 6.29: TEM picture of *70%r* after curing for 60 min at 130°C and cooling down to room temperature at 10°C/min where staining and sectioning took place.

Finally, it is worth mentioning that the interface between crystalline PEO and epoxy in type 3 structures is sharpened up after curing. This can be deduced for the blue electron density profiles in the Figures 6.27 (after curing) and 6.23 (prior to curing). A similar effect was described for *90%r* in Chapter 5 and attributed to a reduced compatibility of PEO with epoxy after curing.

6.10 SUMMARY AND CONCLUSIONS

In this chapter, the thermal behavior and morphology has been discussed of epoxy resins with 40, 50 and 70% Brij® S-20 while being subject to a standard thermal protocol. This protocol started at 60°C right after blending and involved cooling to -50°C, heating to 130°C, an isothermal epoxy resin curing step for 90 min at 130°C, cooling to -50°C and finally heating to the non-crystalline state. Cooling and heating rates were at 10°C/min. The discussion relied on DSC data gathered during the mentioned thermal protocol, combined with time resolved synchrotron WAXD and

SAXS to monitor the material morphology. TEM was used to image the material structure after curing at 130°C and cooling down to room temperature.

No detailed morphological analysis was performed of the high temperature liquid state. Relying on what is known for samples with very low Brij® S-20 content (see Chapter 4), it can be assumed that in *40%r*, *50%r* and *70%r* the stearyl moieties are microphase separated from the epoxy resin. The majority of Brij® S-20 is expected to be present as isolated or stacked bilayers, having a central aliphatic layer composed of interdigitated stearyl units and epoxy compatible PEO layers facing the epoxy matrix on both sides of the aliphatic layer. Likely, small fractions are assuming a cylindrical or worm like micellar morphology with the core and periphery made from respectively stearyl moieties and PEO chains.

Upon cooling from 60°C, the Brij® S-20 structures partially crystallize within the non-cured epoxy resin. Four different semicrystalline morphologies were detected in *40%r*, *50%r* and *70%r* of which the main characteristic can be summarized as follows:

Type 1 structures are Brij® S-20 bilayers with a central, orthorhombically crystalline aliphatic layer composed of interdigitating stearyl units. The PEO chains emanating on both sides of the central layer are facing and partially mixed with the epoxy resin. Such bilayers either occur isolated or in stacks.

Type 2 structures are composed of cylindrical micelles, stacked in a 2D hexagonal lattice with P6/mm symmetry. The aliphatic cores are crystalline, but the crystalline packing is less dense compared to in type 1 structures. The PEO chains, connected to the cylindrical core, radially spread out and mix with the epoxy resin. Likely, in both type 1 and type 2 structures, the aliphatic microphases are only partially crystalline.

Type 3 structures resemble the type 1 structures and can occur isolated or in stacks but rather than the interdigitated aliphatic microphases, the outer PEO layers are crystalline. In this structure the PEO chains are folded.

Type 4 structures are bilayers in which the aliphatic stearyl chains are not interdigitated but facing each other's ends in a double layer. The emanating PEO chains are stretched out on both sides of the bilayer and crystalline. The PEO chains are more orderly packed than in type 3 structures.

PEO crystallization, resulting in type 3 and type 4 structures seems problematic because it requires epoxy resin segregation from the PEO microphases. Only in *70%r*, a small fraction of type 4 structures is formed during the first cooling (cooling 1) at the highest temperatures and remains down to the lowest temperatures. During subsequent heating 1, type 4 structures melt at the highest temperature, implying

that of all structures they are thermodynamically most stable. In *50%r* and *40%r*, the resin concentration is too high for an efficient segregation by which type 4 crystallization does not occur during cooling 1. Instead, at a sufficiently high supercooling, the aliphatic microphases, which are fully segregated form the resin, crystallize. This leads to metastable type 1 and type 2 structures with the type 1 structures being more stable and forming at higher temperatures than type 2 structures. Also in *70%r* type 4 structure formation is followed by type 1 and at higher supercooling type 2 formation because the conversion to type 4 structures in *70%r* is arrested by the associated resin enrichment in the remaining non-crystalline PEO microphases.

The densification associated with the formation of type 1 and type 2 structures is believed to go along with a squeezing out of epoxy resin from the connected PEO microphases, by which PEO crystallization is facilitated. As a result, in *70%r* the type 2 structures during further cooling transform into type 3 structures. The transformation of the type 1 structures is incomplete and leaves a very small fraction of type 1 structures down to the lowest temperatures. In this transformation the aliphatic crystallinity is destroyed but the stearyl interdigitation is preserved, implying that the PEO chains need to fold to assume a crystalline density. Although the driving force for type 4 formation is larger, such structures do not form as this would require PEO chain stretching and the loss of aliphatic interdigitation. The transformation into type 3 structures is mechanistically and kinetically favored as this leaves the interdigitation intact. To create type 3 structures, it is conceivable that folded PEO chains crystallize while concomitantly destroying the aliphatic crystalline phase. For the creation of type 4 structures, the aliphatic crystals would have to melt first before stretched out PEO crystals could form.

The transformation of type 1 and type 2 structures to type 3 structures during cooling 1 is incomplete for *50%r* because it is interrupted by vitrification. In *40%r*, the T_g occurs at an even higher temperature because of the higher resin content. In the latter case, mobility restrictions prevent the transformation entirely. In *70%r*, vitrification happens at a very low temperature by which the transformation virtually runs to completion prior to when mobility restrictions appear.

During subsequent heating the transformation into type 3 structures in *50%r* resumes once the material has devitrified. In *40%r*, the transformation actually starts during heating. In both *40%r* and *50%r* the transformation runs to completion prior to reaching the temperatures at which type 1 and type 2 structures started forming in the preceding cooling run.

Very clearly, the transformation into type 3 structures actively destroys the aliphatic crystallinity. To the best of our knowledge such a phenomenon has not been

described in the literature before. It seems that this conversion happens more readily for type 2 structures than for type 1 structures since the former are fully converted first.

Upon further heating, the type 3 structures melt and partially reorganization into type 4 structures, which melt at very high temperatures. Type 4 structures are formed in both *40%r* and *50%r* during heating. For *70%r* it is not clear whether or not additional type 4 structures form during heating on top of the small fraction that was formed during cooling 1.

At higher temperatures in the liquid state, resin curing sets in and progresses with time during the isothermal stay at 130°C. The ultimate curing degree amounts to 68%, 69% and 58% for *40%r*, *50%r* and *70%r* respectively, implying a gelled matrix for all of the samples at the end of the curing process (albeit 70% is right at the border of the gel point) and the curing rate decreases with increasing Brij® S-20 content.

The lower the actual conversion, the less the thermal behavior and morphology during subsequent second cooling and heating deviates from what was observed during cooling and heating prior to resin curing. The only difference noted in *70%r* is that the type 1 to type 3 structural transformation actually runs to completion during cooling. In *40%r* and *50%r*, curing promotes the formation of type 1 structures and type 2 structures are no longer formed. Transformation from type 1 to type 3 structures happens only during subsequent heating in both *40%r* and *50%r* because curing leads to an upwards shift of the material T_g and mobility restrictions set in at rather high temperatures. During heating, the type 3 structures progressively melt and partially reorganize into type 4 structures, which ultimately melt at the highest temperatures.

Type 1 structures have been observed in all samples with Brij® S-20 concentrations between 20% and 70% whereas the most stable type 4 structures, which are prevailing in *90%r* (see chapter 5), gain importance towards higher Brij® S-20 concentrations. Others structural types occur transiently. Clearly, the phase behavior of epoxy Brij® S-20 blends is a complicated matter. Therefore, Chapter 7 is devoted to systematically comparing the structural transitions in the different samples as a function of the Brij® S-20 concentration. The curing characteristics are compared as well.

CHAPTER 7: THE CURING, THERMAL BEHAVIOR AND MORPHOLOGY OF EPOXY BRIJ® S-20 BLENDS AS FUNCTION OF THE BLEND COMPOSITION

The present chapter is devoted to summarizing and discussing the concentration dependent thermal behavior and morphology of epoxy Brij® S-20 blends during the thermal protocol as depicted in Figure 3.2. The data presented in the chapters 4, 5 and 6 are grouped in single graphs for comparison. Section 7.1 at first focusses on the concentration dependent resin curing and vitrification. Next, the Brij® S-20 crystallization is discussed in uncured and cured blends. Attention is paid to the impact of vitrification on the crystallization behavior. In section 7.2, the temperature and concentration dependent supramolecular organization of Brij® S-20 within the blends is summarized using morphology maps. These maps conclude section II.

7.1 RESIN CURING AND VITRIFICATION AS FUNCTION OF BRIJ® S-20 CONCENTRATION

7.1.1 RESIN CURING

In preceding chapters, the isothermal epoxy resin conversion while being at 130°C for 90 min was calculated from the exothermic resin curing heat, using concentration dependent forms of equation 4.18. The specific heat flow data and the related resin conversion of samples with 0, 20, 30, 40, 50, 70 and 90% Brij® S-20 are grouped in Figure 7.1. Very clearly, the exothermic signals in the Figure 7.1 top panel are larger for lower Brij® S-20 concentrations. This trend is expected as progressively less resin is present to cure. However, the bottom panel in Figure 7.1 demonstrates that in addition, the ultimate resin curing degree (conversion) decreases with increasing Brij® S-20 concentration. In previous chapters this effect was tentatively attributed to a separation of the resin reactants by the impenetrable aliphatic Brij® S-20 walls. In addition, one of the resin components might preferentially dissolve in the Brij® S-20 PEO moieties. The ultimate conversion after 90 min at 130°C decreases linearly (R = -0.98) with increasing Brij® S-20 concentration as illustrated in Figure 7.2.

In Chapter 4, it was demonstrated for *20%r* that the reduced curing kinetics compared to when no Brij® S-20 is present, is purely related to the resin dilution. Upon adding more Brij® S-20 physical entrapment of reacting species may also contribute to the rate reduction. Indeed, the curing rate decreases with increasing Brij® S-20 as can qualitatively be judged from the falling slopes in the Figure 7.1 conversion curves.

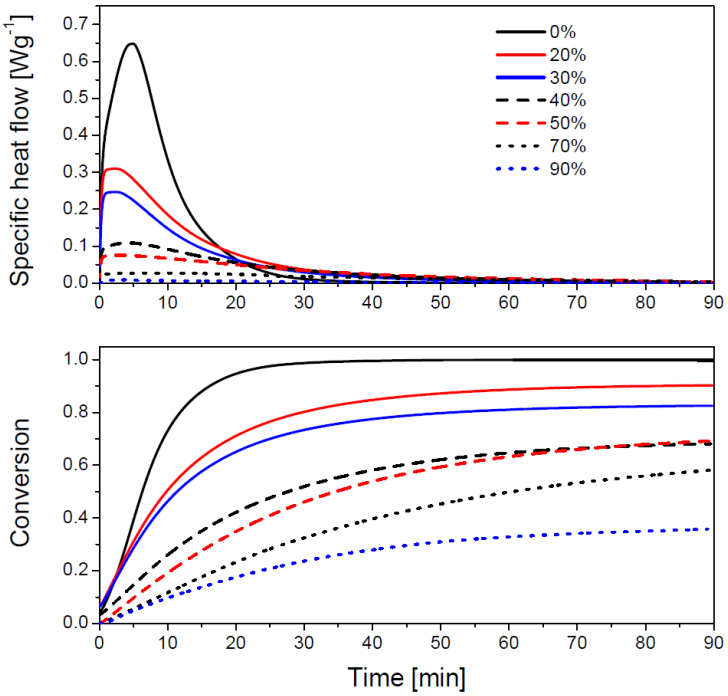


Figure 7.1: Upper panel: the specific heat flow associated with epoxy resin curing during 90 min at 130 °C for blends with the indicated Brij® S-20 concentrations (%). Bottom panel: Epoxy resin conversion for the same samples based on the heat flow data.

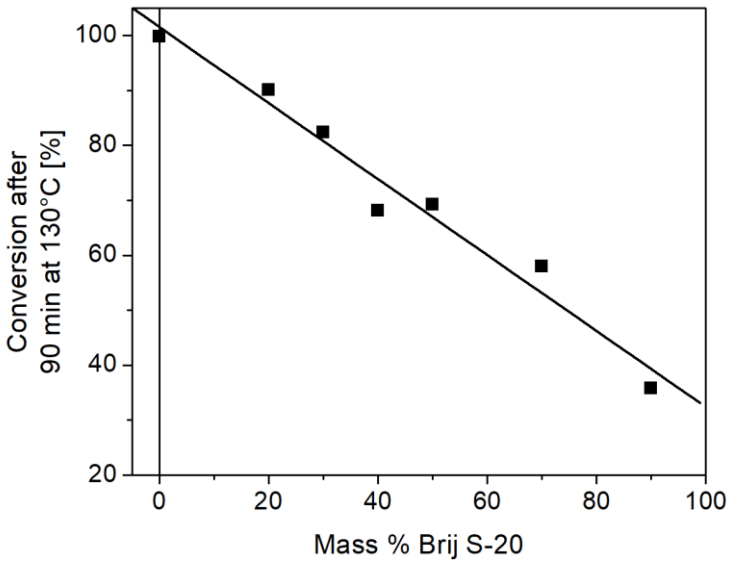


Figure 7.2: The final epoxy resin curing degree after 90 min at 130 °C as function of the Brij® S-20 concentrations (%) and a linear trend line (R = -0.98).

7.1.2 RESIN VITRIFICATION

When cooled to sufficiently low temperatures, epoxy resins vitrify. The glass transition temperature, T_g, depends on the curing degree, with higher conversions leading to higher T_g values. For the resin based on DGBA and MDA, Swier et al.[90] calculated the conversion, α, dependent glass transition temperature, $T_{g\alpha}$, from equation 7.1, with temperatures expressed in Kelvin:

$$ln(T_{g\alpha}) = \frac{(1-\alpha)ln(T_{g0})+K\alpha ln(T_{g\infty})}{(1-\alpha)+K\alpha} \quad \text{(Eq.7.1)}$$

$T_{g\infty}$ refers at the ultimate glass transition temperature of the pure resin after complete curing (α = 1), which has been reported to be 165 °C[89] or 175 °C[90]. T_{g0} refers at the glass transition temperature of unreacted resin (α = 0). The constant K is given by:

$$K = \lambda \frac{\Delta C_{p\infty}}{\Delta C_{p0}} = 0.58 \quad \text{(Eq.7.2)}$$

with $\Delta C_{p\infty}$ and ΔC_{p0} the heat capacity steps at the glass transition of respectively fully cured and uncured resin. λ equals 1 in the present stoichiometric case[90].

Using 170°C for $T_{g\infty}$ (i.e. the average value of the mentioned literature values[89,90]) and -17 °C for T_{g0} (the measured value for uncured epoxy) it is possible to calculate $T_{g\alpha}$ for the resin conversions in the different blends reached after 90 min at 130°C . These values can be found next to the ordinate of Figure 7.3 using large open squares on the 0% Brij® S-20 axis. The $T_{g\alpha}$ values for 90%, 82%, 58% and 36% conversion are related to respectively *20%r*, *30%r*, *70%r* and *90%r*. The $T_{g\alpha}$ for a conversion of 68% counts for both *40%r* and *50%r*, given that the ultimate conversions of these samples were rather identical (68% and 69% respectively). Values for $T_{g\infty}$ (100%) and T_{g0} (0%) are also included in Figure 7.3.

In the present blends, the PEO moieties are epoxy resin compatible while the stearyl chains are not. When mixed with the resin, PEO with its own characteristic glass transition temperature, $T_{g,PEO}$, may act as a plasticizer and lower the blend T_g, $T_{g,blend}$. $T_{g,blend}$ can be calculated using the Fox equation (temperatures are in Kelvin):

$$\frac{1}{T_{g,blend}} = \frac{W_{PEO}}{T_{g,PEO}} + \frac{(1-W_{PEO})}{T_{g\alpha}} \quad \text{(Eq. 7.3)}$$

W_{PEO} and $(1 - W_{PEO})$ represent the PEO and epoxy resin weight fraction in a binary PEO/epoxy system. When starting from the Brij® S-20 fraction and assuming that the stearyl units are fully demixed and not contributing to $T_{g,blend}$ one can calculate W_{PEO} as follows:

$$W_{PEO} = \frac{0.78W_{Brij}}{(1-W_{Brij})+0.78W_{Brij}} \quad \text{(Eq. 7.4)}$$

with W_{brij} and $(1 - W_{Brij})$ being the Brij® S-20 and epoxy resin mass fractions in the blend. The factor 0.78 represents the mass fraction PEO within Brij® S-20, assuming 20 ethylene oxide monomeric units in each molecule. Using the equations 7.3 and 7.4, $T_{g,blend}$ values were calculated as function of the Brij® S-20 percentage for each of the blend specific resin conversions. These curves are represented in Figure 7.3 using grey dotted lines. The curve for 0% conversion is drawn using a full grey line. $T_{g,PEO}$ was empirically determined by imposing that the calculated $T_{g,blend}$ should coincide with the experimental values for cured *20%r* and *30%r*. To find $T_{g,PEO}$ the squared difference between the experimental and calculated values was minimized using the Excel solver. This approach yielded a value for $T_{g,PEO}$ of -95.5 °C. This point is indicated in Figure 7.3 using a black, large open circle at the 100% Brij® S-20 coordinate. This value is much lower than the literature T_g value of -67°C for high molecular weight PEO[112] as expected for a PEO moiety of only 20 units. However, rather unexpectedly, the empirical value is lower than the literature T_g value of -83.1°C for PEO with 17 units (PEG-800)[113]. Clearly, existing literature values cannot easily be extrapolated to the present situation in which the PEO chain are connected to the aliphatic microphases. Therefore, the empirical method was preferred.

The open stars in Figure 7.3 represent the experimental $T_{g,blend}$ values for the cured blends. The closed stars are the experimental $T_{g,blend}$ values of the uncured samples in this study. $T_{g,blend}$ could not reliably be determined in samples with more than 50% Brij® S-20, because of the low resin content and the associated weak DSC vitrification signal. Logically, the dotted lines for the 90% and 82% conversions tend to intersect the *20%r* and *30%r* open stars, as this was imposed by the constraint in the analysis. The dashed grey line was obtained by connecting the points with coordinates given by blend composition and the value in the dotted line curves at the blend specific resin conversion.

The full and dashed grey lines in Figure 7.3 represent the expected $T_{g,blend}$ evolution in absence of Brij® S-20 crystallization for respectively uncured and cured blends. Clearly, the experimental $T_{g,blend}$ values for the uncured blends (filled stars) deviate positively from the full grey line, pointing at crystallization interference (see also section 7.1.3). The dashed line rather closely follows the experimental $T_{g,blend}$ blend values (open stars). This is expected for cured *20%r* and *30%r* because indeed Brij® S-20 crystallization does not interfere (see Chapter 4 and section 7.1.4). Therefore, these experimental $T_{g,blend}$ values were used as boundary condition. However, the dashed curve also approaches the experimental $T_{g,blend}$ for cured

40%r and *50%r* although crystallization in those cases does interfere (see Chapter 6 and section 7.1.4).

7.1.3 BRIJ® S-20 CRYSTALLIZATION AND RESIN VITRIFICATION IN UNCURED BLENDS

An overview of the different crystalline Brij® S-20 structures has been given in the Chapter 6 conclusion section. The crystallization into type 4 structures involves the packing of extended PEO chains and a concomitant full segregation of the epoxy resin. Type 4 structures have the highest melting point and once formed during cooling do not transform into any of the other identified structures during further cooling. On these grounds type 4 structures can be considered as the stable ones below the concentration dependent type 4 melting point. Other structures are metastable. The type 4 DSC melting offset temperatures for the uncured systems, extracted from the DSC experiments discussed in the Chapters 5 and 6, are represented using a red full line (without symbols) in Figure 7.3.

In pure Brij® S-20 and *90%r*, type 4 structures are prevailing (Chapter 5). During cooling 1 only a small fraction of type 4 structures is formed in *70%r* at the highest temperatures and no such structures appear at even lower Brij® S-20 concentrations (Chapter 6 and 4). Cooling 1 refers at cooling form 60°C down to -50°C at 10°C/min while the blend sample is in the uncured state (see Figure 3.2). In Figure 7.3 the type 4 crystallization onset temperatures are indicated with (red full line connected) red full diamonds. For *90%r*, the symbol is hidden behind the open red diamond. In contrast to the crystallization onset line, the type 4 melting offset line stretches down to 40% Brij® S-20 because type 4 structures form and melt in *50%r* and *40%r* during heating 1, i.e. the heating run subsequent to cooling 1 (see Figure 3.2).

Upon melting the type 4 structures, the epoxy resin remixes with the PEO moieties. This process leads to an extra entropy gain on top of the PEO disordering and is larger for higher epoxy resin concentrations because the PEO moieties are accepting more resin at higher resin concentrations. A larger entropy change, ΔS, leads to a lower melting point, T_m, given the relation $T_m = \Delta H/\Delta S$, with ΔH, the enthalpy change associated with melting. This effect qualitatively explains the observed type 4 melting offset depression with decreasing Brij® S-20 concentration in Figure 7.3 (red full line).

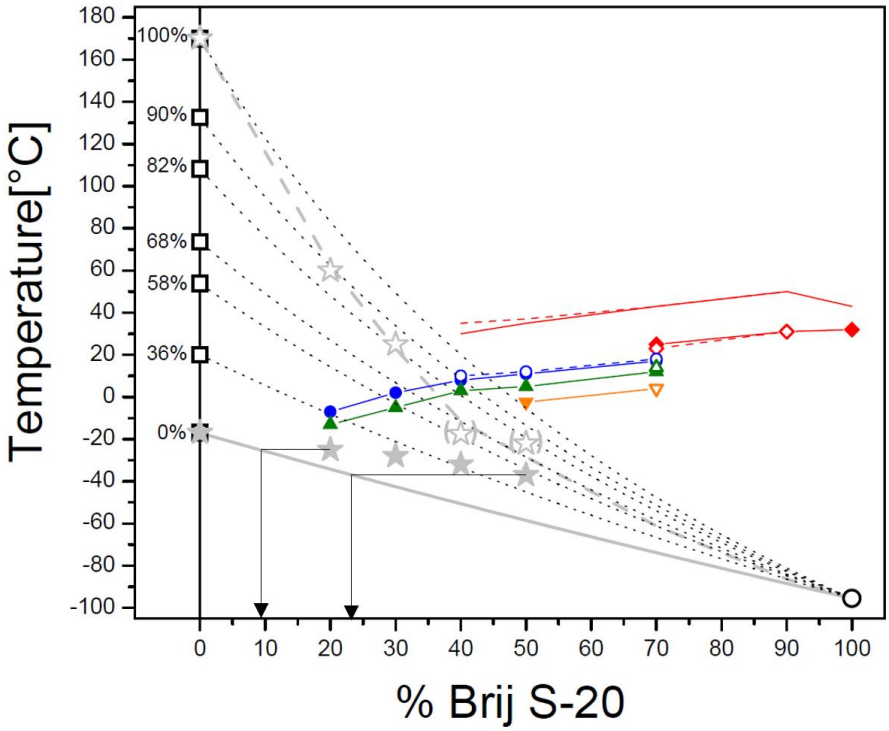


Figure 7.3: Calculated $T_{g\alpha}$ values for pure epoxy resin at the indicated conversions (open black squares); the estimated $T_{g,PEO}$ for PEO in Brij® S-20 (open black circle); theoretical $T_{g,blend}$ values for binary epoxy - Brij® S-20 systems as function of the Brij® S-20 % for each of the resin conversions (full grey curve for a 0% conversion and grey dotted curves for the other conversions); Experimental T_g values for the blends with uncured resin (full grey stars) and for the blends after curing for 90 min at 130°C (open grey stars – the points for *40%r* and *50%r* are put between brackets because these values are merely estimates); crystallization onset temperatures for type 1 structures for blends with uncured epoxy resin (closed blue circles connected using blue lines) and for blends with cured resin (open blue circles connected with dashed blue lines); crystallization onset temperatures of type 2 structures for blends with uncured epoxy resin (closed green triangles connected with green lines) and for blends with cured resin (open green triangles connected with dashed green lines); onset temperatures for the conversion from type 1 and type 2 structures to type 3 structures for blends with uncured epoxy resin (closed down orange triangles connected with orange line) and for the *70%r* with cured resin (open down orange triangle); crystallization onset temperatures of type 4 structures for blends with uncured epoxy resin or without resin for *100%r* (closed red diamonds connected with red lines) and for blends with cured resin (open red diamonds connected with a dashed red line); melting offset temperatures for type 4 structures for blends with uncured resin or without resin for *100%r* (red full line) and for blends with cured resin (red dashed line). Arrows are explained in the text.

Note, however, that the type 4 melting offset for pure Brij® S-20 (Figure 7.3) occurs at a *lower* temperature than the offset of *90%r*, although on entropic grounds a melting point depression for *90%r* is expected. This suggests that the epoxy resin –

PEO mixing is endothermic. This would rise the melting enthalpy and hence also the melting point, given the relation $T_m = \Delta H/\Delta S$.

However, If the mixing of PEO with epoxy resin would be endothermic, a phase behavior with an upper critical solution temperature (UCST) for PEO / epoxy resin systems would be expected. No hints for such a behavior could be found in the literature, which invariably suggests full miscibility in the liquid state[114,115]. Alternatively, the positive mixing enthalpy in the present Brij® S-20 case might be related to the connected aliphatic microphases, which remain separated from the PEO / epoxy resin phases throughout the melting process. The PEO chains should spatially separate to accept epoxy resin, which is not easily accomplished with the stearyl chains facing each other in the type 4 typical bilayers. Adopting an interdigitated configuration does allow PEO chain separation and epoxy resin accommodation. This process towards interdigitation might be endothermic. Furthermore, as in pure Brij® S-20 no epoxy resin is present to mix with the PEO moieties at melting, it is plausible that type 4 like, non-interdigitated structures remain in the liquid state. Therefore, the melting of type 4 *90%r* and pure Brij® S-20 might proceed to a different liquid state, which affects melting point relationships. In support of this statement it is relevant to mention that the liquid state SAXS pattern for pure Brij® S-20 at 43°C (see Figure 5.2) displays a clear maximum at approximately q = 0.05 Å, which might indicate type 4 like melt structures. Such a low angle SAXS maximum is not present in the *90%r* liquid state (Figure 5.8, the SAXS pattern at 49°C). These hypotheses require further investigation.

At the type 4 crystallization onset, the liquid structure is identical to at the melting offset. The temperature difference between this offset line and the type 4 crystallization onset temperatures represents the supercooling of type 4 structure formation, which for *90%r* is 19°C and for *70%r* 18°C. Assuming a similar supercooling for *50%r* and *40%* leads to type 4 crystallization onsets slightly above the experimentally observed type 1 crystallization onsets (the curve with the blue filled spheres in Figure 7.3). No type 4 crystallization is, however, observed for these samples during cooling 1, likely as a result of inefficient type 4 nucleation. Upon cooling to sufficiently low temperatures, the more easily nucleating, metastable type 1 and type 2 structures form instead. In these transitions, the melt typical aliphatic separation and interdigitated chain conformation are largely preserved in contrast to when type 4 structures are formed from such a melt.

The curves with the blue and green filled symbols in Figure 7.3 represent the DSC based crystallization onset temperatures for respectively type 1 and type 2 structures during cooling 1. Formation of Brij® S-20 type 1 and type 2 structures involves crystallization of the aliphatic moieties, which are fully separated from the

epoxy resin already in the liquid state. If crystallization within the aliphatic microphases would happen strictly independent from the connected PEO regions (which are mixed with the epoxy resin), there would be no dependence on the Brij® S-20 concentration. However, a type 1 and type 2 crystallization onset temperature depression is clearly observed with decreasing Brij® S-20 concentration. Rather than to a partial miscibility of the aliphatic moieties with the epoxy resin, this effect is believed to be due to the necessity of squeezing out epoxy resin from the connected PEO zones to allow for the aliphatic densification associated with crystallization. This concomitant demixing in the connected PEO microphases leads to an increased entropy reduction at crystallization. Vice versa, upon melting the type 1 and type 2 structures at their respective T_m, the epoxy resin remixes with the reopened PEO microphase, by which an extra entropy gain on top of that of the aliphatic disordering is realized. This remixing contribution is larger for higher epoxy resin concentrations. A larger entropy change, ΔS, leads to a lower T_m, given the relation $T_m = \Delta H/\Delta S$. The melting point depression with increasing resin concentration translates into the observed crystallization temperature depression for type 1 and type 2 structures because crystallization requires a certain supercooling below T_m to induce crystal nucleation.

Since aliphatic crystallization induces a demixing of PEO from the epoxy resin, the resin plasticization by PEO decreases compared to when no crystallization would have occurred. Hence, the crystallization of type 1 and type 2 structures induces the upward shift of the $T_{g,blend}$ values (full stars in Figure 7.3) from the values expected for a fully mixed, non-crystalline state (full grey curve in Figure 7.3). In fact, the experimental $T_{g,blend}$ values allow estimating the nominal Brij® S-20 concentration within the vitrified resin. The horizontal lines connected to the arrows on the Brij® S-20 concentration axis indicate that these concentrations fall roughly between 10 and 20%, with the low and high side of this range corresponding to samples with low (*20%r*) and high (*50%r*) Brij® S-20 content. In this context it is relevant to mention that in fact also a blend with 10% Brij® S-20 was made and thermally analyzed. This material remained non-crystalline during cooling 1. This is to be expected, since extrapolations of the type 1 and type 2 crystallization onset lines down to this Brij® S-20 concentration intersect the full, grey $T_{g,blend}$ line, where structural developments are prohibited by a lack of molecular mobility.

At lower temperatures during cooling 1, part of the type 1 and type 2 structures in *50%r* and *70%r* transforms into more stable, but still metastable type 3 structures. The orange full triangles in Figure 7.3 represent the estimated onsets of this event (note that the full triangle for *70%r* is hidden behind the open orange triangle). Type 3 structure formation involves PEO folded chain crystallization and disruption of type 1 and type 2 aliphatic crystallites. The transformation into type 3 structures is

mechanistically and kinetically favored above type 4 structure formation as type 3 structures leave the chain interdigitation intact (chapter 6). From type 3 structures, type 4 structures might eventually form in the subsequent heating run at the highest temperatures by a melting and recrystallization process during which the PEO chains stretch out and the chain interdigitation is broken up.

This transformation into type 3 structures during cooling 1 requires a full resin segregation and is only happening (partially) for *50%r* and *70%r* because the resin concentration in the PEO microphases at these compositions after the type 1 and type 2 crystallization is sufficiently low to allow for PEO crystal nucleation. Once type 3 structures start forming, the remaining non-crystalline PEO receives more epoxy resin by which the further conversion is postponed to lower temperatures. A higher resin concentration induces a more pronounced depression of the type 3 transition temperature.

In *70%r*, the transformation virtually runs to completion prior to vitrification. Theoretically, when all PEO would arrive in the crystalline state, the epoxy resin should be pure and display a T_g at -17°C. For *70%r* no clear T_g could be detected in DSC because of the low resin content and potentially also the width of the signal. In any case, the resin T_g in *70%r* is expected to occur above the experimental $T_{g,blend}$ values of the materials with a lower Brij® S-20 concentration because of extensive PEO crystallization and resin deplasticization.

The transformation into type 3 structures for *50%r* occurs at lower temperatures than for *70%r* and is arrested by vitrification. For *40%r, 30%r* and *20%r*, the resin concentration in the PEO phases remains rather high after type 1 or type 2 crystallization. In those cases the strongly depressed type 3 structure formation during cooling 1 is fully prevented by vitrification.

Recall that type 3 formation for *50%r* resumes shortly after having surpassed the experimental $T_{g,blend}$ during heating 1 (Chapter 6). Type 3 structures are also formed during heating 1 in *40%r* (Chapter 6) and *30%r* (Chapter 5). This indicates that type 3 structure formation during cooling 1 is prevented by inefficient PEO crystal nucleation rather than by a thermodynamic depression of the transition temperature to below $T_{g,blend}$. In many system the densification induced by cooling to below T_g facilitates crystal nucleation during a subsequent heating run. This effect seems to apply also in the present case.

A final remark in this section concerns the vitrification of the PEO enriched microphases. When the resin segregates from the PEO microphases as result of aliphatic crystallization, and as far as PEO does not crystallize upon cooling, the PEO enriched microphases are expected to vitrify below the calculated $T_{g,blend}$ for the

fully mixed state (full grey line in Figure 7.3). As no traces of a second, low temperature T_g were found in the temperature range down to -50°C (i.e. the lowest temperature in the DSC experiment, see Figure 3.2), it must be that the PEO concentration in the PEO enriched phases (W_{PEO}) exceeds 35%. The latter value is based on equation 7.3 with -50°C for $T_{g,blend}$, -95.5°C for $T_{g,PEO}$ and -17°C for , $T_{g\alpha}$.

7.1.4 BRIJ® S-20 CRYSTALLIZATION AND RESIN VITRIFICATION IN CURED BLENDS

This section concerns the structural transitions as a result of Brij® S-20 crystallization during cooling 2. Cooling 2 is the cooling at 10°C/min down to -50°C after 90 min resin curing at 130°C (Figure 3.2). The resin conversion (section 7.1) and subsequent vitrification (section 7.3) depend on the Brij® S-20 concentration. The $T_{g,blend}$ values expected in absence of Brij® S-20 crystallization, are represented by the dashed line grey curve in Figure 7.3. Very clearly, curing lifts up the expected $T_{g,blend}$ compared to when no curing has taken place (the grey full curve in Figure 7.3). The $T_{g,blend}$ elevation is most pronounced at low Brij® S-20 concentrations where the conversion is the highest. The crystallization related thermal transitions identified in the cured blends are represented using the same color code as for the uncured blends in Figure 7.3 but the symbols are open and the connecting lines are dashed.

The transitions for cured *90%r* and *70%r* do not differ from those found prior to curing. The low impact of curing is not unexpected, given the low resin conversion for these samples.

In cured *50%r* only type 1 structures are formed during cooling 2. In chapter 6, the lack of type 2 structure formation in cured *40%r* and *50%r* has been related to the absence of cylindrical Brij® S-20 micelles in the liquid state. Resin curing lowers its compatibility with PEO (Chapter 4). Therefore, pronounced resin swelling of the PEO microphases seems to be no longer possible when the conversion is high. As the formation of cylindrical micelles implies a high amount of resin within the PEO microphases, these structures no longer occur. Apparently, resin swelling is less restrictive for vesicular micelles. In cured *70%r*, type 2 structures are formed, implying that the curing degree should be higher than 60% to exclude cylindrical micelles. In cured *50%r*, also no (partial) conversion into type 3 structures is observed. In chapter 6 it was reported that the conversion into type 3 structures most straightforwardly happens from type 2 structures. As the latter are absent, no type 3 structures are formed during cooling 2 in cured *50%r*. Such structures do form during subsequent heating (heating 2) while consuming the type 1 structures. At even higher temperatures during heating 2, type 4 structures are formed, just like in the uncured case.

In cured *50%r* as well as in *40%r* the lifted resin T_g seems to not hinder the full development of type 1 structures. Just like for *50%r*, type 1 structures are the only ones formed in *40%r* during cooling 2. Upon heating, type 3 and type 4 structures are formed. Interestingly, the type 4 melting offset for cured *40%r* occurs at a higher temperature than for the uncured case. In Figure 7.3, the dashed red line at this point is situated above the red full line. This reduced melting point depression might be related to a lower degree of (re)mixing with the cured epoxy resin once the resin conversion is sufficiently high.

The strongly increased $T_{g,blend}$ to above the Brij® S-20 crystallization and melting temperatures, prevents any structure formation in cured *20%r* and *30%r*.

The experimental $T_{g,blend}$ values (bracketed open stars) for cured *40%r* and *50%r* approach the $T_{g,blend}$ values for the case Brij® S-20 would not crystallize (dashed grey line). In fact, the experimental $T_{g,blend}$ values are expected to occur above the calculated values because of type 1 crystallization and the associated deplasticization effect. Note that in these cases the curing degree is too low to induce gelation and that consequently, crystallization induced segregation should be possible. To our opinion experimental $T_{g,blend}$ for cured *40%r* and *50%r* cannot very reliably be extracted because the crystallization and melting trajectories link up with the broad vitrification range. Therefore, the experimental values in Figure 7.3 are put between brackets.

7.2 CONCENTRATION-TEMPERATURE MORPHOLOGY MAPS

Based on a combination of DSC and X-ray data, morphology maps have been created for the cooling and heating runs in the uncured (cooling 1 and heating 1) and cured (cooling 2 and heating 2) states. These maps should not be interpreted as phase diagrams. They merely summarize the different possible structures in the liquid and semicrystalline (type 1 to type 4) state and temperatures at which the structures start to convert to another. The different structures are represented by small, SAXS analysis based cartoons. In addition, the semicrystalline structures are labelled from 1 to 4 according to the structural type as defined in chapter 6. Liquid structures are not labelled. DSC and X-ray based estimates of crystallization and melting onset temperatures are indicated with horizontal full lines. The experimental T_g values (based on the DSC trace inflection points) are indicated as well. A transition always occurs from one structure to another. The structures involved at a given transition are connected with arrows. If the transition is complete, the arrow is drawn using a full line. When the transition it is only partial, a dashed arrow is used. Each type of transition is represented by a different color for the horizontal line and the

associated arrow. If a transition is expected to occur via melting and recrystallization process, the transient liquid state cartoon is depicted on top of the transition arrow. Besides onset temperatures also the type 4 melting offsets are indicated in the heating 1 and heating 2 maps. The color codes used in Figure 7.3 for the different transitions, are also used in the maps.

The maps are largely self-explanatory. However, to assist in the reading process, cooling 1 and heating 1 for *70%r* is outlined in detail below.

Three different, high temperature melt structures can be hypothesized for uncured *70%r*: interdigitated bilayers (vesicular walls), cylindrical micelles and likely a small fraction of non-interdigitated (type 4 like) melt structures. These structures are present in Figure 7.4, at high temperatures for *70%r* in the cooling 1 morphology map. The non-interdigitated fraction is only relevant to *70%r*, *90%r* and pure Brij® S-20 (100%) because such structures do not allow for efficient epoxy resin mixing. From these melt structures type 4 structures are created upon cooling, as indicated by the red dashed arrow for *70%r*. The dashing of this arrow reflects that this transition is partial, i.e. it likely involves only a fraction of the type 4 liquid like material.

Upon further cooling *70%r*, the interdigitated bilayers convert into type 1 structures, starting form where the blue horizontal line is drawn. The blue full arrow suggest that this transition presumably involves all interdigitated melt structures. Cooling down to the temperature where the green line is drawn, triggers the conversion of the cylindrical liquid micelles into semicrystalline type 2 structures. This process too is likely complete (full green arrow). Upon further cooling down to the orange line, type 2 structures fully convert into type 3 structures. Also a fraction of the type 1 structures is converted into type 3 structures. The dashed arrow indicates that the latter process is incomplete.

As a result, at the lowest temperature, a small fraction of type 4 structures is present, together with type 3 structures and the remaining type 1 structures. These structures are the starting point for structural changes during heating 1. Once the orange line is surpassed during heating 1, the conversion from type 1 to type 3 structures resumes. This process is complete, therefore the full orange arrow. Upon further heating when surpassing the purple line, the type 3 structures start melting and reconvert into cylindrical micelles and interdigitated bilayer vesicles. This process is partial (hence the dashed purple arrow) because a fraction of the remaining type 3 structures converts into type 4 structures at approximately the temperature of the light blue line. This presumably involves a recrystallization process after passage through the liquid state. This is indicated by the circled liquid structure on top of the blue dashed arrow. This recrystallization process is also to be considered partial,

since the largest share of the type 3 structures is actually converting to the liquid state. Ultimately, the type 4 structures, formed during cooling 1 or by recrystallization during heating 1, melt and convert into a liquid state, starting from where the red horizontal line is drawn for *70%r* in the heating 1 morphology map. This melting process is over at the temperature where the dashed red horizontal line is drawn. This line represents the offset temperature for type 4 melting.

Reading the transitions of the other compositions in the Figures 7.4 and 7.5 happens in a similar way. Note that no cylindrical micelles are drawn in the morphology maps of cured materials with a Brij® S-20 fraction exceeding 70%. At these high epoxy concentrations the high curing degree inhibits the formation of such structures as discussed in section 7.1.4. Furthermore, the glassy regions in cured samples occupy a larger temperature range. Epoxy resin conversions (%) are indicated in the grey shaded, glassy domains in Figure 7.5. The dashed lines in the grey zones represent the experimental glass transition temperature prior to curing and the arrow highlights the glass transition temperature rise as a result of curing.

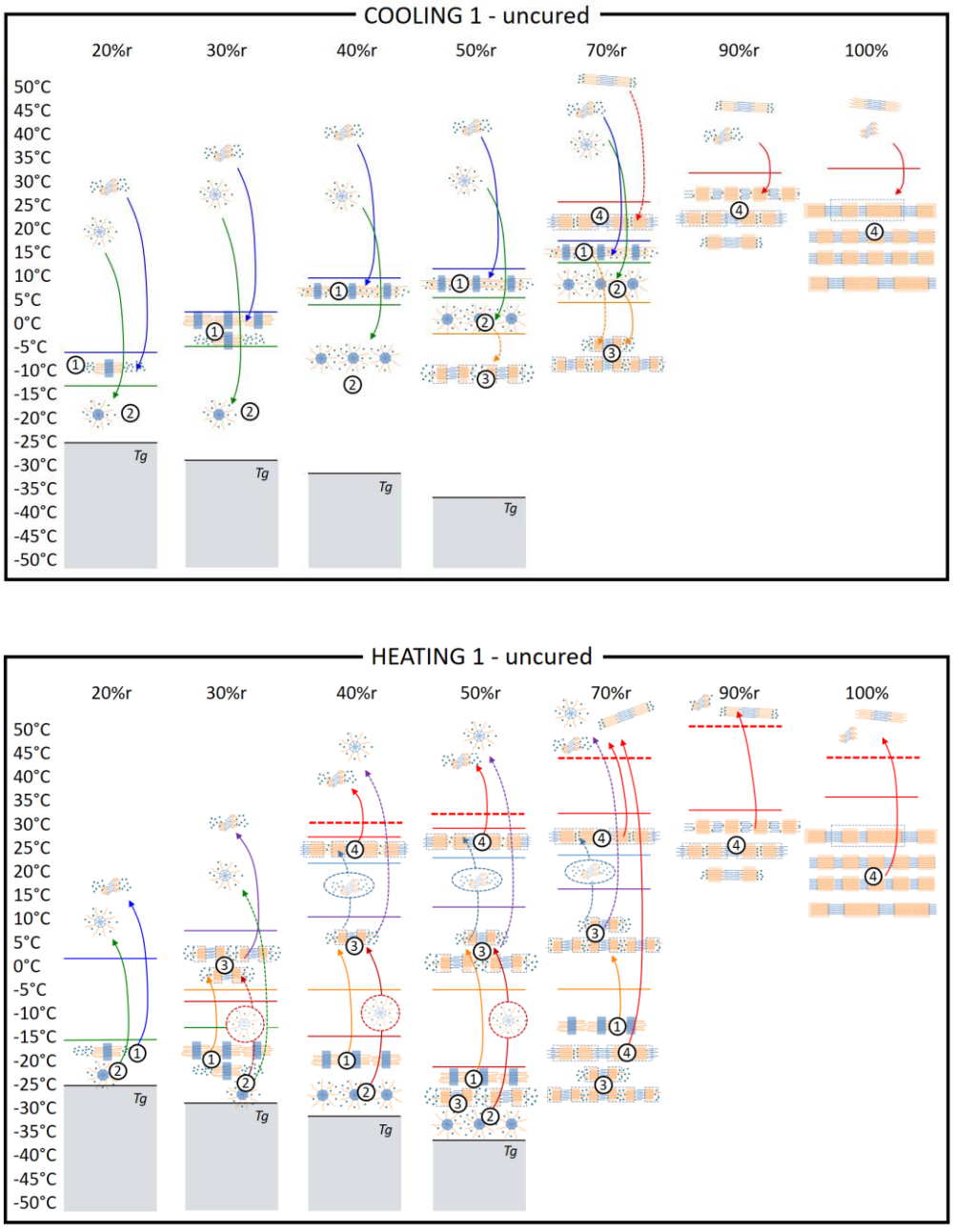


Figure 7.4: Morphology maps, indicating the structures (small cartoons and labels) and onsets (horizontal lines) of structural transitions (arrows) for the uncured epoxy Brij® S-20 blends during cooling 1 and heating 1. Glassy regions are shaded grey. The reader is referred to the text (section 7.2) for an explanation on how to read these maps.

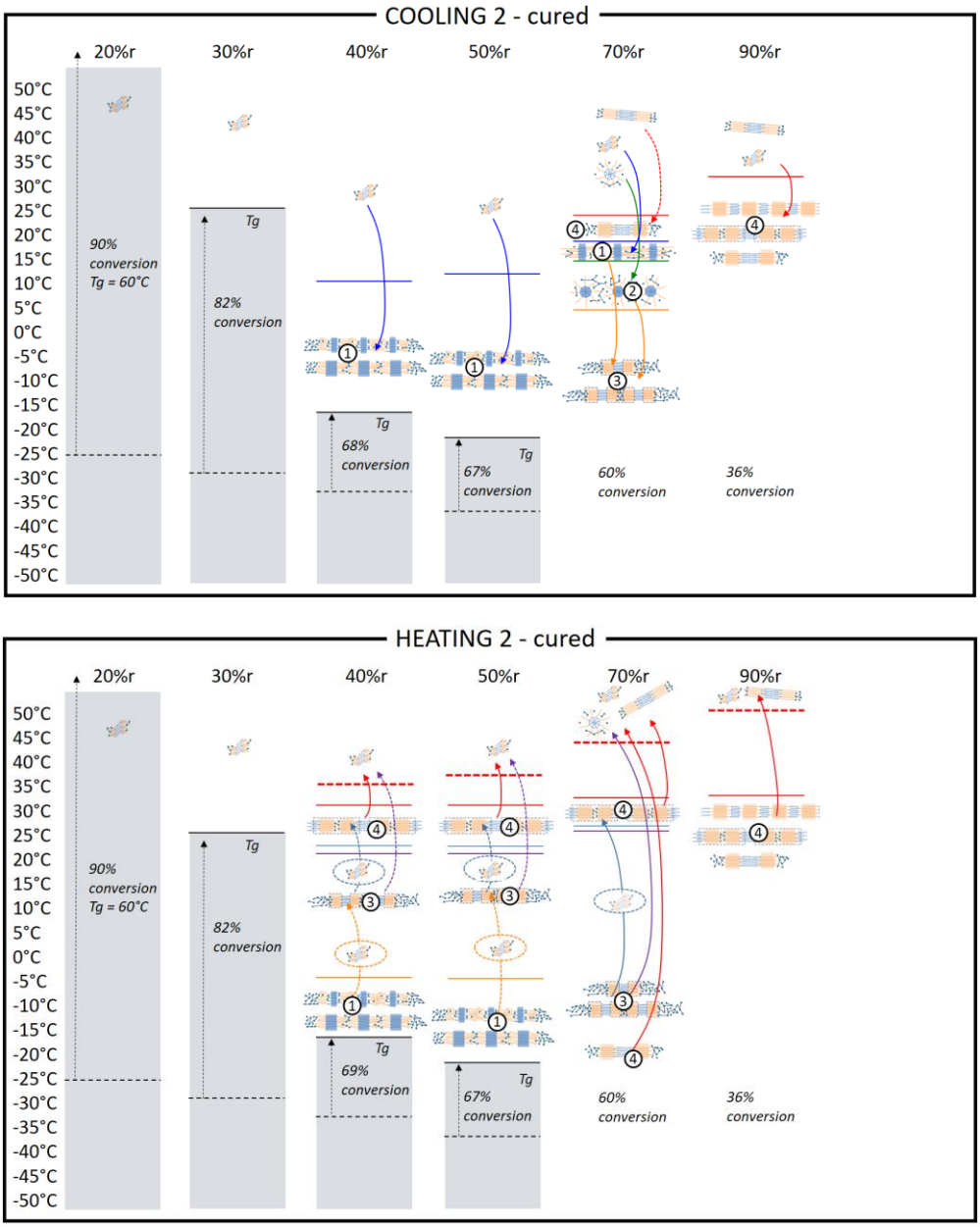


Figure 7.5: Morphology maps, indicating the structures (small cartoons and labels) and onsets (horizontal lines) of structural transitions (arrows) for the cured epoxy Brij® S-20 blends during cooling 2 and heating 2. Glassy regions are shaded grey. The reader is referred to the text (section 7.2) for an explanation on how to read these maps.

PART III

THE DISPERSION OF CARBON NANOTUBES IN EPOXY/STEARYL-BLOCK-POLY(ETHYLENE OXIDE) BLENDS

Collaborator contributions:

R. Van Hooghten was responsible for the rheology measurements and analysis; S. Neyens contributed to the manufacturing and analysis of CNT-loaded blends.

CHAPTER 8: THE CARBON NANOTUBE DISPERSION, EPOXY RESIN CURING AND MORPHOLOGY OF CARBON NANOTUBE CONTAINING EPOXY/STEARYL-BLOCK-POLY(ETHYLENE OXIDE) BLENDS

Brij® S-20 is considered in the present chapter as surfactant to assist the dispersion and control the topology of MWCNTs within an epoxy matrix. Blanch et al.[4] reported that Brij® S-20 can effectively disperse CNTs in aqueous solution. It is anticipated that this surfactant could do a similar job in epoxy resin. Having established in the preceding chapters that Brij® S-20 can adopt very rich morphologies in epoxy resins, it is worth exploring whether this surfactant ordering can be transferred to the CNT topology, just like some amphiphilic LC have been reported to do.[116] The assembly would be fixed at high temperatures by epoxy resin curing.

Unfortunately, it appeared that the epoxy, CNT, Brij® S-20 systems were not stable against CNT agglomeration. The experiments leading to this conclusion are reported in the present chapter as well as selected other findings. Apart from neat (pristine) multi wall carbon nanotubes, also amine functionalized CNTs were used.

8.1 CARBON NANOTUBE BRIJ® S-20 MASTER BATCHES

One can choose to either disperse the CNTs in the epoxy resin or in Brij® S-20 prior to combining all substances. CNTs dispersed in epoxy are offered commercially, which is convenient because CNTs are much less hazardous when dispersed. However, it was decided to not make use of such CNT-epoxy mixtures but to start from a CNT- Brij® S-20 system, hoping that the surfactant would stabilize the dispersion with the aliphatic stearyl moieties being CNT compatible. The combination of CNTs with Brij® S-20 will be called a CNT master batch. In next steps this master batch will be diluted with epoxy resin and cured.

8.1.1 CNT- BRIJ® S-20 MASTER BATCH PREPARATION

Master batches of 0.1 wt% pristine CNTs or amine functionalized CNTs were prepared by mixing the CNTs with Brij® S-20 at 70°C, which is slightly above its melting temperature. The mixtures were either stirred or probe-ultrasonicated for 5 min. Finally, the dispersions were cooled down to room temperature, which is below the Brij® S-20 crystallization temperature.

8.1.2 CNT DISPERSION QUALITY IN CNT- BRIJ® S-20 MASTER BATCHES

Electron and optical microscopy are powerful tools to visualize dispersions in detail. However, only limited amounts of material are being explored very locally without guarantee that the observed specimen is representative for the entire material.

Rheology on the contrary offers an integrated view of the state of dispersion across the volume of the sample. Hence, rheology has been used to probe the state of dispersion in the master batches[117,118]. In what follows, the rheological characterization of the master batches with pristine CNTs is discussed. The dispersion state after stirring is compared to that after sonication. In rheological approaches, the rheological behavior of the matrix without CNTs is compared to that of CNT containing systems. Rheological measurements are done at an elevated temperature of 50°C because the matrix material and the dispersions are solid materials at room temperature.

Dispersion quality was analyzed by applying small sinusoidal shear strains to the sample in the linear viscoelastic regime. In this regime, a fingerprint of the microstructure of the sample is obtained by slightly perturbing the microstructure without destroying it. A sinusoidal strain, γ, with angular frequency, ω, will results in a sinusoidal shear stress σ with the same frequency, but with a different phase (δ).

$$\sigma^* = G^*\gamma^* \qquad \text{(Eq. 8.1)}$$

The constant of proportionality is the complex shear modulus, G^*:

$$G^* = G' + iG'' \qquad \text{(Eq. 8.2)}$$

The storage or elastic modulus G' represents the in-phase part of the stress and describes the solid-like response of the material. The loss or viscous modulus G'' represents the out-phase part of the stress and characterizes the liquid-like behavior of the material.

The matrix material, Brij® S-20, is a Newtonian liquid with a viscosity of 75 ± 5 mPa s at 50 °C. The viscosity is independent of the strain rate and in a frequency sweep experiment G' is proportional to $\omega^1$and G'' is proportional to $\omega^{1.8}$ as seen in Figure 8.1. In theory a power law factor of 2 is expected for G',[119] but this is very difficult to measure accurately and an experimental factor of 1.8 is a very good approximation. Figure 8.1 also shows the response of the CNT master batches prepared with a stirrer or by ultrasound. The data are a little bit scattered due to the low viscosity of the samples. This results in a low overall measurement torque and limits the accuracy of the measurement. A geometry with a higher contact area could resolve this issue to some extent. A cone and plate geometry with diameter of 25 mm was chosen to establish the rheological procedure as described in section 3.2. However the trends are clear: Addition of CNT leads to additional relaxation times as can be seen by the rise of G' at lower frequencies in the top panel of Figure 8.1. The ultrasound sample even displays a plateau in G', indicating long range interactions, hence the existence of a percolating network of CNTs in matrix[120]. As the concentration of CNTs is relatively low, this indicates that the CNTs are very well dispersed in the matrix. As

expected, the CNTs are better dispersed after sonication compared to after stirring[117]. Similar conclusion can be made by considering G''. At high frequencies, the matrix material is predominantly probed[118]. The slope of G'' of the CNT loaded materials should approximate that of the pure matrix material, which is indeed the case. Generally, the matrix material undergoes some degradation during the dispersion process when this is not the case.

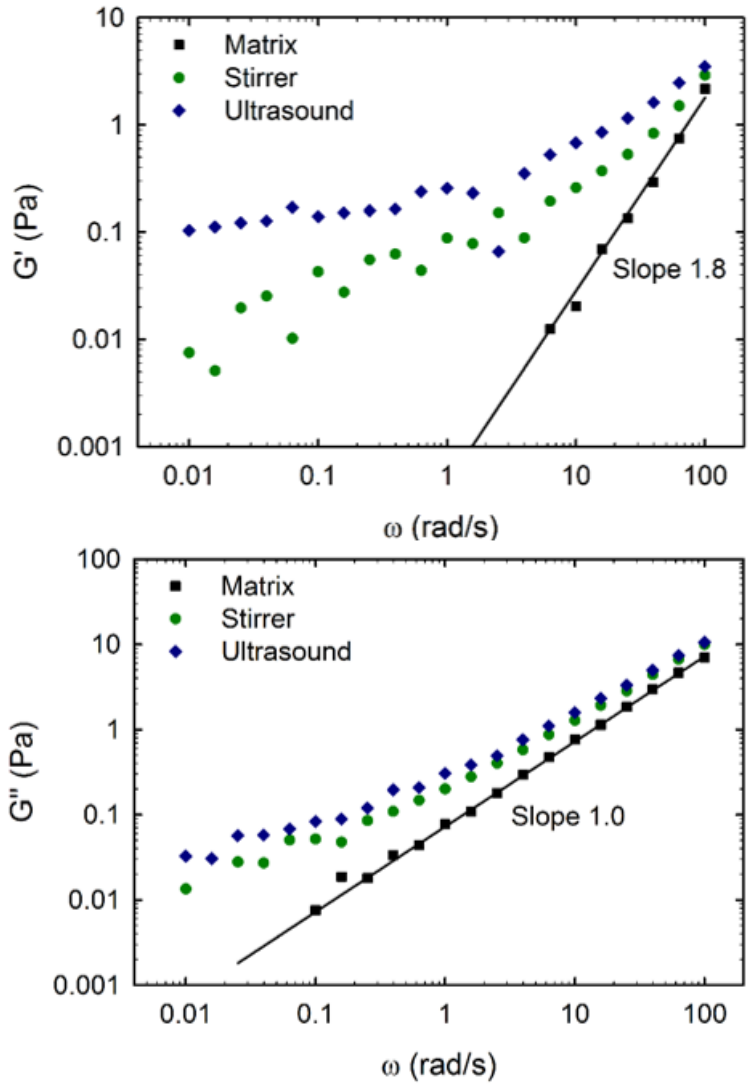


Figure 8.1: Frequency sweep results (top panel) G' and (bottom panel) G'' at 50 °C and γ = 8%.

A Winter-plot[121] can also be used to evaluate the data. Figure 8.2 shows the modulus of the complex viscosity η^* versus the complex modulus G^*. The rise of η^* can be used qualitatively to compare samples at identical concentration. It can be clearly

seen that the rise in complex viscosity is the highest for the sonicated sample, indicating that it is the best dispersed sample.

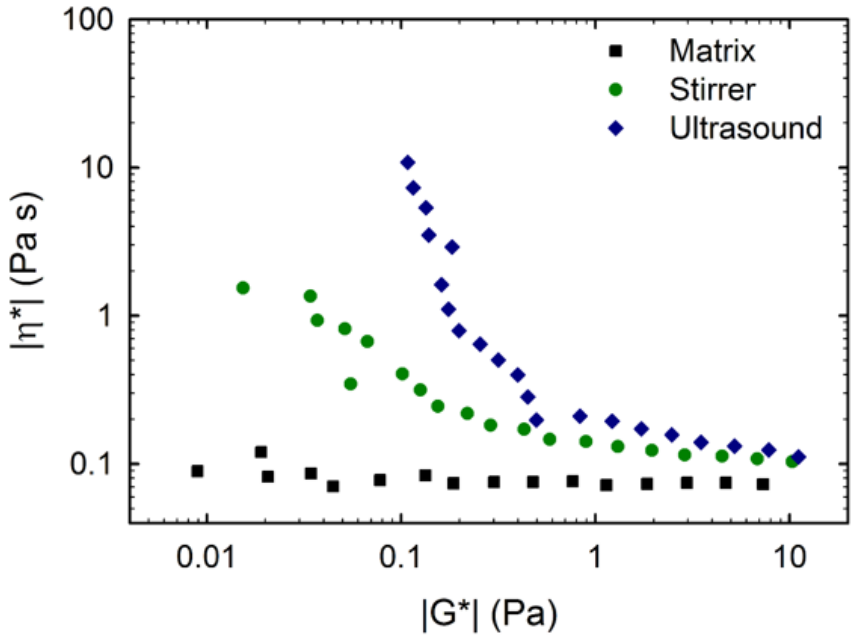


Figure 8.2: Winter-plot of the frequency sweep results of Figure 8.1.

Hence, rheology has proven to be a very effective way to measure dispersion quality of the CNT master batches and shows that the dispersion quality is better after sonication than after simple stirring. Also, the dispersion is quite stable for at least 6 hours after the initial tests. The experiments were repeated after 6 hours and the results were comparable.

8.2 EPOXY RESINS LOADED WITH CNTS THROUGH CNT- BRIJ® S-20 MASTER BATCH MIXING

8.2.1 PREPARATION OF CNT LOADED BRIJ® S-20 EPOXY RESIN SYSTEMS

DGEBA was mixed with a suitable amount of the Brij® S-20/CNT master batch and additional pure Brij® S-20 was added to ensure that final formulation contains 0.01 w% CNTs and the desired amount of Brij® S-20. Mixing happened at 70 °C while stirring for 10 min. Degassing for 60 min at 70 °C in a vacuum oven followed. Finally, the mixtures were brought to 100 °C in an oil bath, probe sonicated for 3 min and mixed with the curing agent as for the blend without CNTs. Curing was executed at 130°C for 90 min.

8.2.2 CNT DISPERSION QUALITY IN CNT LOADED BRIJ® S-20 EPOXY RESIN SYSTEMS

To assess the CNT dispersion in the epoxy resin with the aid of optical microscopy (OM), samples were used in which the master batch was 10 times diluted in the epoxy resin system, leading to systems with 0.01 wt% CNTs and 10wt% Brij® S-20. CNTs are too small to be seen individually by OM. Hence only clustered, not well dispersed CNTs can be detected with this technique. For OM observation the uncured blend was heated to above the Brij® S-20 melting point and melt pressed between two glass plates.

Figure 8.3 shows an OM image of uncured *10%p* (the resin with 10wt% Brij® S-20 and 0.01 wt% pristine CNTs). The huge amount of black dots, to be interpreted as clustered CNTs, indicates a poor CNT dispersion. Considering the results of the preceding section on the master batch, it seems that blending with the resin components induces CNT clustering. It was not further investigated whether this clustering was induced by using increased temperatures or by simply adding the resin components.

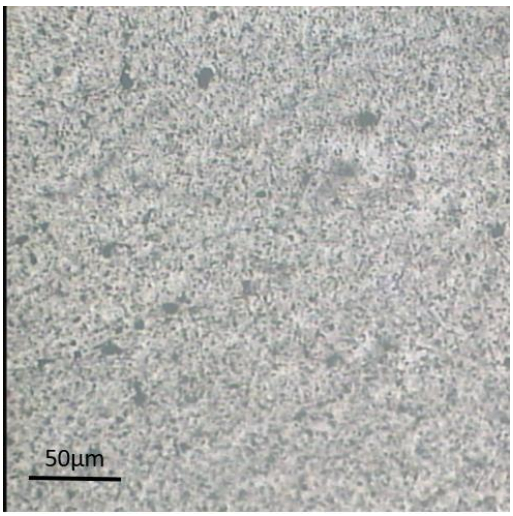


Figure 8.3: Optical Microscopy image of uncured *10%p* at room temperature

TEM is capable of observing individual CNTs. However, this technique does not allow analyzing liquid-like uncured samples. Hence the sample assessed above with optical microscopy was cured prior to TEM analysis. Figure 8.4 shows a typical image, once more revealing that most of the CNTs are heavily clustered and not homogeneously divided over the sample also after curing. A similar analysis in which amine functionalized CNTs were used also lead to images displaying heavily clustered CNTs.

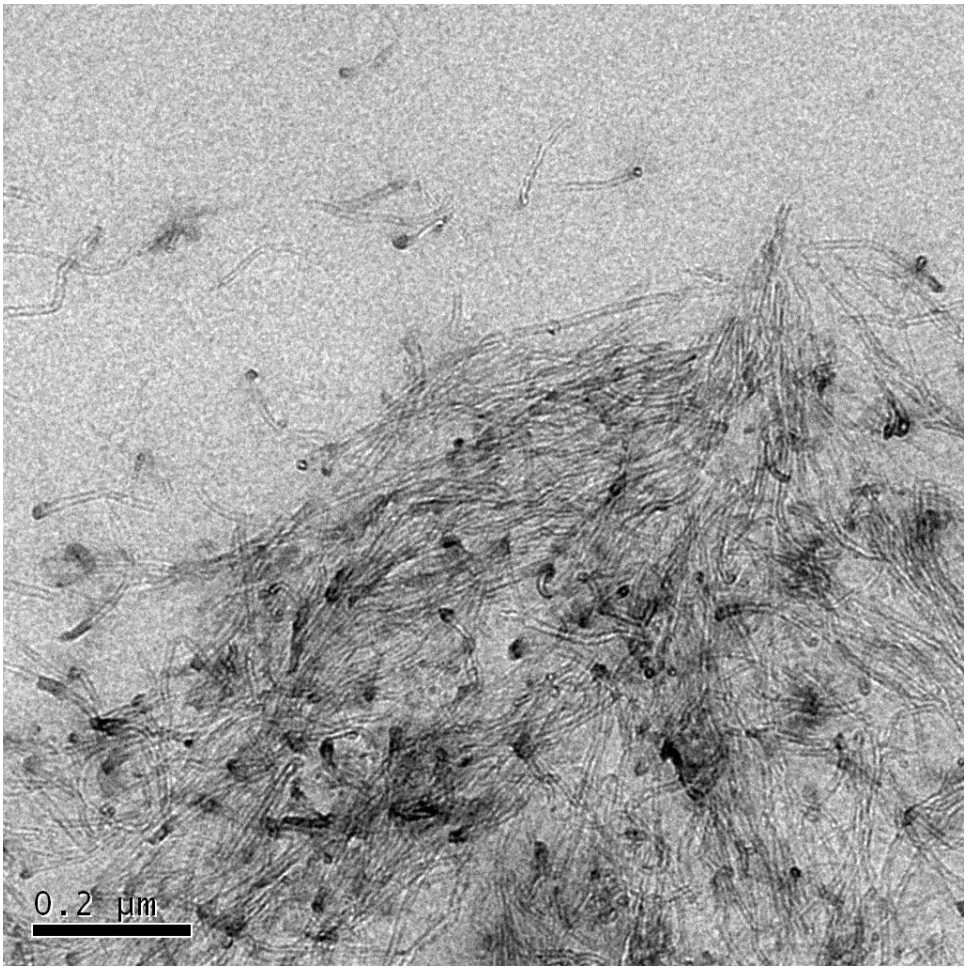


Figure 8.4: TEM image of cured *10%p*

8.2 EPOXY RESIN CURING AND MORPHOLOGY OF CNT LOADED EPOXY-BRIJ® S-20 BLENDS

Negligible differences could be observed in the thermal behavior of CNT loaded samples compared resins without CNTs. The glass transitions temperatures tends to shift a little to lower temperatures and the crystallization temperatures to higher temperatures. At a strong interaction between Brij® S-20 and the CNTs more pronounced changes are to be expected. The lack of interaction likely is at the origin of the poor dispersion stability.

The morphology of CNT-loaded samples was analyzed just like the reference materials discussed in part II. Synchrotron SAXS/WAXD data showed no difference in Brij® S-20 morphology development, indicating that the CNTs are not or very little trapped by the surfactant and mostly reside in separate regions. More research is

required to pinpoint the origin of CNT clustering. It is also worthwhile to investigate whether or not changes to the surfactant structure would lead to a better, more stable morphology development.

CHAPTER 9: CONCLUSIONS AND RECOMMENDATIONS FOR FUTURE WORK

9.1 CONCLUSIONS

Self-assembly is a very elegant process to create structure within materials on different length scales, even down to the nanometer region. This can be exploited to modify the mechanical, electrical or optical properties of materials.

When amphiphilic molecules, such as surfactants or block copolymers are introduced in a matrix with which only one of the chemical moieties is compatible, nanostructuring is readily realized. When using rather high amphiphile concentrations, progressed molecular stacking may lead to structuring from nanometer to micrometer length scales.

Besides purposely synthesized organic molecules, also nanoparticles can be considered. In the latter case, properties may benefit from the establishment of ordered patterns in their topology, which vastly differ from disordered clusters or homogeneous dispersions within a given matrix. For instance theoretical work in the literature has demonstrated that certain patterns in the location of reinforcing nanoparticles may be very advantageous to the overall material toughness. This toughness increase may furthermore be related to the establishment of structural hierarchy, *i.e.* the presence of structural elements at different length scales. A second application of ordered nanoparticles can be found in nano-electronics, in which the conductivity of ordered nano-dispersions can be exploited for wearables or implantable technology applications.

In this dissertation, Brij® S-20, a low molecular weight diblock copolymer containing a stearyl chain covalently connected to a short PEO block was used to induce nanostructures while attempting to simultaneously providing control over the CNT dispersion in the epoxy matrix.

The main emphasis in this work was on the investigation of curing kinetics, thermal behavior and morphology of various epoxy/ Brij® S-20/CNT blends. In the chapters 4-6, blends without CNTs were thoroughly investigated and in the chapter 7 the thermal and morphological findings were cast into morphology maps. In chapter 8 the impact of adding CNTs was considered.

In the following paragraphs, the most important conclusions of the chapters 4-8 are once more highlighted. This summary starts from a discussion of the systems prior to curing, then treats effects during resin curing and ultimately covers systems in the cured state. At the end, the impact of adding CNT's is recapitulated.

9.1.1 CONCLUSIONS UNCURED SAMPLES

Low amounts of block copolymer (30% or less) in uncured epoxy resin self-assemble into vesicular structures (type 1) supplemented by a fraction of spherical and cylindrical micelles (type 2). SAXS revealed that the vesicle walls are composed of a central stearyl layer (composed of tilted and interdigitated aliphatic chains) with PEO layers on both sides, facing the epoxy.

Cooling in the uncured state induces crystallization of the stearyl layer prior to resin vitrification. This crystallization causes a densification within the attached PEO layers which in turn leads to epoxy resin segregation from within the PEO layers. Heating 20%r causes crystal melting after devitrification. In the case of 30%r, heating initiates cold crystallization of the PEO units into a folded configuration (type 3). This process actively disrupts the stearyl crystallinity and - quite remarkably – leads to stearyl layer melting at temperatures *below* the stearyl layer crystallization temperature. This folded PEO-block crystallization seems kinetically favored above stretched out PEO crystallization because the stearyl chains in type 1 structures are interdigitating. For stretched out PEO chain crystallization, the interdigitating should be given up and the stearyl chains should reconfigure into a double layer. Further heating causes the newly formed type 3 PEO crystalline structures to melt.

As PEO crystallization requires epoxy resin segregation, it is logical that increasing the block copolymer content (i.e. decreasing epoxy content) facilitates PEO crystallization. This is indeed observed for materials with intermediate and high block copolymer fractions.

40%r behaves like 30%r during cooling in the uncured state. During subsequent heating type 3 structures form from the type 1 structures, just like for 30%r but upon further heating part of the type 3 structures convert into type 4 structures, i.e. crystal structures with stretched-out interdigitated PEO units. These PEO governed structures are more orderly packed than type 3 structures and the type 3 to type 4 conversion involves a melting and recrystallization process, rather than a solid-solid

transition. This seems conceivable since the folded PEO chains need to stretch out and the aliphatic interdigitating needs to be broken.
Where the transformation of type 1 & 2 structures into type 3 structures during the cooling run in the uncured state is inhibited in 40%r due to vitrification, type 3 structures do form prior to vitrification in 50%r. Facilitated PEO crystallization with increasing block copolymer content already allows type 4 structure formation during the cooling run in 70%r. In fact, type 4 structures are formed first during cooling (although not complete) and remain present until heating again above the type 4 melting temperature. Since epoxy is segregated during the type 4 PEO crystallization, the remaining part of the sample is enriched with epoxy resin, impeding further type 4 crystallization during cooling. Therefore, the rest of the sample behaves like samples with a lower block copolymer content, and converts into type 1 and 2 stearyl crystallized structures. These structures convert into type 3 structures upon reheating. This conversion process virtually runs to completion already during cooling for 70%r. Upon reheating, ultimately the type 3 structures melt and partially convert into additional type 4 crystals, which melt together with the ones formed during cooling at the highest temperatures.

At very high block copolymer fractions as well as in pure Brij® S-20, the metastable type 1, type 2 and type 3 structures are no longer formed. Cooling immediately leads to crystallization into type 4 structures. The rationale is that less epoxy is mixed with PEO, which enables more swift PEO crystallization compared to at low and intermediate block copolymer contents. Since the raison d'être of type 3 structures (lower driving force of conversion from type 1 into type 3 compared to conversion from type 1 into type 4 due to PEO chain folding and aliphatic interdigitation) is no longer relevant, the only observed morphology is type 4.

9.1.2 CONCLUSIONS REGARDING THE CURING PROCESS AND MORPHOLOGY DURING CURING

The curing process itself is affected by the block copolymer amount, which acts as a diluent for the reacting resin chemicals. Hence, increasing the block copolymer content slows down the curing reaction.
Since the activation energy of the curing reaction was found to be not affected by the presence of block copolymer, the block copolymer apparently does not act upon the curing mechanism.

Small amounts of Brij® S-20 act as a plasticizer to the curing resin, which drives the curing to completion at temperatures where otherwise the curing of pure resin would be prematurely arrested by vitrification. At intermediate block copolymer contents the plasticization effect remains but curing no longer reaches completion due to a separation of the resin reactants by the impenetrable aliphatic Brij® S-20 walls. In addition, one of the resin components might preferentially dissolve in the Brij® S-20 PEO moieties. As the ultimate curing degree decreases to 60-70%, gelation no longer occurs since this requires 82% conversion. Increasing the block copolymer further, increasingly hinders the curing process, resulting in only 36% conversion for 90%r.

Vesicles and micelles are also present high temperatures in the liquid state while the resin is curing. During curing the compatibility between the epoxy and PEO-block decreases and leads to a reaction induced (micro) phase separation. As a result, the liquid PEO chains at the borders of the vesicle walls coil up while epoxy monomer is segregating. This effect is most prominent in resins with rather low block copolymer contents because in these materials the resin conversion is the highest.

9.1.3 CONCLUSIONS CURED SAMPLES

Samples with low amount of block copolymer do not crystallization in the cured state. Crystallization is inhibited since the epoxy matrix is in the vitrified state up to temperatures above the Brij® S-20 crystallization range.

Above 30% block copolymer, the curing no longer reaches completion and the ultimate conversion is reduced by which the resin T_g remains rather low, permitting Brij® S-20 crystallization. The higher the Brij® S-20 content the more the crystallization after curing resembles that of the uncured samples. For 40%r and 50%r, the only noteworthy morphological differences are that type 1 structures are promoted in favor of type 2 structures and formation of type 3 structures during the cooling run is inhibited by the slightly increased T_g. The thermal behavior after curing of samples with very high block copolymer content cannot be discriminated from the sample before curing. Curing only leads to a reduced compatibility between PEO and partially cured epoxy, resulting in exclusion of epoxy from within the stacks.

9.1.4 CONCLUSIONS REGARDING CNT-LOADED SAMPLES

Sonicating improves the dispersion quality of the CNT master batches over mechanical stirring. However, while curing a CNT-loaded samples, the dispersion seems to be not stable and the CNTs re-agglomerate prior to gelation. The morphology of the CNT-loaded samples is nearly identical to that of the pristine samples, indicating that the CNTs are heavily clustered in separate regions, while the intention was to trap them by the surfactant. Hence, this path needs further investigation.

In conclusion, the amphiphilic block copolymer did live up to the expectation of creating nanostructures, irrespective of the (studied) curing protocols. Yet they failed to deliver a hierarchical structure with CNTs due to a low CNT dispersion stability. We did successfully map the morphology development of these structures, and discovered that Brij® S-20 self-assembles into concentration and temperature dependent supramolecular structures.

9.2 FUTURE OUTLOOK

Since samples with less than 20% block copolymer self-assemble into vesicles, micelles and wormlike structures, it would be interesting to test the mechanical properties of these samples. Including lower amounts of block copolymer also deserves being considered, since they likely will produce similar (toughening) nanostructures while resin plasticization would be reduced.

Also, it would become possible to relate the different morphologies of the same sample with their associated mechanical properties. This can be achieved by curing at different curing temperatures (although it was demonstrated that for 20%r, the morphology is quite robust towards different curing protocols) or by using a UV-curing agent, so morphology and curing rate can be controlled independently, thereby increasing the amount of flexibility.

The remarkable finding that the (cold) crystallization of the PEO units is able to actively disrupts the stearyl crystallinity at temperatures *below* the stearyl layer crystallization temperature deserves further investigation. It remains to be explored how this phenomenon is affected by the relative block lengths, the adopted cooling and heating rates, the matrix they reside in.

Concerning CNT-loaded samples, it makes sense to extend the research to lower fractions of block copolymer, in order to get a better dispersion quality. Additionally, more research is required to investigate whether changes in the surfactant design could enable heterogeneous dispersion. One (unreported) attempt was made during

this work in the form of a triphenyl group instead of stearyl, but the structure formation changed significantly, which is why it was decided not to proceed on this pathway in the course of this dissertation. Yet alternatively, it deserves being explored whether or not Brij® S-20 would be able to disperse and organize single walled CNT's. After all the CNT's used in the present work were multi walled with a thickness of about 10 nm, which might be too large to fit the block copolymer morphologies.

REFERENCES

1 S. Wu, Q. Guo, S. Peng, N. Hameed, M. Kraska and Y. Mai, *Macromolecules*, 2012, **45**, 3829–3840.

2 M. Larra, E. Serrano, M. D. Martin, A. Tercjak, G. Kortaberria, K. De Caba and C. C. Riccardi, *Polym. Int.*, 2007, **56**, 1392–1403.

3 E. Girard-Reydet, J.-P. Pascault, A. Bonnet, F. Court and L. Leibler, *Macromol. Symp.*, 2003, **198**, 309–322.

4 A. J. Blanch, C. E. Lenehan and J. S. Quinton, *J. Phys. Chem. B*, 2010, **114**, 9805–11.

5 F. F. Denograro, P. Guerrero, M. A. Corcuera and I. Mondragon, *J. Appl. Polym. Sci.*, 1995, **56**, 177–192.

6 K. Fryauf, M. Fedtke and G. Strasse, *Polymer*, 1993, **34**, 323–327.

7 S. Swier, G. Van Assche and B. Van Mele, *J. Appl .Polym. Sci.*, 2003, **91**, 2798–2813.

8 M. Ghaemy, M. Barghamadi and H. Behmadi, *J. Appl. Polym. Sci.*, 2004, **94**, 1049–1056.

9 S. Vyazovkin and N. Sbirrazzuoli, *Macromol. Symp.*, 1996, **29**, 1867–1873.

10 J. Mijovic and J. Wijaya, *Polymer*, 1994, **35**, 2683–2686.

11 M. R. Kamal, *Polym. Eng. Sci.*, 1974, **14**, 231–239.

12 S. Paz-abuin, A. Lopez-quintelat and M. Pazos-pellint, *Polymer*, 1997, **38**, 3117–3120.

13 G. Van Assche, a. Van Hemelrijck, H. Rahier and B. Van Mele, *Thermochim. Acta*, 1995, **268**, 121–142.

14 Flory. P.J., *Principle of Polymer Chemistry*, 1953.

15 J. K. Gillham, *Polym. Eng. Sci.*, 1986, **26**, 1429–1433.

16 M. T. DeMeuse, J. K. Gillham and F. Parodi, *J. Appl. Polym. Sci.*, 1997, **64**, 15–25.

17 F. X. Perrin, T. M. H. Nguyen and J. L. Vernet, *Eur. Polym. J.*, 2007, **43**, 5107–5120.

18 P. A. Oyanguren, P. M. Frontini and R. J. J. Williams, 1996, **37**, 3079–3085.

19 D. Rosu, C.-D. Varganici, L. Rosu and O. M. Mocanu, in *Thermal Degradation of Polymer Blends, Composites and Nanocomposites*, 2015, pp. 17–49.

20 S. Goossens, *Micro- and nanostructured thermoplastic/thermosetting polymer blend systems: Reaction-induced phase separation, crystallization and morphology*, 2006.

21 A. F. Yee and R. A. Pearson, *J. Mater. Sci.*, 1986, **21**, 2462–2474.

22 N. Chikhi, S. Fellahi and M. Bakar, *europ*, 2002, **38**, 251–264.

23 K. P. Unnikrishnan and E. T. Thachil, *Des. Monomers Polym.*, 2006, **9**, 129–152.

24 C. B. Bucknall and I. K. Partridge, *Polym. Eng. Sci.*, 1986, **26**, 54–62.

25 R. A. Pearson and A. F. Yee, *Polymer*, 1993, **34**, 3658–1670.

26 J. H. Hodgkin, G. P. Simon and R. J. Varley, *Polym. Adv. Technol.*, 1996, **9**, 3–10.

27 K. Mimura, H. Ito and H. Fujioka, *Polymer*, 2000, **41**, 4451–4459.

28 S. K. Siddhamalli, *Polym. Compos.*, 2000, **21**, 846–855.

29 S. Goossens, B. Goderis and G. Groeninckx, *Macromolecules*, 2006, **39**, 2953–2963.

30 G. Vanden Poel, S. Goossens, B. Goderis and G. Groeninckx, *Polymer*, 2005, **46**, 10758–10771.

31 S. Goossens and G. Groeninckx, 2007, 19–21.

32 M. Aravand, *Micro and nano structured hierarchical carbon fiber composites*, 2015.

33 M. Aravand, S. V. Lomov and L. Gorbatikh, *Compos. Sci. Technol.*, 2015, **110**, 8–16.

34 T. H. Hsieh, a. J. Kinloch, K. Masania, a. C. Taylor and S. Sprenger, *Polymer*, 2010, **51**, 6284–6294.

35 B. Wetzel, P. Rosso, F. Haupert and K. Friedrich, *Eng. Fract. Mech.*, 2006, **73**, 2375–2398.

36 B. Fiedler, F. H. Gojny, M. H. G. Wichmann, M. C. M. Nolte and K. Schulte, *Compos. Sci. Technol.*, 2006, **66**, 3115–3125.

37 F. Gojny, M. Wichmann, B. Fiedler and K. Schulte, *Compos. Sci. Technol.*, 2005, **65**, 2300–2313.

38 H. Miyagawa and L. T. Drzal, *Polymer*, 2004, **45**, 5163–5170.

39 A. Allaoui, S. Bai, H. M. Cheng and J. B. Bai, *Compos. Sci. Technol.*, 2002, **62**, 1993–1998.

40 F. H. Gojny, M. H. G. Wichmann, U. Köpke, B. Fiedler and K. Schulte, *Compos. Sci. Technol.*, 2004, **64**, 2363–2371.

41 C. S. Grimmer and C. K. H. Dharan, *Compos. Sci. Technol.*, 2010, **70**, 901–908.

42 V. Kostopoulos, a. Baltopoulos, P. Karapappas, a. Vavouliotis and a. Paipetis, *Compos. Sci. Technol.*, 2010, **70**, 553–563.

43 K. Yang, M. Gu, Y. Guo, X. Pan and G. Mu, *Carbon N. Y.*, 2009, **47**, 1723–1737.

44 W. Zhang, I. Srivastava, Y.-F. Zhu, C. R. Picu and N. a Koratkar, *Small*, 2009, **5**, 1403–7.

45 A. Kinloch, R. Mohammed and A. C. Taylor, *J. Mater. Sci.*, 2005, 22–25.

46 L. Ruiz-Pérez, G. J. Royston, J. P. a. Fairclough and A. J. Ryan, *Polymer*, 2008, **49**, 4475–4488.

47 L. Gorbatikh, S. V. Lomov and I. Verpoest, *Procedia Eng.*, 2011, **10**, 3252–3258.

48 Q. Guo, C. Harrats, G. Groeninckx and M. H. . Koch, *Polymer*, 2001, **42**, 4127–4140.

49 H. Lü and S. Zheng, *Polymer*, 2003, **44**, 4689–4698.

50 J. Chen and A. C. Taylor, *J. Mater. Sci.*, 2012, **47**, 4546–4560.

51 P. M. Lipic, F. S. Bates and M. A. Hillmyer, *J. Am. Chem. Soc.*, 1998, **7863**, 8963–8970.

52 M. W. Matsen and F. S. Bates, *Macromolecules*, 1996, **29**, 1091–1098.

53 F. S. Bates and G. H. Fredrickson, *Phys. Today*, 1999, **52**, 32.

54 F. S. Bates and G. H. Fredrickson, *Annu. Rev. Phys. Chem.*, 1990, **41**, 525–557.

55 S. Ritzenthaler, F. Court, L. David, E. Girard-Reydet, L. Leibler and J. P. Pascault, *Macromolecules*, 2002, **35**, 6245–6254.

56 P. Alexandridis, U. Olsson and B. Lindman, *Langmuir*, 1998, **7463**, 2627–2638.

57 J. N. Israelachvili, *Intramolecular and Surface Forces*, Academic Press, 2011.

58 M. Laradji, A.-C. Shi, J. Noolandi and R. C. Desai, *Macromolecules*, 1997, **30**, 3242–3255.

59 S. Zheng, in *Epoxy Polymers*, 2009, pp. 81–109.

60 M. A. Hillmyer, P. M. Lipic, D. A. Hajduk, K. Almdal and F. S. Bates, *J. Am. Chem. Soc.*, 1997, **7863**, 2749–2750.

61 R. B. Grubbs, J. M. Dean, M. E. Broz and F. S. Bates, *Macromolecules*, 2000, **33**, 9522–9534.

62 F. Meng, S. Zheng, H. Li, Q. Liang and T. Liu, *Macromolecules*, 2006, **39**, 5072–5080.

63 M. Sangermano, in *Epoxy Polymers*, 2009, pp. 235–252.

64 I. Hamley, *The Physics of Block Copolymers*, 1999.

65 I. Hamley, *Development in Block Copolymer Science and Technology*, 2004.

66 W. H. de Jeu, *Polymer Crystallization: Observations, Concepts and Interpretations*, 2003.

67 E. A. DiMarzio, C. M. Guttman and J. D. Hoffman, *Macromolecules*, 1980, **13**, 1194.

68 M. D. Whitmore and J. Noolandi, *Macromolecules*, 1988, **21**, 1482.

69 T. Vilgis and A. Halperin, *Macromolecules*, 1991, **24**, 2090.

70 S. Nojima, M. Ono and T. Ashida, *Polym. J.*, 1992, **24**, 1271–1280.

71 V. Balsamo, a J. MÃ¼ller and R. Stadler, *Macromolecules*, 1998, **31**, 7756–7763.

72 V. Balsamo and G. Gil, *Macromolecules*, 2003, **36**, 4515–4525.

73 P. Rangarajan, R. A. Register and L. J. Fetters, *Macromolecules*, 1993, **26**, 4640–4645.

74 D. Qian, G. J. Wagner, W. K. Liu, M.-F. Yu and R. S. Ruoff, *Appl. Mech. Rev.*, 2002, **55**, 495.

75 P.-C. Ma, N. a. Siddiqui, G. Marom and J.-K. Kim, *Compos. Part A Appl. Sci. Manuf.*, 2010, **41**, 1345–1367.

76 J. Sandler, M. S. . Shaffer, T. Prasse, W. Bauhofer, K. Schulte and a. . Windle, *Polymer*, 1999, **40**, 5967–5971.

77 E. Bertels, K. Bruyninckx, M. Kurttepeli, M. Smet, S. Bals and B. Goderis, *Langmuir*, 2014, **30**, 12200–12209.

78 A. I. Isayev, R. Kumar and T. M. Lewis, *Polymer*, 2009, **50**, 250–260.

79 K. Yang, M. Gu and Y. Jin, *J. Appl. Polym. Sci.*, 2008, **110**, 1980–2988.

80 Q. Liu, S. V. Lomov and L. Gorbatikh, *Carbon N. Y.*, 2019, **142**, 141–149.

81 S. Bose, C. Ozdilek, J. Leys, J. W. Seo, M. Wübbenhorst, J. Vermant and P. Moldenaers, *ACS Appl. Mater. Interfaces*, 2010, **2**, 800–7.

82 K. Lakoubovskii, *Cent. Eur. J. Phys.*, 2009, **7**, 645–653.

83 M. Xu, N. Futaba, M. Yumura and K. Hata, *ACS Nano*, 2012, **6**, 5837–5844.

84 G. L. Goh, S. Agarwala and W. Y. Yeong, *Adv. Mater. Interfaces*, 2019, **6**, 1–29.

85 C. Liu, L. Zheng, L. Yuan, Q. Guan, A. Gu and G. Liang, *J. Phys. Chem. C*, 2016, **120**, 28875–28885.

86 W. Jiang, B. Yu, W. Liu and J. Hao, *Langmuir*, 2007, **23**, 8549–8553.

87 J. Lagerwall, M. Scalia, U. Haluska, S. Dettlaff-Weglikowska, S. Roth and F. Giesselmann, *Adv. Mater.*, 2007, **19**, 359–364.

88 C. R. Kasprzak, E. T. Scherzinger, A. Sarkar, M. Mioa, D. H. Porcincula, A. Madriz, Z. M. Pennewell, S. S. Chau, R. Fernando, M. Stefik and S. Zhang, *Macromol. Chem. Phys.*, 2018, **219**.

89 M. Lu and S. Kim, *J. Appl .Polym. Sci.*, 1999, **71**, 2401–2408.

90 S. Swier, G. Van Assche and B. Van Mele, *J. Appl. Polym. Sci.*, 2003, **91**, 2814–2833.

91 M. Kim, Y. Bin Park, O. I. Okoli and C. Zhang, *Compos. Sci. Technol.*, 2009, **69**, 335–342.

92 C. J. Gommes and B. Goderis, *J. Appl. Crystallogr.*, 2010, **43**, 352–355.

93 D. Montezinos, B. G. Wells and J. L. Burns, *J. Polym. Sci. Part C Polym. Lett.*, 1985, **23**, 421–425.

94 T. JS, S. JI and C. PR, *Macromolecules*, 1983, **16**, 589–298.

95 J. I. M. Gonis, G. P. Simon and W. D. Cook, *J. Appl. Polym. Sci.*, 1999, **72**, 1479–1488.

96 Z. Man, J. L. Stanford and B. K. Dutta, *J. Appl. Polym. Sci.*, 2009, **112**, 2391–2400.

97 A. G. Marangoni and S. E. Mcgauley, *Cryst. Growth Des.*, 2003, **3**, 95–108.

98 K. Pielichowska, S. Głowinkowski, J. Lekki, D. Biniaś, K. Pielichowski and J. Jenczyk, *Eur. Polym. J.*, 2008, **44**, 3344–3360.

99 J. Mark, *Polymer data Handbook*, Oxford University Press, 1999.

100 P. Swan, *J. Polym. Sci.*, 1960, **42**, 525–534.

101 L. Li, F. Meng, Z. Zhong, D. Byelov, W. H. De Jeu and J. Feijen, *J. Chem. Phys.*, 2007, **126**.

102 K. Pang and J. Gillham, *J. Appl. Polym. Sci.*, 1989, **37**, 1969–1991.

103 A. Izumi, T. Nakao, H. Iwase and M. Shibayama, *Soft Matter*, 2012, **8**, 8438.

104 J. S. Pedersen, *Adv. Colloid Interface Sci.*, 1997, **70**, 171–210.

105 B. Goderis, J. A. Putseys, J. Gommes, G. M. Bosmans and J. A. Delcour, *Cryst. Growth Des.*, 2014, **14**, 3221–3233.

106 L. Sun, E. A. Ertel, L. Zhu, B. S. Hsiao, C. A. Avila-Orta and I. Sics, *Langmuir*, 2005, **21**, 5672–5676.

107 C. Zachary and S. Torquato, *J. Stat. Mech. Theory Experiement*, 2009, **2009**, P12015.

108 A. Rastogi, A. E. Terry, V. B. F. Mathot and S. Rastogi, *Macromolecules*, 2005, **38**, 4744–4754.

109 S. Nojima, K. Kato, S. Yamamoto and T. Ashida, *Macromolecules*, 1992, **25**.

110 S. Jiang, C. Qiao, S. Tian, X. Ji, L. An and B. Jiang, *Polymer*, 2001, **42**, 5755–5761.

111 S. Förster, L. Apostol and W. Bras, *J. Appl. Crystallogr.*, 2010, **43**, 639–646.

112 H. Suzuki and B. Wunderlich, *J. Polym. Sci. Polym. Phys. Ed.*, 1985, **23**, 1671–1679.

113 F. Lidong, X. Bian, G. Li, Z. Chen, Y. Cui and X. Chen, *Polym. Test.*, 2013, **32**, 1368–1372.

114 Z. Sixun, Z. Naibin, L. Xiaolie and L. Dezhu, *Polymer*, 1995, **36**, 3609–3613.

115 A. Rocco, D. Moreira and R. Pereira, *Eur. Polym. J.*, 2003, **39**, 1925–1934.

116 S.-R. Huang, C.-F. Wu, C.-A. Wang and J. Ruan, *Polymer*, 2018, **140**, 10–21.

117 F. J. Galindo-Rosales, P. Moldenaers and J. Vermant, *Macromol. Mater. Eng.*, 2011, **296**, 331–340.

118 J. Vermant, S. Ceccia, M. K. Dolgovskij, P. L. Maffettone and C. W. Macosko, *J. Rheol. (N. Y. N. Y).*, 2007, **51**, 429–450.

119 C. W. Macosko, *Rheology: Principles, Measurements, and Applications*, 1994.

120 H. M. Hassanabadi and M. Wilhelm, *Rheol. Acta*, 2014, **53**, 869–882.

121 H. H. Winter, *Rheol. Acta*, 2009, **48**, 241–243.

HEALTH, SAFETY AND ENVIRONMENT

Safety in the Chemistry department is extremely important. All lab actions were done while wearing the appropriate personal protective equipment: A lab coat and safety goggles were worn at any time in lab environments. All chemical handling was done wearing gloves and under the fume hood. DGEBA can cause severe allergic reactions. Also MDA can cause allergic reactions, is carcinogenic and can cause harm to organs after single contact, is suspected to cause genetic damage and is toxic for living organisms in aquatic environment. Evidently, working with MDA was done with extreme precautions: It was bought in pellet form instead of powder, reducing the risk. Nonetheless, an FFP3 dust mask was worn at all times. Finally the CNTs can be very harmful after inhalation. Therefore, as a first option the use of CNTs pre-dispersed in epoxy was considered. When this appeared inefficient, CNTs in powder form were used to create CNT/blockcopolymer masterbatches to limit the potential exposure. Handling CNTs was done in a special case under the fume hood and while wearing an FFP3 mask. Lab experiments also involved quenching the blends in liquid nitrogen. When handling liquid nitrogen, a full face shield, cryogenic gloves and safety shoes were used. Also pants were worn over the shoes to avoid liquid nitrogen travelling down into the shoes.

Compressed nitrogen was used in DSC-experiments and at some other instances. The course “Moving and replacing industrial gasses” was followed to become aware of specific risks and to be able to handle them safely.

SAXS/WAXD experiments in principle involved a irradiation risk. Therefor a radiation protection training was followed. However, modern X-ray set-ups are designed to guarantee safe use. The source and beam path are enclosed within a transparent, X-ray absorbing enclosure. When the door of the enclose is not properly closed, a switch is triggered and a shutter blocks all radiation at the source. Experiments at the ESRF were conducted in such a way, that it was impossible to lock someone in the experimental X-ray hutch when the X-ray beam was entering it. The last person exiting the experimental hutch should always check if no one is left behind, push a button at the rear end of the experimental hutch, close the door and push a button next to the door to magnetically seal it. During this protocol, alarms sound which can alert someone who nevertheless may have been overlooked within the experimental hutch. This person can press a safety button, which stops the process and the X-ray beam from entering the hutch.

Lastly, I was also involved in safety at the departmental level, being a member of the HSE-committee for 3 years. In this committee, incidents, new safety processes and other related content is discussed.

LIST OF PUBLICATIONS

PEER-REVIEWED PUBLICATIONS

Bogaerts K., Lavrenova A., Sploelstra A. B., Boyard N., Nies E., Goderis B.; Curing Kinetics and morphology of a Nanovesicular epoxy/stearyl-block-poly(ethylene oxide) surfactant system; *RSC Soft Matter*, 11, 6212-6222 (2015).

Demeyer P.-J., Vandendriessche S., Van Cleuvenberghe S., Carron S., **Bogaerts K.,** Parac-Vogt T., Verbiest T., Clays K.; A Sandwich Approach towards Inverse Opals with Linear and Nonlinear Optical Functionalities; *ACS Appl. Mater. Interfaces*, 6(6), 3870-3878 (2014).

Cabus S., **Bogaerts K**., Van Mechelen J.,Smet M., Goderis B.;Monotropic Polymorphism in Ester-Based Phase Change Materials from Fatty Acids and 1,4-Butanediol; *Cryst. Growth Des*., 13 (8), 3438-3446 (2013)

CONFERENCE PROCEEDINGS

Bogaerts K., Goderis B.; Morphology of Nanostructured Epoxies; Poster Presentation, Belgian Polymer Group 2014, Ghent (Belgium).

Bogaerts K., GoderisB.; Morphology and Mechanical Properties of Reinforced Nanostructured Epoxies; Oral Presentation, X-ray Investigations of Polymer Structure 2013, Zakopane (Poland).

Bogaerts K., Goderis B.; Nanomorphologyof Copolymers and Carbon Nanotubes in a Hybrid Thermosetting Epoxy Resin Blend; Poster Presentation, Belgian Polymer Group 2013, Houffalize (Belgium).

Bogaerts K., Goderis B.; Nanomorphology of Stearyl –Poly(ethylene oxide) Block Copolymers in Blends with a Thermosetting Epoxy Resin; Poster Presentation, Third International Conference on Multifunctional, Hybrid and Nanomaterials 2013, Sorrento (Italy).

Bogaerts K., Lavrenova A., Goderis B.; Stearyl–Poly(ethylene oxide) copolymers in a Thermosetting Epoxy Matrix: Morphology and Curing Kinetics; Poster Presentation, Belgian Polymer Group 2012, Blankenberge (Belgium).

CURRICULUM

Kevin Bogaerts
kevin.bogaerts@outlook.com
03/March/1987
+32 497 05 35 37
Gladiolenstraat 49A
2250 Olen

EDUCATION

PhD in Polymer Chemistry
2010 – 2022
KU Leuven
PhD dissertation:
Curing and Nanostructure Development in Epoxy/Block Copolymer blends
Promotor: Prof. dr. Bart Goderis

Master of Science in Chemistry
2005 – 2010
KU Leuven
Cum laude
Master Thesis:
Structure and stability of Specialty-Lipids: A quest for polymer-like mesomorphic phases
Promotor: Prof. dr. Bart Goderis
Internship (2009): Royal DSM nv (Geleen, NL);
Report: **Fuel Permeability of Polyamides**

WORKING EXPERIENCES

Project Manager Healthcare
Sep 2022 – Present
Plastiflex Group N.V.

R&D Project Manager
Apr 2017 – Sep 2022
Xeikon Manufacturing NV

Junior Project Manager Inkjet Inks
Jun 2015 – Dec 2016
Agfa-Gevaert N.V.